

ABSTRACT

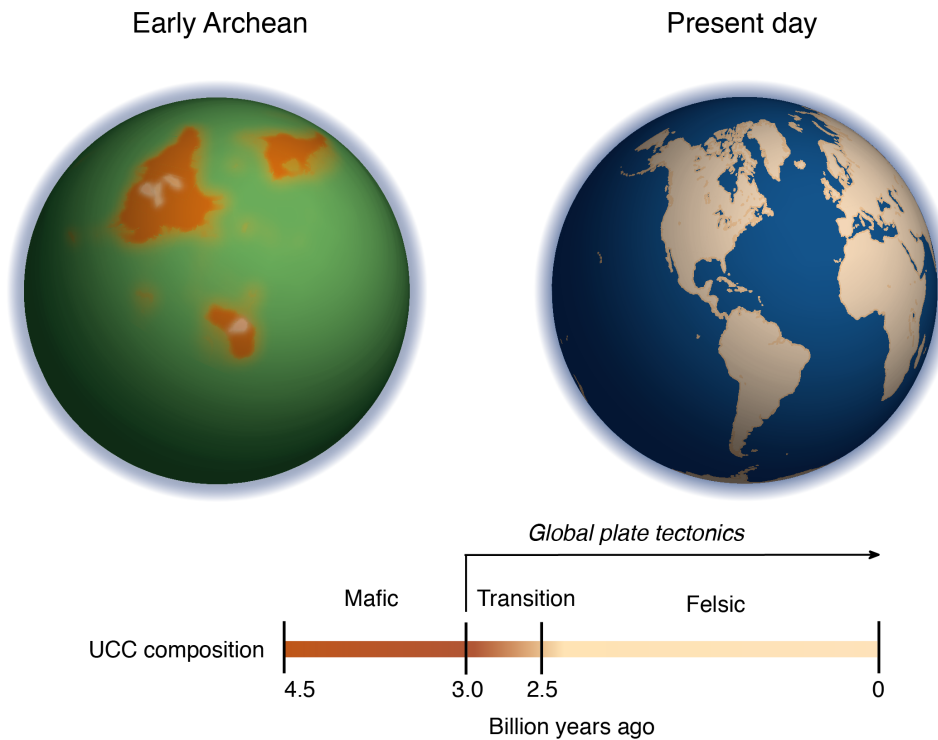
Title of Dissertation: GEOCHEMISTRY OF CRUSTAL
 FORMATION AND EVOLUTION

Ming Tang, Doctor of Philosophy, 2016

Dissertation directed by: Professors William F. McDonough and Roberta
 L. Rudnick, Department of Geology

Terrestrial planets produce crusts as they differentiate. The Earth's bi-modal crust, with a high-standing granitic continental crust and a low-standing basaltic oceanic crust, is unique in our solar system and links the evolution of the interior and exterior of this planet. Here I present geochemical observations to constrain processes accompanying crustal formation and evolution. My approach includes geochemical analyses, quantitative modeling, and experimental studies.

The Archean crustal evolution project represents my perspective on when Earth's continental crust began forming. In this project, I utilized critical element ratios in sedimentary records to track the evolution of the MgO content in the upper continental crust as a function time. The early Archean subaerial crust had >11 wt. % MgO, whereas by the end of Archean its composition had evolved to about 4 wt. % MgO, suggesting a transition of the upper crust from a basalt-like to a more granite-like bulk composition. Driving this fundamental change of the upper crustal composition is the widespread operation of subduction processes, suggesting the onset of global plate tectonics at ~ 3 Ga (Abstract figure).



Abstract figure: Changes in the composition and area of the subaerial crust from the early Archean to the present-day. Before 3 billion years, Earth's proto-continental crust had restricted surface area, and had a mafic composition (rich in magnesium and iron), in contrast to the felsic composition (rich in Al and Si) today. The onset of global plate tectonics at around 3 billion years ago added voluminous granitic rocks to the surface and resulted in the rise of felsic continents. The color of the Archean ocean indicates a high concentration of dissolved Fe^{2+} (hence green) due to the low surface oxygen content at that time.

Three of the chapters in this dissertation leverage the use of Eu anomalies to track the recycling of crustal materials back into the mantle, where Eu anomaly is a sensitive measure of the element's behavior relative to neighboring lanthanoids (Sm and Gd) during crustal differentiation. My compilation of Sm-Eu-Gd data for the continental crust shows that the average crust has a net negative Eu anomaly. This result requires recycling of Eu-enriched lower continental crust to the mantle. Mass balance calculations require that about three times the mass of the modern continental crust was returned into the mantle over Earth history, possibly via density-driven recycling. High precision measurements of Eu/Eu* in selected primitive glasses of mid-ocean ridge basalt (MORB) from global MORs, combined with numerical

modeling, suggests that the recycled lower crustal materials are not found within the MORB source and may have at least partially sank into the lower mantle where they can be sampled by hot spot volcanoes.

The Lesser Antilles Li isotope project provides insights into the Li systematics of this young island arc, a representative section of proto-continental crust. Martinique Island lavas, to my knowledge, represent the only clear case in which crustal Li is recycled back into their mantle source, as documented by the isotopically light Li isotopes in Lesser Antilles sediments that feed into the fore arc subduction trench. By corollary, the mantle-like Li signal in global arc lavas is likely the result of broadly similar Li isotopic compositions between the upper mantle and bulk subducting sediments in most arcs.

My PhD project on Li diffusion mechanism in zircon is being carried out in extensive collaboration with multiple institutes and employs analytical, experimental and modeling studies. This ongoing project, finds that REE and Y play an important role in controlling Li diffusion in natural zircons, with Li partially coupling to REE and Y to maintain charge balance.

Access to state-of-art instrumentation presented critical opportunities to identify the mechanisms that cause elemental fractionation during laser ablation inductively coupled plasma mass spectrometry (LA-ICP-MS) analysis. My work here elucidates the elemental fractionation associated with plasma plume condensation during laser ablation and particle-ion conversion in the ICP.

GEOCHEMISTRY OF CRUSTAL FORMATION AND EVOLUTION

by

Ming Tang

Dissertation submitted to the Faculty of the Graduate School of the
University of Maryland, College Park, in partial fulfillment
of the requirements for the degree of
Doctor of Philosophy
2016

Advisory Committee:
Professor William F. McDonough, Chair
Professor Roberta L. Rudnick
Professor Wenlu Zhu
Professor Haibo Zou

© Copyright by
Ming Tang
2016

Dedication

My PhD dissertation is dedicated to my parents, who respect and support my choices with love, and all the wonderful people that have been painting my life.

“...but in reality nothing is more damaging to the adventurous spirit within a man than a secure future.”

from <Into The Wild> by Jon Krakauer

Acknowledgements

Five years ago, when I was applying for U.S. Ph.D. positions, my undergraduate advisor Xiao-Lei Wang suggested that I also apply for a graduate position at Nanjing University. “In this way I can back you up in case your applications were rejected. You can quit here at any point once you get a good offer from the U.S.,” said Xiao-Lei. I thanked him, but didn’t take this considerate offer and be “safe”. Among the seven universities I applied for, UMD is the only one that accepted my application. It was Bill and Roberta, my Ph.D. advisors, who gave me the opportunity to work in one of the top geochemistry groups in the world.

My life here has been joyful and exciting because of the people that I met.

Bill and Roberta, being two of the top scientists in the world, have distinct personalities, and they have been guiding me through this early stage of my research career from different perspectives. Bill is a “can-do” person, and so is the way he taught me from day one. Being positive has been continuously creating possibilities for my research. Working with Roberta has always been efficient and productive. Her being open-minded boosts my imagination while her being strict on every detail always keeps me on track. Roberta’s expertise in crustal evolution also makes me feel more confident in my research. I know she’s always there to back me up.

Without my collaborators’ efforts, most of my research projects would have gone nowhere. Specifically, the Smithsonian Institute loaned me precious MORB samples for my MORB Eu project, and provided me the access to their SEM and ToF-SIMS instruments; Whenever I had a question or a problem with the ICP-MS instruments in our lab, Richard Ash was always there to help; Rick Arevalo brought in a particle sizer which finally solved a year long debate between Bill and me on the relationship between REE fractionation and particle size distribution; Rick also helped me revise two analytical papers; Catherine Chauvel kindly provided Lesser Antilles arc lava and sediment core samples to me for arc Li

isotope study; Xiao-Ming Liu was my shepherd in the chemistry lab; Yulia Goreva assisted me, for free, in operating ToF-SIMS to map chemical compositions of natural zircons and laser-generated condensation blankets; Dustin Trail taught me step by step in his lab to study Li diffusion in zircons by experiments. At the same time, Dustin and his wife Chiara kindly accommodated me in their place during my multiple visits, with wine, great food and fun; Maitrayee Bose assisted me in operating NanoSIMS at ASU throughout the analytical sessions; Yu Huang kindly shared with me a crustal rock database he compiled, and much of my later compilation work started from this dataset; Kang Chen encouraged and inspired me in the early stage our Archean crustal evolution project, and helped in data compilation and interpretation.

Talking with other people, especially those “big names”, has always been exciting and rewarding experiences during my research. And this is actually how I sold myself to Roberta and Bill five years ago. I remember last year at the Goldschmidt conference, Alex Sobolev, standing in front of my poster, talked to me after our discussion of my work. “...Defend your science, but don’t believe it,” said Alex. When I was visiting my friends in Houston, I got a chance to talk to Cin-Ty Lee, and that’s when I started to know “positive science” and “negative science”, and “there are more things we can do than just killing other people’s ideas”. Not in specific order, I thank feedbacks on my research from Chris Hawkesworth, Kent Condie, Don Lowe, Igor Puchtel, Rich Walker, Mike Brown, Rich Gaschnig, Mike Evans, Angela Hessler, Al Hofmann and my office mates Greg Archer, Emily Worsham, Kristy Long and Mitchell Haller.

My friends here have been giving me lots of fun. We went to the bars and parks. Together we cooked, played games and did sports. Tricks, treats and laughter.

My research was financially supported by NSF grants EAR-0948549, 1067983, 0739006, 1321954, an Ann G. Wylie Fellowship and Summer Research Fellowship from UMD graduate school, a GSA Graduate student research grant, an MGPV student research

award, a Goldschmidt student grant, an ICSSA grant, a Goldhaber travel grant and two
ESSIC travel grants.

01/23/2016

Table of Contents

Dedication	ii
Acknowledgements.....	iii
Table of Contents	vi
List of Tables	IX
List of Figs	IX
Chapter 1: Introduction.....	IX
Chapter 2: High-precision measurement of Eu/Eu* in geological glasses via LA-ICP-MS analysis.....	7
2.1. Introduction	8
5.2. Laser ablation induced fractionation mechanisms	9
2.3. Experimental.....	11
2.3.1. LA-ICP-MS.....	11
2.3.2. Particle size distribution measurement.....	13
2.3.3. Reference materials and data reduction	14
2.4. Results and discussion.....	14
2.4.1. Spectral matrix effects.....	14
2.4.2. Non-spectral matrix effects	15
2.5. Conclusions	29
References	30
Chapter 3: Elemental fractionation during condensation of plasma plumes generated by laser ablation: a ToF-SIMS study of condensate blankets	34
3.1. Introduction	35
3.2. Experimental.....	36
3.2.1. Laser ablation	36
3.2.2. Secondary Electron Microprobe (SEM) imaging	37
3.2.3. ToF-SIMS	37
3.3. Results and discussion.....	38
3.4. Conclusions	49
References	49
Appendix	53
Chapter 4: Europium anomalies constrain the mass of recycled lower continental crust	58
4.1. Introduction	58
4.2. Sm-Eu-Gd systematics in the continental crust.....	59
4.3. The Eu dilemma	63
4.4. Calculating the mass of the recycled lower crust	64
4.5. Conclusions	69
References	70
Appendix	74

Chapter 5: Europium anomaly in the MORB source mantle.....	84
5.1. Introduction	85
5.2. Samples and analytical methods.....	86
5.3. Results	88
5.4. Discussion and modeling.....	90
5.4.1. The MgO criterion.....	90
5.4.2. Modeling	91
5.5. Conclusions	99
References	100
Appendix	103
 Chapter 6: Archean upper crust transition from mafic to felsic marks the onset of plate tectonics	 106
Main text	106
References and notes.....	115
Appendix.....	118
 Chapter 7: Sedimentary input to the source of Lesser Antilles lavas: a Li perspective.....	 124
7.1. Introduction	125
7.2. Geological background and samples	128
7.3. Analytical techniques	132
7.4. Results	133
7.4.1. Martinique lavas.....	133
7.4.2. Sediments from DSDP Sites 543 and 144.....	138
7.5. Discussion.....	139
7.5.1. Low $\delta^7\text{Li}$ subducting sediments	139
7.5.2. High $\delta^7\text{Li}$ lavas.....	145
7.5.3. Low $\delta^7\text{Li}$ components in Martinique lavas.....	145
7.6. Conclusions	153
References	153
Appendix	165
 Chapter 8. Mechanism of Li diffusion in zircon.....	 170
8.1. Introduction: Li in zircon as a tracer of magmatic sources or a geospeedometer?	171
8.1.1. Mechanisms of Li isotopic fractionation.....	172
8.1.2. Li isotopes in zircons	173
8.2. Samples.....	177
8.3. Methods	177
8.3.1. ToF SIMS imaging.....	177
8.3.2. NanoSIMS isotope profiling	178
8.4. Results	178
8.4.1. ToF SIMS imaging.....	178
8.4.2. NanoSIMS.....	183
8.5. Modeling and discussion	183
8.5.1. Assumptions.....	184
8.5.2. Governing equations	186
8.5.3. Implications from modeling.....	190
8.6. Conclusions and future work.....	191
References	192
 Chapter 9. Summary and outlook	 199

9.1. Summary.....	199
9.2. Outlook	201
References	203

List of Tables

Table 2.1. The instrumental operation conditions used for LA-ICP-MS analysis.....	12
Table 4.1. Mean concentrations of Sm, Eu and Gd in the continental crust and candidates of recycled lower continental crust.....	60
Table 5.1. Partition coefficients and diffusion coefficients used in the model.....	92
Table 5.2. Notation used in modelling.....	93
Table 7.1. Li isotope compositions of the sediments from DSDP Sites 543 and 144.....	131
Table 7.2. Li isotope compositions of the Martinique lavas.....	134
Table 7.3. Measured $\delta^7\text{Li}$ and [Li] in rock standards compared with reported values.....	136
Table 8.1. Li isotope and concentration data for reference zircons.....	176
Table 8.2. Notation used in modelling.....	185
Table A4.1. Lognormal means of Sm, Eu and Gd concentrations in the continental crust...74	74
Table A4.2. Bulk continental crust REE composition and Eu/Eu* of published models....79	79
Table A4.3. Lower crust major element compositions from this study (average of samples used to calculate Eu/Eu*) compared with previous studies.....79	79
Table A4.4. Middle crust major element compositions from this study (average of samples used to calculate Eu/Eu*) compared with previous studies.80	80
Table A5.1. Measured Eu/Eu* and MgO contents in high MgO MORBs.....	103

List of Figures

Fig. 2.1. Measured REE isotopic ratios compared with natural abundance ratios.....	16
Fig. 2.2. Relative difference between the measured REE concentrations and GeoRem preferred values.....	17

Fig. 2.3. Relative difference between the measured REE concentrations and GeoRem preferred values.....	19
Fig. 2.4. Number proportion of large particles (> 1 μm) vs. spot size in spot and line scanning modes.....	20
Fig. 2.5. Comparison of proportion of large particles produced in spot and line scanning modes.....	20
Fig. 2.6. Comparison of proportion of large particles produced by samples of different transparency (photon absorption rate).	21
Fig. 2.7. Relative difference between the measured REE concentrations and GeoRem preferred values.....	22
Fig. 2.8. Raw Eu/Eu* and Yb/Yb* increase with He flow rate.	29
Fig. 2.9. Intensity change induced by He flow change vs. condensation temperature from Lodders (Lodders, 2003).....	25
Fig. 2.10. Counts per second (cps) normalized to beam area.....	25
Fig. 2.11. Raw Eu/Eu* measured with 55 to 175 μm spots on BHVO-2G.....	27
Fig. 2.12. Relative difference between the measured Eu/Eu* and GeoRem preferred values.....	27
Fig. 2.13. Long-term analyses of Eu/Eu* in KL-2G and BIR-1G.....	28
Fig. 3.1. BSE images of the condensate blanket adjacent to the laser crater.	39
Fig. 3.2. Control BSE image of a polished section of the same NIST 610 sample after laser ablation, but located far (~5 mm) away from the ablation site.....	40
Fig. 3.3. Ca normalized Mg, Cs, Al, B, Ga and Si distributions across the condensate blanket (first integrated scan).....	42
Fig. 3.4. Depth profiles of Mg, Cs, Al, B, Ga and Si, all normalized to Ca.....	43
Fig. 3.5. Average X/Ca diff% between the inner and outer zonings.....	45

Fig. 3.6. Average X/Ca diff% between the inner and outer zones for alkaline and alkaline earth metal elements as a function of first ionization potential.....	46
Fig. 4.1. Histogram showing Eu/Eu* distribution in granulite facies samples.....	63
Fig. 4.2. Eu/Eu*, Eu vs. Mg# in granulite facies samples.....	65
Fig. 4.3. Mass proportion of recycled LCC (x-axis) needed to compensate the Eu depletion in the modern BCC relative to an original crust with Eu/Eu* = 1.....	67
Fig. 4.4. Eu/Eu* in OIBs and its correlation to Pb isotopes.....	69
Fig. 5.1. Sample locations of the MORB glasses studied.....	86
Fig. 5.2. Reproducibility of measured Eu/Eu* and MgO contents in MORB glasses.....	87
Fig. 5.3. Eu/Eu* vs. MgO in primitive MORB glasses analyzed here from global mid-ocean ridges (n = 72).	88
Fig 5.4. Mean Eu/Eu* observed in MORB with >9 wt.% MgO from this study compared with published estimates.	89
Fig. 5.5. Eu/Eu* in aggregated melts as a function of Eu (II) fraction, melting rate (yr ⁻¹) and melting degree.....	92
Fig. 5.6. Eu/Eu* in the instantaneous (residual) melts derived from a depleted source after 10% degree melting.....	98
Fig. 6.1. Igneous Ni/Co-MgO and Cr/Zn-MgO differentiation trends for Archean and post-Archean rocks.	108
Fig. 6.2. Ni/Co and Cr/Zn ratios in terrigenous fine-grained sedimentary rocks through time (A & C) compared with the present-day upper continental crust (B & D).....	110
Fig. 6.3. Average Ni/Co and Cr/Zn ratios vs. depositional ages in Archean fine-grained terrigenous sedimentary rocks from different localities.....	111
Fig. 6.4. Evolution of MgO content, relative mass (A) and the proportions of major rock types (B) of the upper continental crust in the Archean Eon.....	112

Fig. 7.1. Geological map showing Martinique Island in the Lesser Antilles arc and the two DSDP sites (from Labanieh et al., 2010).....	129
Fig. 7.2. Histogram showing Li isotopic compositions of Martinique lavas compared with MORB and other arc lavas.....	130
Fig. 7.3. $\delta^7\text{Li}$ vs. SiO_2 and $(\text{La}/\text{Sm})_N$ for Martinique lavas.....	136
Fig. 7.4. $\delta^7\text{Li}$ vs. Y/Li , $[\text{Li}]$, $[\text{Rb}]$ and $[\text{Cs}]$ for Martinique lavas.....	137
Fig. 7.5. $\delta^7\text{Li}$ vs. Sr-Nd-Pb-Hf isotopes for Martinique lavas.	138
Fig. 7.6. Distribution of average $\delta^7\text{Li}$ in subducting sediments from global trenches.....	140
Fig. 7.7. $\delta^7\text{Li}$ vs. CIA for subducting sediments from Lesser Antilles (larger symbols) and other arcs after Plank (2014).....	141
Fig. 7.8. $\delta^7\text{Li}$ and $[\text{Li}]$ vs. depth for the sediments from DSDP Sites 543 and 144.....	141
Fig. 7.9. $\delta^7\text{Li}$ vs. Al_2O_3 contents in the subducting sediments.....	142
Fig. 7.10. $\delta^7\text{Li}$ vs. $(\text{La}/\text{Sm})_N$ and Y/Li in the subducting sediments.....	144
Fig. 7.11. $\delta^7\text{Li}$ vs. Pb and Nd isotopes in the subducting sediments.....	144
Fig. 7.12. Plots of $\delta^7\text{Li}$ vs. age (a) and LOI (b) for Martinique lavas.....	146
Fig. 7.13. A two-component mixing model between depleted mantle and sediments from Sites 543 and 144.....	150
Fig. 8.1. Li isotopic compositions of Jack Hills zircons.....	174
Fig. 8.2. Oxygen and Li isotopic compositions in zircons.....	180
Fig. 8.3. CL images of two granulite zircons.....	179
Fig. 8.4. ToF-SIMS positive ion imaging of two granulite zircons.....	180
Fig. 8.5. High-resolution (ion beam ~ 300 nm) $[\text{Li}]$ imaging across the core-rim boundary of zircon LB04_19_02.....	180
Fig. 8.6. left column: CL images of five natural zircon grains.....	181
Fig. 8.7. NanoSIMS profiles of four natural zircons.....	182
Fig. 8.8. Modeled Li isotopic fractionation during zircon growth.....	189

Fig. A3.1. Alkaline metal composition depth profiles.....	53
Fig. A3.2. Alkaline earth metal composition depth profiles.	54
Fig. A3.3. B-Al-Ga composition depth profiles.....	54
Fig. A3.4. Transition metal and Si composition depth profiles.	55
Fig. A3.5. X/Ca distributions across the condensate blanket (first integrated scan).....	56
Fig. A3.6. X/Ca distributions across the condensate blanket (fifteenth integrated scan)....	57
Fig. A4.1. Distributions of Sm, Eu and Gd concentrations in the continental crust.....	76
Fig. A4.2. Distributions of log-transformed Sm, Eu and Gd concentrations in the continental crust.....	76
Fig. A4.3. Distributions of mean Sm, Eu and Gd concentrations (in ppm) and Eu/Eu* in the bulk continental crust (BCC).....	77
Fig. A4.4. Distributions of Sm, Eu, Gd concentrations (in ppm) and Eu/Eu* in the simulated BCC samples. Logarithmic transformation of the data resulted in Gaussian distributions..	78
Fig. A4.5. Published REE composition models for the BCC.	78
Fig. A4.6. BCC Eu/Eu* as functions of LCC Mg#, SiO ₂ content and mid-REE (Sm considered here) concentration, respectively.	81
Fig. A4.7. ⁸⁷ Sr/ ⁸⁶ Sr vs. Eu/Eu* in OIB locality averages.	82
Fig. A6.1. Plot of Ni/Co vs. MgO content in Archean craton samples (n = 9,273).....	118
Fig. A6.2. Plot of Cr/Zn vs. MgO content in Archean craton samples (n = 6,970).....	118
Fig. A6.3. Ni/Co- and Cr/Zn-MgO in simulated mixtures using Archean craton samples. Each dot represents a mixing scenario.....	120
Fig. A7.1. Long-term analyses of Li reference materials UMD-1 and IRMM-016.....	167

Chapter 1: Introduction

Earth is unique in many ways. It is the only planet in the solar system that has continental crust—the high standing crust that has a felsic bulk composition. When and how did the continental crust form on Earth? For a land species like us, this question is more than academic because we owe our existence to Earth’s continents. The composition, growth, and evolution of the continental crust are closely related to many geological processes, including the evolution of life. Although our knowledge of the continental crust has grown enormously since the 19th century when F.W. Clarke first estimated the composition of the continental crust (Clarke, 1889), significant questions regarding its origin and evolution remain today. Below I highlight how the research undertaken in this dissertation contributes to our knowledge of the origin and evolution of the continental crust.

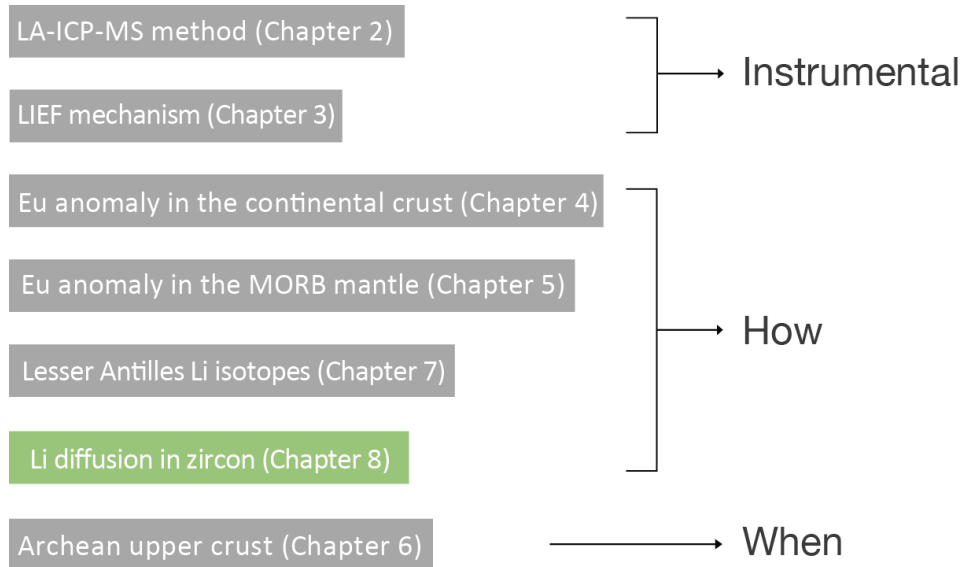


Fig. 1.1. Chart showing my projects grouped by their contributions to three topics including how did continental crust form, when did the continental crust form and methods

development. Projects in gray are completed while the Li diffusion in zircon is an ongoing project.

My PhD study started with method development. Chapters 2 and 3 are devoted to understanding the mechanisms of elemental fractionation during Laser ablation inductively coupled plasma mass spectrometry (LA-ICP-MS) measurements. LA-ICP-MS, after two decades of development, has now become a powerful and cost effective tool in micro-analytical geochemistry. I used this method in my Eu project on mid-ocean ridge basalt (MORB) (Chapter 5) to obtain high precision data on the degree of a Eu anomaly in these lavas. The uncertainty of this laser ablation method largely derives from REE fractionation accompanying particle formation during condensation of laser-induced plasma and subsequent particle-ion conversion in the ICP (Chapter 2). While working on the Li diffusion project, I teamed up with Yulia Goreva (Smithsonian Institution) and further explored the mechanism of elemental fractionation during laser ablation by ion imaging of the condensation blankets (Chapter 3).

How did the continental crust form? The highly differentiated nature of the continental crust has led to the consensus that it cannot be derived directly from a partial melt of the mantle, which is mafic to ultramafic. What's needed is intra-crustal differentiation and crustal recycling to solve this composition problem, and several hypotheses have been proposed, including lower crustal recycling (Arndt and Goldstein, 1989; Kay and Mahlburg-Kay, 1991; Rudnick, 1995; Jull and Kelemen, 2001), upper crustal weathering (Lee et al., 2008; Liu and Rudnick, 2012), subduction erosion (Clift et al., 2009; Lee, 2014, and references therein) and crustal subduction followed by relamination (Hacker et al., 2011). Most of these processes have been observed, but the relative importance of each process in shaping the composition of the continental crust is uncertain, as is the question of whether these processes have changed over Earth history. Geochemical modeling based on large data compilations may

provide first-order constraints on these questions. My efforts have focused on Sm-Eu-Gd systematics in rocks from the crust and mantle (Chapters 2, 4 and 5) in order to quantify the amount of lower crust that has been removed and recycled back into the mantle through Earth history. The fractionation between multi-valent Eu (Eu^{2+} and Eu^{3+}) and mono-valent Sm and Gd (3+) during intra-crustal differentiation (where ascending granitic melts leave behind depleted mafic residues) makes the Eu anomaly a useful tracer of lower crustal recycling versus upper crustal recycling, as the lower crust ends up with a net positive Eu anomaly, while the upper crust inherits a net negative Eu anomaly. Mass balance calculations based on Sm-Eu-Gd systematics in the modern continental crust can thus constrain the total mass of crustal materials lost to the mantle via lower crustal recycling (Chapter 4). The fate of recycled lower crustal materials can then be tracked by measuring mantle-derived samples e.g., MORB and ocean island basalts (OIB). In Chapter 5, I discuss my work on Eu anomalies in primitive MORB glasses from global MORs and where the recycled lower crustal materials may reside in the mantle.

When did the continental crust form? This question is closely related with another fundamental question in geoscience—when did plate tectonics begin? Plate tectonics is another feature unique to Earth. Water is the crucial link between plate tectonics and the formation of continental crust. Generation of the large amount of granite contained within the continental crust requires water in the source region, and subduction is probably the most efficient way to transport water to the deep Earth. Geoscientists have long been seeking evidence of early subduction from Hadean granitic zircons (Harrison et al., 2008), subduction generated diamonds (Richardson and Shirey, 2008; Shirey and Richardson, 2011; Smart et al., 2016), eclogites (Pearson et al., 1995) and arc-type volcanic rocks (Smithies et al., 2007). However, these findings, possibly indicative of local subduction processes, may not reflect the global dynamics in the Archean. On the other hand, determining the timing of the formation of the continental crust, the major product of plate tectonics, provides insights for

when Earth entered the plate tectonics era, i.e., when plate tectonics started to show its influence on the Earth system. In Chapter 6, I use Ni/Co and Cr/Zn ratios in terrigenous sediments deposited over most of the geological record from ~3.3 Ga to present to track the bulk MgO content of the subaerial crust. Using the bulk MgO content of surface sediments of the time, I was able to date when the modern style of felsic continental crust started to form, which in turn constrains the onset of global plate tectonics.

What's the fate of the crustal materials recycled to the convecting mantle? As noted above, crustal recycling is an important process during continental crust formation and evolution. Crustal recycling can take the form of recycling of lower continental crust (through density foundering or subduction) or through subduction of terrigenous sediment in convergent margins. Recycled crustal materials modify the chemical composition of the mantle, and different recycling processes may bring crustal materials of distinct chemical and isotopic compositions to the deep Earth. From a mantle perspective, Chapters 5 and 7 discuss the recycling of lower and upper crustal materials, respectively. In Chapter 5, I evaluated the Eu anomaly in primitive MORB glasses from global MORs in order to determine whether the MORB source contains recycled lower continental crust. Combined with geochemical modeling, I attempted to address where the recycled lower crustal materials reside in the mantle; Chapter 7 is a Li isotopic study of Lesser Antilles arc lavas and subducting sediments. This work aims to understand subducted sedimentary input to the Lesser Antilles arc, with broader implication for Li recycling in arc systems.

Chemical weathering plays a critical role in shaping the composition of the continental crust and regulating the chemistry of the atmosphere and ocean (Lee et al., 2008; Liu and Rudnick, 2011). Tracking chemical weathering on the early Earth has been challenging due to the lack of records that reliably reflect past conditions. Lithium isotopes in zircon have been proposed as a potential tracer of weathering signatures in the Hadean (Ushikubo et al., 2008), based on the highly variable, but significant low $\delta^7\text{Li}$ values observed in some of those

zircons. The interpretation of this record of $\delta^7\text{Li}$ values in the Hadean zircons, however, has been questioned due to uncertainty regarding the extent of differential diffusion of ^6Li and ^7Li in zircon. In fact, Li in zircon may provide a new geo-speedometer if significant differential diffusion of Li isotopes in zircon happens under magmatic and metamorphic conditions. Chapter 8 investigates the mechanism of Li diffusion in zircon based on high-resolution ion imaging and isotope profiling of natural zircons and numerical modeling. This work emphasizes the effect of charge coupling between REE+Y and Li on Li diffusion in zircon.

References

- Arndt, N.T., Goldstein, S.L., 1989. An open boundary between lower continental crust and mantle: its role in crust formation and crustal recycling. *Tectonophysics* 161, 201-212.
- Clift, P.D., Schouten, H., Vannucchi, P., 2009. Arc-continent collisions, sediment recycling and the maintenance of the continental crust. *Geol. Soc. London Spec. Publ.* 318, 75-103.
- Hacker, B.R., Kelemen, P.B., Behn, M.D., 2011. Differentiation of the continental crust by relamination. *Earth Planet. Sci. Lett.* 307, 501-516.
- Harrison, T.M., Schmitt, A.K., McCulloch, M.T., Lovera, O.M., 2008. Early (≥ 4.5 Ga) formation of terrestrial crust: Lu–Hf, $\delta^{18}\text{O}$, and Ti thermometry results for Hadean zircons. *Earth and Planetary Science Letters* 268, 476-486.
- Jull, M., Kelemen, P.B., 2001. On the conditions for lower crustal convective instability. *J. Geophys. Res.: Solid Earth* 106, 6423-6446.
- Kay, R.W., Mahlburg-Kay, S., 1991. Creation and destruction of lower continental crust. *Geologische Rundschau* 80, 259-278.
- Lee, C.-T.A., Morton, D.M., Little, M.G., Kistler, R., Horodyskyj, U.N., Leeman, W.P., Agranier, A., 2008. Regulating continent growth and composition by chemical weathering. *Proceedings of the National Academy of Sciences* 105, 4981-4986.

- Liu, X.-M., Rudnick, R.L., 2011. Constraints on continental crustal mass loss via chemical weathering using lithium and its isotopes. *Proceedings of the National Academy of Sciences* 108, 20873-20880.
- Pearson, D.G., Snyder, G.A., Shirey, S.B., Taylor, L.A., Carlson, R.W., Sobolev, N.V., 1995. Archaean Re-Os age for Siberian eclogites and constraints on Archaean tectonics. *Nature* 374, 711-713.
- Richardson, S.H., Shirey, S.B., 2008. Continental mantle signature of Bushveld magmas and coeval diamonds. *Nature* 453, 910-913.
- Rudnick, R.L., 1995. Making continental crust. *Nature* 378, 571-578.
- Shirey, S.B., Richardson, S.H., 2011. Start of the Wilson cycle at 3 Ga shown by diamonds from subcontinental mantle. *Science* 333, 434-436.
- Shu, Q., Brey, G.P., Hofer, H.E., Zhao, Z., Pearson, D.G., 2016. Kyanite/corundum eclogites from the Kaapvaal Craton: subducted troctolites and layered gabbros from the Mid- to Early Archean. *Contr. Mineral. and Petrol.* 171, 1-24.
- Smart, K.A., Tappe, S., Stern, R.A., Webb, S.J., Ashwal, L.D., 2016. Early Archaean tectonics and mantle redox recorded in Witwatersrand diamonds. *Nature Geosci* advance online publication.
- Smithies, R.H., Van Kranendonk, M.J., Champion, D.C., 2007. The Mesoarchean emergence of modern-style subduction. *Gondwana Research* 11, 50-68.
- Ushikubo, T., Kita, N.T., Cavosie, A.J., Wilde, S.A., Rudnick, R.L., Valley, J.W., 2008. Lithium in Jack Hills zircons: Evidence for extensive weathering of Earth's earliest crust. *Earth and Planetary Science Letters* 272, 666-676.

Chapter 2: High-precision measurement of Eu/Eu* in geological glasses via LA-ICP-MS analysis

[1] Tang, M., McDonough, F. W., Arevalo, R., Jr. (2014) High-precision measurement of Eu/Eu* in geological glasses via LA-ICP-MS analysis. *Journal of Analytical Atomic Spectrometry*, 29(10), 1835-1843.

[2] M.T. designed the experiments, carried out the analyses, interpreted the data and wrote the manuscript; W.F.M. helped in data interpretation and provided comments on the manuscript; R.A. helped in experimental design and commented on the manuscript.

Abstract

Elemental fractionation during laser ablation inductively coupled plasma mass spectrometry (LA-ICP-MS) analysis has been historically documented between refractory and volatile elements. In this work, however, we observed fractionation between light rare earth elements (LREE) and heavy rare earth elements (HREE) when using ablation strategies involving large spot sizes ($>100\ \mu\text{m}$) and line scanning mode. In addition (1) ion yields decrease when using spot sizes above $100\ \mu\text{m}$; (2) $(\text{Eu}/\text{Eu}^*)_{\text{raw}}$ positively correlates with carrier gas (He) flow rate, which provides controls over the particle size distribution of the aerosol reaching the ICP; (3) $(\text{Eu}/\text{Eu}^*)_{\text{raw}}$ shows positive correlation with spot size, and (4) the changes in REE signal intensity, induced by the He flow rate change, roughly correlate with REE condensation temperatures. The REE fractionation is likely driven by the slight but significant difference in their condensation temperatures. Large particles may not be completely dissociated in the ICP and result in preferential evaporation of the less refractory LREEs and thus non-stoichiometric particle-ion conversion. This mechanism may also be responsible for Sm-Eu-Gd fractionation as Eu is less refractory than Sm and Gd. The extent

of fractionation depends upon particle size distribution of the aerosol, which in turn, is influenced by the laser parameters and matrix. Ablation pits and lines defined by low aspect ratios produce a higher proportion of large particles than high aspect ratio ablation, as confirmed by measurements of particle size distribution in the laser induced aerosol. Therefore, low aspect ratio ablation introduces particles that cannot be decomposed and/or atomized by the ICP and thus results in exacerbated elemental fractionation. Accurate quantification of REE concentrations and Eu/Eu* requires reduction of large particle production during laser ablation. For the reference materials analyzed in this work, the 100 μm spot measurements of Eu/Eu* agreed with GeoRem preferred values within 3%. Our long-term analyses of Eu/Eu* in MPI-DING glass KL-2G and USGS glass BIR-1G were reproducible at 3% (2 RSD).

2.1. Introduction

Laser ablation-inductively coupled plasma-mass spectrometry (LA-ICP-MS) can provide spatially resolved, high-precision measurements of elemental concentrations. Accurate quantitation by LA-ICP-MS relies on effective external and internal standard calibration to address elemental and isotopic fractionation. However, the fractionation process is matrix dependent (Becker et al., 2000; Eggins et al., 1998), and may vary with ablation and ICP conditions (Aeschliman et al., 2003; Guillong and Gunther, 2002; Kuhn et al., 2004).

Rare earth element (REE) geochemistry, such as REE normalized abundances and Eu anomalies, can provide insights into various geological processes. Europium anomalies (Eu/Eu*, defined as $\text{Eu}_N/\sqrt{\text{Sm}_N \times \text{Gd}_N}$, where the subscript N indicates chondrite normalized concentrations) have been used as oxybarometers of planetary bodies (McKay et al., 1994; Shearer et al., 2006; Wadhwa, 2001) due to the multivalent nature of Eu under planetary redox conditions. Eu/Eu* in zircon has also been used to investigate redox

potentials in magmas (Trail et al., 2012). A recent study (Niu and O'Hara, 2009) revealed a regional correlation between Eu/Eu* and MgO in mid-ocean ridge basalts (MORBs) from the East Pacific Rise (EPR), and suggested the potential use of Eu/Eu* as an indicator of magmatic evolution and crustal recycling processes. However, accurate and high-precision in situ determination of REEs at low concentrations (sub-ppmw to tens of ppmw) is challenging. Complications derived from matrix effects, laser parameters and dynamics within the ablation plume and the ICP torch serve to inhibit the precision and accuracy of these measurements. Although REEs are refractory (having condensation temperatures in a gas at 10^{-4} atm > 1000 °C (Lodders, 2003), they can nonetheless be fractionated relative to one another during LA-ICP-MS analysis, leading to systematic errors even when the reference materials are compositionally well-matched to the sample unknowns. In this work, we measured REE concentrations and Eu/Eu* in glasses of various compositions (*i.e.*, SiO₂ from 45.5% to 58.6%), and characterized the mechanisms and sources of REE fractionation by studying the relative impacts of different laser parameters (repetition rate, beam size and ablation pattern) and carrier gas (He) flow rates.

5.2. Laser ablation induced fractionation mechanisms

Multiple physical and chemical processes are involved in laser ablation processing. Generally, sample decomposition is induced by photon absorption, denoted as a photophysical process including both photothermal (thermal) and photochemical (non-thermal) activation (Bäuerle, 2011). Photothermal activation occurs when thermal relaxation rates are shorter than the pulse width. Photothermal activation results in thermal ablation by increasing the temperature in the radiation–matter interaction zone, leading to surface melting, sublimation and vaporization. In this case, the laser beam can be simply regarded as a heat source. On the other hand, photochemical activation results in direct bond breaking by

on timescales shorter than phonon relaxation rates. Both thermal and non-thermal ablation mechanisms contribute to mass removal for most nanosecond- and picosecond-pulsed lasers. These two types of ablation processes may also contribute to laser induced elemental fractionation (LIEF), or non-stoichiometric ablation, via different mechanisms. In the case of thermal ablation, distinct thermal properties (*e.g.*, melting and boiling point) of different elements or geological matrices (*e.g.*, minerals, phases, *etc.*) give rise to preferential evaporation (Liu et al., 2003; Mao et al., 1996; Mao et al., 1998). In addition, surface melting and convection may lead to surface deformation, zone refinement of the melt, and chemical inhomogeneities of the resolidified material (Bäuerle, 2011; Cromwell and Arrowsmith, 1995). Elemental fractionation induced by photochemical ablation may be associated with ionization potentials of elements and subsequent selective ionization during photon-electron coupling (Bäuerle, 2011; Mao et al., 1998).

The primary drivers behind the fractionation mechanisms described above are laser parameters (*e.g.*, wavelength, intensity and pulse duration) and the physical and chemical properties of the material (Bäuerle, 2011). An example is laser ablation of brass, a notoriously challenging material to analyze by LA-ICP-MS or LA-ICP-AES. The distinct thermal and ionization properties of its two major chemical components, *i.e.*, Cu and Zn, lead to their contrasting behaviors when brass is ablated by nanosecond and picosecond lasers due to differences in condensation temperatures and electronic structures of these elements (Mao et al., 1998). Generally, the efficiency of coupling between laser energy and the sample inversely correlates with laser wavelength, pulse duration and sample transparency. High-energy photons (*e.g.*, ultraviolet and shorter wavelengths) can ionize more efficiently via single-photon absorption components in the sample (Guillong et al., 2003; Horn et al., 2001). Long-pulse lasers (*e.g.*, 10^{-9} to 10^{-12} s) generate more thermal effects as a consequence of thermal relaxation within the radiation-matter interacting zone (Richardson et al., 2004) and plasma shielding effect (Eggins et al., 1998; J. G. Mank and R. D. Mason, 1999; Mao et al.,

1996; Shannon et al., 1995). A laser induced plasma extending from the sample surface towards the incident radiation serves to absorb the laser energy that would otherwise couple to the sample; the absorption of incident photons during long laser pulses causes the plume to expand and results in direct heating of the sample via plasma-sample interaction. Since the work of Guillong and Günther (2002), particle size distribution has been recognized as another proxy of elemental fractionation because (1) elemental composition may be particle size dependent (Guillong et al., 2003; Kuhn et al., 2004) and (2) conversion of large particles into ions in the plasma may be incomplete and/or non-stoichiometric (Guillong and Gunther, 2002; Jeong et al., 1999; Krosiakova and Gunther, 2007). Crater development has been shown to influence laser-matter interaction, particle size distribution and elemental fractionation (Borisov et al., 2000; Eggins et al., 1998; Guillong et al., 2003; J. G. Mank and R. D. Mason, 1999). The aerosols produced can be significantly enriched in volatile elements (*e.g.*, Zn, Cd, Te, Se, Bi, etc.) during ablation of deep craters (depth-to-diameter ratio > 6) (Eggins et al., 1998). Despite significant signal reduction, negligible fractionation of refractory elements (*e.g.*, REEs, Y, U, Ca, etc.) was observed even when the crater aspect ratios exceed 10 in Mank and Mason's study (1999), with fractionation between volatiles and non-volatiles dominantly attributed to plasma-sample interaction in deep craters. Moreover, González *et al.* (González et al., 2004) and Zhu et al. (Zhu et al., 2013) compared scanning and spot ablation, and found that spot ablation provided better accuracy and precision, and was less matrix-dependent than scanning ablation.

2.3. Experimental

2.3.1. LA-ICP-MS

The measurements of REEs in multiple geological reference glasses were performed using a Thermo Finnigan Element 2 (Thermo Fisher Scientific, Waltham, Massachusetts,

USA), a single-collector, sector field, ICP-MS, coupled to a New Wave Research, frequency-quintupled (213 nm) Nd: YAG laser system (Electro Scientific Industries, Inc. Portland, OR, USA) in the Department of Geology, Plasma Laboratory at the University of Maryland.

Detailed operating conditions are reported in Table 2.1.

The sampler cone and skimmer cone were cleaned to remove surface oxides each day. Both the ICP-MS and laser ablation system were allowed to warm up for 3 to 4 hours after plasma ignition. Prior to analysis, the ion lenses and ICP-MS torch position were tuned to maximize the signals on ^{43}Ca , ^{139}La and ^{180}Hf while maintaining $^{238}\text{U}^{16}\text{O}/^{238}\text{U} \leq 0.2\%$ during ablation of NIST612. Each analytical session was limited to no longer than 8 hours after tuning.

Each individual analysis incorporated a 30 s background acquisition followed by 90 s spot or scanning analysis. The isotopes measured include ^{23}Na , ^{24}Mg , ^{27}Al , ^{29}Si , ^{43}Ca , ^{49}Ti , ^{55}Mn , ^{57}Fe , ^{139}La , ^{140}Ce , ^{141}Pr , ^{146}Nd , ^{147}Sm , ^{153}Eu , ^{157}Gd , ^{159}Tb , ^{163}Dy , ^{165}Ho , ^{166}Er , ^{169}Tm , ^{172}Yb and ^{175}Lu .

Table 2.1. The instrumental operation conditions used for LA-ICP-MS analysis

New Wave Nd: YAG laser parameters	
Wavelength	213 nm
Energy density	2–3 J cm ⁻²
Pulse duration	5 ns
Carrier gas	He
Ablation pattern	Single spot / line scanning
Laser beam size	55 μm, 80 μm, 100 μm, 125 μm, 150 μm, 175 μm
Repetition rate	5 Hz, 10 Hz, 20 Hz
Scanning speed	10 μm/s

Thermo Finnigan Element2 ICP-MS parameters

RF power	1250 W
HV	8 kV
Scan optimization	Speed
Mass resolution	300 (m/ Δ m)
Detection mode	Analogue or both
Sampler cone	1.0 mm ID Al-alloy
Skimmer cone	0.7 mm ID Al-alloy
Cool gas flow	16 L min ⁻¹ Ar
Auxiliary gas flow	1.5 L min ⁻¹ Ar
*Sample gas flow	0.8 L min ⁻¹ Ar
*Carrier gas flow	0.6 L min ⁻¹ He
Dwell time	5 ms at masses 23, 24, 27, 29, 43, 49, 55, 57; 30 ms at masses 139, 140, 141, 146, 147, 159, 163, 165, 166, 169, 172, 175; 50 ms at masses 147, 157/158; 100 ms at masses 153

* These gas flows were coupled at a T-junction prior to the plasma torch.

2.3.2. Particle size distribution measurement

The particle counter employed for this study was an Airy Technology P611, which has 6 channels of cumulative and different particle counts simultaneously, allowing for the detection of particles up to 0.3, 0.5, 0.7, 1.0, 2.0 and 5.0 microns. The counter detects about 50% of particles at 0.3 μ m, but 100% at >0.45 μ m. Reproducibility is better than 6%. The data are available in the supplementary material.

2.3.3. Reference materials and data reduction

The materials analyzed in this work were three basaltic USGS glasses (BHVO-2G, BIR-1G and BCR-2G) and five MPI-DING glasses including KL-2G (tholeiitic basalt), ML3B-G (tholeiitic basalt), GOR128-G (basaltic komatiite), GOR132-G (basaltic komatiite) and T1-G (andesitic quartz-diorite). The USGS reference materials BHVO-2G, BIR-1G and BCR-2G were used as external standards for calibration. The assumed values for the reference materials were taken from GeoRem (<http://georem.mpch-mainz.gwdg.de/>). Following Liu *et al.* (2008) and Humayun *et al.* (2010), we applied internal standardization by assuming that the sum of major element oxides ($\text{SiO}_2 + \text{CaO} + \text{FeO} + \text{MgO} + \text{Al}_2\text{O}_3 + \text{MnO} + \text{Na}_2\text{O} + \text{TiO}_2$) equals 100%. The advantage of this method is that it doesn't require a second analytical measurement to obtain the concentration for a single element used as an internal standard. This method led to a maximum of 2% absolute overestimation of element concentrations, as K_2O and P_2O_5 were not included. All data are provided in the supplementary file.

2.4. Results and discussion

2.4.1. Spectral matrix effects

Spectral matrix effects occur when specific isotope currents in the mass spectrum are overlapped by spectrometric species. These types of interferences include isobaric spectral overlap, polyatomic molecular ion overlap, multiple charged species, and background contribution to the measurement of the ion current (Taylor, 2001). In addition, space charge effect, which results in beam defocusing, also contributes to spectral matrix effect. To examine spectral matrix effects, isotopic ratios of seven REEs, which were measured prior to concentration determination, mostly agree with the true values within uncertainty (Fig. 2.1). These analyses were not corrected for mass fractionation, which would induce ~1% offset per

amu for the REE. Although poorly resolved by the precision, the measured isotopic ratios 143/146, 147/149, 151/153 and 157/158 appear to be systematically higher than the true values. This is because when scanning 143 through 174, the magnet mass was set at 143 and 167. Within each magnet mass, the Element2 performed high voltage scan (E-scan) and reached the next mass peak by decreasing the acceleration voltage. This results in continuous sensitivity reduction when scanning from low mass to high mass, and thus elevated ratios of light isotopes to heavy isotopes.

2.4.2. Non-spectral matrix effects

Non-spectral matrix effects can be induced by non-stoichiometric sampling during laser ablation, particle loss during transport and material dissociation and ionization in the ICP. Non-spectral matrix effects may not be effectively calibrated by external standards, particularly those that are poorly matrix-matched with the sample unknowns, and result in analytical error. Understanding the mechanisms of non-spectral matrix effects and reducing their impact is key to achieving quantitative data accuracy and reproducibility. In order to reduce non-spectral matrix effects, we maintained a constant laser energy density at 2–3 J cm⁻² throughout the experiments.

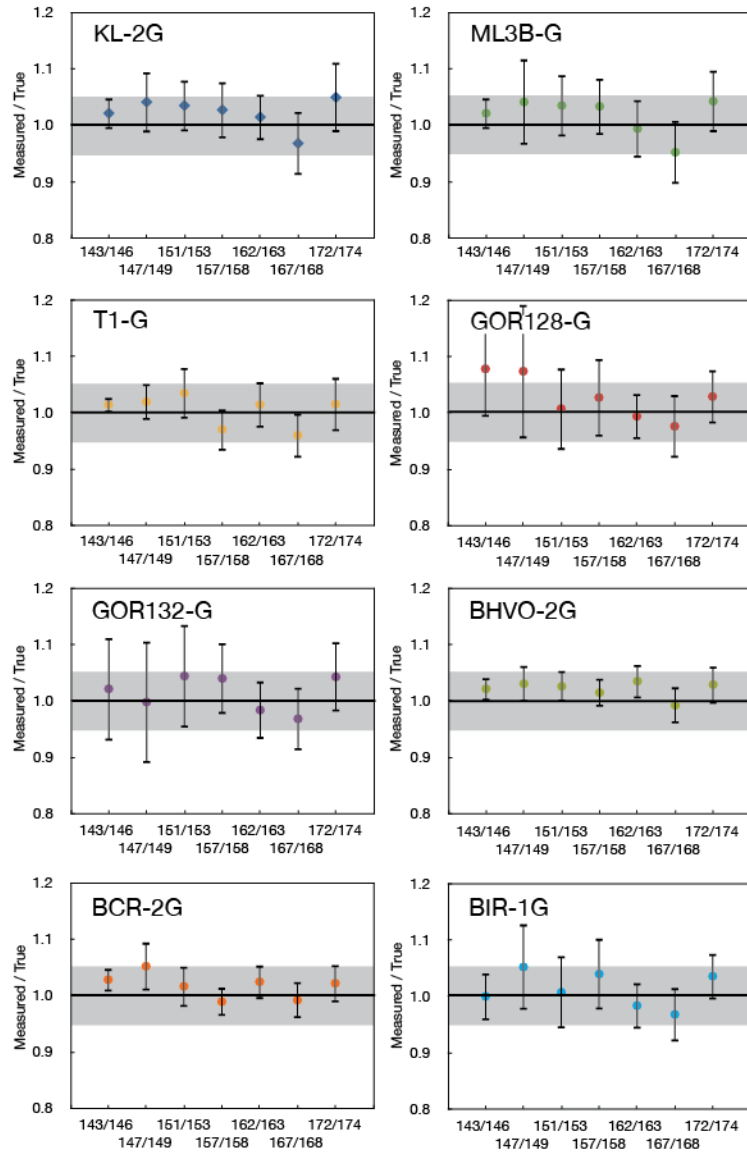


Fig. 2.1. Measured REE isotopic ratios compared with natural abundance ratios. The number ratios on the x-axis represent $^{143}\text{Nd}/^{146}\text{Nd}$, $^{147}\text{Sm}/^{149}\text{Sm}$, $^{151}\text{Eu}/^{153}\text{Eu}$, $^{157}\text{Gd}/^{158}\text{Gd}$, $^{162}\text{Dy}/^{163}\text{Dy}$, $^{167}\text{Er}/^{168}\text{Er}$ and $^{172}\text{Yb}/^{174}\text{Yb}$, respective. The error bars are $2\sigma_m$.

Repetition rate

The repetition rate controls the rate of ablation/mass removal, and by extension crater depth and crater depth-to-diameter ratio. To investigate the influence of repetition rate on LIEF, we conducted a set of 100 μm laser beam spot analyses with 5, 10 and 20 Hz repetition rate. Under these conditions, the measured REE concentrations agree with GeoRem preferred values within 10% (Fig. 2.2a-c). Although the signal intensities decayed 50–70% after 90s during 20 Hz ablation, no significant REE elemental fractionation was observed.

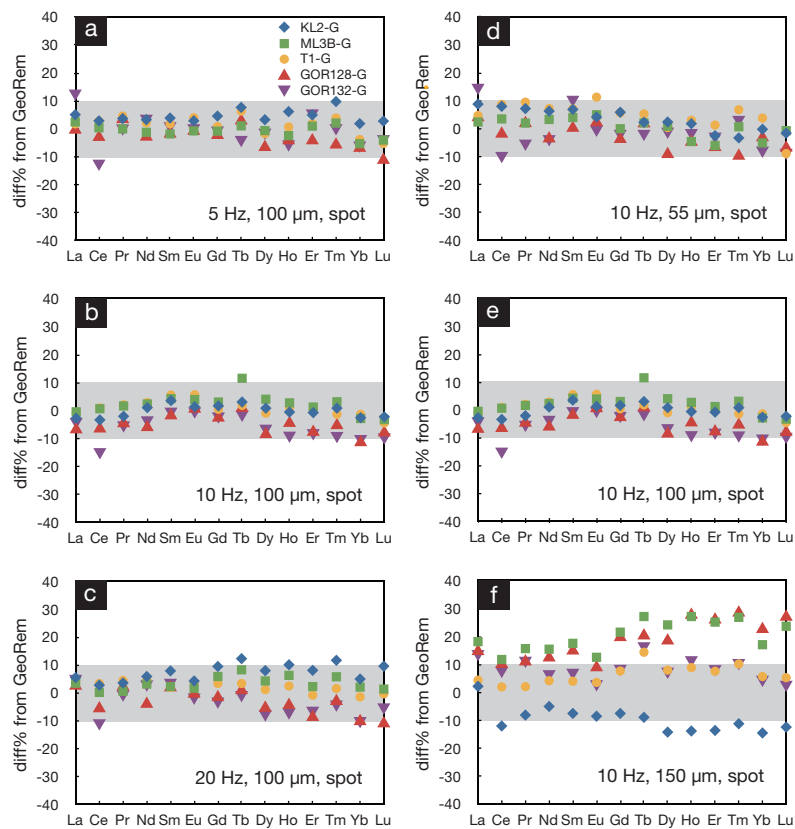


Fig. 2.2. Relative difference between the measured REE concentrations and GeoRem preferred values obtained in spot mode with 5, 10 and 20 Hz repetition rate at 100 μm spot size (a-c) and 55, 100 and 150 μm spot size at 10 Hz repetition rate (d-f).

Spot size

Ablation surface area and crater aspect ratio are associated with spot size (amongst other variables). Maintaining a constant repetition rate (10 Hz) and laser energy density (2–3 J cm⁻²), we compared spot analyses at 55, 100 and 150 µm beam diameters (Fig. 2.2d-e). The 55 and 100 µm analyses yielded REE concentrations matching GeoRem preferred values within 10%. However, the HREE concentrations measured with 150 µm spots systematically deviated from the preferred values, indicating significant fractionation of HREE from LREE. Such elemental fractionation cannot be well calibrated even when the calibrating reference materials and sample unknowns have similar matrix compositions (*e.g.*, USGS basaltic glasses vs. MPI-DING basaltic glasses in this study).

Scanning mode ablation

Line scanning mode promotes low depth-to-diameter aspect ratios and stable ion beam signals (*i.e.*, minimal signal degradation versus time). Scanning mode ablation was examined with combinations of repetition rate (5 and 10 Hz) and beam size (55 and 100 µm) at a fixed scan rate of 10 µm /s. None of the experiments, however, gave results with acceptable overall accuracy (Fig. 2.3) with HREEs being significantly fractionated from LREE, indicating non-stoichiometric sample processing.

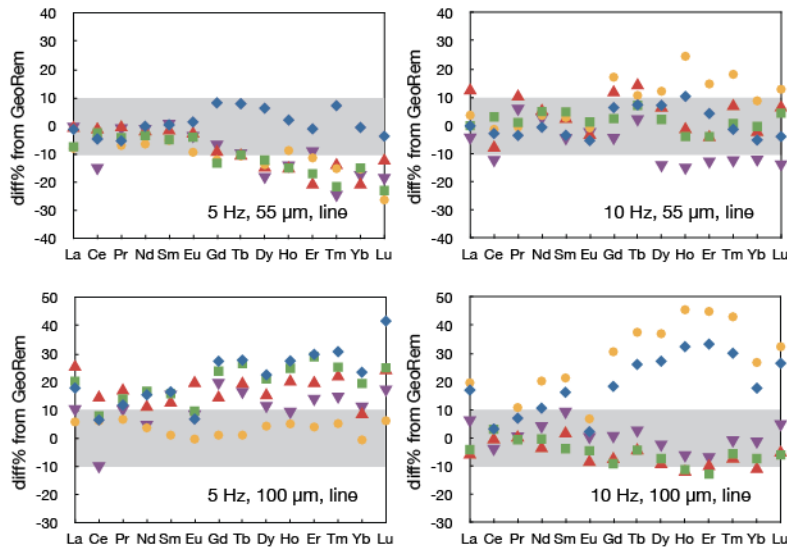


Fig. 2.3. Relative difference between the measured REE concentrations and GeoRem preferred values obtained in line scanning mode. Same legends as Fig. 2.2.

Particle size distribution in laser induced aerosols

We measured particle size distribution in the laser-induced aerosols for BHVO-2G, NIST610 and NIST614. These reference materials cover the transparency range of most geological materials. When testing the spot mode, BHVO-2G generated low total counts for particles above 1 μm and there is no clear relationship between the proportion of large particles (>1 μm) and spot size (Fig. 2.4a). For NIST610, significantly greater proportion of large particles were produced, and a positive correlation between the proportion of large particles and spot size is observed (Fig. 2.4b). This relationship holds when using line scanning mode on BHVO-2G with an exception at 175 μm (Fig. 2.5). The lack of correlation in the BHVO-2G spot mode experiment might result from counting statistics, as the majority of particles produced are likely smaller than 0.3 μm. In the experiments comparing spot mode vs. line scanning mode, we observed that, at the same beam size, significantly more large particles were produced during line scanning ablation. The particle size distribution is also

dependent upon sample transparency, and more transparent samples generated a greater proportion of large particles (Fig. 2.6).

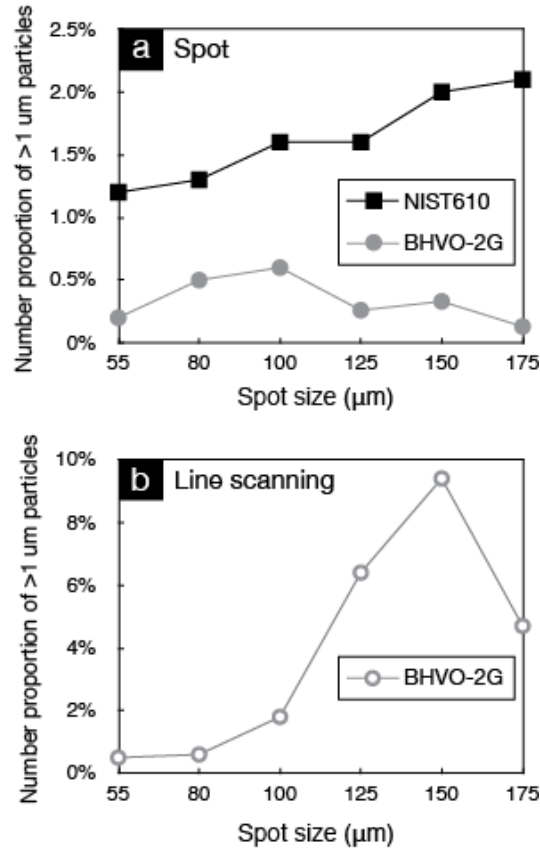


Fig. 2.4. Number proportion of large particles (> 1 μm) vs. spot size in spot and line scanning modes.

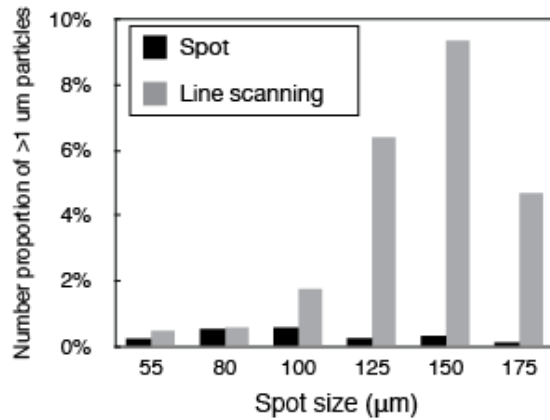


Fig. 2.5. Comparison of proportion of large particles produced in spot and line scanning modes.

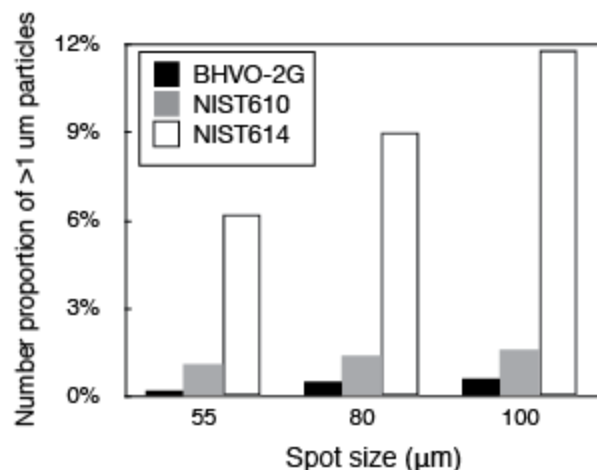


Fig. 2.6. Comparison of proportion of large particles produced by samples of different transparency (photon absorption rate). Transparency increases in the order of BHVO-2G < NIST610 < NIST614. The experiments were done in spot mode.

Assessment

The above observations lead us to conclude that (1) HREE can be fractionated from LREE during LA-ICP-MS analysis; (2) ablation using large laser spots (> 100 μm) and line scanning mode induces significant matrix-dependent fractionation irrespective of the repetition rate and (3) Low aspect ratio ablation (large spot size and line scanning) and low photon absorption (high transparency) give rise to higher production rate for large particles.

Preferential photon-electron coupling is unlikely to account for large REE fractionation observed here due to their similar ionization potentials (*i.e.*, 5.5 to 6.8 eV). Furthermore, such fractionation was rather limited, if present, when using spot ablation with 55 and 100 μm beams (relatively large depth-to-diameter aspect ratio). The deep crater effect on REE fractionation was examined with a set of 20 Hz 55 μm spot experiments, which generated a total of 1800 shots at each spot. The measured concentrations agree with preferred values (Fig. 2.7). Guillong and Günther (2002) observed that even closely matched elements, such as Th and U, could be fractionated when a significant portion of large particles cannot be fully

decomposed and excited in the ICP. The effect of particle size distribution was also emphasized by subsequent studies (González et al., 2004; Guillong et al., 2003; Plotnikov et al., 2008).

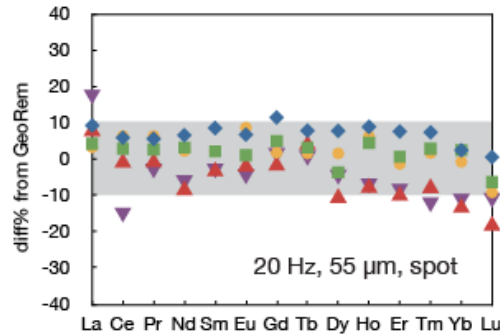


Fig. 2.7. Relative difference between the measured REE concentrations and GeoRem preferred values obtained in spot mode with 55 μm spot size and 20 Hz repetition rate. Same legends as Fig. 2.2.

To examine the effect of particle size distribution on REE fractionation, we compared the measurements conducted under various He flow rates ($0.7 - 0.2 \text{ L min}^{-1}$). By decreasing He flow rate from 0.70 L min^{-1} to 0.2 L min^{-1} the signals were reduced by a factor of 2–5 (element dependent). The reduction of counts induced by lowering the He flow rate may partially result from loss of ablated materials due to gravitational filtering of large particles during transport. Particle separation during transport inevitably leads to a change in particle size distribution. The raw Eu/Eu^* and raw Yb/Yb^* ($^{172}\text{Yb}/\sqrt{\text{^{165}\text{Tm} \cdot ^{175}\text{Lu}}}$) positively correlates with He flow rate, which translates into a faster increase of Eu and Yb counts compared with their neighboring REEs. Europium and ytterbium, as well as their oxides, have lower condensation temperatures than the other REEs, and they are, irrespective of the matrix, more sensitive to He flow rate than their neighboring REEs (Fig. 2.8). And because He flow rate influences particle size distribution of the aerosol reaching the ICP, the above

observations point to a relationship between elemental fractionation, condensation temperature and particle size distribution. In addition to condensation temperature, electronic structures likely exert an effect on elemental fractionation (Jenner and O'Neill, 2012), but this mechanism does not explain the correlations in Fig. 2.8. The link between REE fractionation and condensation temperature is further supported by the rough positive correlation between $\text{cps}_{0.2} / \text{cps}_{0.7}$ (the ratio of cps at 0.2 L min^{-1} He flow rate to cps at 0.7 L min^{-1} He flow rate) and condensation temperature (Fig. 2.9). The difference in condensation temperature may account for the observed LREE-HREE fractionation as LREEs are generally less refractory than HREEs (Lodders, 2003). As to melting and boiling temperatures, we found no correlation between these physical parameters and REE fractionation.

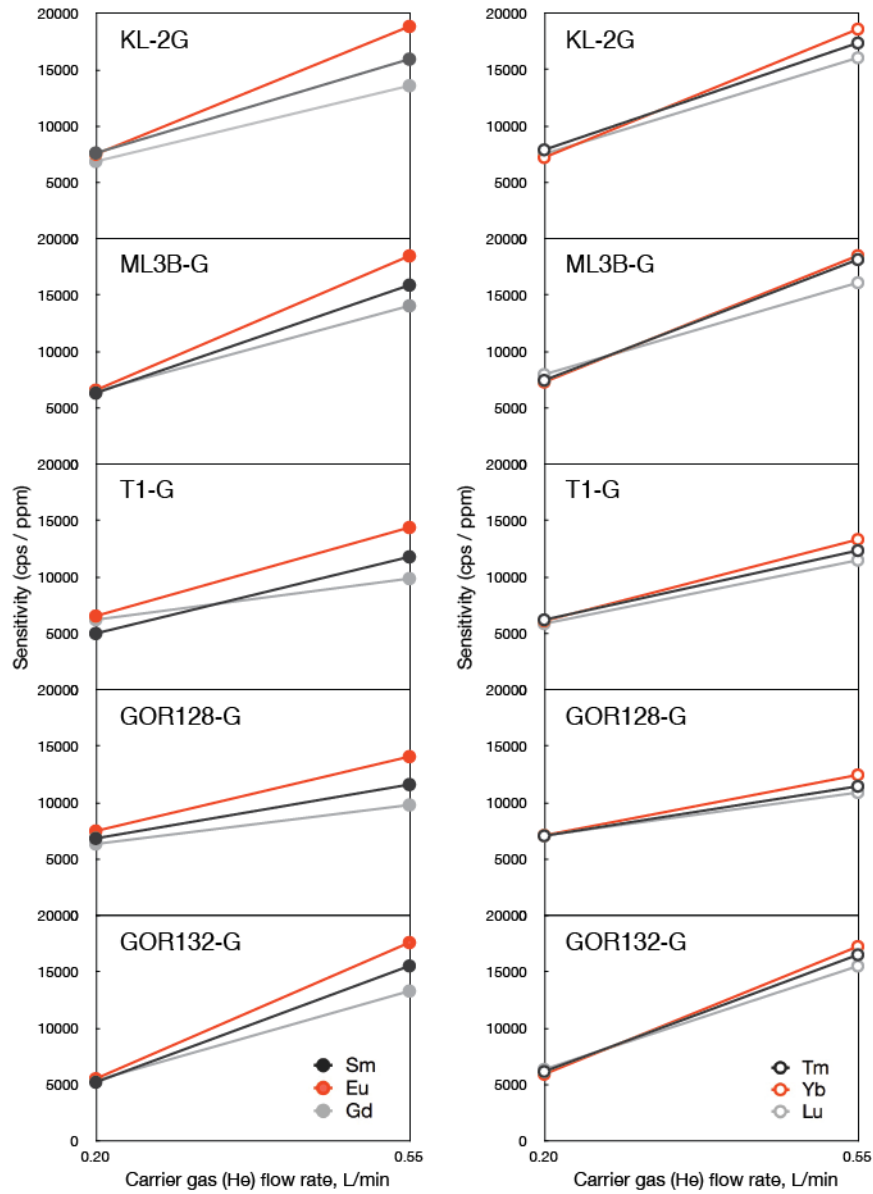


Fig. 2.8. Raw Eu/Eu* and Yb/Yb* increase with He flow rate. The 2 σ_m error bars on the sensitivities are about the size as the symbols.

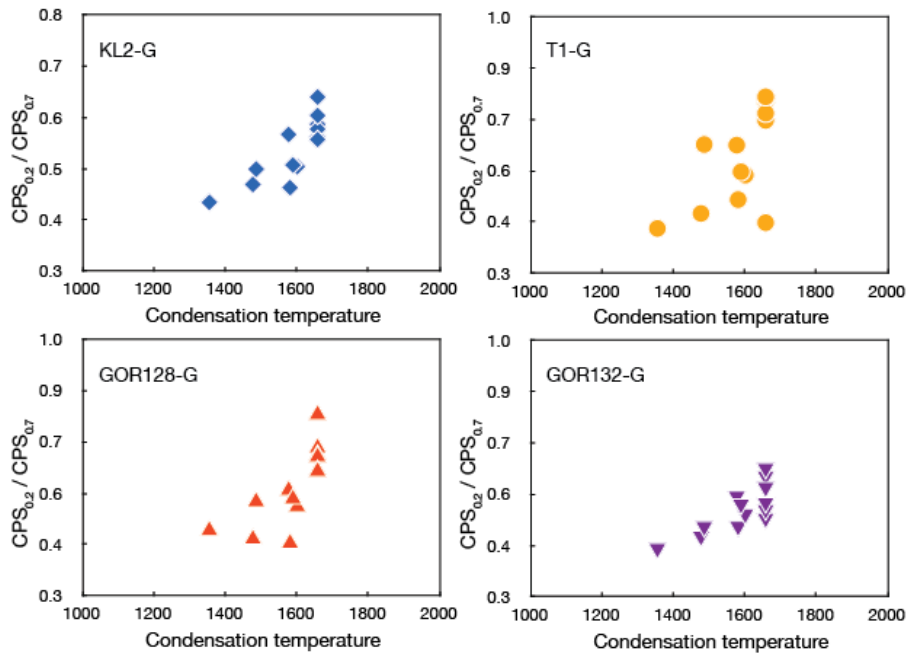


Fig. 2.9. Intensity change induced by He flow change vs. condensation temperature from Lodders (Lodders, 2003).

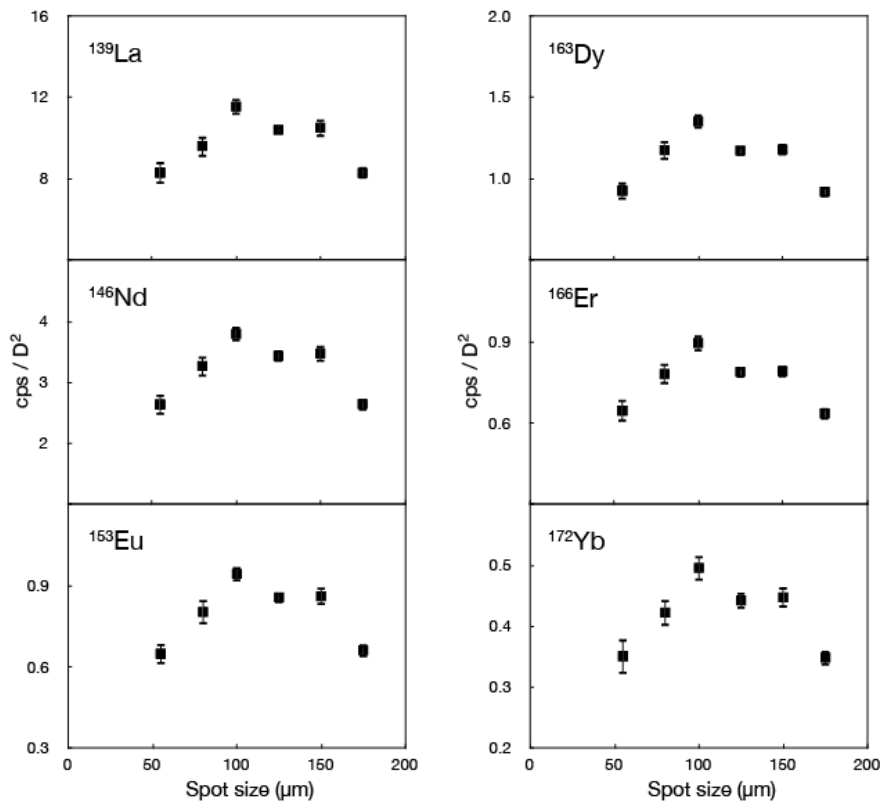


Fig. 2.10. Counts per second (cps) normalized to beam diameter squared (D^2), as a proxy for combined photon flux and ionization efficiency, obtained with 55 to 175 μm spots on BHVO-2G. A linear time drift calibration was applied to each analysis.

Figure 2.10 plots the ion yields (cps/spot diameter squared) at various mass stations as a function of spot size (10 Hz repetition rate). The low ion yields at small spot sizes (55 and 80 μm) may result from significant plasma shielding effect in relatively narrow craters. However, the ion yield starts to decrease when spot size exceeds 100 μm . This negative correlation from 100 to 175 μm may reflect the reduction of ionization efficiency of aerosols in the plasma, which may be caused by mass loading effect due to (1) the large mass flux introduced into the plasma and/or (2) broader particle size distribution or a greater amount of large particles produced by low depth-to-diameter ablation. The formation of large particles is usually linked to surface melting and hydrodynamic sputtering (Hergenroder, 2006), or Gaussian distribution of photon density within the laser beam, the latter of which is unlikely since the laser used in this work is fluence homogenized. The measured $(\text{Eu}/\text{Eu}^*)_{\text{raw}}$ ($(\text{Eu}/\text{Eu}^*)_{\text{raw}} = {}^{153}\text{Eu} / \text{sqrt} ({}^{147}\text{Sm} * {}^{157}\text{Gd})$, external standard calibration not applied) in BHVO-2G increases with spot size, or the proportion of large particles (Fig. 2.11), suggesting that the Sm-Eu-Gd fractionation is sensitive to particle size distribution. Despite more counts delivered by larger spots, the progressively more spiky signals resulted in the increasing error bars ($2 \sigma_m$) from 125 to 175 μm (Fig. 2.11).

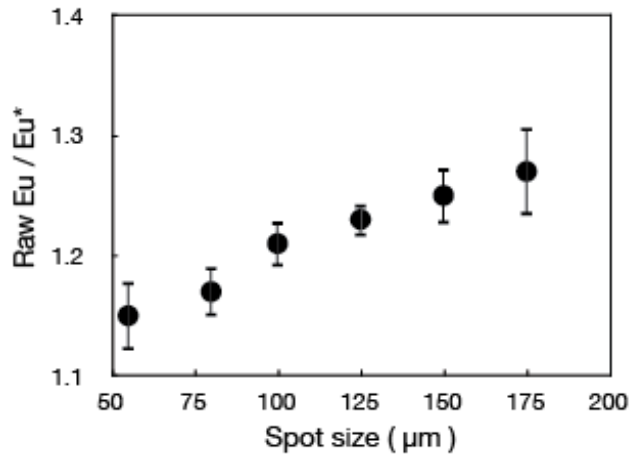


Fig. 2.11. Raw Eu/Eu* measured with 55 to 175 µm spots on BHVO-2G. A linear time drift calibration was applied to each analysis. The error bars are $2 \sigma_m$.

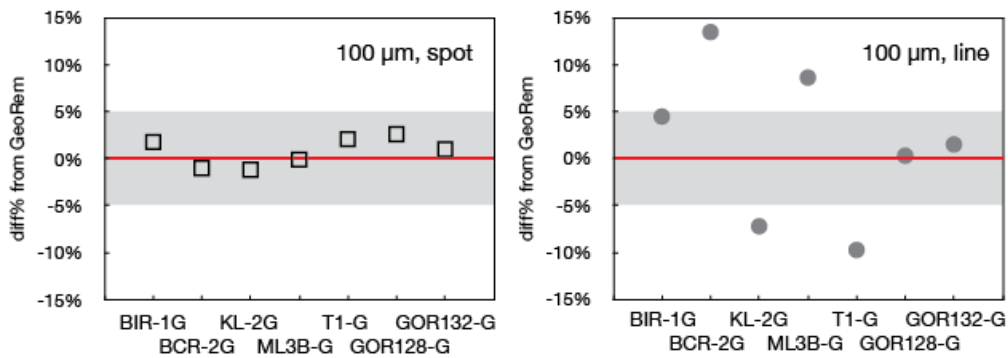


Fig. 2.12. Relative difference between the measured Eu/Eu* and GeoRem preferred values obtained in spot mode with 100 µm spot size and scanning mode with 100 µm spot size. The repetition rate was 10 Hz.

These observations lead us to link REE fractionation and condensation temperature. Low depth-to-diameter ratio ablation generates more large particles. The difference in condensation temperature results in non-stoichiometric ion yields if ionization of particles is non-quantitative in the ICP. It remains unclear whether or not REEs are also fractionated at the ablation site, as the chemical composition of the aerosol may also be particle size

dependent. However, if this is true, given that volatile elements tend to be enriched in small particles (Kuhn et al., 2004), the intensities of the less refractory LREEs should be less sensitive to carrier gas flow rate, which is not the case (Fig. 2.8 and 2.9). Therefore, LIEF, if present, has relatively minor contribution to the fractionations observed here. To further clarify this issue, future work needs to determine REE compositions of particles collected at different size cuts.

Figure 2.12 compares the measured Eu/Eu* values with GeoRem preferred values in spot (100 μm) and scanning (100 μm) mode (calibrated against BHVO-2G). The 100 μm spot measurements yielded results that agree with the preferred values within 3% while the scanning mode suffered from significant non-spectral matrix effects. The basaltic MPI-DING glasses KL-2G and ML3B-G cannot be well calibrated by the USGS standard BHVO-2G in scanning mode, which is surprising given they are all Hawaiian basalts with similar bulk compositions. Particle size distribution is thus highly sensitive to even subtle differences in physical and chemical properties or surface morphology of different matrices. Shown in Fig. 2.13 is our long-term measurement of Eu/Eu* in KL-2G and BIR-1G reproducible at 3% (2RSD).

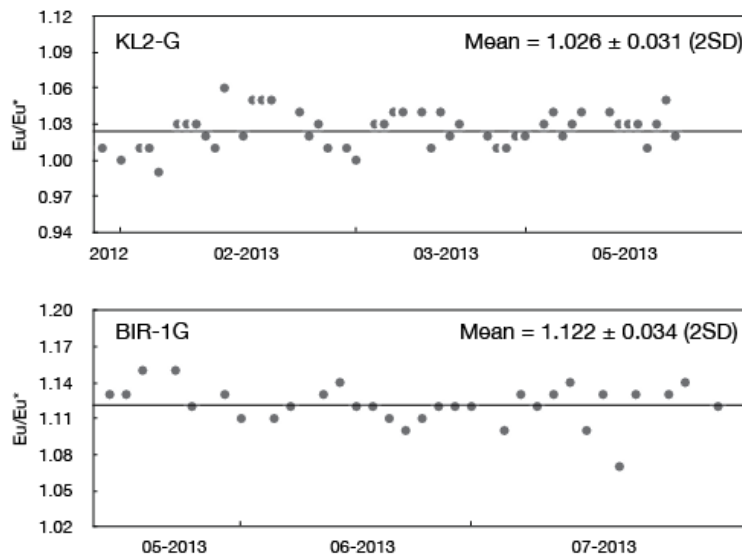


Fig. 2.13. Long-term analyses of Eu/Eu* in KL-2G (top panel) and BIR-1G (bottom panel). The solid lines indicate the mean values for both glasses.

2.5. Conclusions

1. Refractory elements, such as REEs, can be fractionated during LA-ICP-MS analysis. Line scanning and spot analyses using large laser beams ($> 100 \mu\text{m}$) promote statistically significant fractionation effects. Such REE fractionation is also sensitive to carrier gas flow rate and is matrix dependent;
2. Low aspect ratio ablation (large spot size and line scanning) and low photon absorption (high sample transparency) result in production of more large particles proportionally;
3. The primary fractionation mechanism invoked is associated with condensation temperature. Low depth-to-diameter aspect ratio ablation generates a significant amount of large particles that may be poorly decomposed and ionized in the ICP. In this case, the less refractory REEs may be preferentially evaporated and ionized. Non-quantitative ionization of particles of various sizes may result in condensation temperature dependent REE fractionation (*e.g.*, LREE-HREE, Sm-Eu-Gd, Tm-Yb-Lu). The extent of fractionation is sensitive to particle size distribution of the aerosol.
4. Controlled laser parameters can minimize the production of large particles and significant REE fractionation, as demonstrated by the Eu/Eu* values in a set of reference materials which agreed with GeoRem preferred values within 3%. A long-term reproducibility of 3% (2 RSD) was achieved for Eu/Eu* in KL-2G and BIR-1G.

References

- Aeschliman, D.B., Bajic, S.J., Baldwin, D.P. and Houk, R.S. (2003) High-speed digital photographic study of an inductively coupled plasma during laser ablation: comparison of dried solution aerosols from a microconcentric nebulizer and solid particles from laser ablation. *J. Anal. At. Spectrom.* 18, 1008-1014.
- Bäuerle, D.W. (2011) *Laser Processing and Chemistry*. Springer.
- Becker, J.S., Pickhardt, C. and Dietze, H.-J. (2000) Laser Ablation Inductively Coupled Plasma Mass Spectrometry for Determination of Trace Elements in Geological Glasses. *Microchimica Acta* 135, 71-80.
- Borisov, O.V., Mao, X. and Russo, R.E. (2000) Effects of crater development on fractionation and signal intensity during laser ablation inductively coupled plasma mass spectrometry. *Spectrochimica Acta Part B: Atomic Spectroscopy* 55, 1693-1704.
- Cromwell, E.F. and Arrowsmith, P. (1995) Semiquantitative Analysis with Laser Ablation Inductively Coupled Plasma Mass Spectrometry. *Anal. Chem.* 67, 131-138.
- Eggins, S.M., Kinsley, L.P.J. and Shelley, J.M.G. (1998) Deposition and element fractionation processes during atmospheric pressure laser sampling for analysis by ICP-MS. *Applied Surface Science* 127–129, 278-286.
- González, J.J., Fernández, A., Mao, X. and Russo, R.E. (2004) Scanning vs. single spot laser ablation ($\lambda=213$ nm) inductively coupled plasma mass spectrometry. *Spectrochimica Acta Part B: Atomic Spectroscopy* 59, 369-374.
- Guillong, M. and Gunther, D. (2002) Effect of particle size distribution on ICP-induced elemental fractionation in laser ablation-inductively coupled plasma-mass spectrometry. *J. Anal. At. Spectrom.* 17, 831-837.

- Guillong, M., Horn, I. and Gunther, D. (2003) A comparison of 266 nm, 213 nm and 193 nm produced from a single solid state Nd:YAG laser for laser ablation ICP-MS. *J. Anal. At. Spectrom.* 18, 1224-1230.
- Hergenroder, R. (2006) Hydrodynamic sputtering as a possible source for fractionation in LA-ICP-MS. *J. Anal. At. Spectrom.* 21, 517-524.
- Horn, I., Guillong, M. and Günther, D. (2001) Wavelength dependant ablation rates for metals and silicate glasses using homogenized laser beam profiles — implications for LA-ICP-MS. *Applied Surface Science* 182, 91-102.
- Humayun, M., Davis, F.A. and Hirschmann, M.M. (2010) Major element analysis of natural silicates by laser ablation ICP-MS. *J. Anal. At. Spectrom.* 25, 998-1005.
- J. G. Mank, A. and R. D. Mason, P. (1999) A critical assessment of laser ablation ICP-MS as an analytical tool for depth analysis in silica-based glass samples. *J. Anal. At. Spectrom.* 14, 1143-1153.
- Jenner, F.E. and O'Neill, H.S.C. (2012) Major and trace analysis of basaltic glasses by laser-ablation ICP-MS. *Geochem. Geophys. Geosyst.* 13, Q03003.
- Jeong, S.H., Borisov, O.V., Yoo, J.H., Mao, X.L. and Russo, R.E. (1999) Effects of Particle Size Distribution on Inductively Coupled Plasma Mass Spectrometry Signal Intensity during Laser Ablation of Glass Samples. *Anal. Chem.* 71, 5123-5130.
- Kroslakova, I. and Gunther, D. (2007) Elemental fractionation in laser ablation-inductively coupled plasma-mass spectrometry: evidence for mass load induced matrix effects in the ICP during ablation of a silicate glass. *J. Anal. At. Spectrom.* 22, 51-62.
- Kuhn, H.R., Guillong, M. and Gunther, D. (2004) Size-related vaporisation and ionisation of laser-induced glass particles in the inductively coupled plasma. *Anal Bioanal Chem* 378, 1069-1074.

- Liu, C., Mao, X.L., Mao, S.S., Zeng, X., Greif, R. and Russo, R.E. (2003) Nanosecond and Femtosecond Laser Ablation of Brass: Particulate and ICPMS Measurements. *Anal. Chem.* 76, 379-383.
- Liu, Y., Hu, Z., Gao, S., Günther, D., Xu, J., Gao, C. and Chen, H. (2008) In situ analysis of major and trace elements of anhydrous minerals by LA-ICP-MS without applying an internal standard. *Chem. Geol.* 257, 34-43.
- Lodders, K. (2003) Solar System Abundances and Condensation Temperatures of the Elements. *The Astrophysical Journal* 591, 1220.
- Mao, X., Chan, W.-T., Caetano, M., Shannon, M.A. and Russo, R.E. (1996) Preferential vaporization and plasma shielding during nano-second laser ablation. *Applied Surface Science* 96–98, 126-130.
- Mao, X.L., Borisov, O.V. and Russo, R.E. (1998) Enhancements in laser ablation inductively coupled plasma-atomic emission spectrometry based on laser properties and ambient environment. *Spectrochimica Acta Part B: Atomic Spectroscopy* 53, 731-739.
- McKay, G., Le, L., Wagstaff, J. and Crozaz, G. (1994) Experimental partitioning of rare earth elements and strontium: Constraints on petrogenesis and redox conditions during crystallization of Antarctic angrite Lewis Cliff 86010. *Geochim. Cosmochim. Acta* 58, 2911-2919.
- Niu, Y. and O'Hara, M.J. (2009) MORB mantle hosts the missing Eu (Sr, Nb, Ta and Ti) in the continental crust: New perspectives on crustal growth, crust–mantle differentiation and chemical structure of oceanic upper mantle. *Lithos* 112, 1-17.
- Plotnikov, A., Vogt, C., Wetzig, K. and Kyriakopoulos, A. (2008) A theoretical approach to the interpretation of the transient data in scanning laser ablation inductively coupled plasma mass spectrometry: Consideration of the geometry of the scanning area. *Spectrochimica Acta Part B: Atomic Spectroscopy* 63, 474-483.

- Richardson, M.C., Zoubir, A., Shah, L., Rivero, C., Lopez, C., Richardson, K.A., Ho, N. and Vallee, R. (2004) Ablation and optical property modification of transparent materials with femtosecond lasers, pp. 472-481.
- Shannon, M.A., Mao, X.L., Fernandez, A., Chan, W.-T. and Russo, R.E. (1995) Laser ablation mass removal versus incident power density during solid sampling for inductively coupled plasma atomic emission spectroscopy. *Anal. Chem.* 67, 4522-4529.
- Shearer, C., Papike, J. and Karner, J. (2006) Pyroxene europium valence oxybarometer: Effects of pyroxene composition, melt composition, and crystallization kinetics. *Am. Mineral.* 91, 1565-1573.
- Taylor, H.E. (2001) Chapter 8 - Interferences, in: Taylor, H.E. (Ed.), *Inductively Coupled Plasma-Mass Spectrometry*. Academic Press, San Diego, pp. 125-142.
- Trail, D., Bruce Watson, E. and Tailby, N.D. (2012) Ce and Eu anomalies in zircon as proxies for the oxidation state of magmas. *Geochim. Cosmochim. Acta* 97, 70-87.
- Wadhwa, M. (2001) Redox State of Mars' Upper Mantle and Crust from Eu Anomalies in Shergottite Pyroxenes. *Science* 291, 1527-1530.
- Zhu, L., Liu, Y., Hu, Z., Hu, Q., Tong, X., Zong, K., Chen, H. and Gao, S. (2013) Simultaneous Determination of Major and Trace Elements in Fused Volcanic Rock Powders Using a Hermetic Vessel Heater and LA-ICP-MS. *Geostand. Geoanal. Res.* 37, 207-229.

Chapter 3: Elemental fractionation during condensation of plasma plumes generated by laser ablation: a ToF-SIMS study of condensate blankets

[1] Tang, M., Arevalo, R. Jr., Goreva, Y., McDonough, W.F. (2015). Elemental fractionation during condensation of plasma plumes generated by laser ablation: a ToF-SIMS study of condensate blankets. *Journal of Analytical Atomic spectrometry*, 30(11), 2316-2322.

[2] M.T. designed the experiments, interpreted the data and wrote the manuscript; R.A. provided the standard and commented on the manuscript; G.Y. assisted in analyses and commented on the manuscript; W.F.M. commented on the manuscript.

Abstract

Ion imaging of the condensate blanket around a laser ablation site provides a window to study elemental fractionation during condensation of a plasma plume. Here we used a time-of-flight secondary ion mass spectrometer (ToF-SIMS) to conduct depth profiling of the condensate blanket produced by excimer 193 nm laser ablation of NIST 610 glass.

Compositional zoning (Ca normalized) revealed by ToF-SIMS are associated with texture gradients in the condensate blanket, as characterized by secondary electron microprobe (SEM) images. Elements that are more volatile than Ca are relatively enriched in the inner zones (proximal to the ablation site) while more refractory elements are variable in their distributions. Volatility and ionization potential influence elemental fractionation in plasma plume condensation processes, as documented by the contrasting fractionation behaviors of alkaline and alkaline earth metals. Compositional zoning in the condensate blanket is due to physical and chemical zoning (e.g., temperature, pressure, electron density, speciation, etc.) within the condensing plume as it expands and cools. Zoned condensation may be a primary mechanism driving the elemental fractionation associated with laser ablation.

3.1. Introduction

Elemental and isotopic fractionations have been documented for laser ablation (LA) of various materials (Arevalo, 2014 and references therein). Progressive localized ablation, leading to deeper incision of the sample substrate, exacerbates laser-induced fractionation and serves as one of the largest contributions to the uncertainty when characterizing the products of laser ablation - inductively coupled plasma - mass spectrometry (LA-ICP-MS). Chemical and isotopic fractionation during plasma condensation and particle formation should not be underestimated. Understanding these fractionation mechanisms is key to achieving high accuracy and precision in quantitative analysis using laser micro-sampling techniques such as LA-ICP-MS.

Laser processing of geological materials (insulators to conductors) involves photochemical and photothermal activation (Bäuerle, 2011), which are primarily controlled by the pulse irradiance duration of the incident laser light. Specifically, lasers with nanosecond pulse durations (the vast majority of commercial laser ablation systems) remove materials via inducing electronic transitions attended by significant melting and evaporation (Bäuerle, 2011), as most rocks and minerals are defined by phonon relaxation rates on the order of 10^{-12} s (e.g., Bauerle, 1996). In addition to pulse duration, the ablation mechanisms are also controlled by laser wavelength (Guillong et al., 2003a; Horn et al., 2001) and fluence (Bäuerle, 2011; Mao et al., 1996; Mao et al., 1998). Elements with different physical (e.g., volatility) and chemical (e.g., electronic structure) affinities fractionate significantly during laser-matter interaction and plasma condensation (Eggins et al., 1998; Horn et al., 2001; Jenner and O'Neill, 2012; Kosler et al., 2005; Kros拉克ova and Gunther, 2007; Tang et al., 2014). Laser-induced elemental fractionation results in non-stoichiometric composition of the aerosol, which scales critically on particle size distributions (Guillong and Gunther, 2002; Koch et al., 2004; Kosler et al., 2005; Kuhn and Günther, 2003; Mikova et al., 2009). Such

elemental fractionation is further aggravated during aerosol transportation (particle loss) and ionization (incomplete ionization) of large particles ($> \sim 1 \mu\text{m}$) in the ICP (Guillong and Gunther, 2002; Guillong et al., 2003b; Jeong et al., 1999; Krosiakova and Gunther, 2007). Non-stoichiometric compositions of ablated aerosols are at least partially generated from particle formation processes, of which plasma-to-particle conversion plays an important role. Plasma-to-particle conversion progresses from nucleation to condensation coalescence and agglomeration within the expanding plume (Hergenroder, 2006). These particles ultimately form a condensate blanket near the ablation site if not extracted by carrier gas.

Here we present a Time-of-Flight Secondary Ion Mass Spectrometry (ToF-SIMS) study of the condensate blanket produced by laser ablation of NIST 610 glass with nanosecond pulses of 193 nm wavelength laser radiation. ToF-SIMS is a surface-sensitive technique that uses a pulsed primary ion beam and images only the outmost ($n = 1 - 2$) atomic layers of the surface analyzed. Elements and a wide range of molecular species can be detected, though there is a wide range of sensitivities among the elements based on their first ionization potentials (Stephan, 2001). Ion imaging of laser condensate blankets represents a snapshot of the compositional variation within the laser induced plume, and provides key information for characterizing elemental fractionation during particle formation processes.

3.2. Experimental

3.2.1. Laser ablation

A freshly polished section of the standard reference material NIST 610 (~ 400 parts per million by weight concentrations of most trace elements. Detailed compositional data are available at GeoReM: http://georem.mpch-mainz.gwdg.de/sample_query_pref.asp) was irradiated by a Photon Machines Analyte G2 excimer (ArF) laser ablation system at NASA Goddard Space Flight Center. This laser produces 193 nm wavelength radiation in 4 ns pulses

at repetition rates up to 100 Hz. For this study, a laser spot with the following parameters was processed on the reference material: 110 μm spot diameter, 10 Hz repetition rate, 2.0 J/cm² fluence, and 500 total shots.

Prior to irradiation, the sample chamber (Helix cell) was purged with a He gas flow up to 2 L/min in order to evacuate any particulate contamination. During sample processing, however, the flow of helium was disengaged (i.e., 0 L/min He) and the reference material was ablated under a static He atmosphere.

3.2.2. Secondary Electron Microprobe (SEM) imaging

Backscattered Electron (BSE) imaging and Energy Dispersive Spectrometry (EDS) analysis were performed using a 7 kV *electron beam with a 4.5 micron diameter and gaseous analytical detector (GAD)* on the FEI Nova nanoSEM 600 instrument at the Smithsonian Institution. Low vacuum (1 mbar water vapor pressure) conditions allowed imaging and analysis of glass samples that were not conductively coated.

3.2.3. ToF-SIMS

Ion imaging and depth profiling were performed using the ION TOF GmbH IV TOF-SIMS instrument at the Smithsonian Institution. A primary 25 keV Bi⁺ beam (pulsed current of 0.3 pA) was rastered over an area of 250 \times 250 μm for 6000 seconds, producing 600 consecutive each scans with \sim 2 μm /pixel lateral resolution. To improve counting statistics we integrated every 40 scans to make an integrated scan, thus 15 integrated scans in total were made. Each integrated scan has a sputtering depth of \sim 3 nm for a total penetration depth of \sim 48 nm for the 6000 s scanning. This sputtering rate was estimated based on the sputtering rate obtained on silica glass, which is \sim 0.02 $\text{\AA}/\text{s}$ for a 500 \times 500 μm^2 area.

3.3. Results and discussion

A distinct condensation blanket $\sim 300 \mu\text{m}$ in diameter around the $110 \mu\text{m}$ laser crater is apparent in BSE images (Fig. 3.1A). The surface texture varies across the condensation blanket. The laser crater is surrounded by a narrow belt of beads that are 100 nm to $1 \mu\text{m}$ in diameter (Fig. 3.1B, Zone 1). Farther from the ablation site (Zones 2 – 6), more fiber-like condensates can be seen extending towards the boundary of inner zoning at $200 \mu\text{m}$ from the crater (top of Zone 6); individual particles cannot be resolved in this “fiber” zone. On the edge of the boundary (e.g., Fig 3.1C, Zones 5 – 7) are particle agglomerates of $10^2 - 10^3 \text{ nm}$, which show a clear preferred orientation. The surface area in the outer zone appears to be filled with smaller ($< 10 \text{ nm}$) condensates (e.g., Zones 8 – 9). The BSE images also reveal massive particle agglomerates (up to $10 \mu\text{m}$) scattered throughout the surface covering both the laser pit ejecta blankets and remote areas of the sample (all Zones). These agglomerates have a similar composition as NIST 610 glass based on EDS spectra, and thus were likely generated during laser ablation processing. For comparison, we provide a “control” SEM image of an area far ($\sim 5 \text{ mm}$ away from the ablation site) from the laser crater (Fig. 3.2).

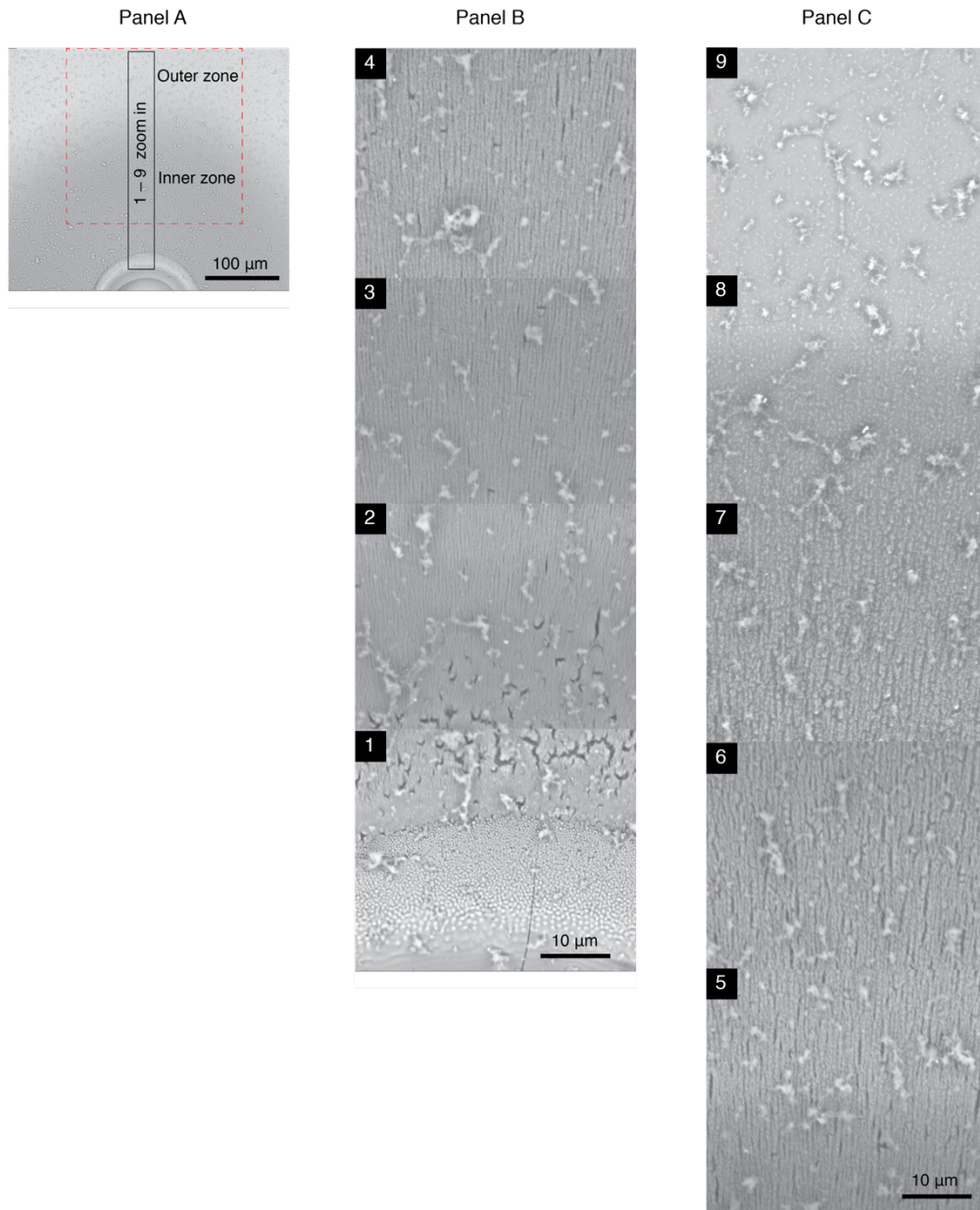


Fig. 3.1. BSE images of the condensate blanket adjacent to the laser crater. Panel A provides an overview of the condensate blanket, which can be broken down into well-defined inner and outer zones based on particle morphology. Panel B and C are zoom-in images of Zones 1 – 9 (total length is 300 μm), each section representing approximately 40 μm x 35 μm and progressing away from the ablation site. The red dashed square in the left panel denotes the 250 x 250 micron area for ToF-SIMS imaging.

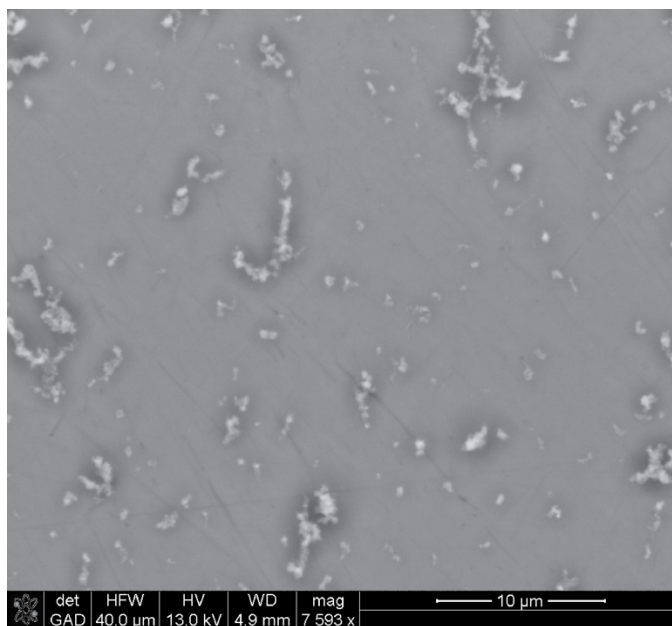


Fig. 3.2. Control BSE image of a polished section of the same NIST 610 sample after laser ablation, but located far (~5 mm) away from the ablation site. Note the reduced distribution of small particle condensates compared to those seen in the outer zone of the condensation blanket (Fig. 3.1C, Zones 8 – 9).

We used a ToF-SIMS instrument to produce ion images of an area that included representative regions of the two distinct zones of condensation blanket (Fig. 3.1, panel A). For ToF-SIMS data, we normalized all isotopes to ^{40}Ca ; the less abundant ^{43}Ca is routinely used as an internal standard in LA-ICP-MS data reduction. It's worth noting that the X/Ca intensity ratios measured by ToF-SIMS do not reflect the accurate atomic ratios in the blanket. Calcium and other metals fractionate during sputtering due to different X-O bonding energies (Henkel and Gilmour, 2014; Ireland, 2014; Vickerman et al., 2013). For our purpose, we focused on the relative X/Ca variation across the condensate blanket. Thus no external standard calibration was applied. Examples of the distributions of X/Ca ratios (X is an element other than Ca) in the first integrated scan are plotted in Fig. 3.3 (a complete set of integrated scans 2–15 are available in the Electronic Supporting Information, *ESI*). Similar to

the textural variation across the condensate region, as revealed through BSE images, the ToF-SIMS images show compositional zonings (Fig. 3.3). For ${}^7\text{Li}$, ${}^9\text{Be}$, ${}^{11}\text{B}$, ${}^{48}\text{Ti}$, ${}^{51}\text{V}$, ${}^{55}\text{Mn}$, ${}^{56}\text{Fe}$, ${}^{58}\text{Ni}$, ${}^{65}\text{Cu}$, ${}^{69}\text{Ga}$, ${}^{87}\text{Rb}$ and ${}^{133}\text{Cs}$, the inner zones are demarked by higher X/ ${}^{40}\text{Ca}$ intensity ratios; for ${}^{27}\text{Al}$, ${}^{88}\text{Sr}$ and ${}^{138}\text{Ba}$, the outer zones have higher X/Ca intensity ratios. ${}^{26}\text{Mg}$ shows less apparent fractionation across the frame. Sodium and potassium were also imaged by ToF-SIMS; however, both Na and K are major surface contaminants. In addition, Na oversaturated the detector. Therefore, Na and K data are not discussed here.

There are primarily two factors that may result in X/Ca variation: (1) laser induced elemental fractionation; and (2) topography induced matrix effects during ToF-SIMS analysis. The latter is a result of non-equilibrium sputtering. Generally, pre-sputtering can destroy surface structure and remove surface contaminants so as to avoid non-equilibrium sputtering effects. However, the non-equilibrium sputtering depth range is both matrix- and element-dependent. In this study, we did not apply pre-sputtering, but used the depth profiles to evaluate the non-equilibrium sputtering effect for each element. Relative differences (in %) in average X/Ca between the outer zone (farthest 100 μm from the ablation site) and inner zone (100 μm nearest the ablation site) for each integrated scan, as a function of sputtering depth (integrated scan number), are calculated in Fig. 3.4 and ESI. If disproportionate enrichments or depletions in elemental abundances revealed by ToF-SIMS are solely due to topography changes across the condensation blanket, the normalized X/Ca zoning trends shown in these figures (i.e., $X/Ca_{\text{outer}}/XCa_{\text{inner}}$) should “flatten out” with depth, as continuous sputtering is expected to resurface the sample and approach equilibrium sputtering conditions. Consequently, it is unlikely that our depth profiling penetrated through the condensate blanket, since the boundary between the inner and outer zoning neither disappeared nor changed its position in the ToF-SIMS images throughout the depth profile. Therefore our depth profile, sample the condensate blanket and should reflect the plume composition at the late stage of the ablation.

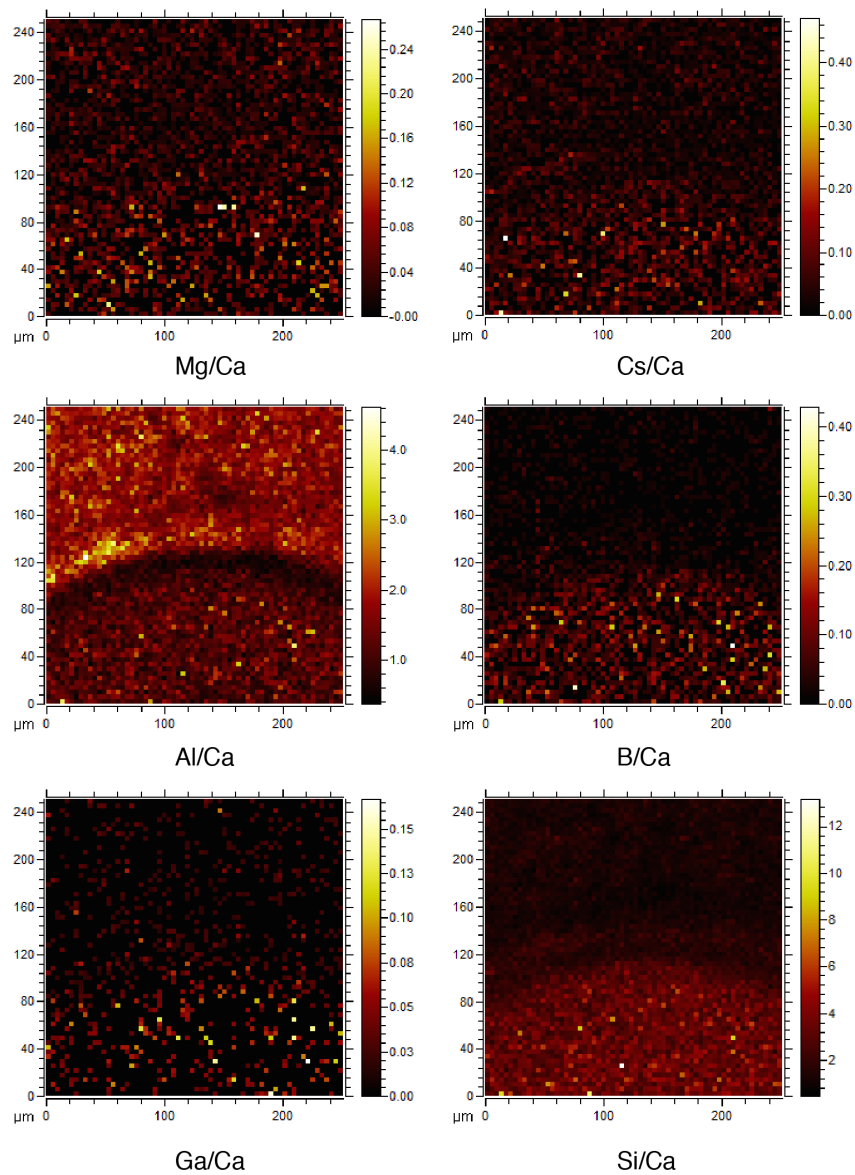


Fig. 3.3. Ca normalized Mg, Cs, Al, B, Ga and Si distributions across the condensate blanket (first integrated scan). Thermal scale reflects relative ion intensity from low (black) to high (white).

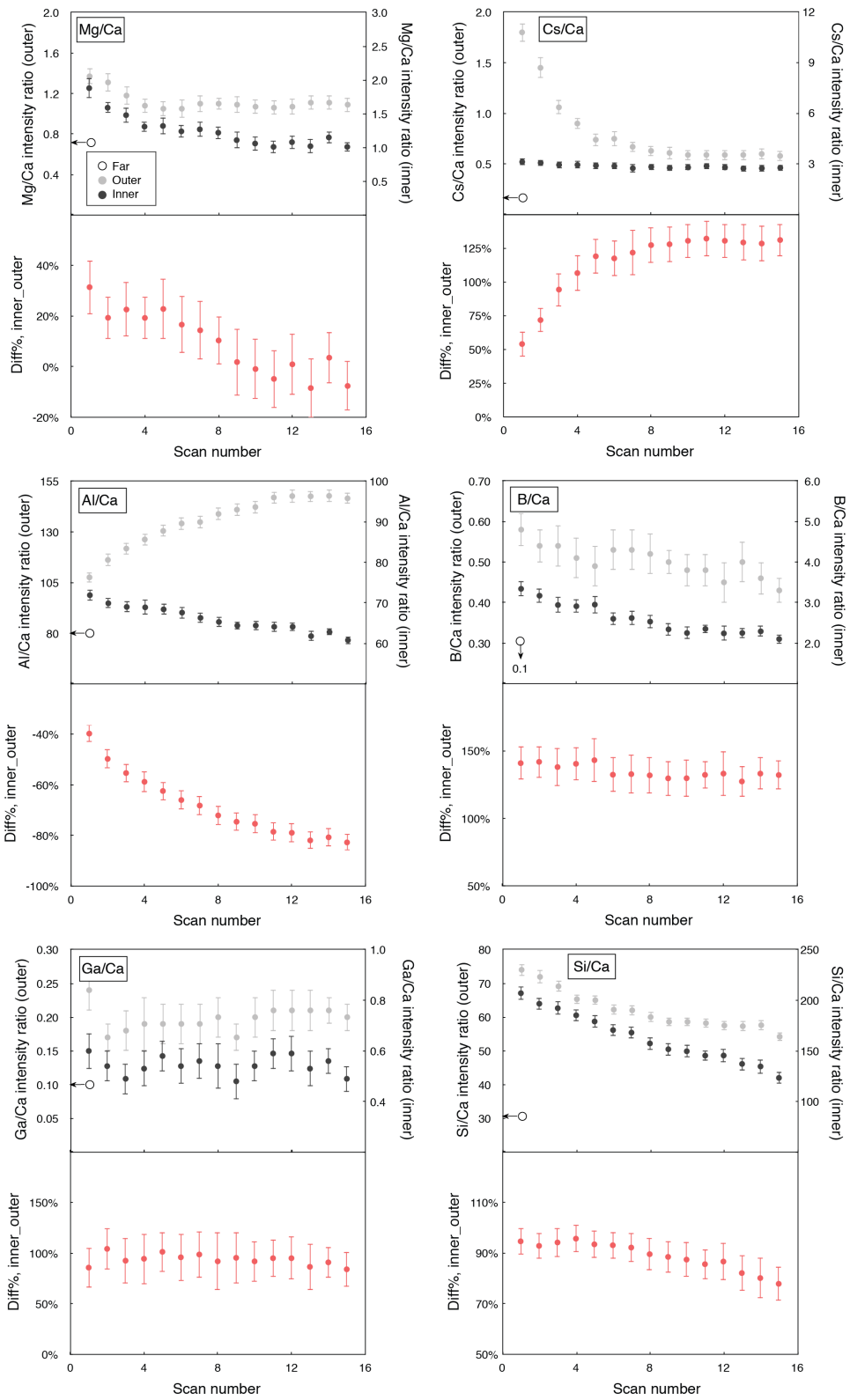


Fig. 3.4. Depth profiles of Mg, Cs, Al, B, Ga and Si, all normalized to Ca. A larger scan number on the x-axis corresponds to a deeper integrated scan. Note the dual y-axes in the

uppermost plots. The gray dots represent the average X/Ca of the 100 μm outermost area (outer zone), the black dots the average X/Ca of the 100 μm innermost area (inner zone, nearest the ablation site), and the open circles represent the scan of a far area on the same NIST 610 glass after ablation. For each X/Ca panel, the diff% inner_outer is calculated as $(X/Ca_{\text{inner}} - X/Ca_{\text{outer}}) / [(X/Ca_{\text{inner}} + X/Ca_{\text{outer}})/2] * 100\%$. Error bars are $2 \sigma_m$. See text for more explanation.

Among the geochemical proxies investigated here, Mg/Ca, Cs/Ca and Al/Ca may have non-equilibrium sputtering effects during early sputtering. For Mg, the Mg/Ca diff% between the outer and inner zonings continuously decreases with depth and reaches a plateau with a diff% of $\sim 0\%$ (Fig. 3.4), which suggests little Mg-Ca fractionation across the condensation blanket. For Cs, Cs/Ca in the outer zoning continuously decreases with sputtering depth while Cs/Ca in the inner zoning stays constant (Fig. 3.4), resulting in an increasing Cs/Ca diff% from integrated scan #1-5 followed by a plateau with a diff% of $\sim 125\%$, indicating significant Cs-Ca fractionation induced by laser ablation. Al/Ca in the inner and outer zonings evolve in the opposite directions with no diff% plateau reached throughout the depth profile (Fig. 3.4); because of this, the fractionation between Al-Ca observed here likely represents only a lower bound on the actual fractionation between these elements. Although poorly resolved, Si/Ca and Cr/Ca appear to show decreased diff% between the outer and inner zones with sputtering depth. For the remainder, X/Ca diff% are significantly different from 0% with no resolvable systematic changes with sputtering depth, reflecting reproducible X-Ca fractionation of various sizes across the condensation blanket (see the ESI for depth profiles of all elements analyzed here).

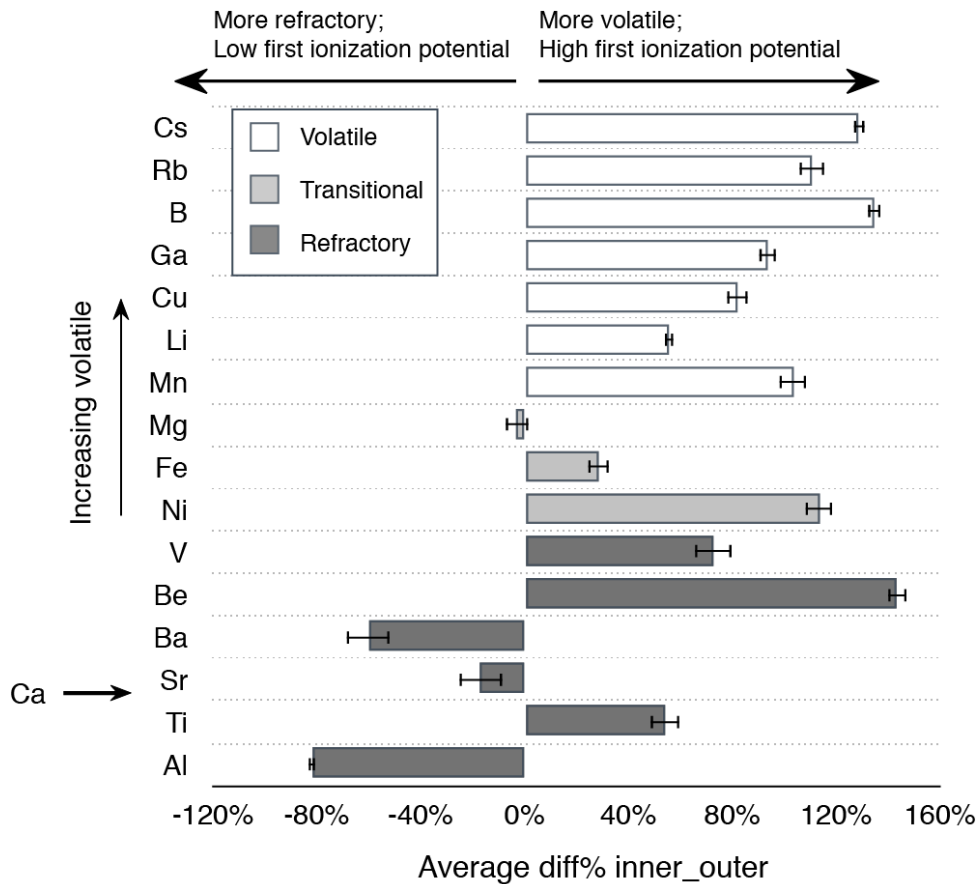


Fig. 3.5. Average X/Ca diff% between the inner and outer zonings. Negative values indicate relative enrichments in the outer zoning. Elements are defined as volatile, transitional or refractory based on condensation temperatures derived from Lodders (2003); note that these condensation temperatures are determined for a hydrogen atmosphere, while laser ablation was conducted in a helium atmosphere. Errors are $2 \sigma_m$.

Laser induced elemental fractionation has been attributed to different chemical and physical properties of elements e.g., volatility (Eggins et al., 1998; Liu et al., 2003; Mao et al., 1996; Mao et al., 1998; Tang et al., 2014), electronic structure (Jenner and O'Neill, 2012; Mao et al., 1998), etc., resulting in preferential evaporation, ionization and condensation during laser ablation processes. Figure 3.5 shows that volatile and transitional elements (Ni to Cs, 50% condensation temperature < 1360 K) are mostly enriched in the inner zone while

elements that are similarly refractory as Ca (V to Al, 50% condensation temperature > 1360 K) can be enriched in either outer or inner zones, reflecting multiple factors controlling elemental fractionation. Multiple fractionation mechanisms can be further elucidated by comparing the contrasting fractionation directions between alkaline metals and alkaline earth metals (Fig. 3.6). Alkaline metals (Period IA elements) are volatile and increasingly so with increasing atomic mass (Lodders, 2003), with the enrichment in alkaline metals increasing from Li to Cs in the inner zone (Fig. 3.6a). Alkaline earth metals (Period IIA elements), however, share similar volatilities but transition from relative enrichments to progressive depletions in between the inner zone as a function of first ionization potential (Fig. 3.6b), reflecting the control of electronic structure on the fractionation between alkaline earth metals. The opposite fractionation directions between alkaline metals and alkaline earth metals suggests the dominance of volatility effect over electronic structure effect on laser induced elemental fractionation (LIEF). The volatility control may also be responsible for the distinct fractionation behavior of Al compared with B and Ga since Al is enriched in the outer zoning while the more volatile B and Ga are both enriched in the inner zone (Fig. 3.4).

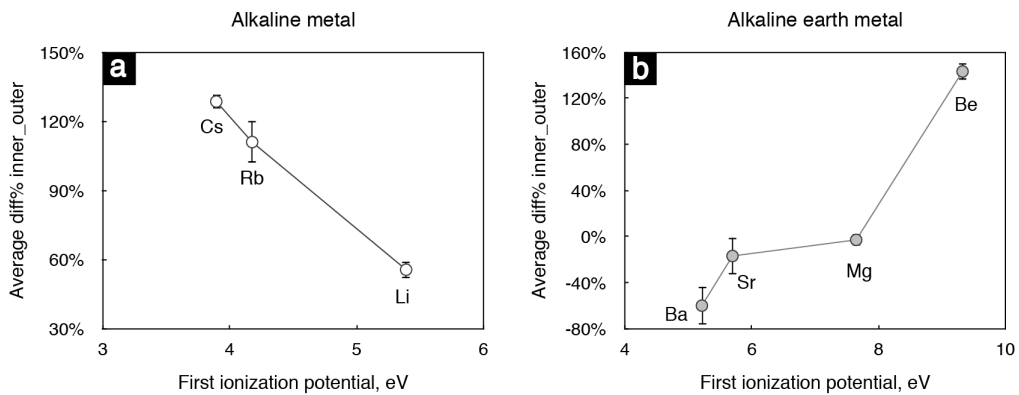


Fig. 3.6. Average X/Ca diff% between the inner and outer zones for alkaline and alkaline earth metal elements as a function of first ionization potential. Error bars are 2σ , and some are smaller than the markers.

The compositional zonings around the laser crater are likely related to condensation behaviors and the spatial – temporal evolution of particle formation and deposition processes. Dynamically, during plasma plume initiation (10^{-10} s post-irradiation) the ascending material also undergoes laser-induced ionization at the sample surface during active irradiation with nanosecond (or longer) laser pulses (Bogaerts and Chen, 2004, 2005; Chen and Bogaerts, 2005). Photothermally and photochemically activated materials irradiated with $\sim 10^9$ W/cm² (i.e., ~ 2 J/cm², 4 ns, and 193 nm λ) rise from the sample surface and form a plasma plume, which in turn interacts with the incident laser irradiation and absorbs significant amounts (circa $\geq 50\%$) of laser energy that would otherwise couple with the sample, known as the plasma shielding effect (Bäuerle, 2011; Russo et al., 2002). The absorption of incident photons results in elevated temperatures (up to 10^4 K) and electron densities in the plume. During plume expansion, the temperature drops down and the excited species condense, aggregate and (eventually) form mostly sub-micron- and micron-sized particles. Within the expanding plume, temperature, pressure, electron density, and speciation (e.g., ionization degree) are zoned (Bogaerts and Chen, 2004, 2005; Bogaerts et al., 2003; Chen and Bogaerts, 2005). Moreover, for plume residence time of 1 millisecond or longer, material in the pulse path will absorb the next incoming light pulse at 100 Hz repetition rates. As a result, the temporal and spatial scale condensation properties are expected to form condensates that compositionally vary as a function of distance from the ablation center. Although specifically developed for laser ablation of metallic substrates, Bogaerts and Chen's models (Bogaerts and Chen, 2005; Chen and Bogaerts, 2005) show that the spatial distribution of temperatures within the expanding plume is complex, and the plume develops a low temperature center after the laser pulse terminates. This may explain the relative enrichments of many volatile elements (e.g., alkaline earth metals, B, etc.) in the inner zone of the condensation blanket. With condensation being the primary stage of particle formation (as opposed to less dominant

evaporation processes, not discussed here), elemental fractionation during condensation corroborates the linkage between LIEF and particle size distribution.

Because elemental fractionation happens during laser plume condensation, achieving high accuracy and precision LA-ICP-MS data requires either complete mass transport and ionization in the ICP, or well matched internal standard element that fractionates in the same way as the unknown element during laser ablation of both the external standard and sample (Gaboardi and Humayun, 2009; Jenner and O'Neill, 2012). The former option requires well-designed laser ablation chamber and small aerosol particles produced by laser ablation; the latter option requires dedicated analysis of only a limited range of elements with similar physicochemical properties (such as condensation temperature and first ionization potential) of the internal standard.

Finally, the findings of this study need to be placed into the context of active ablation with a He gas stream of 2 L/min, typical of modern laser ablation sampling for chemical and/or isotopic analyses. Under these conditions additional effects need to be considered, given plume trajectories of 10^4 m s^{-1} and strong gas flow velocities. Fractionation of volatile/refractory element species is likely to be enhanced, particularly for highly volatile elements Zn, Tl, Pb, In, Bi, Br and I. Horn et al (2000) observed correlation between element fractionation (U/Pb) and spot geometry (their Fig. 3.7) and suggested that the laser-induced elemental fractionation also reflected the relative efficiency of element transport for volatile versus refractory elements from the site of ablation to the ICP-MS.

3.4. Conclusions

- (1) ToF-SIMS imaging reveals compositional zoning in the condensate blanket produced by ablation of NIST 610 glass with a pulsed (4 ns) ArF excimer (193 nm) laser system.
- (2) The observed elemental fractionation is controlled by volatility as well as electronic structure (ionization potential), with volatility being the more influential factor; volatile and transitional elements (50% condensation temperature < 1360 K) tend to be enriched in the inner zone relative to refractory elements, and low first ionization potential elements tend to be enriched in the inner zone relative to high first ionization potential elements.
- (3) The elemental fractionation is associated with condensation and subsequent particle formation processes, during which the gradients in physical and chemical conditions result in uneven condensation within the plasma plume.
- (4) ToF-SIMS imaging of laser condensate blanket provides a new approach to study the mechanisms of laser induced elemental and isotopic fractionation.

References

- Arevalo Jr, R. (2014) 15.23 - Laser Ablation ICP-MS and Laser Fluorination GS-MS, in: Turekian, H.D.H.K. (Ed.), *Treatise on Geochemistry (Second Edition)*. Elsevier, Oxford, pp. 425-441.
- Bäuerle, D.W. (2011) *Laser Processing and Chemistry*. Springer.
- Bogaerts, A. and Chen, Z. (2004) Nanosecond laser ablation of Cu: modeling of the expansion in He background gas, and comparison with expansion in vacuum. *Journal of Analytical Atomic Spectrometry* 19, 1169-1176.

- Bogaerts, A. and Chen, Z. (2005) Effect of laser parameters on laser ablation and laser-induced plasma formation: A numerical modeling investigation. *Spectrochimica Acta Part B: Atomic Spectroscopy* 60, 1280-1307.
- Bogaerts, A., Chen, Z., Gijbels, R. and Vertes, A. (2003) Laser ablation for analytical sampling: what can we learn from modeling? *Spectrochimica Acta Part B: Atomic Spectroscopy* 58, 1867-1893.
- Chen, Z. and Bogaerts, A. (2005) Laser ablation of Cu and plume expansion into 1atm ambient gas. *Journal of Applied Physics* 97, 063305.
- Eggin, S.M., Kinsley, L.P.J. and Shelley, J.M.G. (1998) Deposition and element fractionation processes during atmospheric pressure laser sampling for analysis by ICP-MS. *Applied Surface Science* 127–129, 278-286.
- Gaboardi, M. and Humayun, M. (2009) Elemental fractionation during LA-ICP-MS analysis of silicate glasses: implications for matrix-independent standardization. *Journal of Analytical Atomic Spectrometry* 24, 1188-1197.
- Guillong, M. and Gunther, D. (2002) Effect of particle size distribution on ICP-induced elemental fractionation in laser ablation-inductively coupled plasma-mass spectrometry. *Journal of Analytical Atomic Spectrometry* 17, 831-837.
- Guillong, M., Horn, I. and Gunther, D. (2003a) A comparison of 266 nm, 213 nm and 193 nm produced from a single solid state Nd:YAG laser for laser ablation ICP-MS. *Journal of Analytical Atomic Spectrometry* 18, 1224-1230.
- Guillong, M., Kuhn, H.-R. and Günther, D. (2003b) Application of a particle separation device to reduce inductively coupled plasma-enhanced elemental fractionation in laser ablation-inductively coupled plasma-mass spectrometry. *Spectrochimica Acta Part B: Atomic Spectroscopy* 58, 211-220.
- Henkel, T. and Gilmour, J. (2014) 15.22 - Time-of-Flight Secondary Ion Mass Spectrometry, Secondary Neutral Mass Spectrometry, and Resonance Ionization Mass Spectrometry,

- in: Turekian, H.D.H.K. (Ed.), *Treatise on Geochemistry (Second Edition)*. Elsevier, Oxford, pp. 411-424.
- Hergenroder, R. (2006) Hydrodynamic sputtering as a possible source for fractionation in LA-ICP-MS. *Journal of Analytical Atomic Spectrometry* 21, 517-524.
- Horn, I., Guillong, M. and Günther, D. (2001) Wavelength dependant ablation rates for metals and silicate glasses using homogenized laser beam profiles — implications for LA-ICP-MS. *Applied Surface Science* 182, 91-102.
- Horn, I., Rudnick, R.L. and McDonough, W.F. (2000) Precise elemental and isotope ratio determination by simultaneous solution nebulization and laser ablation-ICP-MS: application to U–Pb geochronology. *Chemical Geology* 164, 281-301.
- Ireland, T.R. (2014) 15.21 - Ion Microscopes and Microprobes, in: Turekian, H.D.H.K. (Ed.), *Treatise on Geochemistry (Second Edition)*. Elsevier, Oxford, pp. 385-409.
- Jenner, F.E. and O'Neill, H.S.C. (2012) Major and trace analysis of basaltic glasses by laser-ablation ICP-MS. *Geochemistry, Geophysics, Geosystems* 13, Q03003.
- Jeong, S.H., Borisov, O.V., Yoo, J.H., Mao, X.L. and Russo, R.E. (1999) Effects of Particle Size Distribution on Inductively Coupled Plasma Mass Spectrometry Signal Intensity during Laser Ablation of Glass Samples. *Analytical Chemistry* 71, 5123-5130.
- Koch, J., von Bohlen, A., Hergenroder, R. and Niemax, K. (2004) Particle size distributions and compositions of aerosols produced by near-IR femto- and nanosecond laser ablation of brass. *Journal of Analytical Atomic Spectrometry* 19, 267-272.
- Kosler, J., Wiedenbeck, M., Wirth, R., Hovorka, J., Sylvester, P. and Mikova, J. (2005) Chemical and phase composition of particles produced by laser ablation of silicate glass and zircon-implications for elemental fractionation during ICP-MS analysis. *Journal of Analytical Atomic Spectrometry* 20, 402-409.
- Kroslakova, I. and Gunther, D. (2007) Elemental fractionation in laser ablation-inductively coupled plasma-mass spectrometry: evidence for mass load induced matrix effects in the

- ICP during ablation of a silicate glass. *Journal of Analytical Atomic Spectrometry* 22, 51-62.
- Kuhn, H.-R. and Günther, D. (2003) Elemental fractionation studies in laser ablation inductively coupled plasma mass spectrometry on laser-induced brass aerosols. *Analytical chemistry* 75, 747-753.
- Liu, C., Mao, X.L., Mao, S.S., Zeng, X., Greif, R. and Russo, R.E. (2003) Nanosecond and Femtosecond Laser Ablation of Brass: Particulate and ICPMS Measurements. *Analytical Chemistry* 76, 379-383.
- Lodders, K. (2003) Solar System Abundances and Condensation Temperatures of the Elements. *The Astrophysical journal* 591, 1220.
- Mao, X., Chan, W.-T., Caetano, M., Shannon, M.A. and Russo, R.E. (1996) Preferential vaporization and plasma shielding during nano-second laser ablation. *Applied Surface Science* 96–98, 126-130.
- Mao, X.L., Borisov, O.V. and Russo, R.E. (1998) Enhancements in laser ablation inductively coupled plasma-atomic emission spectrometry based on laser properties and ambient environment. *Spectrochimica Acta Part B: Atomic Spectroscopy* 53, 731-739.
- Mikova, J., Kosler, J., Longerich, H.P., Wiedenbeck, M. and Hanchar, J.M. (2009) Fractionation of alkali elements during laser ablation ICP-MS analysis of silicate geological samples. *Journal of Analytical Atomic Spectrometry* 24, 1244-1252.
- Russo, R.E., Mao, X., Liu, H., Gonzalez, J. and Mao, S.S. (2002) Laser ablation in analytical chemistry—a review. *Talanta* 57, 425-451.
- Stephan, T. (2001) TOF-SIMS in cosmochemistry. *Planetary and Space Science* 49, 859-906.
- Tang, M., McDonough, W.F. and Arevalo, R.J. (2014) High-precision measurement of Eu/Eu* in geological glasses via LA-ICP-MS analysis. *Journal of Analytical Atomic Spectrometry* 29, 1835-1843.

Appendix

Depth profiles of elements imaged in this study

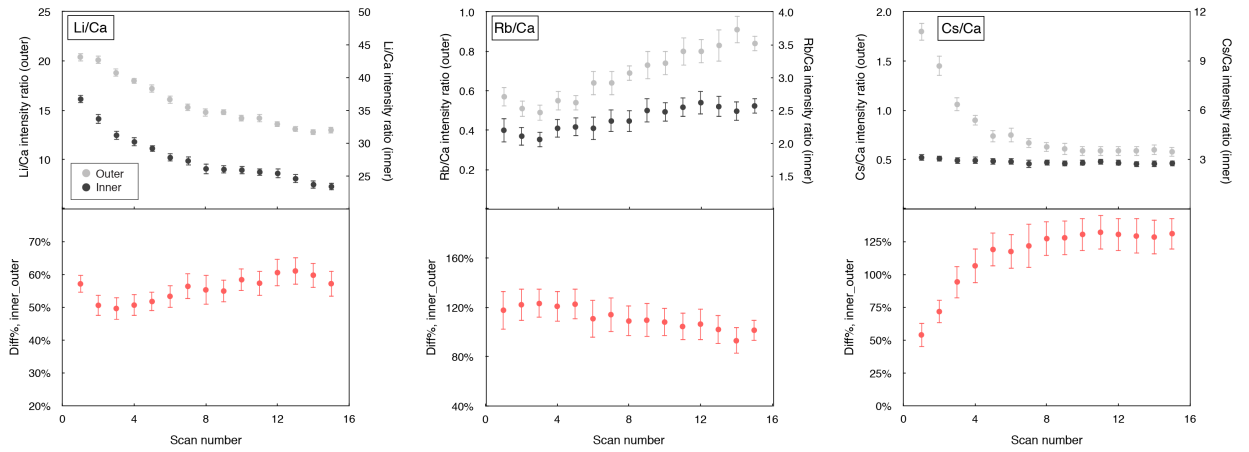


Fig. A3.1. Alkaline metal composition depth profiles.

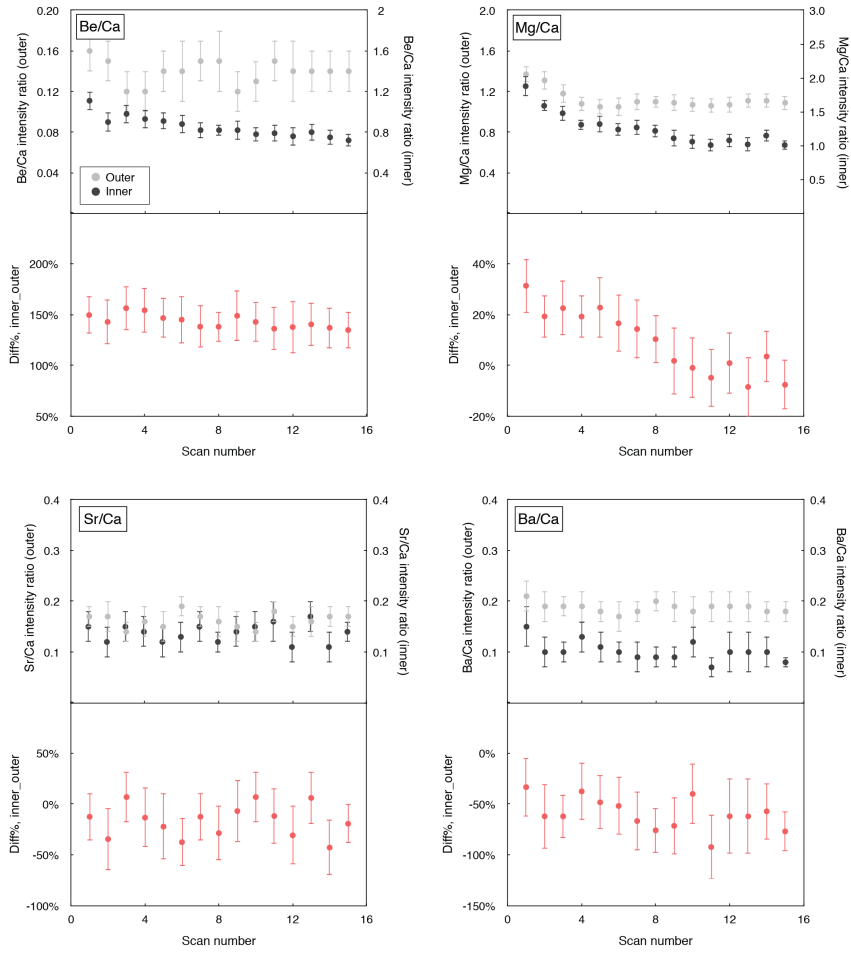


Fig. A3.2. Alkaline earth metal composition depth profiles.

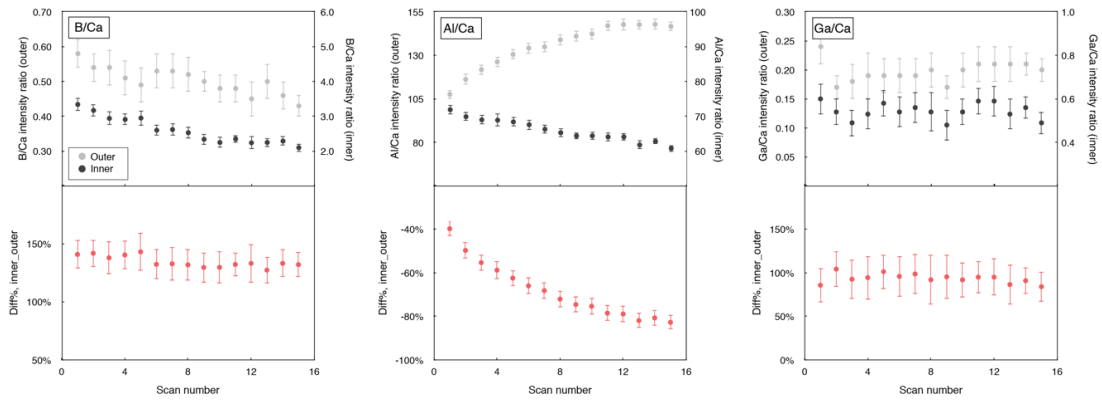


Fig. A3.3. B-Al-Ga composition depth profiles.

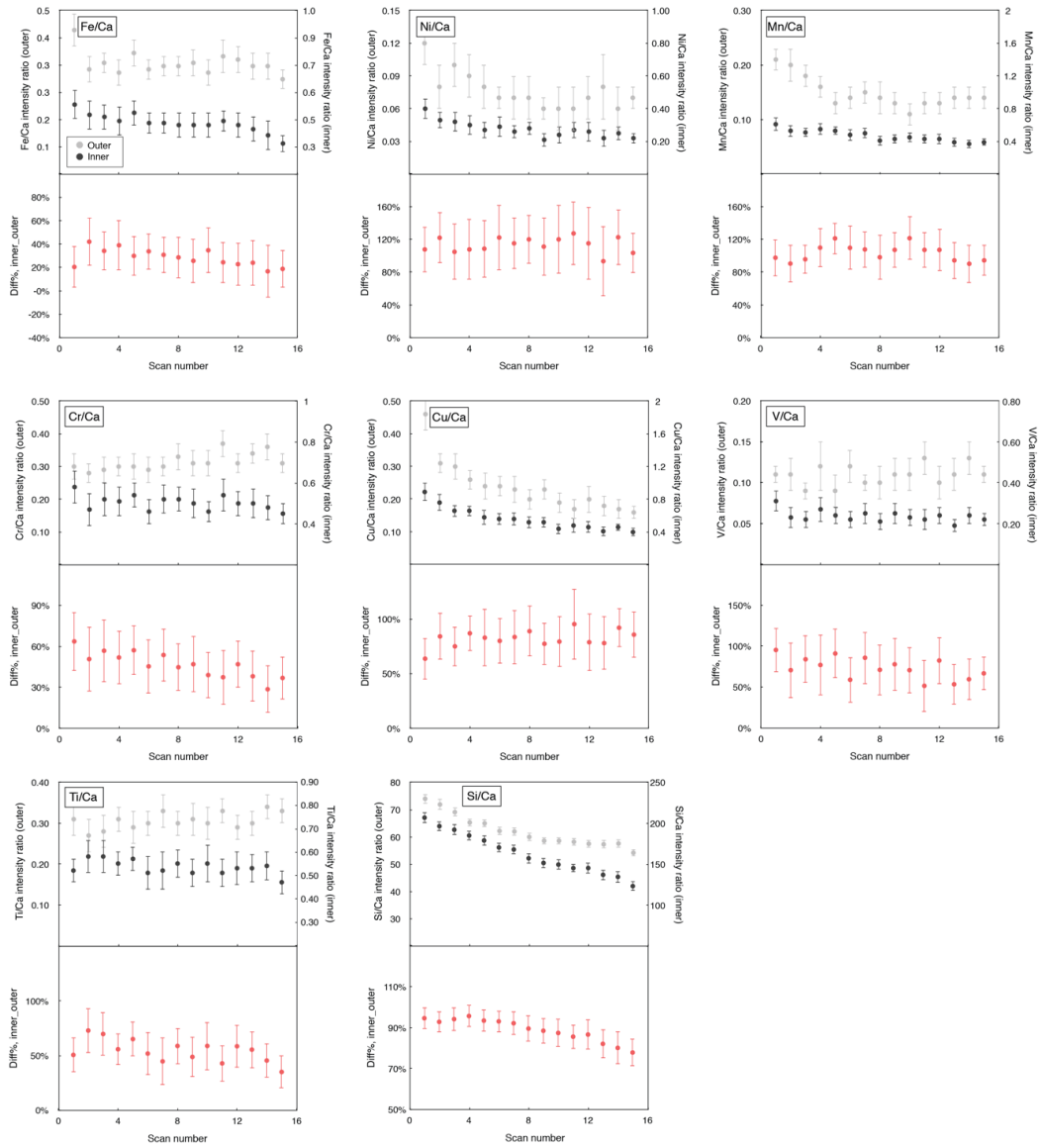


Fig. A3.4. Transition metal and Si composition depth profiles.

First and last integrated scans of X/Ca in the condensate blanket

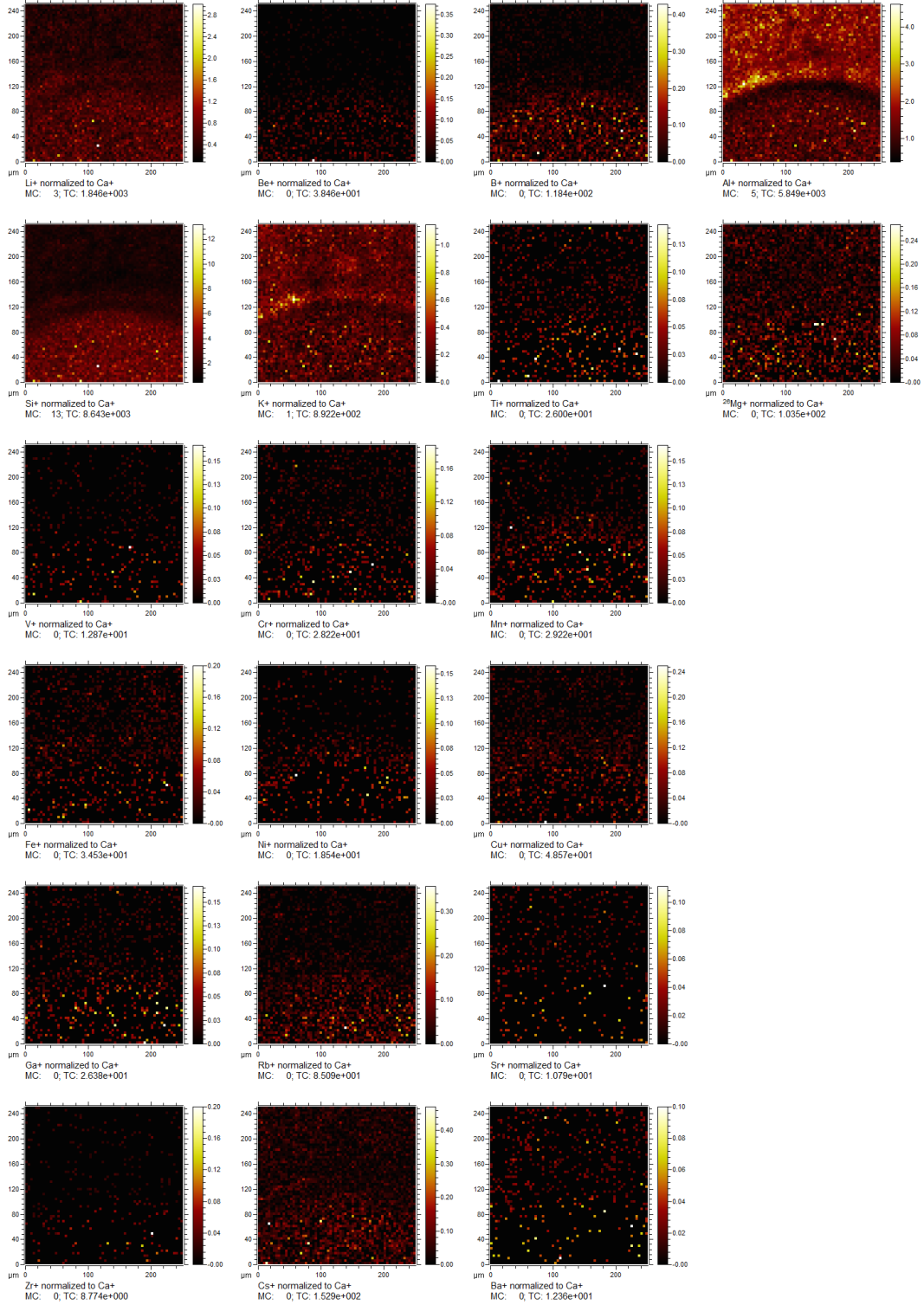


Fig. A3.5. X/Ca distributions across the condensate blanket (first integrated scan).

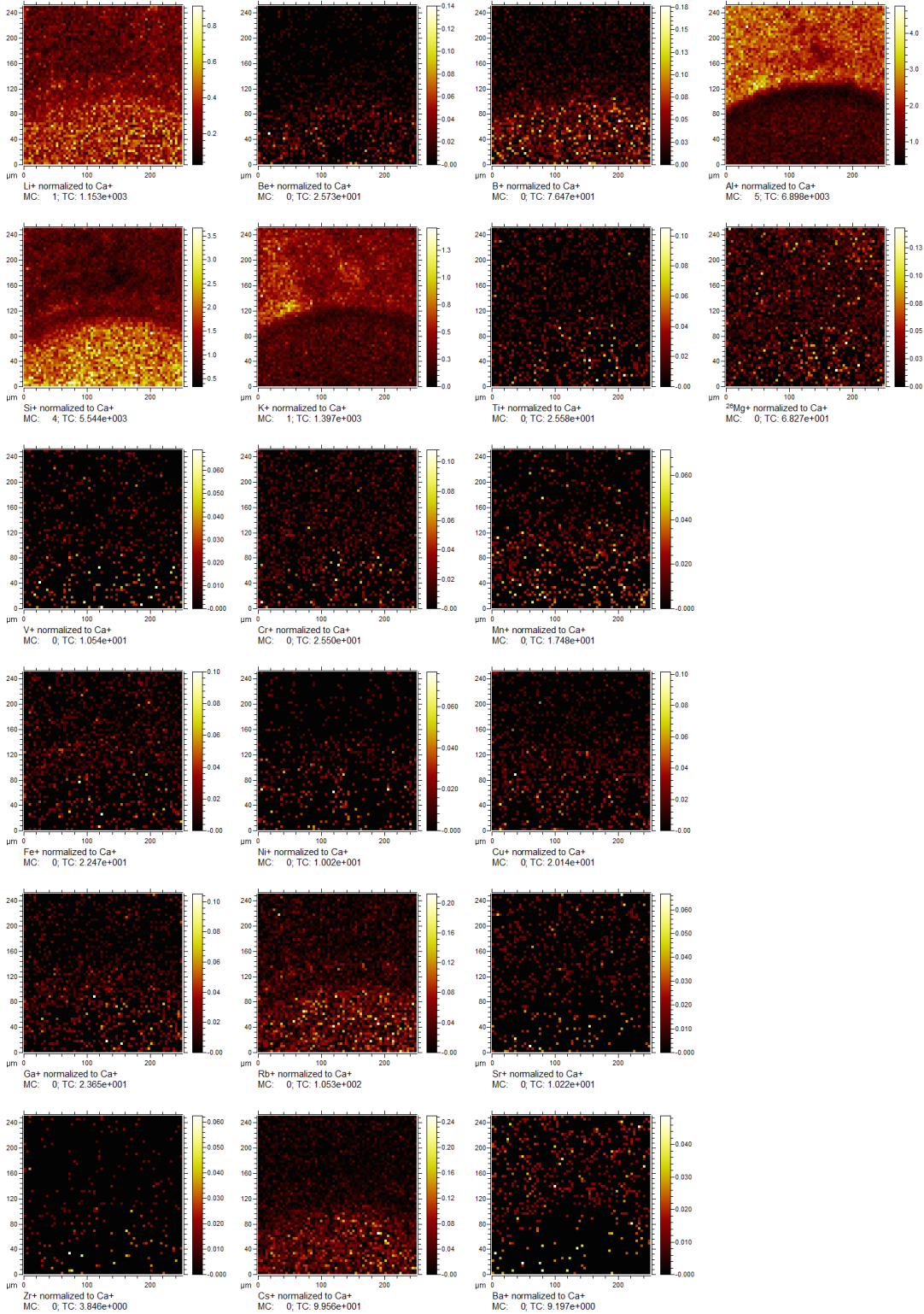


Fig. A3.6. X/Ca distributions across the condensate blanket (fifteenth integrated scan).

Chapter 4: Europium anomalies constrain the mass of recycled lower continental crust

[1] Tang, M., Rudnick, L.R., McDonough, F.W., Gaschnig, R.M., Huang, Y. (2015). Europium anomalies constrain the mass of recycled lower continental crust. *Geology*, 43(8), 703-706.

[2] M.T. compiled the data, designed the project, did the calculation and wrote the manuscript; R.L.R. and W.F.M. improved the design of this project and helped to revise the manuscript; R.M.G. provided diamictite data used in this work and commented on the manuscript; Y.H. helped in data compilation and statistics analysis, and commented on the manuscript.

Abstract

Statistical analyses of Sm-Eu-Gd concentrations in over 3000 samples from the upper, middle and lower continental crust reveal that the enrichment of Eu in the lower continental crust cannot compensate for the Eu deficit in the upper and middle continental crust, leaving the bulk continental crust with a significant negative Eu anomaly. Since the building blocks of the continental crust (mantle-derived basalts or tonalitic slab melts) do not possess a negative Eu anomaly, removal of Eu-enriched lower continental crust is required. Using Sm-Eu-Gd systematics and a mass conservation model, at least $2.9^{+1.1}_{-0.9}$ (95% confidence) crustal masses ($\sim 6 \times 10^{22}$ kg) appear to have been lost to the mantle over Earth's history via lower crustal recycling. Such a lower crustal component in the mantle may reappear in some ocean island basalts that have positive Eu anomalies and unradiogenic Pb isotopes.

4.1. Introduction

The compositional differences within the continental crust are manifestations of intra-crustal differentiation (Taylor and McLennan, 2008), which may occur in mature continental

crust or pre-cursor arc crust. It is widely accepted that the composition of the bulk continental crust is andesitic and is too evolved to be derived directly from the mantle (Arculus, 1981; Green et al., 2014; Rudnick, 1995). To explain the evolved crust composition, recycling of mafic to ultramafic lower crust has been proposed to occur through processes such as density foundering (Arndt and Goldstein, 1989; Kay and Mahlburg-Kay, 1991; Rudnick, 1995; Jull and Kelemen, 2001; Davidson and Arculus, 2005), subduction erosion (Clift et al., 2009; Lee, 2014, and references therein), or crustal subduction followed by relamination (Hacker et al., 2011).

Lower crustal recycling is poorly documented due to its non-observable nature in most circumstances (Taylor and McLennan, 2008). The geochemical evidence provided here supports the hypothesis that intra-crustal differentiation followed by lower crustal recycling is important in crustal evolution. Though lower crustal recycling is mostly studied in Phanerozoic arc systems (e.g., Greene et al., 2006; Jagoutz and Schmidt, 2013), it may also occur in cratons (e.g., Gao et al., 2004). Our geochemical approach using Sm-Eu-Gd systematics constrains the total mass of recycled lower continental crust (LCC) throughout Earth history, independent of the tectonic environments, processes, and timing of recycling.

4.2. Sm-Eu-Gd systematics in the continental crust

Europium is present in two valence states (+2 and +3). During intra-crustal differentiation, Eu is fractionated from Sm and Gd, as Eu^{2+} substitutes for Ca^{2+} and Na^+ in feldspar (Ren, 2004), which is stable under crustal pressure-temperature (P - T) conditions. The magnitude of Eu enrichment or depletion in a sample is calculated as a “Eu anomaly” relative to the neighboring rare earth elements Sm and Gd: $\text{Eu}/\text{Eu}^* = \text{Eu}_N / \sqrt{\text{Sm}_N * \text{Gd}_N}$, where the subscript N indicates normalization to chondritic values (Sun and McDonough, 1989). Feldspar left behind in the lower continental crust during intracrustal differentiation

causes a Eu deficit in the upper continental crust (UCC) and enrichment in the LCC (Taylor and McLennan, 2008). However, whether the current deep crustal reservoir compensates the Eu deficit in the UCC is unclear. Among the published compositional models for the bulk continental crust (BCC) (plotted in Appendix 1), all but one have negative Eu anomalies of varying magnitude (0.78–0.97), while only Taylor and McLennan (2008) proposed $\text{Eu}/\text{Eu}^* = 1$ for the BCC.

Here we evaluate Eu/Eu^* in the UCC, middle continental crust (MCC) and LCC using an updated data compilation following that of Huang et al. (2013). This data set has three subsets: high-*P* granulite facies rocks, amphibolite facies rocks, and shales + loess + tillites. For simplicity, we assume that the bulk compositions of samples in the three data sets represent those of the LCC, MCC, and UCC, respectively. We have applied no weighting of samples based on their bulk compositions nor have we used any geophysical information regarding the bulk composition of the deep crust. For our calculation, we used only samples that have Sm, Eu and Gd concentration data, comprising 970 samples from the LCC, 1702 samples from the MCC and 411 samples from the UCC. The amphibolite and granulite facies data compilations include samples having both metasedimentary and metaigneous protoliths. We excluded 10% of the samples with high and low Sm and Gd concentrations (removing 2.5% from the top and bottom of the Sm concentration distribution, then repeating the process for Gd), and then removed another 10% of samples with high and low Eu/Eu^* . This double filter, which eliminates 20% of the samples, helps to reduce the chance of incorporating atypical samples or bad analyses without shifting the results significantly (<10%).

Table 4.1. Mean concentrations of Sm, Eu and Gd in the continental crust and candidates of recycled lower continental crust.

	UCC	MCC	LCC	BCC
Mass (%) ^a	35.9 ± 6.0%	33.5 ± 4.3%	30.6 ± 3.4%	100%
This work ^b				
<i>n</i> ^c	328	1362	776	
Sm	5.3 ± 0.2	4.1 ± 0.1	3.6 ± 0.2	4.4 ± 0.2
Eu	1.08 ± 0.03	1.13 ± 0.03	1.22 ± 0.04	1.14 ± 0.03
Gd	4.5 ± 0.1	4.1 ± 0.1	3.7 ± 0.1	4.1 ± 0.1
Eu/Eu*	0.67 ± 0.01	0.84 ± 0.01	1.02 ± 0.02	0.82 ± 0.04
Rudnick and Gao, 2003				
Sm	4.7 ± 0.3	4.6	2.8	3.9
Eu	1 ± 0.1	1.4	1.1	1.1
Gd	4 ± 0.3	4	3.1	3.7
Eu/Eu*	0.72	0.96	1.14	0.89
Candidates for recycled LCC				
	JS13 ^d	K14 ^c	RG03 ^f	This study ^g
Sm	1.04	1.03	2.8	2.7 ± 0.2
Eu	0.55	0.47	1.1	1.00 ± 0.06
Gd	1.77	1.09	3.1	2.9 ± 0.2
Eu/Eu*	1.24	1.36	1.14	1.10 ± 0.03
$(m_{\text{recycled LCC}}/m_{\text{BCC}})^{\text{h}}$	2.6	2.0	1.9	2.9 + 1.1/-0.9

Note: The estimates of Rudnick and Gao (2003) are listed for comparison. The uncertainties in the estimates from this work are at the 95% confidence level. The uncertainties in the upper continental crust (UCC) values recommended by Rudnick and Gao (2003) are 1 σ standard deviation. MCC—middle continental crust; LCC—lower continental crust; BCC—bulk continental crust. $m_{\text{recycled LCC}}/m_{\text{BCC}}$ —mass proportion of recycled LCC relative to present-day continental crust. JS13—Arc delaminants from Jagoutz and Schmidt (2013). K14—Talkeetna arc lower crustal cumulates from Kelemen et al. (2014). RG03—LCC from Rudnick and Gao (2003).

^a The mass proportions of the UCC, MCC and LCC are from Huang et al. (2013)

^b Concentrations given in ppm by weight;

^c After filtering for extreme values, as described in text.

^d Means of granulite facies samples with Mg# > 50 and SiO₂ < 54%;

Table 4.1 lists the mean Sm, Eu, and Gd concentrations in UCC, MCC and LCC, the number of samples that went into the calculations after filtering, the values from Rudnick and Gao (2003), and the calculated mean concentrations of Sm, Eu, and Gd in the bulk

continental crust (BCC), which are made using a bootstrap method with 100,000 times resampling of the compositional data set. This technique allows estimation of the bulk composition and associated uncertainties with all samples taken into account. The mass proportions of UCC, MCC and LCC are based on global seismic data, as described in Huang et al. (2013), and the uncertainties were simulated using a Monte Carlo scheme (details in Appendix). Uncertainties or biases associated with the sampling of the UCC, MCC and LCC were not taken into account in these calculations. Although there are fewer UCC samples than MCC and LCC samples, sediments are powerful predictors of the bulk rare earth element (REE) composition of the UCC as REEs are insoluble and are transported quantitatively from the site of weathering to the site of deposition (Taylor and McLennan, 2008).

Our results suggest, along with previous estimates tabulated here, that the average UCC and MCC have negative Eu anomalies, while the average LCC possesses a small positive Eu anomaly. To reconcile the Eu/Eu* mass balance in the *absence* of lower crustal recycling, the Eu/Eu* of the modern LCC would need to be at least ~1.7 (using our estimated Sm-Eu-Gd concentrations in the BCC and Sm-Gd in the LCC), and this seems unlikely in light of the existing data (Fig. 4.1). Although one could argue that the data compiled here may be biased toward lower Eu/Eu* relative to the true composition of the LCC, we note that as Eu/Eu* increases in granulites, Eu concentration decreases (Fig. 4.2), so a more mafic (higher Mg#) lower crust with higher Eu/Eu* would have less leverage on the overall Eu/Eu* of the crust due to its lower REE concentration (see Appendix DR1 for sensitivity tests of assumed LCC composition). That is probably the reason that the Rudnick and Gao (2003) BCC, which incorporates a relatively mafic, high Eu/Eu* LCC, still has a significant negative Eu anomaly (Table 4.1).

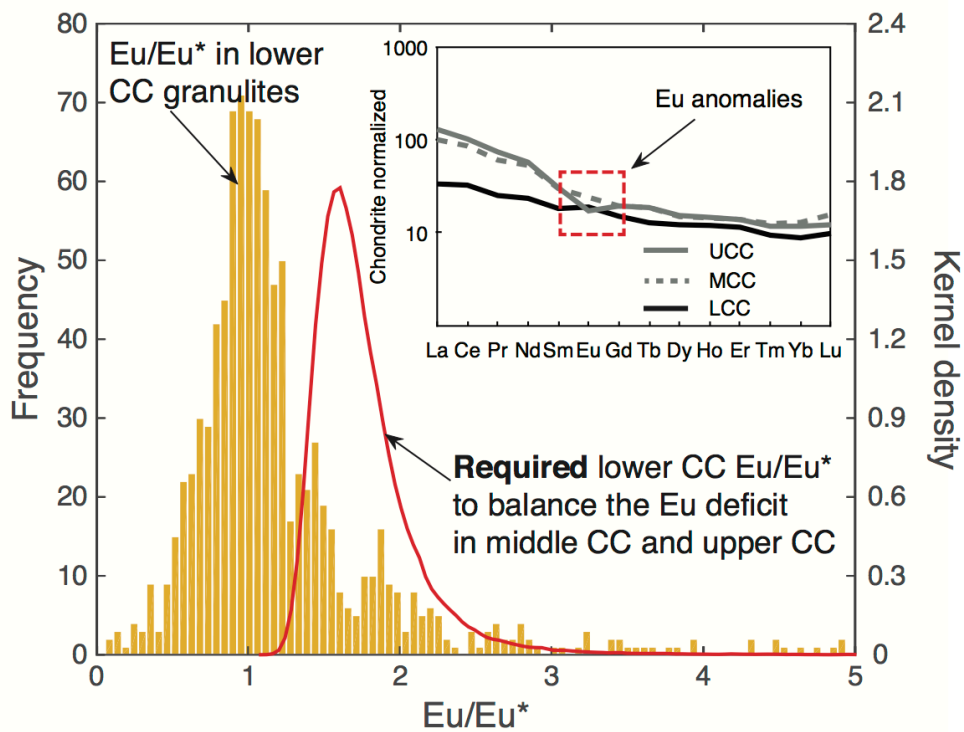


Fig. 4.1. Histogram showing the distribution of Eu/Eu^* values in granulite facies samples ($n = 970$), compared with the Eu/Eu^* of LCC required to make the BCC $\text{Eu}/\text{Eu}^* = 1$ (black assuming the LCC has the Sm and Gd concentrations from this study). Kernel density is an estimate of probability function. Inset: Chondrite-normalized rare earth element patterns for the upper continental crust (UCC, solid gray curve), middle continental crust (MCC, dashed gray curve) and lower continental crust (LCC, black curve), from Rudnick and Gao (2003).

4.3. The Eu dilemma

We assume, as many have (e.g., Taylor and McLennan, 2008; Gao et al., 1998), that the original crust produced by mantle melting has $\text{Eu}/\text{Eu}^* = 1$. However, rather than possessing no Eu anomaly, the modern BCC shows significant Eu depletion relative to Sm and Gd (Table 4.1). These observations require that materials with positive Eu anomalies be

transferred from the continental crust to the mantle. Our observations cannot constrain these processes, but can provide limits on the composition and mass of the recycled crust.

4.4. Calculating the mass of the recycled lower crust

Generally, crustal recycling takes two forms: sediment subduction and LCC recycling (via gravitationally driven processes e.g., density foundering, subduction erosion, relamination, etc.). Sediment subduction returns upper crustal materials to the mantle. Terrigenous sediments, which dominate the REE budget of global subducting sediments (Plank, 2014), have negative Eu anomalies, and thus cannot account for the Eu deficit in the continental crust. By contrast, recycling of the LCC is a plausible mechanism for decreasing the bulk crust Eu/Eu^* , as the LCC is observed to be enriched in Eu.

In our modeling, we make the following assumptions:

1. The present-day bulk continental crust has the composition provided in Table 4.1 and discussed herein.
2. Juvenile crust has a $\text{Eu}/\text{Eu}^* = 1.0$;
3. The loss of upper crustal mass due to sediment subduction removes material with $\text{Eu}/\text{Eu}^* < 1.0$ from the continental crust.
4. The Eu/Eu^* of recycled lower crust can be characterized using the following four compositional models: (1) an estimate of recycled intraoceanic arc lower crust (Jagoutz and Schmidt, 2013; 2) an estimate of high density cumulates in arc lower crust (Kelemen et al., 2014); (3) an estimate of the recycled LCC from this work (see following) and (4) the Rudnick and Gao's (2003) estimate of the modern LCC;

The latter two of these assumptions bear further discussion. Given the complexities associated with sediment subduction (i.e., the degree to which sediments melt in the subarc environment and how this may influence their REE patterns (Plank, 2005), and whether they

are relaminated to the lower crust (Behn et al., 2011)), we ignore sediment subduction in our mass balance model. Based on assumption #4 above, ignoring the subducted sediment flux leads to a minimum estimate of the mass of recycled lower crust.

The composition of the recycled LCC is difficult to assess except that these components may be denser than bulk crust, and possibly mantle peridotite¹, given their mafic to ultramafic bulk compositions. We therefore used four different lower crustal compositional estimates as candidates for the recycled lower crust (Table 4.1):

1. Arc lower crustal delaminates. Jagoutz and Schmidt (2013) calculated the composition of missing negatively buoyant cumulates from the crustal section of the Kohistan arc using a major element mass balance approach.
2. Arc lower crustal cumulates. Kelemen et al. (2014) calculated the average composition of Talkeetna arc high density lower crustal cumulates that may be subject to foundering.
3. Mafic LCC granulites. We estimate the Sm-Eu-Gd composition of recycled lower crust based on the average compositions of granulites with $Mg\# > 50$ ($Mg\# = \text{molar ratio of Mg to Mg + Fe}$) and $SiO_2 < 54\%$ (double filter applied, as described above), which limits the recycled component to mafic compositions. The density of these mafic granulites, with an average SiO_2 and $Mg\#$ of 48% and 64, respectively, can increase by ~10% during eclogitization (Austrheim, 1987) and exceed that of the underlying mantle (Krystopowicz and Currie, 2013). Although high $Mg\#$ granulites, on average, have more positive Eu anomalies (Fig. 4.2), this is counterbalanced by the fact that high $Mg\#$ granulites have low average Eu concentrations (Fig. 4.2).
- iv) We also considered the LCC composition of Rudnick and Gao (2003) as an end member scenario.

¹ A density greater than peridotite is not a precondition for recycling, as mafic granulites may transform to high-density eclogite upon subduction or during crustal thickening.

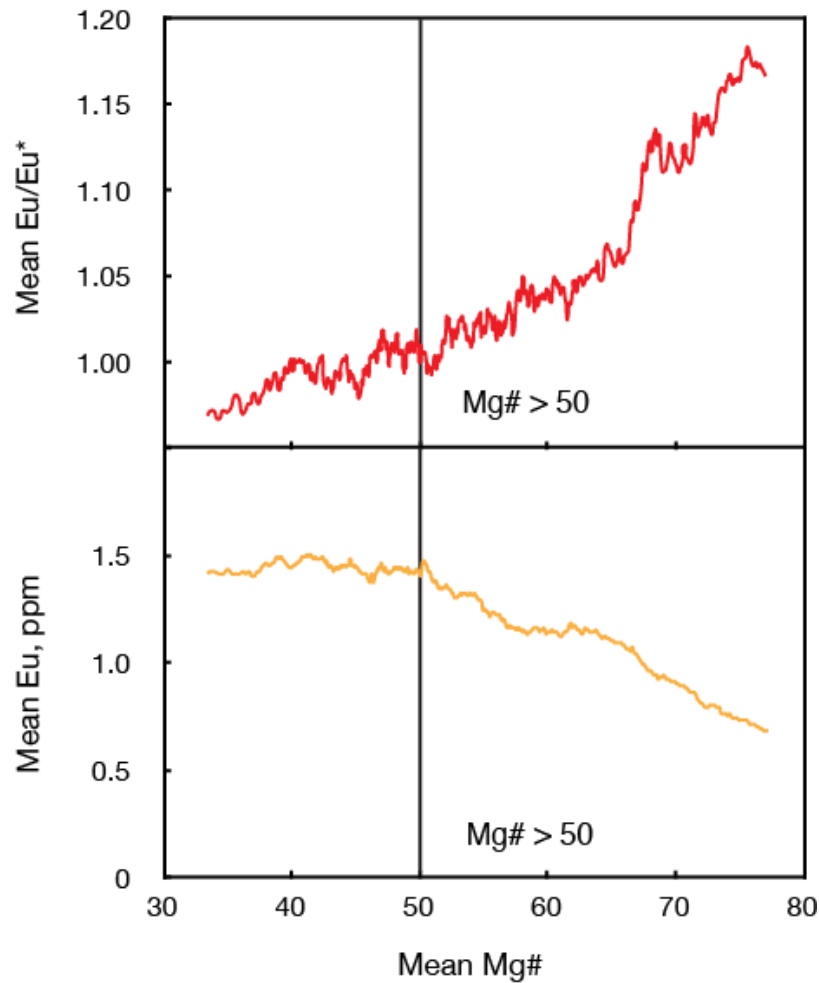


Fig. 4.2. Correlations between Eu/Eu^* , Eu concentration and $\text{Mg}\#$ in granulite facies samples. The mean Eu/Eu^* , Eu concentration and $\text{Mg}\#$ represent incremental averages. Each increment consists of 100 samples. High $\text{Mg}\#$ samples have high Eu/Eu^* but low Eu concentrations.

The mass of recycled LCC is calculated using mass conservation equations for Sm-Eu-Gd (i.e., the Eu/Eu^* in modern BCC + recycled LCC = bulk juvenile crust) (Appendix). Using the Sm-Eu-Gd compositions for the BCC estimated in this work, we calculated the mass of the recycled LCC to be at least $2.9^{+1.1}_{-0.9}$ (95% confidence) times the mass of the modern continental crust (Table 4.1 and Fig. 4.3). The results are not significantly different

whether using the recycled lower crust compositions of arc cumulates (Jagoutz and Schmidt, 2013; Kelemen et al., 2014) or the Rudnick and Gao's LCC (2003) (Fig. 4.3). Such consistency is not surprising given the anti-correlation between Eu/Eu^* and Eu concentration in various estimates of the recycled LCC (Table 4.1), similar to the observation in granulites (Fig. 4.2). This trade-off between Eu/Eu^* and Eu concentration makes the model relatively insensitive to the type of samples one chooses to calculate the composition of the recycled LCC. Our model is sensitive to the composition of BCC, which is subject to the uncertainties in sampling of deep crust. However, we show in the appendix that the BCC Eu/Eu^* is insensitive to the greatest unknown i.e., the LCC composition.

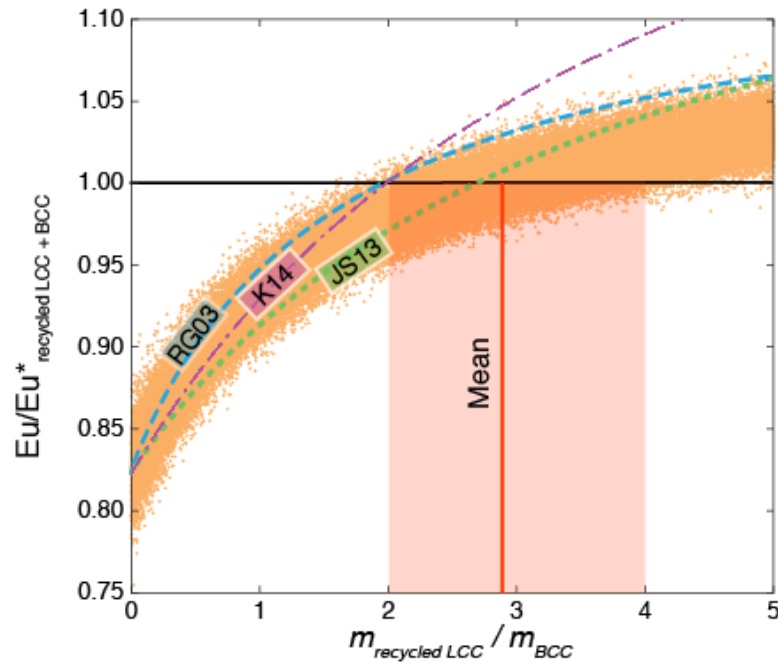


Fig. 4.3. Mass proportion of recycled LCC (x-axis) needed to compensate the Eu depletion in the modern BCC relative to an original crust with $\text{Eu}/\text{Eu}^* = 1$. By mass conservation the modern BCC plus the recycled LCC equals the initial juvenile crust. The field of gray dots is generated by Monte Carlo resampling, and represents the predicted distribution using our estimate for the recycled LCC derived from granulite facies samples with $\text{Mg}\# > 50$ and $\text{SiO}_2 < 54\%$ (the vertical black solid and dotted lines are the projected mean value and 95%

confidence interval, respectively, of the mass proportion of recycled LCC). Curve JS13 represents the model outcome using Jagoutz and Schmidt's Kohistan arc estimate (2013) for the recycled lower crust; curve K14 is calculated using Talkeetna arc high-density lower crustal cumulates; curve RG03 uses the LCC from Rudnick and Gao (2003).

The recycled LCC/BCC mass fraction required by our results over Earth history is within uncertainty of most previous estimates, all but one of which are based on regional case studies. Using Eu/Eu* and Sr/Nd, Gao et al. (1998) estimated 1–2 crustal masses (37–82 km) of LCC were recycled in Central East China. In the Mesozoic Sierra Nevada continental arc, 60%–75% of the original juvenile basalt (i.e., 1.5–3.0 crustal masses) is estimated to have been removed from the arc lower crust (Lee et al., 2007). This same ratio calculated by Jagoutz and Schmidt (2013) for the Kohistan arc ranges from 1.3 to 2.4 crustal masses. A somewhat lower estimate of recycled lower crust (25%–60% by mass foundering of arc lower crust, which translates into > 0.3–1.5 modern crustal masses) was obtained by Plank (2005) using Th/La systematics of modern arcs and average continental crust composition. However, as she pointed out, this range is a minimum estimate.

The recycled LCC mass (ca. 6×10^{22} kg) may form a significant reservoir within the mantle. It has a positive Eu anomaly and low μ ($^{238}\text{U}/^{204}\text{Pb}$) (e.g., Kramers and Tolstikhin, 1997), unradiogenic Sr and Nd isotopes, and radiogenic Os isotopes (e.g., Lee, 2014). Average ocean island basalts (OIB) also have a bulk positive Eu anomaly (Fig. 4.4a), which correlates negatively with $^{206}\text{Pb}/^{204}\text{Pb}$ (Fig. 4.4b). This negative correlation may reflect mixing between mantle components and recycled LCC with positive Eu anomalies and low $^{206}\text{Pb}/^{204}\text{Pb}$. Recycled LCC has been suggested to explain the geochemical characteristics of EM I type (enriched mantle I) OIB, typified by Kerguelen Plateau samples (e.g., Frey et al., 2002), which show pronounced positive Eu anomalies (mean Eu/Eu* = 1.12) and unradiogenic Pb isotopes (mean $^{206}\text{Pb}/^{204}\text{Pb}$ = 18.3). The recycled LCC, together with the

modern continental crust, may balance the depleted mantle in the Sr and Nd isotope systems if the recycling occurred relatively early in Earth's history.

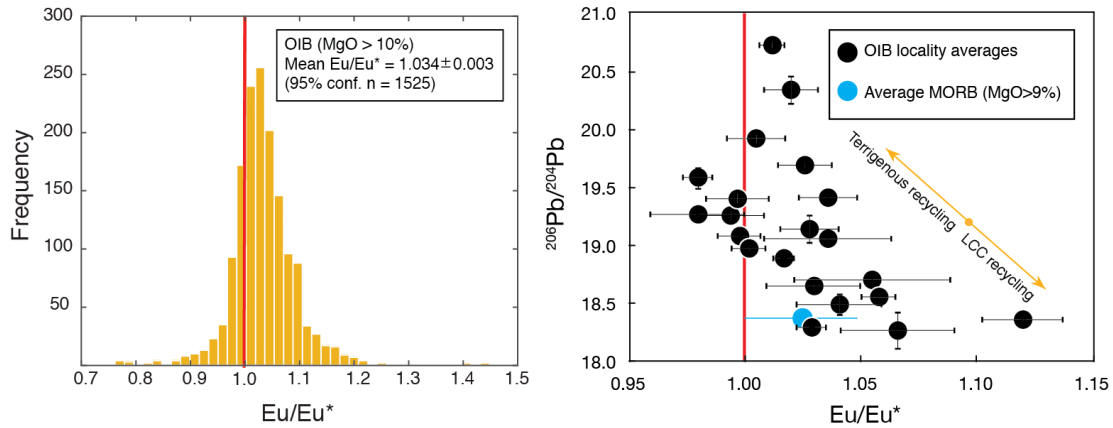


Fig. 4.4. a) Distribution of Eu/Eu^* values in primitive ocean island basalts (OIBs) with $\text{MgO} > 10\%$ (wt. %), and (b) $^{206}\text{Pb}/^{204}\text{Pb}$ versus Eu/Eu^* for OIB locality averages for OIBs with $\text{MgO} > 10\%$ (to avoid any influence from shallow magma differentiation); locality averages of Pb isotopes are calculated using all samples from each ocean island system. OIB data are from GeoRoc (<http://georoc.mpch-mainz.gwdg.de/georoc/>). Average MORB Eu/Eu^* is from our unpublished global primitive MORB data and average MORB Pb isotopes are from Gale et al. (2013).

4.5. Conclusions

Using available REE data for upper, middle and lower crustal samples, we show that the bulk continental crust has a significant negative Eu anomaly ($\text{Eu}/\text{Eu}^* = 0.82 \pm 0.04$, 95% conf.), a result consistent with most previous estimates of Eu/Eu^* in the continental crust. Assuming that the original crust extracted from the mantle has no Eu anomaly, recycling of Eu-enriched LCC (mass proportion $m_{\text{recycled LCC}} / m_{\text{BCC}}$ of $2.9^{+1.1}_{-0.9}$, 95% confidence) is required to account for the Eu deficit.

These findings affirm the important roles that intra-crustal differentiation and lower crustal recycling play in the formation and evolution of the continental crust. Moreover, they characterize the mass and composition of a component in the mantle (which could be spatially dispersed or concentrated) that plays a significant role in the chemical budget of the bulk silicate Earth. Consequently, models of growth of the continental crust (mass versus time) must consider that the total original crustal mass fraction could be a factor of four greater than the present mass of continental crust.

References

- Arculus, R.J., 1981, Island arc magmatism in relation to the evolution of the crust and mantle: *Tectonophysics*, v. 75, no. 1–2, p. 113–133, doi:10.1016/0040-1951(81)90212-2.
- Arndt, N.T., and Goldstein, S.L., 1989, An open boundary between lower continental crust and mantle: its role in crust formation and crustal recycling: *Tectonophysics*, v. 161, no. 3–4, p. 201–212, doi:10.1016/0040-1951(89)90154-6.
- Austrheim, H., 1987, Eclogitization of lower crustal granulites by fluid migration through shear zones: *Earth and Planetary Science Letters*, v. 81, no. 2–3, p. 221–232, doi:10.1016/0012-821X(87)90158-0.
- Behn, M.D., Kelemen, P.B., Hirth, G., Hacker, B.R., and Massonne, H.-J., 2011, Diapirs as the source of the sediment signature in arc lavas: *Nature Geoscience*, v. 4, no. 9, p. 641–646, doi:10.1038/ngeo1214.
- Clift, P.D., Schouten, H., and Vannucchi, P., 2009, Arc-continent collisions, sediment recycling and the maintenance of the continental crust, in Cawood, P.A., and Kröner, A., eds., *Earth Accretionary Systems in Space and Time*: Geological Society of London, Special Publications, v. 318, no. 1, p. 75–103, doi:10.1144/SP318.3.

- Davidson, J.P., and Arculus, R.J., 2005, The significance of Phanerozoic arc magmatism in generating continental crust: in Michael Brown and Tracy Rushmer ed., *Evolution and Differentiation of the Continental Crust*: Cambridge, Cambridge University Press, 156–158.
- Frey, F. A., Weis, D., Borisova, A. Y., and Xu, G., 2002, Involvement of Continental Crust in the Formation of the Cretaceous Kerguelen Plateau: New Perspectives from ODP Leg 120 Sites: *Journal of Petrology*, v. 43, no. 7, p. 1207-1239.
- Gale, A., Dalton, C. A., Langmuir, C. H., Su, Y., and Schilling, J.-G., 2013, The mean composition of ocean ridge basalts: *Geochemistry, Geophysics, Geosystems*, v. 14, no. 3, p. 489-518.
- Gao, S., Zhang, B.-R., Jin, Z.-M., Kern, H., Ting-Chuan, L., and Zhao, Z.-D., 1998, How mafic is the lower continental crust?: *Earth and Planetary Science Letters*, v. 161, no. 1–4, p. 101–117, doi:10.1016/S0012-821X(98)00140-X.
- Gao, S., Rudnick, R.L., Yuan, H.L., Liu, X.M., Liu, Y.S., Xu, W.L., Ling, W.L., Ayers, J., Wang, X.C., and Wang, Q.H., 2004, Recycling lower continental crust in the North China craton: *Nature*, v. 432, no. 7019, p. 892–897, doi:10.1038/nature03162.
- Greene, A.R., DeBari, S.M., Kelemen, P.B., Blusztajn, J., Clift, P.D., 2006, A detailed geochemical study of island arc crust: The Talkeetna arc section, South–Central Alaska: *Journal of Petrology*, v. 47, p. 1051–1093, doi:10.1093/petrology/egl002.
- Green, D.H., Hibberson, W.O., Rosenthal, A., Kovács, I., Yaxley, G.M., Falloon, T.J., and Brink, F., 2014, Experimental Study of the Influence of Water on Melting and Phase Assemblages in the Upper Mantle: *Journal of Petrology*, v. 55, no. 10, p. 2067–2096, doi:10.1093/petrology/egu050.
- Hacker, B.R., Kelemen, P.B., and Behn, M.D., 2011, Differentiation of the continental crust by relamination: *Earth and Planetary Science Letters*, v. 307, no. 3–4, p. 501–516, doi:10.1016/j.epsl.2011.05.024.

- Huang, Y., Chubakov, V., Mantovani, F., Rudnick, R.L., and McDonough, W.F., 2013, A reference Earth model for the heat-producing elements and associated geoneutrino flux: *Geochemistry Geophysics Geosystems*, v. 14, no. 6, p. 2003–2029, doi:10.1002/ggge.20129.
- Jagoutz, O., and Schmidt, M.W., 2013, The composition of the founder complement to the continental crust and a re-evaluation of fluxes in arcs: *Earth and Planetary Science Letters*, v. 371–372, no. 0, p. 177–190, doi:10.1016/j.epsl.2013.03.051.
- Jull, M., and Kelemen, P.B., 2001, On the conditions for lower crustal convective instability: *Journal of Geophysical Research. Solid Earth*, v. 106, no. B4, p. 6423–6446, doi:10.1029/2000JB900357.
- Kay, R.W., and Mahlburg-Kay, S., 1991, Creation and destruction of lower continental crust: *Geologische Rundschau*, v. 80, no. 2, p. 259–278, doi:10.1007/BF01829365.
- Kelemen, P.B., Hanghøj, K., and Greene, A.R., 2014, One View of the Geochemistry of Subduction-Related Magmatic Arcs, with an Emphasis on Primitive Andesite and Lower Crust, *in* Rudnick, R.L., ed., *The Crust: Treatise on Geochemistry (Second Edition)*: Oxford, Elsevier, v. 3, p. 749–806.
- Kramers, J.D., and Tolstikhin, I.N., 1997, Two terrestrial lead isotope paradoxes, forward transport modelling, core formation and the history of the continental crust: *Chemical Geology*, v. 139, no. 1–4, p. 75–110, doi:10.1016/S0009-2541(97)00027-2.
- Krystopowicz, N.J., and Currie, C.A., 2013, Crustal eclogitization and lithosphere delamination in orogens: *Earth and Planetary Science Letters*, v. 361, no. 0, p. 195–207, doi:10.1016/j.epsl.2012.09.056.
- Lee, C.-T.A., 2014, Physics and Chemistry of Deep Continental Crust Recycling, *in* Rudnick, R.L., ed., *The Crust: Treatise on Geochemistry (Second Edition)*: Oxford, Elsevier, v. 3, p. 423–456.

- Lee, C.-T.A., Morton, D.M., Kistler, R.W., and Baird, A.K., 2007, Petrology and tectonics of Phanerozoic continent formation: From island arcs to accretion and continental arc magmatism: *Earth and Planetary Science Letters*, v. 263, no. 3–4, p. 370–387, doi:10.1016/j.epsl.2007.09.025.
- Plank, T., 2005, Constraints from Thorium/Lanthanum on Sediment Recycling at Subduction Zones and the Evolution of the Continents: *Journal of Petrology*, v. 46, no. 5, p. 921–944, doi:10.1093/petrology/egi005.
- Plank, T., 2014, The Chemical Composition of Subducting Sediments, *in* Rudnick, R.L., ed., *The Crust: Treatise on Geochemistry (Second Edition)*: Oxford, Elsevier, v. 3, p. 607–629.
- Ren, M., 2004, Partitioning of Sr, Ba, Rb, Y, and LREE between alkali feldspar and peraluminous silicic magma: *The American Mineralogist*, v. 89, no. 8–9, p. 1290–1303.
- Rudnick, R.L., 1995, Making continental crust: *Nature*, v. 378, no. 6557, p. 571–578, doi:10.1038/378571a0.
- Rudnick, R., and Gao, S., 2003, Composition of the continental crust: *in* Rudnick, R.L., ed., *The Crust: Treatise on Geochemistry*: Oxford, Elsevier, v. 3, p. 1–64.
- Sun, S.-S., and McDonough, W.F., 1989, Chemical and isotopic systematics of oceanic basalts: Implications for mantle composition and processes, *in* Saunders, A.D., and Norry, M.J., eds., *Magmatism in the Ocean Basins*: Geological Society of London, Special Publications, v. 42, no. 1, p. 313–345, doi:10.1144/GSL.SP.1989.042.01.19.
- Taylor, S.R., and McLennan, S., 2008, *Planetary Crusts: Their Composition, Origin and Evolution*: Cambridge, Cambridge University Press, 1–4.

Appendix

1. Method of statistical analysis

One has to be careful and use only samples with complete Sm-Eu-Gd concentration data to study Eu/Eu* in the crust. This is because REEs are heterogeneous in the deep crust samples. Sm-Eu-Gd concentrations derived from different sets of crustal samples (e.g., Hacker et al., 2015) may not provide accurate Eu/Eu* estimates for the crust.

Concentrations of Sm, Eu and Gd in the UCC, MCC and LCC are significantly skewed by high concentration samples (Fig A4.1). Logarithmic transformation fits these concentration data to Gaussian distribution (Fig A4.2).

To calculate the mean concentrations of Sm, Eu and Gd and their associated uncertainties in the BCC, we used a bootstrapping resampling method. This technique allows estimation of the bulk composition and associated uncertainties with all samples taken into account. To do this, we first randomly resampled the UCC, MCC and LCC datasets. The size of each resample is equal to that of the original dataset. For example, our UCC dataset size is 328 (= 411*(1-20%)), and we resampled this dataset 328 times to make one UCC resample. For each resample, we calculated the mean Sm, Eu and Gd concentrations. Then we summed up the means of UCC, MCC and LCC resamples multiplied by their weighing factors (the mass proportions of the UCC, MCC and LCC). We repeated this step 100,000 times to get 100,000 resamples of mean BCC, with which we calculated the mean Sm, Eu, Gd concentrations and Eu/Eu* in the BCC (Fig A4.3).

Table A4.1. Lognormal means of Sm, Eu and Gd concentrations in the UCC, MCC and LCC. The asymmetrical uncertainties are two standard deviations of the populations.

	UCC	MCC	LCC
Sm, ppm	$5.1^{+3.6}_{-2.1}$	$3.6^{+7.1}_{-2.4}$	$3.0^{+8.2}_{-2.2}$
Eu, ppm	$1.05^{+0.65}_{-0.40}$	$1.02^{+1.5}_{-0.6}$	$1.08^{+1.9}_{-0.7}$
Gd, ppm	$4.4^{+3.3}_{-1.9}$	$3.7^{+5.6}_{-2.2}$	$3.2^{+7.2}_{-2.2}$

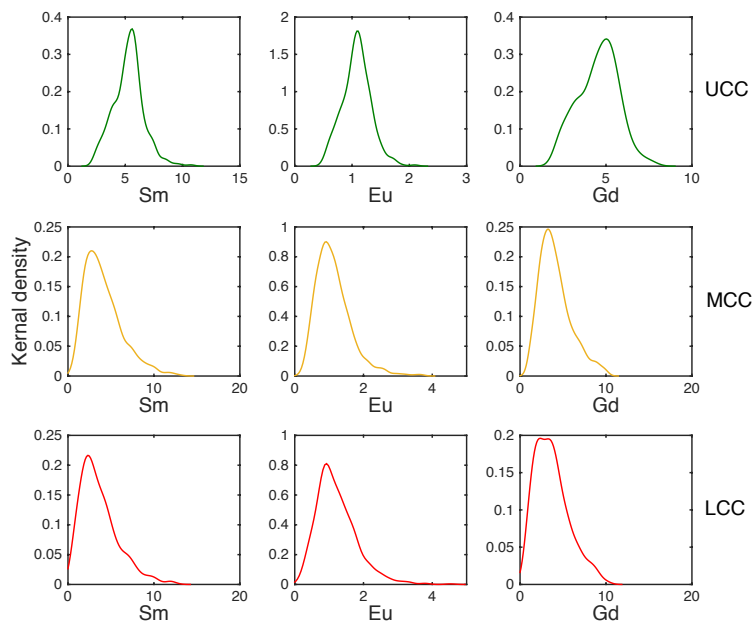


Fig. A4.4. Distributions of Sm, Eu and Gd concentrations (ppm) in the UCC, MCC and LCC.

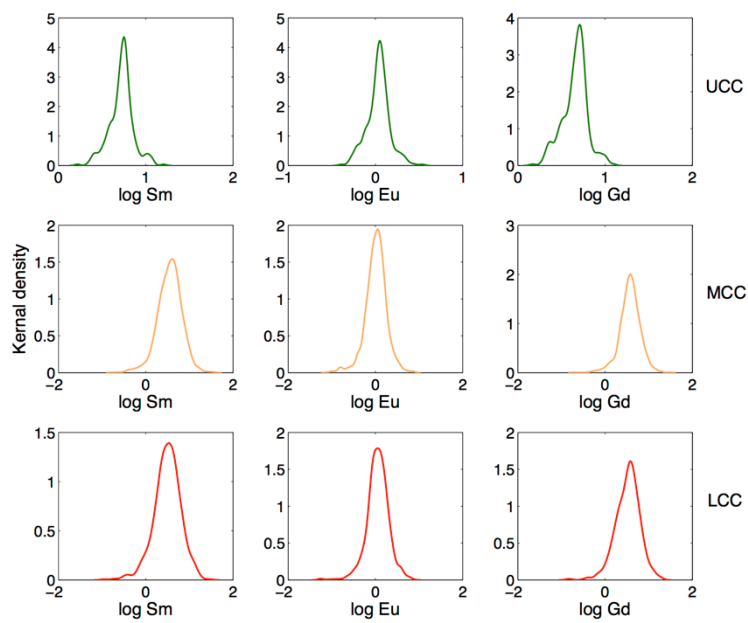


Fig. A4.5. Distributions of log-transformed Sm, Eu and Gd concentrations in the UCC, MCC and LCC.

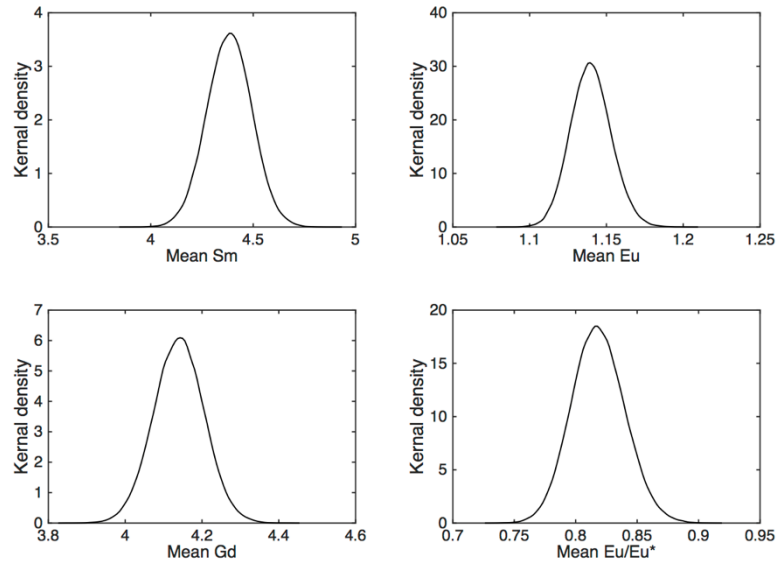


Fig. A4.6. Distributions of mean Sm, Eu and Gd concentrations (in ppm) and Eu/Eu* in the BCC.

We also simulated BCC samples and estimated the populations of Sm, Eu and Gd concentrations and Eu/Eu* in the simulated BCC samples. Each BCC sample is composed of one sample from the UCC, MCC and LCC, respectively, each of which was randomly selected from the UCC, MCC and LCC datasets and multiplied by the weighing factor. We obtained 100,000 simulated BCC samples by this scheme. The distributions of Sm, Eu, Gd concentrations and Eu/Eu* in the BCC samples are shown in Fig A4.

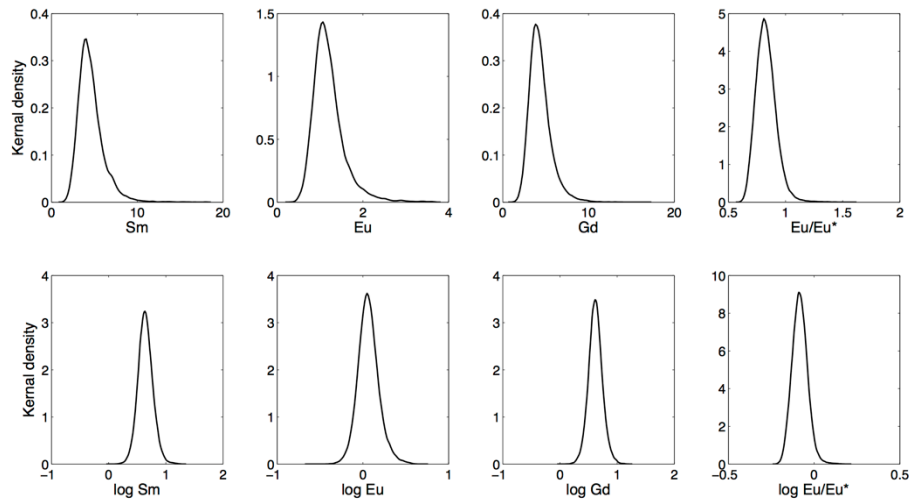


Fig. A4.4. Distributions of Sm, Eu, Gd concentrations (in ppm) and Eu/Eu* in the simulated BCC samples. Logarithmic transformation of the data resulted in Gaussian distributions.

2. Comparison of REE patterns and major element compositions of various BCC models

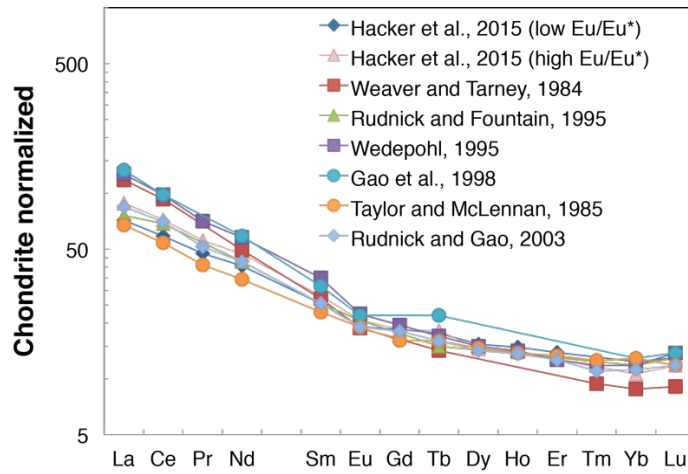


Fig. A4.5. Published REE composition models for the BCC.

Table A4.2. Bulk continental crust REE composition and Eu/Eu* of published models.

	Hacker et al., 2015 (low Eu/Eu*)	Hacker et al., 2015 (high Eu/Eu*)	Weaver and Tarney, 1984	Rudnick and Fountain, 1995	Wedepohl, 1995	Gao et al., 1998	Taylor and McLennan, 1985	Rudnick and Gao, 2003
La	17.0	21.0	28.0	18.0	30.1	31.5	16.0	20.0
Ce	36.0	44.0	57.0	42.0	60.0	60.0	33.0	43.0
Pr	4.5	5.3			6.7		3.9	4.9
Nd	19.0	22.0	23.0	20.0	27.0	27.4	16.0	20.0
Sm	3.9	4.3	4.1	3.9	5.4	4.8	3.5	3.9
Eu	1.1	1.2	1.1	1.2	1.3	1.3	1.1	1.1
Gd	3.8	3.8			4.0		3.3	3.7
Tb	0.66	0.68	0.5	0.6	0.6	0.8	0.6	0.6
Dy	3.9	3.7			3.8		3.7	3.6
Ho	0.84	0.79			0.80		0.78	0.77
Er	2.3	2.1			2.1		2.2	2.1
Tm			0.24		0.30		0.32	0.28
Yb	2.1	1.8	1.5	2.0	2.0	2.2	2.2	1.9
Lu	0.33	0.30	0.23	0.33	0.35	0.35	0.30	0.30
Eu/Eu*	0.87	0.91	0.86	0.97	0.86	0.78	0.99	0.89

Note: Eu/Eu* of BCC models that do not report Gd concentrations are calculated as $\text{Eu}/\text{Eu}^* = \text{Eu}_N / (\text{Sm}_N^{2/3} * \text{Tb}_N^{1/3})$.

Table A4.3. Lower crust major element compositions from this study (average of samples used to calculate Eu/Eu*) compared with previous studies. More studies of LCC major element compositions are available in Rudnick and Gao (2003). Errors are $2 \sigma_m$.

	This study	Rudnick and Gao, 2003	Hacker et al., 2015 (mafic endmember)	Hacker et al., 2015 (felsic endmember)
SiO ₂	53.3 ± 0.6	53.4	48.6	61.9
TiO ₂	1.0 ± 0.1	0.82	1.40	0.78

Al ₂ O ₃	16.3 ± 0.3	16.9	18.1	16.1
FeO _T	9.0 ± 0.3	8.57	10.44	6.52
MnO	0.18 ± 0.04	0.10	0.18	0.11
MgO	7.3 ± 0.4	7.24	6.87	3.14
CaO	8.9 ± 0.3	9.59	10.11	5.77
Na ₂ O	2.8 ± 0.1	2.65	2.85	3.92
K ₂ O	1.0 ± 0.1	0.61	1.22	1.54
P ₂ O ₅	0.18 ± 0.01	0.10	0.23	0.21
Total	100	100	100	100

Table A4.4. Middle crust major element compositions from this study (average of samples used to calculate Eu/Eu*) compared with previous studies. More studies of MCC major element compositions are available in Rudnick and Gao (2003). Errors are 2 σ_m .

	This study	Rudnick and Gao, 2003	Hacker et al., 2015 (mafic endmember)	Hacker et al., 2015 (felsic endmember)
SiO ₂	60.1 ± 0.6	63.5	53.1	67.7
TiO ₂	1.0 ± 0.1	0.69	1.26	0.55
Al ₂ O ₃	15.2 ± 0.2	15.0	16.7	15.6
FeO _T	6.0 ± 0.3	6.02	10.32	4.46
MnO	0.16 ± 0.01	0.10	0.21	0.08
MgO	5.5 ± 0.2	3.59	5.98	1.72
CaO	7.5 ± 0.3	5.25	7.48	3.62
Na ₂ O	2.9 ± 0.1	3.39	3.38	3.88
K ₂ O	1.6 ± 0.1	2.30	1.29	2.26
P ₂ O ₅	0.16 ± 0.01	0.15	0.24	0.18
Total	100	100	100	100

3. Sensitivity tests of how LCC composition affects BCC Eu/Eu*

The amount of recycled lower continental crust is a function of the BCC Eu/Eu*, and our BCC has next to the lowest Eu/Eu* of existing compositional models (Table A4.2, Fig.

A4.5). Because previous estimates of the BCC composition did not filter samples for reliability in calculations of Eu/Eu^* (as described in section 1 of this appendix), and because most used log-normal means to calculate trace element abundances (e.g., Rudnick and Fountain, 1995; Rudnick and Gao, 2003, Hacker et al., 2015) these previous estimates cannot be used to determine how BCC composition affects the mass of recycled LCC. Instead, we have performed a series of sensitivity tests of our BCC composition, focusing on the LCC composition, which is the only portion of the crust to show a positive Eu anomaly. The LCC is highly heterogeneous, is also the least accessible, and arguably the poorest known in terms of bulk composition.

We investigate the variability of the LCC using the granulite database we have compiled for Eu/Eu^* . We sorted these granulites by their $\text{Mg}\#$, SiO_2 content, and mid-REE (Sm considered here) concentrations, and then calculated the running averages of granulite composition ($n = 100$) as possible LCC compositions. Fig A4.6 shows that the calculated BCC Eu/Eu^* does not change beyond our uncertainty, no matter which flavor of granulite we adopt for the LCC. This demonstrates the robustness of BCC Eu/Eu^* against the uncertainty in sampling of the LCC i.e., the proportion of mafic granulites to felsic granulites and high mid-REE granulites to low mid-REE granulites. This is due to the trade-off between Eu/Eu^* and Eu concentration in granulites (Fig. 4.2 in the paper). Generally, mafic granulites have higher Eu/Eu^* but lower Eu concentrations than felsic granulites.

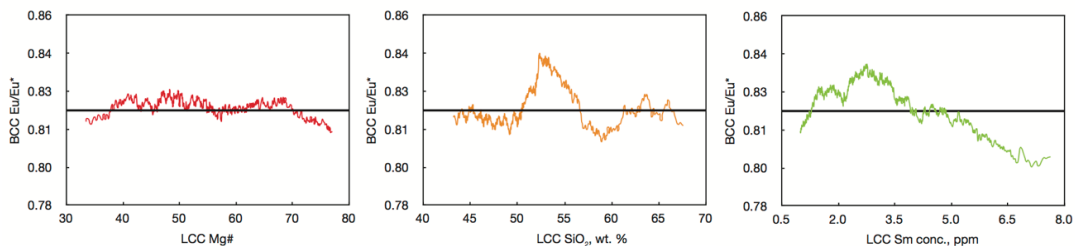


Fig. A4.6. BCC Eu/Eu^* as functions of LCC $\text{Mg}\#$, SiO_2 content and mid-REE (Sm considered here) concentration, respectively. The black lines (corresponding to $\text{Eu}/\text{Eu}^* =$

0.82) indicate the BCC Eu/Eu^* in Table 4.1 and the entire scale of the y-axis represents the adopted uncertainty of BCC Eu/Eu^* .

4. Eu/Eu^* and Sr isotopes in OIBs.

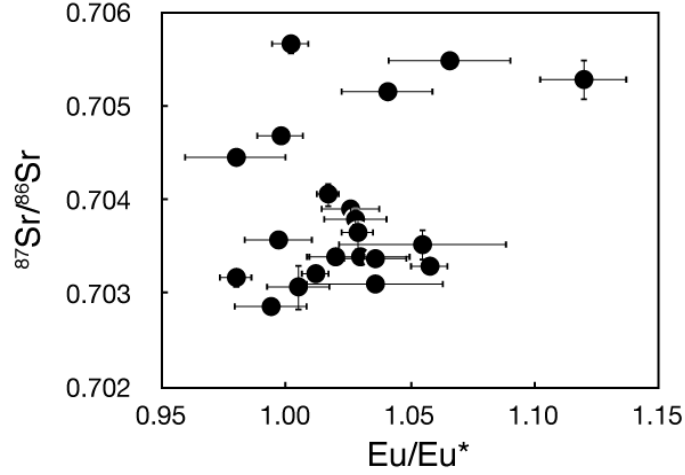


Fig. A4.7. $^{87}\text{Sr}/^{86}\text{Sr}$ vs. Eu/Eu^* in OIB locality averages. Locality averages of Eu/Eu^* are calculated using only OIBs with $\text{MgO} > 10\%$ to avoid any influence from shallow magma differentiation; locality averages of Sr isotopes are calculated using all samples from each ocean island system.

5. Mass conservation equations

$$\text{Sm}_{\text{JCC}} * m_{\text{JCC}} = \text{Sm}_{\text{BCC}} * m_{\text{BCC}} + \text{Sm}_{\text{recycled_LCC}} * m_{\text{recycled_LCC}} \quad (\text{A4.1})$$

$$\text{Eu}_{\text{JCC}} * m_{\text{JCC}} = \text{Eu}_{\text{BCC}} * m_{\text{BCC}} + \text{Eu}_{\text{recycled_LCC}} * m_{\text{recycled_LCC}} \quad (\text{A4.2})$$

$$\text{Gd}_{\text{JCC}} * m_{\text{JCC}} = \text{Gd}_{\text{BCC}} * m_{\text{BCC}} + \text{Gd}_{\text{recycled_LCC}} * m_{\text{recycled_LCC}} \quad (\text{A4.3})$$

$$m_{\text{JCC}} = m_{\text{BCC}} + m_{\text{recycled_LCC}} \quad (\text{A4.4})$$

$$Eu / Eu^*_{JCC} = \frac{(Eu_{JCC})_N}{\sqrt{(Sm_{JCC})_N * (Gd_{JCC})_N}} \geq 1 \quad (A4.5)$$

The subscript N in equation A2.5 indicates chondrite value normalized.

References

- Gao, S., Luo, T.-C., Zhang, B.-R., Zhang, H.-F., Han, Y.-w., Zhao, Z.-D., and Hu, Y.-K., 1998, Chemical composition of the continental crust as revealed by studies in East China: *Geochimica et Cosmochimica Acta*, v. 62, no. 11, p. 1959-1975.
- Hacker, B. R., Kelemen, P. B., and Behn, M. D., 2015, Continental lower crust: Annual Reviews of Earth and Planetary Sciences, in press.
- Hans Wedepohl, K., 1995, The composition of the continental crust: *Geochimica et cosmochimica Acta*, v. 59, no. 7, p. 1217-1232.
- Rudnick, R., and Gao, S., 2003, Composition of the continental crust: *Treatise on geochemistry*, v. 3, p. 1-64.
- Rudnick, R. L., and Fountain, D. M., 1995, Nature and composition of the continental crust: A lower crustal perspective: *Reviews of Geophysics*, v. 33, no. 3, p. 267-309.
- Taylor, S. R., and McLennan, S. M., 1985, *The Continental Crust*, Wiley.
- Weaver, B. L., and Tarney, J., 1984, Empirical approach to estimating the composition of the continental crust: *Nature*, v. 310, no. 5978, p. 575-577.

Chapter 5: Europium anomaly in the MORB source mantle

[1] Tang, M., McDonough, W.F., Rudnick, L.R. (201X). Europium anomaly in the MORB source mantle. *Geochimica et Cosmochimica Acta*, in revision.

[2] M.T. carried out the analyses, did the calculation and wrote the manuscript; W.F.M. designed the project and provided comments on the manuscript; R.L.R. commented on the manuscript.

Abstract

We report high precision Eu/Eu* data for 72 primitive MORB glasses (MgO > 8.5%) from the Pacific, Indian, and Atlantic mid-ocean ridges. The mean Eu/Eu* of the 46 MORB glasses with MgO \geq 9 wt.% is 1.025 ± 0.025 ($2 \sigma_m$), thus the upper mantle, as sampled by MORB, is unlikely to possess a positive Eu anomaly that compensates the Eu deficit in the continental crust. The primitive MORB samples show both positive and negative Eu anomalies, with no correlation between Eu/Eu* and MgO contents. Such a correlation might be expected if plagioclase fractionation (which co-precipitates with olivine) controlled the Eu/Eu*. The lack of correlation suggests that other processes created the variability seen in Eu/Eu*. Modeling Sm-Eu-Gd fractionation during spinel peridotite partial melting suggests that the weak positive and negative Eu anomalies seen in primitive MORBs may result from greater incompatibility and faster diffusivity of Eu (II) relative to Sm and Gd during generation of early vs. late melt fractions, respectively. If the MORB source mantle is insufficient to counterbalance the Eu deficit in the continental crust, a third reservoir is required to establish the Sm-Eu-Gd mass balance for the bulk silicate earth. This reservoir may be lower continental crust that has been at least partially recycled into the mantle source of ocean island basalts.

5.1. Introduction

Europium is present in two valence states (+2 and +3) in most magmatic systems. Europium (II) behaves like Sr^{2+} due to their similar ionic radii (1.25 vs. 1.26 Angstroms, respectively, Shannon, 1976). In the crust, where plagioclase is stable, Eu (II) is strongly partitioned into plagioclase and thus fractionated from Sm and Gd. During intra-crustal differentiation, Eu can be removed from the melt by fractional crystallization of plagioclase or retained in the residual plagioclase at the source. As a consequence, the upper continental crust is distinctly depleted in Eu while the lower continental crust possesses a Eu excess. The bulk continental crust likely has a negative Eu anomaly based on observations of crustal samples (Tang et al., 2015), and most compositional models for the continental crust have a negative Eu anomaly (Rudnick and Gao, 2014 and the references therein). Such Eu depletion in the crust likely results from lower crustal recycling.

Niu and O'Hara (2009) observed a positive correlation between Eu/Eu^* ($\text{Eu}/\text{Eu}^* = \text{Eu}_N/\sqrt{\text{Sm}_N * \text{Gd}_N}$) and MgO content in MORB samples from the East Pacific Rise. They also observed that MORB samples having $\text{MgO} > 8.5 \text{ wt.}\%$ all have positive Eu anomalies ($\text{Eu}/\text{Eu}^* > 1$). These authors suggested that all primitive MORBs have positive Eu anomalies, and that the depleted MORB mantle (DMM, the source region of MORB) might host the Eu that is missing from the continental crust. More recently, Arevalo and McDonough (2010) failed to reproduce the correlation between Eu/Eu^* and MgO in their global MORB dataset, which shows large variation in Eu/Eu^* for MORB samples having MgO contents $> 8.5\%$. In addition, both positive and negative Eu anomalies in global MORB were observed by Jenner and O'Neill (2012a) and Gale et al. (2013). However, none of these studies were dedicated to high precision measurement of Eu/Eu^* in MORB. The total variation of Eu/Eu^* is limited ($\sim 20\%$) in primitive MORB and requires that the Sm-Eu-Gd fractionation induced by Laser Ablation Inductively Coupled Mass Spectrometry (LA-ICP-MS) method be controlled in

order to avoid significant analytical errors (Tang et al., 2014). To investigate this issue further, we developed a new LA-ICP-MS method (Tang et al., 2014), and measured Eu/Eu^* at high precision and accuracy in 72 primitive MORB glasses globally. Our results do not support a significant positive Eu anomaly in the upper mantle as sampled by MORB.

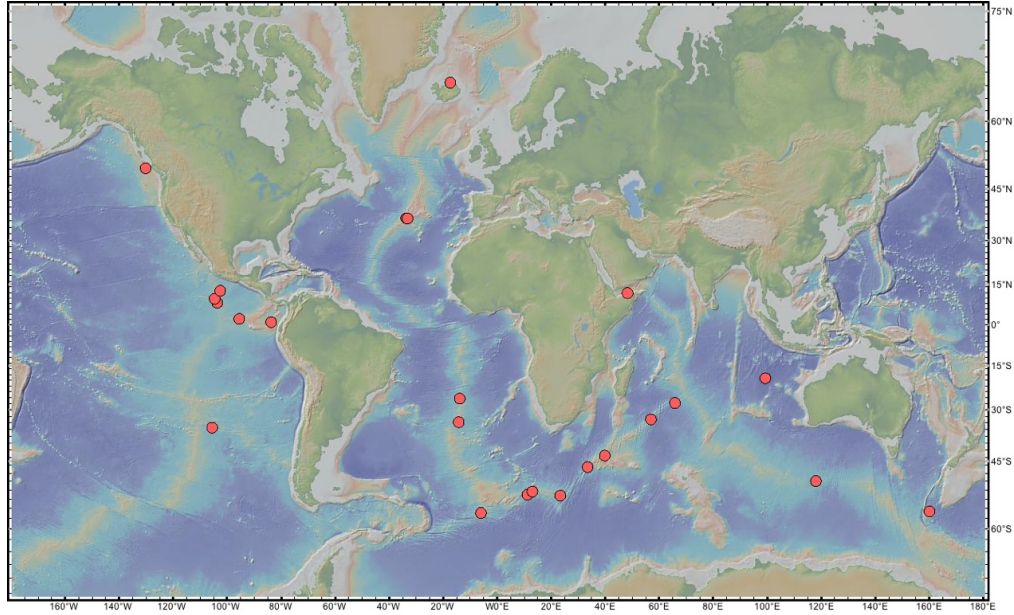


Fig. 5.1. Sample locations (red circles) of the MORB glasses analyzed in this study.

5.2. Samples and analytical methods

A total of 72 MORB glasses from 21 sites (Fig. 5.1) were measured for their Eu/Eu^* and MgO contents. Of these samples, 28 are from the Pacific, 22 are from the Indian and 22 are from the Atlantic. All samples have MgO contents $> 8.5\%$, and are thus relatively primitive.

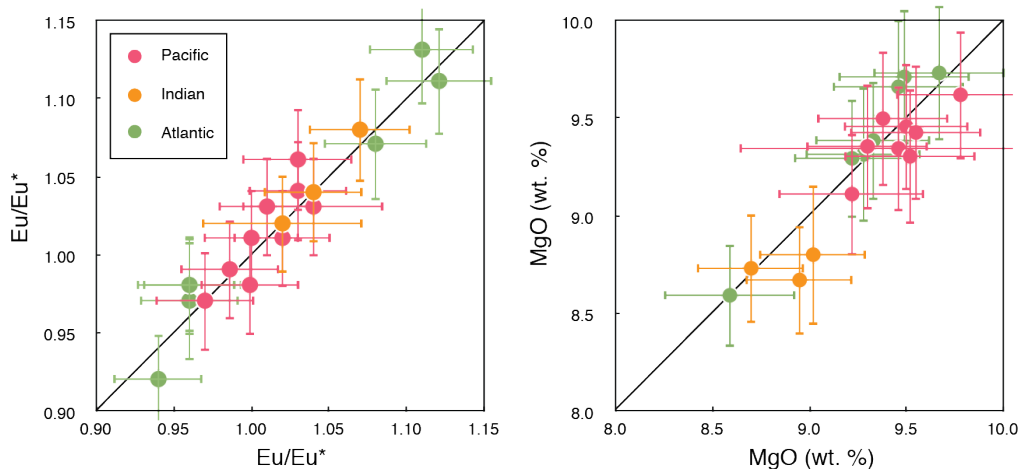


Fig. 5.2. Reproducibility of measured Eu/Eu^* and MgO contents for samples analyzed on different days. See text for calculation of errors.

The LA-ICP-MS method used here, adopted from Liu et al. (2008), allows simultaneous determination of major and trace element concentrations in volatile-free samples. One of the two basaltic reference materials, KL2-G and BIR-1G, were analyzed after every one or two samples (three to four repeated analyses for each sample). A long-term reproducibility of $\sim 3\%$ (2 SD) was achieved for both Eu/Eu^* and MgO in KL2-G and BIR1-G. The Eu/Eu^* measured in reference materials over a wide range of compositions agree with GeoReM preferred values (<http://georem.mpch-mainz.gwdg.de/>) within 3%. To avoid potential heterogeneities such as micro-inclusions, we measured each glass chip three to four times at different sites. We excluded individual spot analyses having distinct Eu/Eu^* (> 2 SD long-term reproducibility different from the remainder) or major element composition compared to the remainder of the analyses on the same sample, and took the average values of the remainder as the Eu/Eu^* and MgO content for each sample. Twenty-five analyses (marked in red in the supplementary file) were thus discarded from the total of 320 analyses (7.8% of the population). We compared the long-term reproducibility of the two reference materials, and standard deviation of multiple analyses of each sample, and took whichever is greater as the

uncertainty. Nineteen randomly selected samples were re-analyzed on different days to check the reproducibility (Fig. 5.2).

5.3. Results

The primitive MORB samples we analyzed show both positive and negative Eu anomalies (Eu/Eu^* from 0.92 to 1.13). Negative Eu anomalies are present even in samples with $\text{MgO} > 9\%$ where plagioclase is undersaturated (Fig. 5.3). More primitive MORB samples are unlikely to have significant positive Eu anomalies, as there is no correlation between Eu/Eu^* and MgO when MgO exceeds 8.5%, precluding extrapolation to higher MgO . The three ocean basins, Pacific, Indian, and Atlantic, show no discernable difference in their mean Eu/Eu^* (1.011 ± 0.013 , 1.023 ± 0.020 and 1.030 ± 0.024 , respectively).

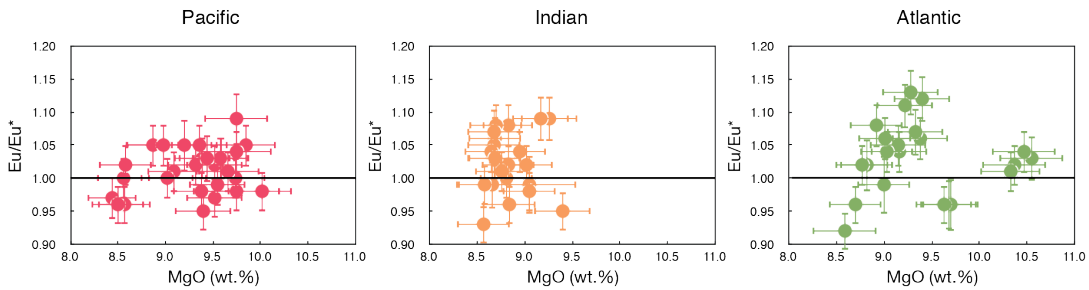


Fig. 5.3. Eu/Eu^* vs. MgO in primitive MORB glasses analyzed here from global mid-ocean ridges ($n = 72$).

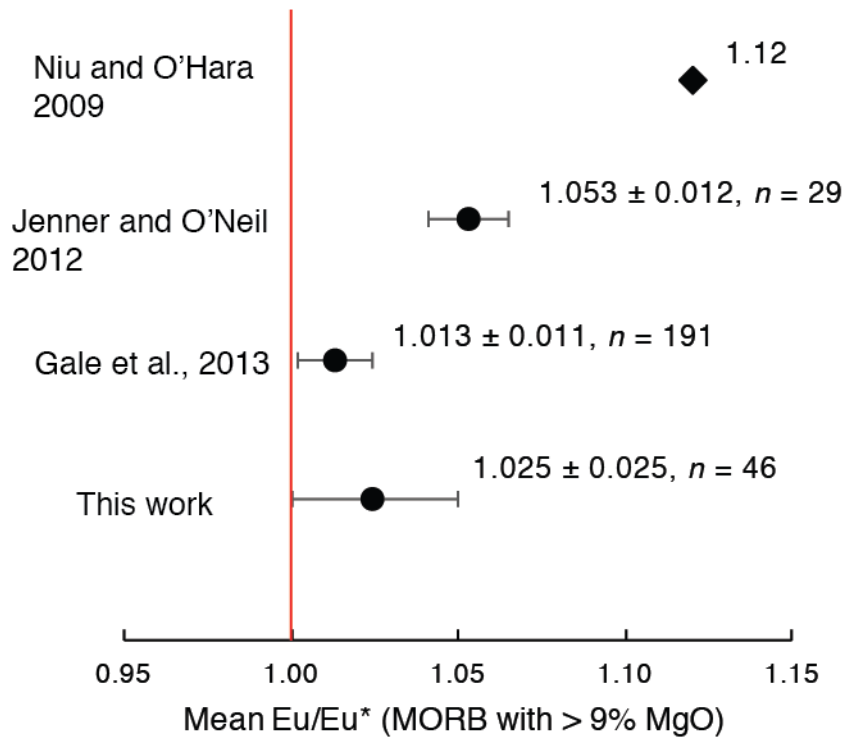


Fig 5.4. Mean Eu/Eu* observed in MORB with >9 wt.% MgO from this study compared with published estimates. Gale et al.'s (2013) data are from their own analyses plus their compilation, while the mean Eu/Eu* values from Jenner and O'Neill (2012) and Niu and O'Hara (2009) are based their own analyses of MORB. Error bars are 2 σ_m .

The full dataset yields a mean Eu/Eu* of 1.020 ± 0.011 (2 σ_m , n = 72). Considering that plagioclase begins to crystallize at ~9% MgO (Bender et al., 1984; Niu et al., 2002; Niu and O'Hara, 2009), samples with MgO < 9% were filtered out to minimize the effect of plagioclase fractionation. The remaining 46 samples yield a mean Eu/Eu* of 1.025 ± 0.013 (2 σ_m), which is not significantly different from the full dataset mean Eu/Eu*. Considering ~2% (2 σ) uncertainty for the Eu/Eu* of our calibration standard BHVO-2G (<http://georem.mpch-mainz.gwdg.de/>), global primitive MORBs (MgO > 9%) have a mean Eu/Eu* of 1.025 ± 0.025 (2 σ_m). Our mean Eu/Eu* for global MORBs with MgO > 9% is consistent with results

from the previous studies of Jenner and O'Neill (2012a) and Gale et al. (2013) (Fig. 5.4). The repeated analysis of Eu/Eu* in USGS standard BCR-2G by Jenner and O'Neill (2012b) is 5% higher than the GeoReM preferred value, which may account for their slightly higher Eu/Eu* derived for high MgO MORBs (Fig. 5.4). Niu and O'Hara's mean Eu/Eu* value was estimated using a set of local samples from the East Pacific Rise, and their detailed sample information was not provided.

5.4. Discussion and modeling

5.4.1. The MgO criterion

Here we followed Niu and O'Hara (2009) and used MgO content as a filter during sample selection. Primitive MORB samples are non-existent since fractional crystallization readily occurs at mantle depths beneath mid ocean ridges (Wanless and Shaw, 2012). However, the early crystallizing phases olivine and spinel have no effect on Eu/Eu* in the melts, which is only sensitive to plagioclase fractionation. Therefore, MORB samples that are undersaturated in plagioclase should represent the primitive Eu/Eu*. Although plagioclase contains little MgO, co-crystallization of olivine and plagioclase produces positive correlations between MgO and plagioclase crystallization indices such as Sr/Sr* and Eu/Eu* (e.g., Gale et al., 2013; Jenner and O'Neill, 2012a; Niu and O'Hara, 2009). These observations justify the use of the MgO content as a criterion in selecting samples that can represent the primitive/bulk Eu/Eu*.

Interaction with plagioclase cumulates in the lower oceanic crust can potentially alter the Eu/Eu* in the MORB melts. Despite the complexities of such cumulate-melt interaction, high MgO (>9%) MORB melts are mostly undersaturated in plagioclase, and would, thus, tend to dissolve plagioclase in the cumulates. Chemical re-equilibration may also happen during cumulate-melt interaction. In this process, Eu (II), which diffuses faster than Sm (III) and Gd

(III) (Cherniak and Liang, 2007), is more likely to diffuse from the plagioclase into the high MgO melts because the cumulates formed from MORB melts with various compositions but on average more evolved compositions and higher Eu concentrations than primitive MORB (see Supplementary file for Eu concentration vs. MgO in MORB). The net effect of either plagioclase dissolution or chemical re-equilibration is to increase the average Eu/Eu* in the high MgO melts during ascent through the crystal mush. Therefore, the primitive melts may have had even lower Eu/Eu* than our high MgO MORB samples, depending on the extent of cumulate-melt interaction.

Recycled oceanic crust can produce silica-rich melts that react with peridotite to form pyroxenite (Sobolev et al., 2005). Partial melting of pyroxenite in the mantle may produce melts with lower MgO contents than those of peridotite (Lambart et al., 2013). Pyroxenite-derived melts have been estimated to contribute between 10–30% by mass to MORB melts (Sobolev et al., 2007). Assuming peridotite-derived melts have primitive MgO contents > 11% (the most primitive MORB sample analyzed here has 10.5% MgO), mixing pyroxenite- and peridotite-derived melts does not generate MORB with MgO < 9%, even assuming incorporation of a maximum of 30% pyroxenite-derived melts with ~4% MgO. Therefore, our MgO filter (>8.5%) may include primitive MORB samples with significant contributions from recycled crust in their source regions.

5.4.2. Modeling

Though small, Eu anomalies are present in many of the primitive MORB samples analyzed here. Here we show how both equilibrium and kinetic effects that occur during partial melting of spinel peridotite can fractionate Eu from Sm and Gd leading to variation in Eu/Eu* of MORB. Europium (II), like Sr (II), is slightly more incompatible than Sm and Gd (see Table 5.1), which will lead to a slight enrichment of Eu relative to Sm and Gd during partial melting. In addition, Eu (II) diffuses faster than Sm and Gd, which may enhance the

fractionation (Cherniak and Liang, 2007). The dynamic melting model considered below is developed from Qin (1992). A list of parameters and their definitions can be found in Table 5.2. We ignored the density difference between the melt and solid phases, as this will not affect the calculated mass ratios such as Eu/Eu*.

Assumptions:

- (1) Eu (II) has the same partition and diffusion coefficients as Sr;
- (2) The MORB source has the mineral assemblage: 51.3% olivine (ol) + 34.1% orthopyroxene (opx) + 13.1% clinopyroxene (cpx) + 1.5% spinel (spl) (Niu, 1997);
- (3) The following melting reaction occurs: $0.466 \text{ cpx} + 0.652 \text{ opx} = 0.167 \text{ ol} + 1 \text{ melt}$ (Niu, 1997);
- (4) The melting temperature is 1300 °C;
- (5) The normalized melting rate is 10^{-6} - 10^{-8} yr^{-1} (mass fraction per year);
- (6) Eu (II) fraction is 10-30%;
- (7) For the diffusion calculations, all cpx and opx crystals are assumed to be spherical and have an initial radius of 3 mm;
- (8) The porosity of the mantle remains at 1% during partial melting;
- (9) The melts are rapidly extracted once the melt fraction exceeds the porosity, and are chemically separated from the residue.

We discuss the rationale for these assumptions next.

Table 5.1. Partition coefficients and diffusion coefficients used in the model

	Partition coefficients		Diffusion coefficients (cm ² /s)	
	cpx ¹	opx ²	cpx ³	opx ⁴
Sm	0.35	0.023	$3.1 * 10^{-16}$	$1.2 * 10^{-16}$
Eu (II) ⁵	0.26	0.0036	$6.4 * 10^{-14}$	$2.6 * 10^{-14}$
Eu (III)	0.38	0.0286	$3.9 * 10^{-16}$	$1.6 * 10^{-16}$
Gd	0.41	0.036	$4.6 * 10^{-16}$	$2.2 * 10^{-16}$

1. Niu et al. (1996);

2. Taken or interpolated from Frei et al. (2009);
3. Taken or interpolated from Van Orman et al. (2001) and Sneeringer et al. (1984) and corrected for pressure effect;
4. Taken Cherniak and Liang (2007) and corrected for pressure effect using the D-P relationship from Van Orman et al. (2001).
5. Partition coefficients and diffusion coefficients of Eu(II) are assumed to be the same as Sr due to the similarity between the two elements.

Table 5.2. Notation used in modelling

Variable	Description	Unit
α	ratio of melt extraction rate to melting rate	
C_j^i	concentration of element i in mineral j	ppm
C_a^i	concentration of element i in aggregated melt	ppm
C_r^i	concentration of element i in residual melt	ppm
D_j^i	diffusion coefficient of element i in mineral j	cm ² /s
f_j	initial proportion of mineral j	
F	melting degree	
K_j^i	partition coefficient of element i between melt and j	
R_j	radius of mineral j	cm
r_j	distance to the crystal center of mineral j	cm
t	time	s
V_j	volume of mineral j	cm ³
V_a	volume of aggregated melt	cm ³
V_r	volume of residual melt	cm ³
ω	relative/normalized melting rate	yr ⁻¹
ω_e	melt extraction rate	cm ³ /s
ω_m	melting rate	cm ³ /s

X_j	reaction coefficient of mineral j during melting
ϕ	porosity at the source

Diffusivity of pure Eu (II) has not yet been reported. However, under reducing conditions, Eu diffuses over an order of magnitude faster than under oxidizing conditions (Cherniak and Liang, 2007). Here we used the diffusivity of Sr (Sneeringer et al., 1984), which is up to three orders of magnitude faster than those of most REEs, to approximate that of Eu (II) (Table 5.1). The results of the model presented below change only a few percent when using a lower estimate of Eu (II) diffusivity (1.5 orders of magnitude faster than Sm and Gd).

The average relative melting rate, estimated using spreading rate, is on the order of 10^{-7} to 10^{-8} yr^{-1} . The instantaneous melting rate may have greater variability. Faster melting promotes greater Sm-Eu-Gd fractionation as long as the melt remains in equilibrium with the residue for Eu (II) (i.e., melting rate $< \sim 10^{-4}$ yr^{-1}). In Iceland, the estimated melting rate ranges from 10^{-6} to 10^{-8} yr^{-1} , possibly influenced by pressure release caused by deglaciation (Jull and McKenzie, 1996). The samples with the largest positive Eu anomalies in our dataset ($\text{Eu}/\text{Eu}^* = 1.07\text{--}1.13$), and one of the reference materials, BIR-1G, which also has a high Eu/Eu^* (~ 1.12), are from Iceland or nearby ridge segments.

The fraction of Eu (II) depends on oxygen fugacity and the standard redox potential (Schreiber, 1986), the latter of which is dependent upon the composition of the system. Traditionally, $\text{Eu (II)}/\text{Eu}_{\text{total}}$ in MORB is approximated using plagioclase-melt Sr-Eu partition coefficients. Since partition coefficients are sensitive to composition, temperature and pressure, the calculated Eu (II) fraction shows significant variation in the literature. The early work by Sun et al. (1974) indicated 8-13% Eu (II) in mid-ocean ridge basalts. Aigner-Torres et al. (2007) determined 5-15% Eu (II) in a Pacific MORB sample under the quartz-

magnetite-fayalite (QFM) buffer. More recently, Laubier et al.'s (2014) partition coefficient data showed that, in MORB, Eu (II) decreases from ~20% at QFM to ~12% at the nickel-nickel oxide (NNO) buffer. The oxygen fugacity at the top of the upper mantle falls within ± 2 log units of the QFM buffer, and is heterogeneous on a small scale (Frost and McCammon, 2008). By measuring $Fe^{3+}/\Sigma Fe$ ratios in MORB glasses, Bézou and Humler (2005) and Cottrell and Kelley (2013) estimated that MORB oxygen fugacity is buffered at \sim QFM. Based on Fe_2O_3 systematics during partial melting, Bézou and Humler (2005) further proposed a fO_2 of QFM-1 for the MORB source region. Recently, the oxidation state of Eu in silicate melts was directly measured by X-ray absorption near edge structure (XANES) (Burnham et al. (2015). According to their empirical equation for $Eu(III)/Eu_{total}$ as a function of oxygen fugacity, melt composition and temperature, the Eu (II) fraction is 20–30% in MORB melts. Given the above observations, we explored the Sm-Eu-Gd fractionation during partial melting by assuming 10-30% Eu (II) in the MORB source mantle. Less Eu (II) translates into a smaller Eu anomaly.

In our model below, we considered only diffusion in clinopyroxene (cpx) and orthopyroxene (opx), which control the REE budgets in spinel peridotites.

Assuming all crystals are spherical, the redistribution of the element concentration (C) within the crystals is controlled by volume diffusion:

$$\frac{\partial C_j^i}{\partial t} = D_j^i \left(\frac{\partial^2 C_j^i}{\partial r_j^2} + \frac{2}{r_j} \frac{\partial C_j^i}{\partial r_j} \right), \quad 0 \leq r_j \leq R_j(t); j = cpx, opx; i = Eu(II), Eu(III), Sm, Gd \quad (1)$$

Three initial conditions are assumed:

(1) All minerals are initially homogeneous

$$\frac{\partial C_j^i}{\partial r_j} \Big|_{t=0} = 0, \quad 0 \leq r_j \leq R_j \Big|_{t=0} \quad (2)$$

(2) Clinopyroxene and orthopyroxene are in equilibrium before melting

$$\frac{C_{cpx}^i|_{t=0}}{K_{cpx}^i} = \frac{C_{opx}^i|_{t=0}}{K_{opx}^i} \quad (3)$$

Two boundary conditions are:

(1) There is no chemical gradient in the center of the crystals

$$\frac{\partial C_j^i}{\partial r_j} \Big|_{r_j=0} = 0 \quad (4)$$

(2) The crystal rims maintain equilibrium with the melt

$$C_j^i|_{r_j=R_j} = K_j^i C_r^i \quad (5)$$

Following Qin (1992), the concentrations (ppm) of an element i in the residual (C_r^i) and aggregated (C_a^i) melt are given by the two equations below, respectively:

$$\frac{d(V_r C_r^i)}{dt} = - \frac{d}{dt} \left\{ \sum_j f_j \int_0^{R_j} 4\pi r_j^2 C_j^i dr_j \right\} - \omega_e C_r^i \quad (6)$$

$$C_a^i = \frac{1}{V_a} \left\{ - \left[\sum_j (f_j \int_0^{R_j} 4\pi r_j^2 C_j^i dr_j) - \sum_j (f_j \int_0^{R_j|_{t=0}} 4\pi r_j^2 C_j^i dr_j) \right] - V_r C_r^i \right\} \quad (7)$$

The radius of mineral j is given by:

$$R_j = R_j|_{t=0} \sqrt[3]{1 - \frac{X_j}{f_j} \omega t} \quad (8)$$

X_j used in the third assumption and here is the reaction coefficient of mineral j during melting.

$$\frac{dV_r}{dt} = \omega_m - \omega_e = \omega_m (1 - \alpha) \quad (9)$$

$$\frac{dV_a}{dt} = \alpha \omega_m \quad (10)$$

$$\alpha = 0, \text{ when } F \leq \phi; \quad (11a)$$

$$\alpha = \frac{1}{(1-\phi)}, \quad \text{when } F > \phi \quad (11b)$$

$$F = \omega t \quad (12)$$

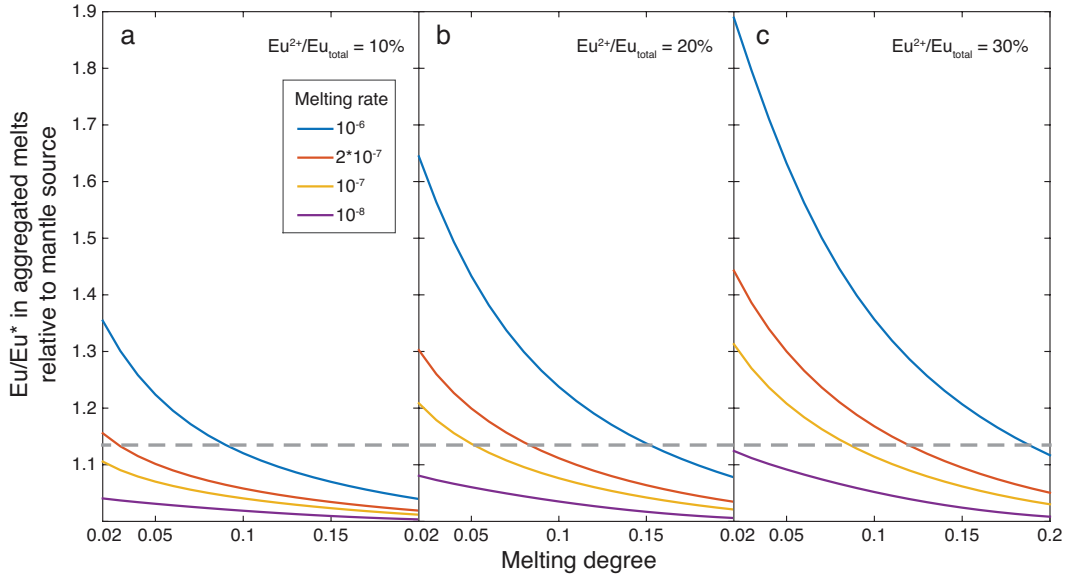


Fig. 5.5. Eu/Eu* in aggregated melts as a function of Eu (II) fraction, melting rate (yr^{-1}) and melting degree. The colors of the curves indicate melting rates. The gray dashed line indicates the most positive Eu anomaly in the data reported here for primitive MORB.

As shown in Fig. 5.5, Eu can be enriched over Sm and Gd in aggregated melts from spinel peridotite. The extent of Sm-Eu-Gd fractionation rapidly decreases with increasing degree of melting, and greater fractionation is produced under faster melting rates. The mean Eu/Eu* in primitive MORB (1.025 ± 0.025) can be produced if the MORB source mantle has an average Eu (II) proportion of 10-20% at 10% average melting degree and 10^{-8} to 10^{-7} yr^{-1} average melting rate. Negative Eu anomalies can be generated in later (instantaneous) melts

derived from residual peridotite that has experienced large degrees of melting (Fig. 5.6). The Sm-Eu-Gd systematics in primitive MORB may be further complicated by the interaction between the melts and lower crustal cumulates during melt transport (Wanless and Shaw, 2012), as discussed above. Although magmatic processes can fractionate Eu from Sm and Gd, mixing of melts generated at various depths and melting degrees tends to reduce the kinetic effects seen in the aggregated melts. Collectively, these processes may explain the small positive Eu/Eu* in the average primitive MORB.

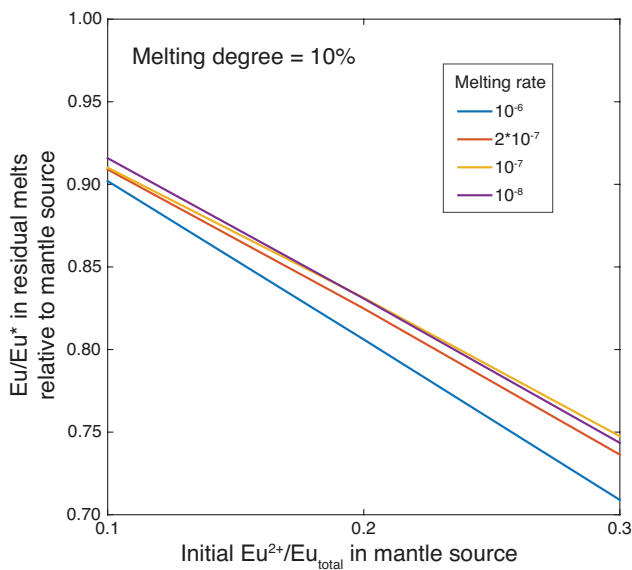


Fig. 5.6. Eu/Eu* in the instantaneous (residual) melts derived from a depleted source after 10% degree melting.

In contrast to the >10% positive Eu anomaly proposed by Niu et al. (2009), our data suggest that primitive MORBs, on average, possess only a ~2% positive Eu anomaly (1.025 ± 0.025 , $n = 46$). Considering the preferential Eu extraction during partial melting (Fig. 5.5), the upper mantle should have a Eu/Eu* less than 1.025 ± 0.025 . Within these uncertainty bounds, it is possible that the MORB source mantle have zero or even a slight negative Eu

anomaly. Therefore, the MORB source mantle may not completely counterbalance the Eu deficit in the continental crust.

Where is the missing Eu in the bulk silicate earth? Although the Earth might start from a non-chondritic composition (Campbell and O'Neill, 2012 and references therein), significant Eu anomalies have not been proposed in the non-chondritic Earth composition models. Alternatively, a reservoir may exist in the mantle that is not sampled by MORB. The negative Eu anomaly in the continental crust may result from lower crustal recycling (Tang et al., 2015). The recycled lower continental crust carries a positive Eu anomaly and sinks into the mantle and may either enter the deep mantle or exist as blobs that are not well mixed within the convecting upper mantle as sampled by MORB. Ocean island basalts (OIB), which tap the lower mantle, have positive Eu anomalies on average (mean $\text{Eu}/\text{Eu}^* = 1.034 \pm 0.003$, 2 se, $n = 1525$, OIBs with $\text{MgO} > 10\%$) and a negative correlation between Eu/Eu^* and Pb isotopes for locality averages (Tang et al., 2015). These findings suggest that the recycled lower continental crust is at least partially stored in the OIB source mantle (Tang et al., 2015; Willbold and Stracke, 2010).

5.5. Conclusions

There is no correlation between Eu/Eu^* and MgO in relatively primitive MORB ($\text{MgO} > 8.5\%$) from the Pacific, Indian and Atlantic oceans. These MORB glasses show both positive and negative Eu anomalies. MORB glasses with $\text{MgO} > 9\%$ have a small (2%) positive Eu anomaly that is within uncertainty of zero (i.e., $\text{Eu}/\text{Eu}^* = 1.025 \pm 0.025$ $2 \sigma_m$).

The Eu/Eu^* variations observed in primitive MORB may be due to the combined effect of different partition coefficients and diffusivities of Sm-Eu-Gd during partial melting +/- melt transport. Based on these results, the upper mantle sampled by MORB may not possess a

significant positive Eu anomaly that completely balances the Eu deficit observed in the continental crust.

References

- Arevalo, R. and McDonough, W.F. (2010) Chemical variations and regional diversity observed in MORB. *Chemical Geology* 271, 70-85.
- Bender, J., Langmuir, C. and Hanson, G. (1984) Petrogenesis of basalt glasses from the Tamayo region, East Pacific Rise. *Journal of Petrology* 25, 213-254.
- Bézos, A. and Humler, E. (2005) The Fe³⁺/ΣFe ratios of MORB glasses and their implications for mantle melting. *Geochimica et Cosmochimica Acta* 69, 711-725.
- Burnham, A.D., Berry, A.J., Halse, H.R., Schofield, P.F., Cibin, G. and Mosselmans, J.F.W. (2015) The oxidation state of europium in silicate melts as a function of oxygen fugacity, composition and temperature. *Chemical Geology* 411, 248-259.
- Campbell, I.H. and O'Neill, H.S.C. (2012) Evidence against a chondritic Earth. *Nature* 483, 553-558.
- Cherniak, D.J. and Liang, Y. (2007) Rare earth element diffusion in natural enstatite. *Geochimica et Cosmochimica Acta* 71, 1324-1340.
- Cottrell, E. and Kelley, K.A. (2013) Redox heterogeneity in mid-ocean ridge basalts as a function of mantle source. *Science* 340, 1314-1317.
- Frei, D., Liebscher, A., Franz, G., Wunder, B., Klemme, S. and Blundy, J. (2009) Trace element partitioning between orthopyroxene and anhydrous silicate melt on the lherzolite solidus from 1.1 to 3.2 GPa and 1,230 to 1,535°C in the model system Na₂O–CaO–MgO–Al₂O₃–SiO₂. *Contrib Mineral Petrol* 157, 473-490.
- Frost, D.J. and McCammon, C.A. (2008) The redox state of Earth's mantle. *Annual Review of Earth and Planetary Sciences* 36, 389-420.

- Gale, A., Dalton, C.A., Langmuir, C.H., Su, Y. and Schilling, J.-G. (2013) The mean composition of ocean ridge basalts. *Geochemistry, Geophysics, Geosystems* 14, 489-518.
- Jenner, F.E. and O'Neill, H.S.C. (2012a) Analysis of 60 elements in 616 ocean floor basaltic glasses. *Geochemistry, Geophysics, Geosystems* 13.
- Jenner, F.E. and O'Neill, H.S.C. (2012b) Major and trace analysis of basaltic glasses by laser-ablation ICP-MS. *Geochemistry, Geophysics, Geosystems* 13, Q03003.
- Jull, M. and McKenzie, D. (1996) The effect of deglaciation on mantle melting beneath Iceland. *Journal of Geophysical Research: Solid Earth* 101, 21815-21828.
- Lambart, S., Laporte, D. and Schiano, P. (2013) Markers of the pyroxenite contribution in the major-element compositions of oceanic basalts: Review of the experimental constraints. *Lithos* 160–161, 14-36.
- Laubier, M., Grove, T.L. and Langmuir, C.H. (2014) Trace element mineral/melt partitioning for basaltic and basaltic andesitic melts: An experimental and laser ICP-MS study with application to the oxidation state of mantle source regions. *Earth and Planetary Science Letters* 392, 265-278.
- Liu, Y., Hu, Z., Gao, S., Günther, D., Xu, J., Gao, C. and Chen, H. (2008) In situ analysis of major and trace elements of anhydrous minerals by LA-ICP-MS without applying an internal standard. *Chemical Geology* 257, 34-43.
- Niu, Y. (1997) Mantle Melting and Melt Extraction Processes beneath Ocean Ridges: Evidence from Abyssal Peridotites. *Journal of Petrology* 38, 1047-1074.
- Niu, Y., Gilmore, T., Mackie, S., Greig, A. and Bach, W. (2002) Mineral chemistry, whole-rock compositions, and petrogenesis of Leg 176 gabbros: data and discussion, *Proceedings of the Ocean Drilling Program, Scientific Results*, pp. 1-60.

- Niu, Y. and O'Hara, M.J. (2009) MORB mantle hosts the missing Eu (Sr, Nb, Ta and Ti) in the continental crust: New perspectives on crustal growth, crust–mantle differentiation and chemical structure of oceanic upper mantle. *Lithos* 112, 1-17.
- Niu, Y., Waggoner, D.G., Sinton, J.M. and Mahoney, J.J. (1996) Mantle source heterogeneity and melting processes beneath seafloor spreading centers: The East Pacific Rise, 18°–19°S. *Journal of Geophysical Research: Solid Earth* 101, 27711-27733.
- Qin, Z. (1992) Disequilibrium partial melting model and its implications for trace element fractionations during mantle melting. *Earth and planetary science letters* 112, 75-90.
- Rudnick, R.L. and Gao, S. (2014) 4.1 - Composition of the Continental Crust, in: Holland, H.D., Turekian, K.K. (Eds.), *Treatise on Geochemistry (Second Edition)*. Elsevier, Oxford, pp. 1-51.
- Schreiber, H.D. (1986) Redox processes in glass-forming melts. *Journal of Non-Crystalline Solids* 84, 129-141.
- Shannon, R.t. (1976) Revised effective ionic radii and systematic studies of interatomic distances in halides and chalcogenides. *Acta Crystallographica Section A: Crystal Physics, Diffraction, Theoretical and General Crystallography* 32, 751-767.
- Sneeringer, M., Hart, S.R. and Shimizu, N. (1984) Strontium and samarium diffusion in diopside. *Geochimica et Cosmochimica Acta* 48, 1589-1608.
- Sobolev, A.V., Hofmann, A.W., Kuzmin, D.V., Yaxley, G.M., Arndt, N.T., Chung, S.-L., Danyushevsky, L.V., Elliott, T., Frey, F.A., Garcia, M.O., Gurenko, A.A., Kamenetsky, V.S., Kerr, A.C., Krivolutsкая, N.A., Matvienkov, V.V., Nikogosian, I.K., Rocholl, A., Sigurdsson, I.A., Sushchevskaya, N.M. and Teklay, M. (2007) The Amount of Recycled Crust in Sources of Mantle-Derived Melts. *Science* 316, 412-417.
- Sobolev, A.V., Hofmann, A.W., Sobolev, S.V. and Nikogosian, I.K. (2005) An olivine-free mantle source of Hawaiian shield basalts. *Nature* 434, 590-597.

- Sun, C.-o., Richard J, W. and Sun, S.-s. (1974) Distribution coefficients of Eu and Sr for plagioclase-liquid and clinopyroxene-liquid equilibria in oceanic ridge basalt: an experimental study. *Geochimica et Cosmochimica Acta* 38, 1415-1433.
- Tang, M., McDonough, W.F. and Arevalo, R.J. (2014) High-precision measurement of Eu/Eu* in geological glasses via LA-ICP-MS analysis. *Journal of Analytical Atomic Spectrometry* 29, 1835-1843.
- Tang, M., Rudnick, R.L., McDonough, W.F., Gaschnig, R.M. and Huang, Y. (2015) Europium anomalies constrain the mass of recycled lower continental crust. *Geology* 43, 703-706.
- Van Orman, J., Grove, T. and Shimizu, N. (2001) Rare earth element diffusion in diopside: influence of temperature, pressure, and ionic radius, and an elastic model for diffusion in silicates. *Contrib Mineral Petrol* 141, 687-703.
- Wanless, V.D. and Shaw, A.M. (2012) Lower crustal crystallization and melt evolution at mid-ocean ridges. *Nature Geosci* 5, 651-655.
- Willbold, M. and Stracke, A. (2010) Formation of enriched mantle components by recycling of upper and lower continental crust. *Chemical Geology* 276, 188-197.

Appendix

Table A5.1. Measured Eu/Eu* and MgO contents in high MgO MORBs

Pacific						
Sample ID	Latitude	Longitude	MgO	2 SD	Eu/Eu*	2 SD
7393	-35.37	-105.58	9.52	0.30	0.97	0.03
5215	1.23	-83.73	8.57	0.28	0.96	0.03
5216	1.23	-83.73	9.39	0.30	1.03	0.03
7394	-35.37	-105.58	9.55	0.30	0.99	0.03

4955	2.43	-95.55	9.75	0.46	0.98	0.03
4953	2.43	-95.55	9.09	0.28	1.01	0.03
4954	2.43	-95.55	9.74	0.32	1.00	0.03
8195	50.23	-130.25	9.02	0.28	1.00	0.03
720	-56.56	160.07	8.56	0.28	1.00	0.03
8196	50.23	-130.25	9.20	0.30	1.05	0.04
8194	50.23	-130.25	8.87	0.28	1.05	0.03
8420	9.87	-104.62	9.36	0.30	1.05	0.03
719	-56.56	160.07	8.44	0.26	0.97	0.03
5213	8.38	-103.68	9.52	0.30	1.02	0.03
5212	8.38	-103.68	9.85	0.32	1.05	0.03
4956	2.43	-95.55	10.02	0.32	0.98	0.03
718	-56.56	160.07	8.50	0.28	0.96	0.03
725	-56.56	160.07	8.58	0.28	1.02	0.03
7397	-35.37	-105.58	9.38	0.30	0.98	0.03
5211	8.38	-103.68	9.66	0.34	1.01	0.03
8193	50.23	-130.25	8.98	0.40	1.05	0.03
7396	-35.37	-105.58	9.40	0.30	0.95	0.03
8421	9.87	-104.62	9.32	0.30	1.02	0.03
11408	12.72	-102.58	9.75	0.38	1.04	0.03
11407	12.72	-102.58	9.75	0.34	1.09	0.04
8422	9.87	-104.62	9.59	0.30	1.03	0.03
11409	12.72	-102.58	9.58	0.30	1.03	0.03
8423	9.87	-104.62	9.44	0.30	1.03	0.04

Indian

Sample ID	Latitude	Longitude	MgO	2 SD	Eu/Eu*	2 SD
11893	-46.38	33.51	9.05	0.50	0.99	0.04
6859	-27.60	65.84	8.69	0.28	1.06	0.03
11891	-46.38	33.51	9.05	0.28	0.98	0.03
11940	-43.38	39.85	9.26	0.30	1.09	0.03
6683	-49.86	118.00	8.68	0.28	1.05	0.03
6680	-49.86	118.00	8.68	0.28	1.03	0.03
6681	-49.86	118.00	8.65	0.28	1.04	0.03
12339	-53.21	23.36	8.95	0.28	1.04	0.03
671	11.89	48.25	8.66	0.38	0.99	0.04
12368	-52.99	11.16	8.83	0.28	1.02	0.03
12337	-52.99	11.16	9.02	0.28	1.02	0.03
12546	-52.30	13.06	8.83	0.27	1.08	0.03
670	11.89	48.25	8.58	0.28	0.99	0.03

6858	-27.60	65.84	8.81	0.28	1.00	0.03
6856	-27.60	65.84	8.84	0.28	0.96	0.03
6684	-27.60	65.84	8.76	0.28	1.01	0.03
649	-19.19	99.30	9.40	0.30	0.95	0.03
673	11.89	48.25	8.57	0.28	0.93	0.03
12334	-53.21	23.36	8.70	0.28	1.08	0.03
6855	-32.85	56.95	8.69	0.28	1.03	0.03
12336	-53.21	23.36	8.68	0.28	1.07	0.04
12547	-52.30	13.06	9.17	0.30	1.09	0.03

Atlantic

Sample ID	Latitude	Longitude	MgO	2 SD	Eu/Eu*	2 SD
7300	-33.72	-14.25	10.55	0.34	1.03	0.03
7298	-33.72	-14.25	10.47	0.34	1.04	0.03
7299	-33.72	-14.25	10.37	0.34	1.02	0.03
7301	-33.72	-14.25	10.33	0.32	1.01	0.03
3380	36.82	-33.27	9.68	0.30	0.96	0.04
3376	36.82	-33.27	9.70	0.30	0.96	0.04
3377	36.82	-33.27	9.63	0.30	0.96	0.03
9968	66.51	-17.34	9.40	0.30	1.12	0.03
845	36.88	-33.64	9.38	0.30	1.06	0.03
9969	66.51	-17.34	9.33	0.30	1.07	0.04
9967	66.51	-17.34	9.28	0.30	1.13	0.04
9970	66.51	-17.34	9.22	0.30	1.11	0.03
844	36.88	-33.64	9.16	0.30	1.04	0.03
5779	-56.89	-6.04	9.15	0.30	1.05	0.03
5778	-56.89	-6.04	9.03	0.28	1.04	0.03
5776	-56.89	-6.04	9.01	0.28	1.06	0.03
843	36.88	-33.64	9.00	0.28	0.99	0.04
846	36.88	-33.64	8.92	0.28	1.08	0.03
9024	-26.13	-13.86	8.82	0.28	1.02	0.04
5777	-56.89	-6.04	8.77	0.28	1.02	0.03
9025	-26.13	-13.86	8.70	0.28	0.96	0.03
9022	-26.13	-13.86	8.59	0.34	0.92	0.03

Chapter 6: Archean upper crust transition from mafic to felsic marks the onset of plate tectonics

[1] Tang, M., Chen, K., Rudnick, R.L. (2016). Archean upper crust transition from mafic to felsic marks the onset of plate tectonics. *Science*, 351(6271), 372-375.

[2] M.T. designed the project, compiled the data and wrote the manuscript; K.C. assisted in data compilation, data interpretation and writing; R.L.R. improved the project design and commented on the manuscript.

Abstract

The Archean Eon witnessed the production of early continental crust, the emergence of life and fundamental changes to the atmosphere. The nature of the first continental crust, the interface between the surface and deep Earth, has been obscured by weathering, erosion, and tectonism following its formation. Here we use Ni/Co and Cr/Zn ratios in Archean terrigenous sedimentary rocks and Archean igneous/metavolcanic rocks to track the bulk MgO composition of the Archean upper continental crust. This crust evolved from a highly mafic bulk composition before 3.0 Ga to a felsic bulk composition by 2.5 Ga. This compositional change was attended by a five-fold mass increase of the upper continental crust due to addition of granitic rocks, suggesting the onset of global plate tectonics at ~3.0 Ga.

Main text

Magnesium content (and its ratio to other elements) is commonly used as an index of igneous differentiation and melting conditions, which are responsible for much of the compositional variation seen in silicate rocks. Thus, MgO content serves as a first-order measure of silicate rock differentiation. Estimating the average MgO content in the upper continental crust, and from that the bulk composition of this crust is, however, challenging.

There are two basic approaches to determine the composition of the upper continental crust (Condie, 1993; Rudnick and Gao, 2014; Taylor and McLennan, 1985): (1) weighted averages of surface rocks, and (2) average compositions of terrigenous sediments such as shales (Condie, 1993; Taylor and McLennan, 1985) and glacial diamictites (Gaschnig et al., 2014) that naturally sample large areas of the upper continental crust. The surface rock method is compromised by sampling bias, which becomes increasingly critical with age since erosion removes the upper continental crust with time, and ultramafic and mafic (magnesium- and iron-rich) rocks may be eroded faster than felsic (silica- and aluminum- rich) rocks (Condie, 1993). The terrigenous sediment method cannot provide robust average concentrations of soluble elements such as Mg, which are preferentially dissolved and transported to the oceans during chemical weathering (Holland, 1984).

Here, we compiled geochemical data for Archean shales (including pelites and graywackes), glacial diamictites (Gaschnig et al., 2014), and igneous rocks from 18 Archean cratons (Tang et al., 2015a), to demonstrate that Ni/Co and Cr/Zn ratios provide relatively tight constraints on the MgO content in the Archean upper continental crust. We use the term “continental crust” here, although the nature of the crust that was emergent (i.e., exposed to weathering, hence generation of terrigenous sedimentary deposits) in the Archean may have been very different from the felsic crust that we know today (Dhuime et al., 2015).

First row transition metal ratios Ni/Co and Cr/Zn show positive correlations with MgO content in igneous and metagneous rocks from Archean cratons (Fig. 6.1) due to the differences in their partition coefficients between the crystallizing phases and melts. In particular, Ni and Cr are more compatible than Co and Zn in likely fractionating phases (olivine, spinel, pyroxenes, (Bougault and Hekinian, 1974; Horn et al., 1994; Leeman and

Scheidegger, 1977), making Ni/Co and Cr/Zn ratios sensitive to the earliest stages of igneous differentiation.

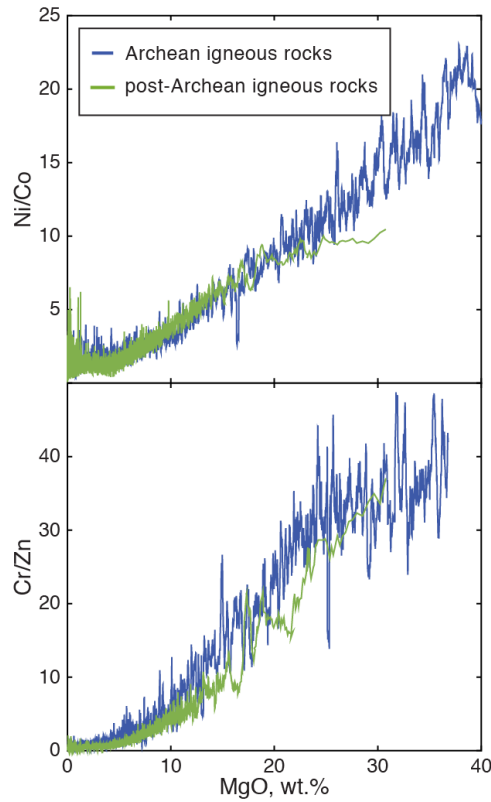


Fig. 6.1. Igneous Ni/Co-MgO and Cr/Zn-MgO differentiation trends for Archean and post-Archean rocks. We averaged every 20 samples to reduce scatter. Archean igneous trajectories are based on compiled igneous and metaigneous rocks from Archean cratons (Tang et al., 2015a); post-Archean trajectories are plotted using compiled data from (Keller et al., 2015)

Nickel, Co, Cr, and Zn are generally insoluble during chemical weathering (Taylor and McLennan, 1985), and their ratios should thus reflect the provenance of fine-grained terrigenous sedimentary rocks. The Ni/Co and Cr/Zn ratios show secular trends in sedimentary records (Fig. 6.2). Archean sedimentary rocks are characterized by high Ni/Co and Cr/Zn ratios while post-Archean sedimentary rocks have much lower and relatively constant Ni/Co and Cr/Zn ratios. The average Ni/Co and Cr/Zn ratios in the latter In

calculating the post-Archean average we excluded data for Paleoproterozoic (2.5–2.0 Ga) sedimentary rocks, which might oversample the Archean upper crust and thus show slightly higher Ni/Co and Cr/Zn ratios. are consistent with estimates of the present-day upper continental crust composition derived from average loess and from large-scale surface sampling (Fig. 6.2). Chromium can be oxidized to soluble Cr⁶⁺ in contact with present-day atmosphere (Frei et al., 2009). However, the low concentrations of Cr in present-day seawater i.e., $\sim 4.0 \times 10^{-9}$ mol/kg <http://www.mbari.org/chemsensor/pteo.htm>, which hosts large amounts of soluble elements from the continents ($\sim 4.7 \times 10^{-1}$ mol/kg Na, $\sim 5.3 \times 10^{-2}$ mol/kg Mg), does not support significant Cr loss from the upper crust due to oxidative weathering. In the anoxic Archean, Cr is expected to be even less mobile. Lithology-sensitive weathering rates may potentially bias the composition of terrigenous sediments, but currently we don't see evidence for this effect on Ni/Co and Cr/Zn ratios (Tang et al., 2015a). We thus conclude that there is limited fractionation between Ni and Co, or Cr and Zn due to the processes that occur during weathering, erosion, sedimentation and diagenesis.

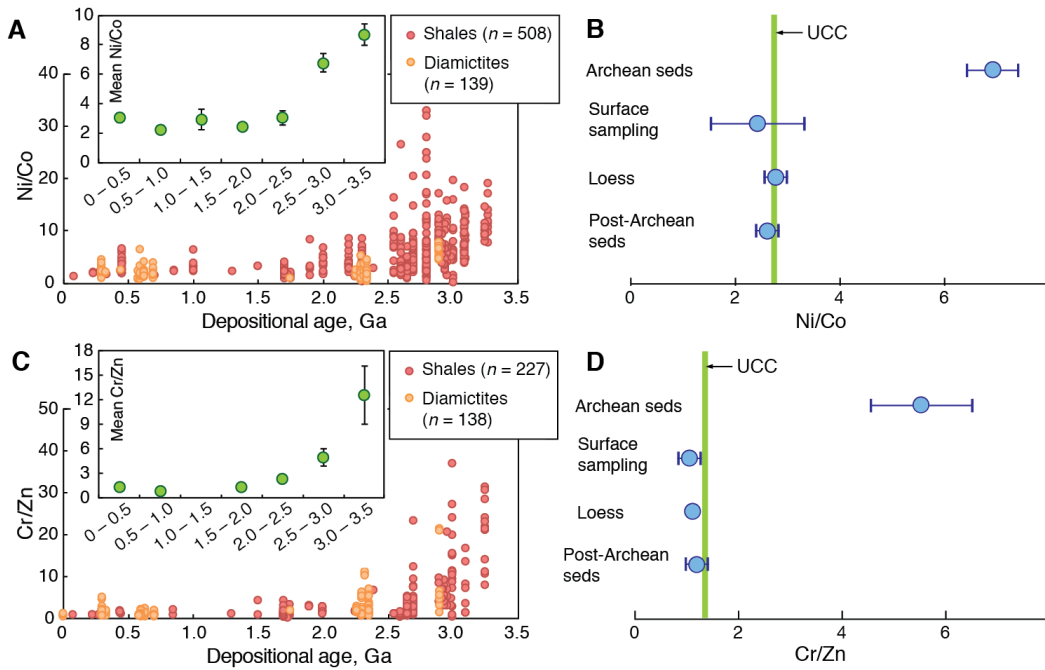


Fig. 6.2. Ni/Co and Cr/Zn ratios in terrigenous fine-grained sedimentary rocks through time (A & C) compared with the present-day upper continental crust (B & D). Insets in A and C show age binned Ni/Co and Cr/Zn ratios in terrigenous sediments (bin size = 0.5 Ga). Shale and diamictite data are provided in (Tang et al., 2015a); loess data are from (Tang et al., 2015b); large-scale surface sampling data are from (Rudnick and Gao, 2014 and references therein). The green bars in panels B and D denote the reference values for present-day upper continental crust (UCC) (Rudnick and Gao, 2014). Error bars are two standard errors (2 SE, hereafter).

The Ni/Co and Cr/Zn ratios in fine-grained terrigenous sedimentary rocks decrease with time within the Archean Eon, approaching the values of the present-day upper continental crust at the end of Archean (Fig. 6.3). The decreasing Ni/Co and Cr/Zn with time reflect progressively more felsic (lower MgO) upper continental crust from the Mesoarchean (3.5–3.0 Ga) to the Neoproterozoic (3.0–2.5 Ga). The Ni/Co- and Cr/Zn-age correlations established for samples from many continents suggest that these systematics reflect global crustal evolution rather than regional phenomena.

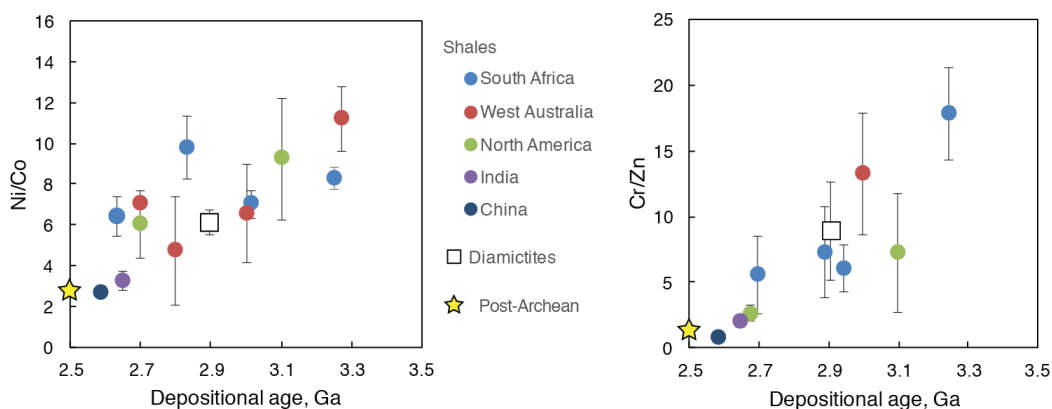


Fig. 6.3. Average Ni/Co and Cr/Zn ratios vs. depositional ages in Archean fine-grained terrigenous sedimentary rocks from different localities. Data for individual samples were grouped by their localities (reflected by different colors) within 0.2 Ga bins. Error bars are 2 SE.

We conducted a Monte Carlo mixing simulation to determine the average MgO content of the Archean upper crust (Tang et al., 2015a), which we assumed was comprised of rocks represented in the compiled Archean craton rock dataset ($n = 5,063$ for samples with complete SiO₂, MgO, Ni, Co, Cr and Zn data), in order to match the average Ni/Co and Cr/Zn ratios are recorded by the Archean sediments. The mixing scenarios that pass the Ni/Co and Cr/Zn filters yield the average MgO content for the Archean upper continental crust. Using this approach, we track the evolution of the MgO content in the Archean upper continental crust (Fig. 6.4) based on binned locality average Ni/Co and Cr/Zn (Fig. 6.3). We find that the MgO content in the upper continental crust decreases from > 11 wt.% in the Mesoarchean to ~ 4 wt.%, close to present-day level of 2–3 wt.% (Rudnick and Gao, 2003), at the end of Archean. The mafic upper continental crust in the early Archean was gradually replaced by a felsic upper continental crust in the Neoproterozoic and reached an average composition much like that of today around the Archean-Proterozoic boundary. The consistently low Ni/Co and

Cr/Zn ratios in post-Archean sediments (Fig. 6.2) suggest a nearly constant composition for the upper continental crust since 2.5 Ga.

Though it has a high MgO content, the Archean upper continental crust may contain up to 40% tonalite-trondhjemite-granodiorites (TTG) (Fig. 6.4). The budgets of incompatible elements in the sediments are controlled by the TTG components (yielding high La/Sm ratios), whereas transition metals (Ni, Co, Cr, Zn) are controlled by mafic components.

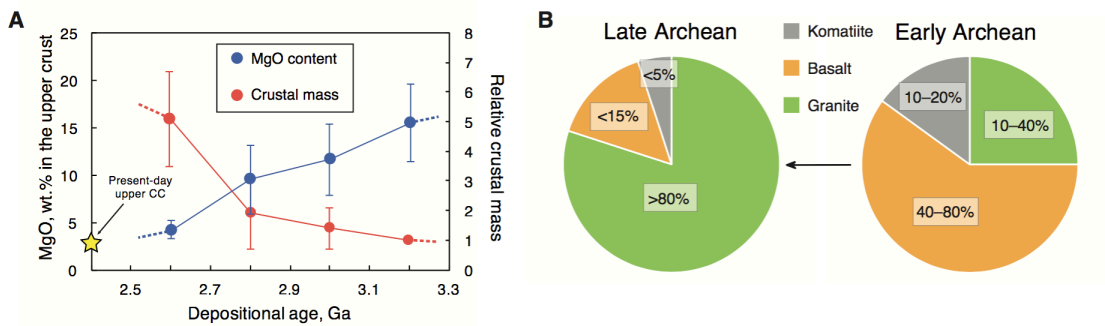


Fig. 6.4. Evolution of MgO content, relative mass (A) and the proportions of major rock types (B) of the upper continental crust in the Archean Eon. A: MgO content was calculated based on the locality average Ni/Co and Cr/Zn ratios within each 0.2 Ga time interval so that larger numbers of samples for particular localities do not have an undue influence on the outcome. Since depositional ages of sedimentary rocks represent the minimum formation ages of the crust being sampled, both the MgO and upper crustal growth curves could shift toward older ages. Upper crustal masses are relative to that of the Mesoproterozoic upper continental crust. Error bars are 2 SD. B: we assumed that TTG, basalts and komatiites have average MgO contents of 1.4 wt.% (Martin and Moyen, 2002), 11 wt.% (from compiled Archean craton samples with SiO₂ of 45–54%) and 30 wt.% (Herzberg et al., 2007), respectively.

Through most of the Archean, the upper continental crust has a mafic bulk composition (Fig. 6.4). This mafic composition, however, is not reflected in the mineralogy of Archean clastic sediments, which typically contain felsic minerals (e.g., detrital quartz, muscovite and feldspar) (McLennan et al., 1983). This disconnect between geochemical and mineralogical observations, as well as the low MgO contents in most Archean terrigenous sedimentary rocks (e.g., Feng and Kerrich, 1990), likely reflects preferential dissolution of mafic components (minerals and glasses) during chemical weathering (Tang et al., 2015a). Minerals such as olivine weather congruently, releasing Mg, which is then transported to the ocean where it may be sequestered into altered seafloor basalts through reverse weathering (Michalopoulos and Aller, 1995). Mafic to ultramafic volcanic glasses weather in a similar manner. In contrast to MgO, Ni, Co, Cr and Zn may be incorporated into clay minerals, or incorporated as metal-rich accessory phases after their release from the primary igneous phases.

We constructed a growth curve for the Archean upper continental crust based on MgO mass conservation. We assumed dilution of the upper continental crust MgO by addition of TTG with an average of 1.4 wt.% MgO (Martin and Moyen, 2002). To make an upper continental crust with MgO of 4 wt.% at the end of Archean requires addition of a TTG mass that is four times that of the mafic upper continental crust older than 3.0 Ga (Fig. 6.4). Addition of mafic igneous rocks to the upper continental crust would require even more felsic magma to balance the MgO content. Together, these observations suggest at least a five-fold mass increase of the upper crust in the Archean, with much of the felsic rocks delivered in the Neoproterozoic. This inferred massive crustal growth in the Neoproterozoic is in line with certain crustal growth models (Condie and Aster, 2010; Taylor and McLennan, 1985) and corresponds to the peaks at ~2.7 Ga seen in both zircon U-Pb age (Condie, 1998; Condie and Aster, 2010) and mantle xenolith Re depletion age (Pearson et al., 2007) spectra. Because our

calculations are based on insoluble elements, the results are insensitive to weathering processes.

Such dramatic changes in the composition and mass of upper continental crust suggest a profound and fundamental change in the processes that formed the Archean crust (Fig. 6.4). The rise of voluminous felsic magmatism that produced the TTG, and the processes that formed the Archean TTG might have driven the evolution of the Archean crust. TTG may be generated from both non-subduction (melting of mafic rocks in the lower crust) (Albarède, 1998; Bédard, 2006; Rudnick, 1995; Smithies, 2000) and subduction (melting of subducted plates) (Condie, 2013; Martin, 1994; Martin and Moyen, 2002) origins. Recycling and melting of lower crustal mafic granulites might have persisted throughout the Archean Eon due to the high mantle temperature at that time (Johnson et al., 2014). However, lower crust is generally depleted in water, which is important in the generation of granitic melts, including TTG (Arndt, 2013). It is thus doubtful that lower crustal melting would be efficient in producing large amounts of TTG that increased the mass of Archean upper continental crust by a factor of five. Assuming Earth experienced a period of stagnant lid or drip tectonics prior to the onset of plate tectonics (Gerya, 2014), the subaerial crust, which probably evolved from oceanic plateaus, had a total area of a fraction of present-day continental crust and a composition dominated by basalt mixed with komatiites and minor TTG generated by lower crustal melting. Approaching 3.0 Ga, the onset of plate tectonics would have provided a continuous supply of water to the mafic source (such as subducted oceanic crust) that resulted in the rise of voluminous TTG and other felsic magmas (29). Modern style continental crust started to emerge, attended by extensive subduction in the Neoproterozoic. Significantly earlier plate tectonics (>3.5 Ga) is unlikely, considering the rapid mafic-felsic transition within the last 0.5 Ga of the Archean Eon. This timing is consistent with the constraints from diamonds from subcontinental mantle (Shirey and Richardson, 2011),

secular changes in Hf and O isotopes in zircon (Dhuime et al., 2012), and Rb-Sr systematics in magmatic records (Dhuime et al., 2015).

References and notes

- Albarède, F. (1998) The growth of continental crust. *Tectonophysics* 296, 1-14.
- Arndt, N.T. (2013) Formation and Evolution of the Continental Crust. *Geochemical Perspectives* 2, 405- 533.
- Bédard, J.H. (2006) A catalytic delamination-driven model for coupled genesis of Archaean crust and sub-continental lithospheric mantle. *Geochimica et Cosmochimica Acta* 70, 1188-1214.
- Bougault, H. and Hekinian, R. (1974) Rift Valley in the Atlantic Ocean near 36° 50' N: petrology and geochemistry of basaltic rocks. *Earth and Planetary Science Letters* 24, 249-261.
- Condie, K.C. (1993) Chemical composition and evolution of the upper continental crust: contrasting results from surface samples and shales. *Chemical Geology* 104, 1-37.
- Condie, K.C. (1998) Episodic continental growth and supercontinents: a mantle avalanche connection? *Earth and Planetary Science Letters* 163, 97-108.
- Condie, K.C. (2013) *Plate Tectonics & Crustal Evolution*. Elsevier Science.
- Condie, K.C. and Aster, R.C. (2010) Episodic zircon age spectra of orogenic granitoids: The supercontinent connection and continental growth. *Precambrian Research* 180, 227-236.
- Dhuime, B., Hawkesworth, C.J., Cawood, P.A. and Storey, C.D. (2012) A change in the geodynamics of continental growth 3 billion years ago. *Science* 335, 1334-1336.
- Dhuime, B., Wuestefeld, A. and Hawkesworth, C.J. (2015) Emergence of modern continental crust about 3 billion years ago. *Nature Geosci* 8, 552-555.

- Feng, R. and Kerrich, R. (1990) Geochemistry of fine-grained clastic sediments in the Archean Abitibi greenstone belt, Canada: Implications for provenance and tectonic setting. *Geochimica et Cosmochimica Acta* 54, 1061-1081.
- Frei, R., Gaucher, C., Poulton, S.W. and Canfield, D.E. (2009) Fluctuations in Precambrian atmospheric oxygenation recorded by chromium isotopes. *Nature* 461, 250-253.
- Gaschnig, R.M., Rudnick, R.L., McDonough, W.F., Kaufman, A.J., Hu, Z. and Gao, S. (2014) Onset of oxidative weathering of continents recorded in the geochemistry of ancient glacial diamictites. *Earth and Planetary Science Letters* 408, 87-99.
- Gerya, T. (2014) Precambrian geodynamics: Concepts and models. *Gondwana Research* 25, 442-463.
- Herzberg, C., Asimow, P.D., Arndt, N., Niu, Y., Leshner, C.M., Fitton, J.G., Cheadle, M.J. and Saunders, A.D. (2007) Temperatures in ambient mantle and plumes: Constraints from basalts, picrites, and komatiites. *Geochemistry, Geophysics, Geosystems* 8, Q02006.
- Holland, H.D. (1984) *The Chemical Evolution of the Atmosphere and Oceans*. Princeton University Press, Princeton New Jersey.
- Horn, I., Foley, S.F., Jackson, S.E. and Jenner, G.A. (1994) Experimentally determined partitioning of high field strength- and selected transition elements between spinel and basaltic melt. *Chemical Geology* 117, 193-218.
- Johnson, T.E., Brown, M., Kaus, B.J.P. and VanTongeren, J.A. (2014) Delamination and recycling of Archaean crust caused by gravitational instabilities. *Nature Geosci.* 7, 47-52.
- Keller, C.B., Schoene, B., Barboni, M., Samperton, K.M. and Husson, J.M. (2015) Volcanic-plutonic parity and the differentiation of the continental crust. *Nature* 523, 301-307.
- Leeman, W. and Scheidegger, K. (1977) Olivine/liquid distribution coefficients and a test for crystal-liquid equilibrium. *Earth and Planetary Science Letters* 35, 247-257.

- Martin, H. (1994) The Archean grey gneisses and the genesis of continental crust. *Archean crustal evolution*, 205-259.
- Martin, H. and Moyon, J.-F. (2002) Secular changes in tonalite-trondhjemite-granodiorite composition as markers of the progressive cooling of Earth. *Geology* 30, 319-322.
- McLennan, S.M., Taylor, S.R. and Kröner, A. (1983) Geochemical evolution of Archean shales from South Africa. I. The Swaziland and Pongola Supergroups. *Precambrian Research* 22, 93-124.
- Michalopoulos, P. and Aller, R.C. (1995) Rapid Clay Mineral Formation in Amazon Delta Sediments: Reverse Weathering and Oceanic Elemental Cycles. *Science* 270, 614-617.
- Pearson, D.G., Parman, S.W. and Nowell, G.M. (2007) A link between large mantle melting events and continent growth seen in osmium isotopes. *Nature* 449, 202-205.
- Rudnick, R.L. (1995) Making continental crust. *Nature* 378, 571-578.
- Rudnick, R.L. and Gao, S. (2003) 3.01 - Composition of the Continental Crust, in: Rudnick, R.L. (Ed.), *The Crust, Treatise on Geochemistry Volume 3* Pergamon, Oxford, pp. 1-64.
- Rudnick, R.L. and Gao, S. (2014) 4.1 - Composition of the Continental Crust, in: Holland, H.D., Turekian, K.K. (Eds.), *Treatise on Geochemistry (Second Edition)*. Elsevier, Oxford, pp. 1-51.
- Shirey, S.B. and Richardson, S.H. (2011) Start of the Wilson cycle at 3 Ga shown by diamonds from subcontinental mantle. *Science* 333, 434-436.
- Smithies, R.H. (2000) The Archaean tonalite-trondhjemite-granodiorite (TTG) series is not an analogue of Cenozoic adakite. *Earth and Planetary Science Letters* 182, 115-125.
- Tang, M., Arevalo, R., Goreva, Y. and McDonough, W.F. (2015a) Elemental fractionation during condensation of plasma plumes generated by laser ablation: a ToF-SIMS study of condensate blankets. *Journal of Analytical Atomic Spectrometry* 30, 2316-2322.

Tang, M., Rudnick, R.L., McDonough, W.F., Gaschnig, R.M. and Huang, Y. (2015b)

Europium anomalies constrain the mass of recycled lower continental crust. *Geology* 43, 703-706.

Taylor, S.R. and McLennan, S.M. (1985) *The Continental Crust*. Wiley.

Appendix

Materials and Methods:

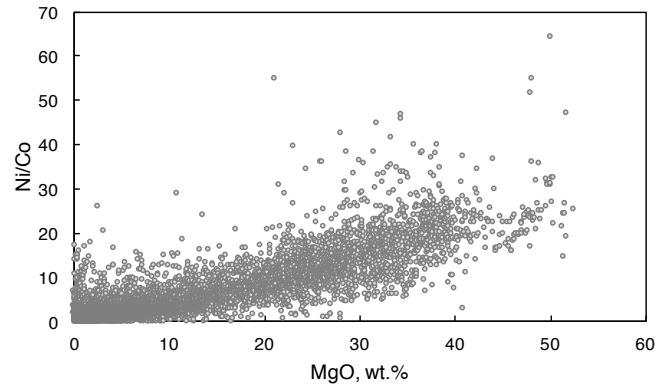


Fig. A7.1. Plot of Ni/Co vs. MgO content in Archean craton samples (n = 9,273).

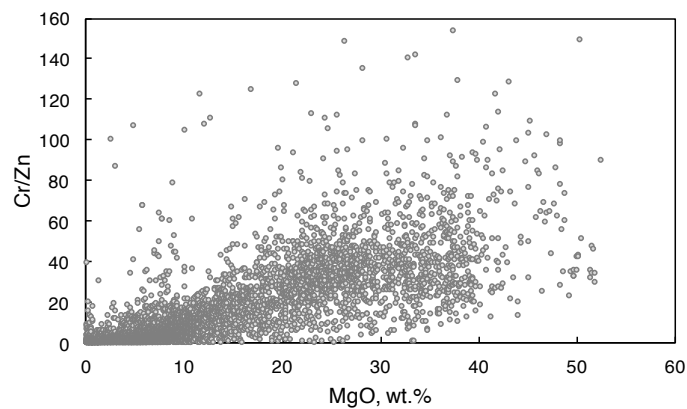


Fig. A6.2. Plot of Cr/Zn vs. MgO content in Archean craton samples (n = 6,970).

The Archean craton rock database ($n = 5,063$ for samples with complete SiO_2 , MgO, Ni, Co, Cr and Zn data) was subdivided into three subsets of rock types: felsic and intermediate ($\text{SiO}_2 > 54$ wt.%, $n = 1,647$), mafic (45 wt.% $< \text{SiO}_2 < 54$ wt.%, $n = 2,791$) and ultramafic ($\text{SiO}_2 < 45$ wt.%, $n = 715$). This step, together with the sampling strategy below, is done to remove sampling bias during the subsequent mixing simulation so that rocks of felsic, mafic and ultramafic compositions can be sampled with equal chance and not affected by the size of each database subset. Each simulated mixture contains 100 individual samples. To explore the composition range of mixtures under all possible felsic and intermediate–mafic–ultramafic mixing ratios, we randomly selected n samples from the felsic and intermediate subset ($n = 1, 2, 3 \dots 100$), and then m samples from the mafic subset ($m = 1, 2, 3 \dots 100 - n$), and then l samples from the ultramafic subset ($l = 1, 2, 3 \dots 100 - n - m$). Note that in each simulated mixture, the number of rock samples is always 100. We then calculated the average SiO_2 , MgO, Ni, Co, Cr and Zn compositions of each simulated mixture and plotted their Ni/Co, Cr/Zn vs. MgO (Fig. A6.3). This mixing simulation yields a total of 161,700 mixing scenarios (i.e., one for each point in Fig. A6.3). To determine the average MgO of the upper continental crust at a given time period, we take the average Ni/Co and Cr/Zn from the fine-grained terrigenous sedimentary rocks of that time period and filter the mixing simulation results to exclude any results that do not fall within the two standard errors of the average. Using these filtered data, we calculate the average MgO and two standard deviations. We repeated the above steps five to ten times to confirm reproducibility of the projected MgO content.

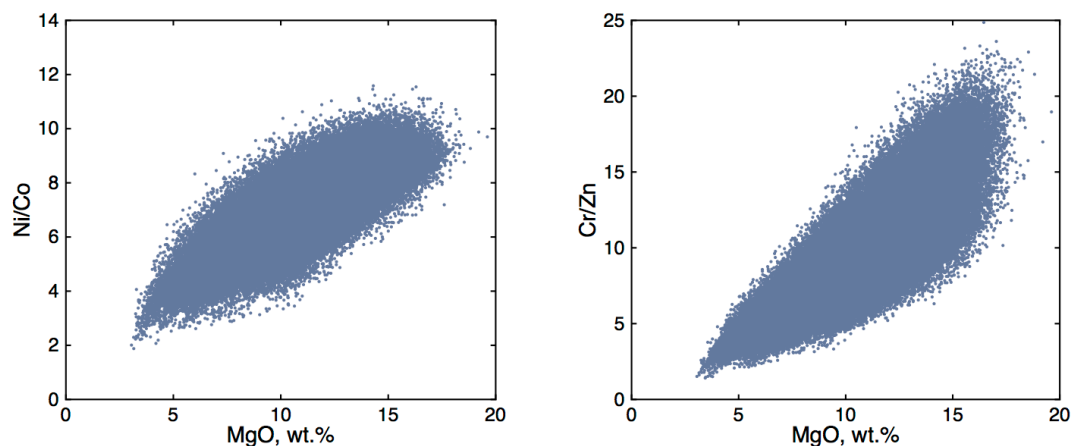


Fig. A6.3. Ni/Co- and Cr/Zn-MgO in simulated mixtures using Archean craton samples. Each dot represents a mixing scenario.

Lithology-sensitive weathering of upper crustal rocks

Basalts tend to weather faster than felsic rocks (Dessert et al., 2015 and references therein), although this difference in weathering rate is yet to be quantified. Basalts lose mass faster than more evolved rocks due to the congruent weathering of mafic minerals e.g., olivine during reaction with CO₂ compared with incongruent weathering of felsic minerals e.g., feldspar in granites. Does this differential weathering rate bias the Ni/Co and Cr/Zn ratios of terrigenous sediments? Right now we cannot quantify this potential bias in order to decide whether it is significant or not. But there are several observations that suggest it is not significant. First, Ni/Co and Cr/Zn ratios in post-Archean shales are consistent with those obtained from average loess and from large-scale surface sampling (McLennan, 2001; Rudnick and Gao, 2014). Therefore post-Archean shales show no significant bias towards mafic rocks relative to other estimates of upper crust composition. One may argue that post-Archean UCC may have much fewer mafic rocks (which is also our finding here). However,

mafic rocks have higher Ni, Co, etc. concentrations, so one should be able to see elevated Ni/Co and Cr/Zn ratios in post-Archean shales if the shale sampling bias is significant. Second, our diamictite data are consistent with the shale trends. However, the diamictites also show weathering signatures that they inherited from the crust that the glaciers traversed (Gaschnig et al., 2014). Third, terrigenous sediments may tend to sample younger crustal rocks (Peucker-Ehrenbrink et al., 2010). If the upper continental crust became progressively more felsic during the late Archean (our Ni/Co-, Cr/Zn-age trends), this bias translates into preferential sampling of felsic rocks, and tends to cancel any bias towards mafic rocks. These are clearly interesting topics for future investigations.

Present-day examples of the mineralogy-geochemistry disconnect in sediments?

As discussed in the text, transition metal geochemistry in Archean terrigenous sedimentary rocks suggest their derivation from mafic sources, yet Archean clastic sedimentary rocks are typically dominated by felsic minerals including quartz and feldspar, and have low MgO contents. We explain this disconnect as a result of preferential dissolution of mafic components during chemical weathering, which removes soluble elements e.g., Mg from the upper continental crust. We are not aware of any published studies of terrigenous sediments derived only from weathering of mafic sources. However, a recent paper published by Dessert et al. (Dessert et al., 2015) provides insights into this question. These authors studied the soils from the island of Guadeloupe in the Lesser Antilles island arc, which is dominated by basalts and andesites. The soils developed on these relatively mafic volcanic rocks contain quartz, feldspar, Fe-hydroxides and clay minerals, of which clay minerals account for 70% of the bulk. The quartz, feldspar and cristobalite are suggested to be derived from atmospheric deposition. As a highly weathered product, these soils contain little mafic minerals and have lost 85-90% of their Mg. Another relevant observation was made by van

de Kamp and Leake (van de Kamp and Leake, 1995), who reported petrographic and geochemical data for turbidites from the Northern Apennines, Italy. They found that sandstones from the Macigno (mid-Oligocene-lower Miocene) and Cervarola (lower Miocene) Formations are distinguished by the presence of serpentine, gabbro and diabase fragments, suggesting the presence of significant amounts of mafic-ultramafic components in their source. Both the sandstones and associated shales also have high Ni/Co ratios (up to 8). Nevertheless quartz and muscovite account for up to 50% of the shales, with the remainder consisting of clays (mainly illite and chlorite). Future work characterizing the weathering products of mafic rocks should provide more insights on the mineralogy of sediments derived from weathering of mafic and ultramafic rocks, as well as the mineralogical hosts of insoluble Ni, Co, Cr and Zn.

References

- Dessert, C., Lajeunesse, E., Lloret, E., Clergue, C., Crispi, O., Gorge, C. and Quidelleur, X. (2015) Controls on chemical weathering on a mountainous volcanic tropical island: Guadeloupe (French West Indies). *Geochim. Cosmochim. Acta* 171, 216-237.
- Gaschnig, R.M., Rudnick, R.L., McDonough, W.F., Kaufman, A.J., Hu, Z. and Gao, S. (2014) Onset of oxidative weathering of continents recorded in the geochemistry of ancient glacial diamictites. *Earth Planet. Sci. Lett.* 408, 87-99.
- McLennan, S.M. (2001) Relationships between the trace element composition of sedimentary rocks and upper continental crust. *Geochem. Geophys. Geosyst.* 2, 1021.
- Peucker-Ehrenbrink, B., Miller, M.W., Arsouze, T. and Jeandel, C. (2010) Continental bedrock and riverine fluxes of strontium and neodymium isotopes to the oceans. *Geochem. Geophys. Geosyst.* 11, Q03016.

Rudnick, R.L. and Gao, S. (2014) 4.1 - Composition of the Continental Crust, in: Holland, H.D., Turekian, K.K. (Eds.), Treatise on Geochemistry (Second Edition). Elsevier, Oxford, pp. 1-51.

van de Kamp, P.C. and Leake, B.E. (1995) Petrology and geochemistry of siliciclastic rocks of mixed feldspathic and ophiolitic provenance in the Northern Apennines, Italy. *Chem. Geol.* 122, 1-20.

Chapter 7: Sedimentary input to the source of Lesser Antilles lavas: a Li perspective

[1] Tang, M., Rudnick, L.R., Chauvel, C. (2014). Sedimentary input to the source of Martinique lavas: a Li perspective. *Geochimica et Cosmochimica Acta*, 144, 43-58.

[2]. M.T. carried out the analyses, led the interpretation and wrote the manuscript; R.L.R. conceived of the project, helped in data interpretation and manuscript writing; C.C. provided the samples and commented on the manuscript.

Abstract

Li isotopes in compositionally diverse Martinique lavas, as well as sea floor sediments cored at the southern (DSDP Site 144) and northern part (DSDP Site 543) of the subducting slab were analyzed in order to investigate the origin of the continental crust compositional signature seen in Lesser Antilles lavas and to investigate Li cycling in arcs. Although the subducting sediments display marked mineralogical and chemical shifts from south to north, the concentration-weighted mean $\delta^7\text{Li}$ for sediments from the two cores are indiscernible from each other (bulk $\delta^7\text{Li} = -0.5 \pm 1.8$, 1σ , $n = 15$, $\delta^7\text{Li} = -4.4$ to $+2.9$). This is the lowest bulk $\delta^7\text{Li}$ seen in subducting sediments from any trenches, and is significantly lower than that of MORB ($\delta^7\text{Li} \sim +4 \pm 1$). These low $\delta^7\text{Li}$ values reflect the dominance of terrigenous input and the influence of chemical weathering in the sediment's continental provenance. With a few exceptions, the Li isotopic compositions of the Martinique lavas are also systematically lighter than MORB, yielding an average $\delta^7\text{Li}$ of $+1.8 \pm 1.3$ (1σ , $n = 24$, excluding three outliers that are isotopically heavy, erupted below seawater and may have incorporated sea water Li). The $\delta^7\text{Li}$ values in the lavas show no correlation with most radiogenic isotope ratios ($^{87}\text{Sr}/^{86}\text{Sr}$, $^{143}\text{Nd}/^{144}\text{Nd}$ and $^{176}\text{Hf}/^{177}\text{Hf}$), Li/Y, La/Sm or SiO_2 . There is also no correlation between $\delta^7\text{Li}$ and radiogenic isotopes in the subducting sea floor sediments. Thus, the low $\delta^7\text{Li}$ in the Martinique lavas likely reflects a mantle source that incorporated

isotopically light subducted sediments. A two-end-member mixing model requires sedimentary input of <1% to 5% by mass to a depleted mantle source to reproduce the Li isotopic compositions of the mafic samples, consistent with the range of sediment input (0.1–5%) inferred from radiogenic isotope data. The Lesser Antilles is the first arc shown to have $\delta^7\text{Li}$ systematically lower than MORB, reflecting the influence of subducted terrigenous sediments. Our data suggest that the enrichment of Li in most arc lavas is due to the addition of subducted sediment-derived Li, and that the isotopic signature of this Li can traverse the mantle wedge with little modification. It is only in arcs such as the Lesser Antilles where the Li isotopic composition of subducted sediments is very different from MORB that the slab signature is apparent in the lavas.

7.1. Introduction

Crustal materials are recycled to the mantle and juvenile arc crust is generated via arc magmatism above subduction zones. Arc lavas are chemically distinct from mid-ocean ridge basalts (MORB), in part due to incorporation of subducted continental and oceanic crustal components in their source regions (Ryan and Chauvel, 2014, and references therein). Understanding the origin of crustal signatures in arc lavas provides insights into the mass exchange and recycling processes in subduction zones.

Lithium isotopes are potentially useful tracers of recycling in subduction zones as they are readily fractionated at the Earth's surface because of the relatively large mass difference between ^6Li and ^7Li (17%). Significant Li isotopic fractionation is generated during both sea floor and subaerial weathering of silicate rocks (Boumann et al., 2004; Chan et al., 1992; Huh et al., 1998; Kısakürek et al., 2004; Kısakürek et al., 2005; Liu et al., 2013; Pistiner and Henderson, 2003; Pogge von Strandmann et al., 2006; Rudnick et al., 2004; Wimpenny et al., 2010). The net effect is that the fluid phase is enriched in ^7Li relative to the rock. Therefore,

the Li isotopic compositions of rivers ($\delta^7\text{Li} = +6$ to $+32$, Huh et al., 1998) and seawater ($+31$, Millot et al., 2004) are significantly heavier than those of the continental crust ($\sim +1$, Teng et al., 2008) and mantle ($\sim +4$, Seitz et al., 2004; Pogge von Strandmann et al., 2011) (see caption to Table 7.1 for definition of $\delta^7\text{Li}$). Moreover, the upper continental crust ($\delta^7\text{Li} = 0 \pm 2$ at 1σ , Teng et al., 2004) is lighter than the upper mantle, as inferred from fresh MORB compositions ($+3.7 \pm 1.0$ at 1σ Tomascak et al., 2008), which has been attributed to a weathering signature in the continental crust. It has been shown that equilibrium Li isotopic fractionation is limited during metamorphic dehydration, partial melting and fractional crystallization (Marschall et al., 2007; Qiu et al., 2011a, 2011b and 2009; Teng et al., 2007 and 2009; Tomascak et al., 1999). Therefore, Li isotopes may provide direct evidence for mass exchange between isotopically distinct reservoirs.

Previous studies of Li isotopes in intraoceanic arc lavas have, with a few exceptions (e.g., Moriguiti et al., 1999; Tomascak et al., 2000), found no systematic difference between arc lavas and MORB (Tomascak et al., 2002; Chan et al., 2002; Moriguiti et al., 2004). The lack of slab Li signature in most intraoceanic arc magmas has led to the suggestion of a “mantle chromatograph”, which attenuates the Li signal during slab fluid ascent through the mantle wedge (e.g., Caciagli et al., 2011; Halama et al., 2009; Tomascak et al., 2002). However, this process fails to explain the evident Li enrichment (relative to Y) in arc magmas (Plank, 2014).

The Lesser Antilles island arc is a compositional end-member of global intraoceanic arcs due to the high proportion of continental crustal materials and a consequently large range of chemical and isotopic compositions in its lavas (Davidson, 1987; Labanieh et al., 2010; White and Dupré, 1986). However, the source of the crustal signature is debated. Does it come from crustal contamination during magma ascent (Davidson, 1985; Davidson, 1986; Davidson and Harmon, 1989; Thirlwall et al., 1994; Thirlwall and Graham, 1984; Thirlwall et

al., 1996; Van Soest et al., 2002; Bezard et al., 2014)? Or does it originate from melting of subducted slab components in the source region (Carpentier et al., 2008; Labanieh et al., 2012; Labanieh et al., 2010; White and Dupré, 1986)? Or could both processes have influenced lava compositions?

Previous work employed chemical compositions and Sr-Nd-Pb-Hf-O isotopes in the lavas to address this question. Early work (e.g., Davidson, 1983) suggested the incorporation of subducted sediments in the source of Lesser Antilles lavas. However, later studies (e.g., Davidson, 1986; Davidson and Harmon, 1989; Van Soest et al., 2002) found that the Pb isotopes in the subducting sediments cored at DSDP Site 543 (Fig. 7.1) are not radiogenic enough to cover the most radiogenic lavas found in the southernmost islands of the arc (from Martinique to Grenada). These authors thus argued that crustal contamination is required to account for the extreme Pb isotopic compositions in these lavas. This argument was also supported by the high $\delta^{18}\text{O}$ of whole-rock samples from Martinique Island (Davidson, 1985, 1986; Davidson and Harmon, 1989). Recently, Carpentier et al. (2008, 2009) published a Sr-Nd-Pb-Hf isotope study of sediments cored at DSDP Site 144 (Fig. 7.1) and showed that these sediments may provide a potential crustal component in the genesis of the southern Lesser Antilles lavas, including highly radiogenic Pb isotopes found in a black shale unit. More recent studies by Labanieh et al. (2010, 2012) confirmed this hypothesis and showed that the composition of Martinique lavas can be reproduced by mixing between depleted mantle and sediments from DSDP Sites 543 and 144.

We have analyzed Li isotopes in Martinique lavas and subducting sea floor sediments from DSDP Sites 144 and 543 near the Lesser Antilles trench in order to determine the degree to which the Li isotopic signature of subducted sediments is preserved in overlying arc lavas. We find that the terrigenous sediments subducted beneath the arc are isotopically some of the lightest subducting sediments world-wide (as previously documented by Bouman et al., 2004), and that this isotopically light signature is also seen in the Martinique lavas,

suggesting that slab Li is not totally consumed in the mantle wedge and makes it through the subduction filter to reappear in arc lavas.

7.2. Geological background and samples

Atlantic lithosphere subducts beneath the Caribbean plateau (Fig. 7.1) in an east–west direction at a rate of ~2 cm/yr (Jordan, 1975; Minster and Jordan, 1978), producing the Lesser Antilles island arc, which extends 750 km from Saba in the north, to Grenada in the south. Magmatic activity initiated in the Late Oligocene (~25 Ma, Germa et al., 2011a) and has continued until the present. Martinique, located in the middle of the island chain, records the most complete magmatic history of the arc (Coulon et al., 1991; Germa et al., 2011a). Martinique lavas are subdivided into three volcanic groups: the old arc (20.8–24.8 Ma), the intermediate arc (7.1–16.1 Ma) and the recent arc (0–5.1 Ma). Each group is composed of a variety of volcanic phases, which are described in Westercamp et al. (1989), Germa et al. (2010, 2011b) and Labanieh et al. (2012).

The accretionary complex that dominates the forearc of the Lesser Antilles is a mixture of pelagic sediments and terrigenous turbidites. The Orinoco River drains the South American continent, in particular, the Guyana Precambrian shield, and introduces a large amount of detrital materials to the forearc region of the Lesser Antilles (White et al., 1985). The sedimentary pile shows south-north gradients in lithology and thickness, with a thicker accretionary complex (>10 km) and more detrital materials deposited in the southern part, which is consistent with its proximity to the continent.

DSDP 78A Site 543, drilled at 5630 m water depth to the northeast of Martinique Island, samples a 410 m thick sedimentary sequence overlying 82 Ma basaltic oceanic crust. This sedimentary sequence mainly comprises pelagic and radiolarian clays. Seismic reflection profiles reveal a décollement surface at a depth of 170 m (Biju-Duval et al., 1982; Moore et

al., 1982; Westbrook and Smith, 1983; Westbrook et al., 1982), beneath which, the underthrusting sediments are subducted into the mantle.

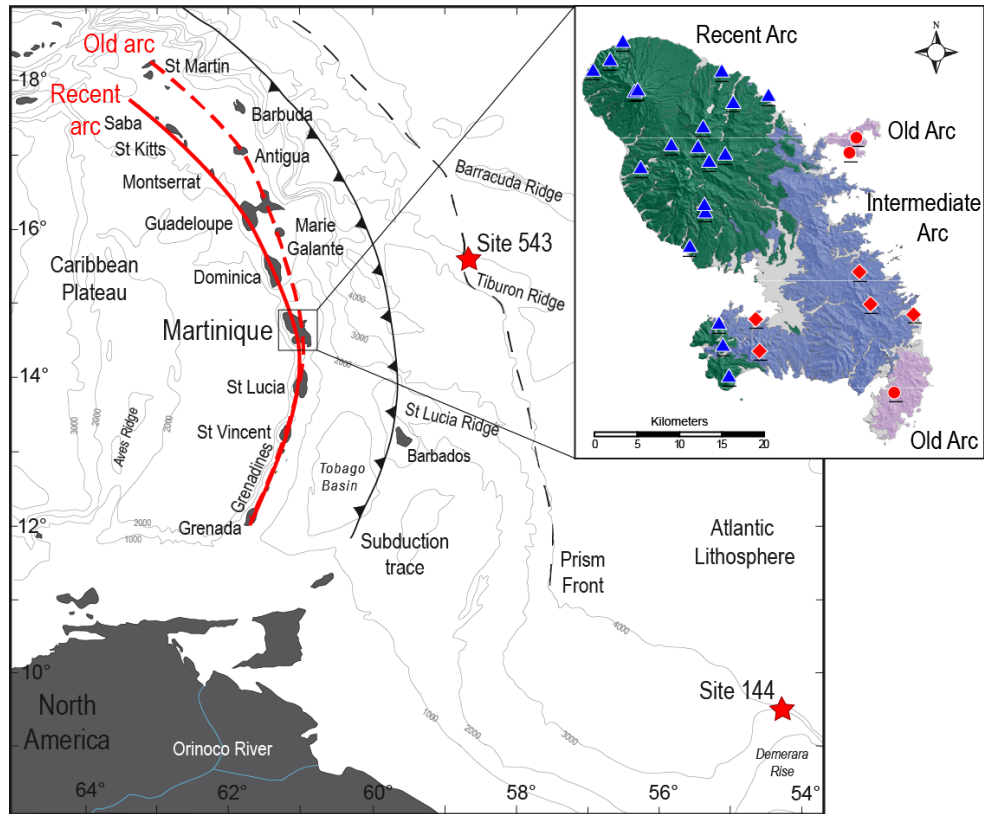


Fig. 7.1. Geological map showing Martinique Island in the Lesser Antilles arc and the two DSDP sites (from Labanieh et al., 2010). The inset shows the locations of lavas measured for Li isotopes (red dots – old arc lavas, red diamonds – intermediate arc lavas, blue triangles – recent arc lavas).

DSDP 14 Site 144 is located to the southeast of Martinique, and recovered a 340 m thick sedimentary sequence at 2960 m water depth. Since this is well above the carbonate compensation depth (CCD), calcium carbonate is a major constituent of all sediments. In addition to calcium carbonate, this sedimentary pile contains terrigenous claystones, sandstones, black shale, chinks and marls. Detailed descriptions of the sediments recovered at Site 543 and Site 144 can be found in Carpentier et al. (2009).

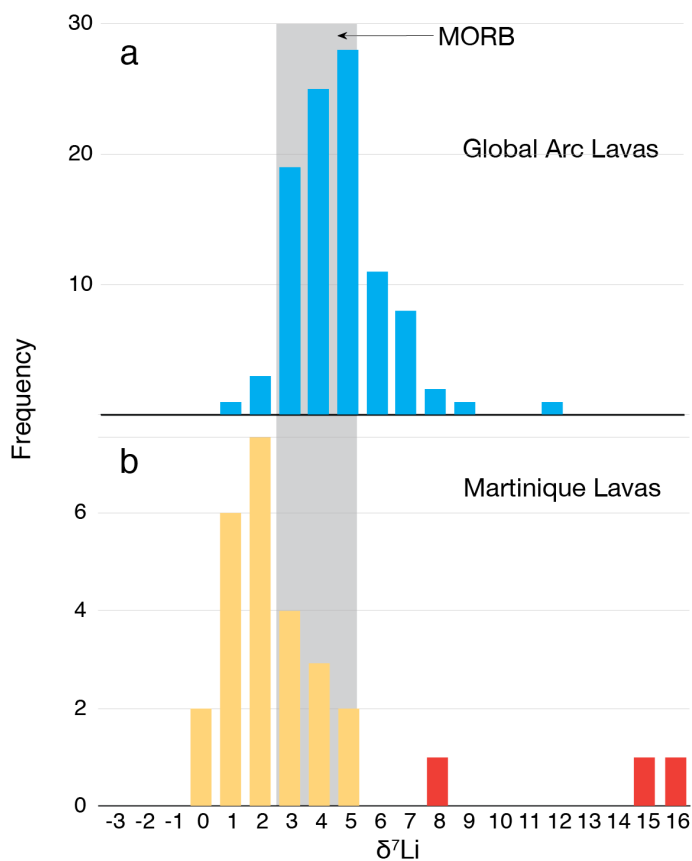


Fig. 7.2. Histogram showing Li isotopic compositions of Martinique lavas compared with MORB and other arc lavas. Published arc lava data include Central American Volcanic Arc (Tomascak et al., 2000; Chan et al., 2002b), Izu Arc and Northeastern Japan Arc (Moriguti et al., 1998 and 2004), Kurile Arc, Sunda Arc and Aleutian Arc (Tomascak et al., 2002) and Mt. Shasta (Magna et al., 2006). Three isotopically heavy samples from Martinique are shown in red. These samples are likely affected by sea water Li (see text for discussion). MORB average ($\delta^7\text{Li} = 3.7 \pm 1, 1 \sigma$) from Tomascak et al. (2008).

To determine the Li isotopic composition of the subducting sediments, we analyzed eight samples from Site 144 and seven from Site 543 (beneath the décollement surface), chosen to

span the range of lithologies present, including chalky ooze, terrigenous sediments, and pelagic clays (Table 7.1). In addition, Bouman et al. (2004) report Li isotope data for Site 543 pelagic clays. However, their sediments are from above the décollement, and thus do not reflect Li recycling in Lesser Antilles. The chemical and radiogenic isotopic compositions of our samples were reported by Carpentier et al. (2008, 2009). These sediments have highly variable CaO (0.38–53.8%), Al₂O₃ (0.31–18.6%) and SiO₂ (1.4–61.7%) contents, which correlate with the contents of biogenic carbonates, clays, and detrital quartz or biogenic silica in the sediments. Trace element concentrations and radiogenic isotopic compositions of these sediments also vary widely.

Table 7.1. Li isotope compositions of the sediments from DSDP Sites 543 and 144.

Sample ID	Depth, m	CaO, wt. %	Al ₂ O ₃ , wt. %	Lithology	δ ⁷ Li	[Li], ppm	Y/Li
Site 144 (9.454 N, 54.342 W)							
144-9	41	36.3	4.6	chalk ooze	-3.9	19	0.73
144-12 144-12 replicate	62	38.2	2.4	chalk ooze	-4.1 -4.6	11	0.84
144-18 144-18 replicate	144	42.8	2.8	gray marl	-3.3 -1.7	7.1	1.49
144-20 144-20 redissolution	163	33.2	4.5	gray marl	-4.2 -4.0	12	1.23
144-28	190	23.0	3.2	black shale	+2.0	9.2	1.75
144-33 144-33 replicate1 144-33 replicate2	295	14.3	6.5	terrigenous seds	+3.5 +2.9 +2.4	25	0.65
144-34	299	3.4	14.4	terrigenous seds	-1.1	58.	0.31
144-35 144-35 replicate	299	8.0	11.5	terrigenous seds	+0.6 -0.1	49.	0.44
Site 543 (15.712 N, 58.654 W)							
543-4	220	0.5	18.5	pelagic clays	-2.1	77	0.31
543-7	248	1.2	18.6	pelagic clays	-2.4	74	0.32
543-8	280	0.6	13.9	pelagic clays	-0.9	62	0.58
543-10	295	0.4	14.5	pelagic clays	-0.9	58	0.34
543-12	315	0.4	12.0	pelagic clays	-1.6	41	0.39
543-19	364	0.7	17.6	pelagic clays	+0.8	61	0.53
543-24	408	26.3	7.2	carb/pelagic clays	+1.8	22	1.59

Note: Major and trace element data are from Carpentier et al. (2009).

δ⁷Li = (⁷Li/⁶Li_{sample} / ⁷Li/⁶Li_{L-SVEC} - 1)*1000, where L-SVEC is the internationally recommended reference material introduced by Flesch et al., 1973), is used to describe Li isotopic composition.

We analyzed Li isotopes in 28 lavas, spanning the three age groups found on Martinique Island (Fig. 7.1). These samples were selected on the basis of freshness, as documented by petrographic examination of thin sections (e.g., no secondary minerals such as chlorite have been observed) (Labanieh et al., 2012). Loss on ignition (LOI, Table 7.2) is below 2% for 90% of the samples analyzed here and does not exceed 3.8%. The ages of these samples, determined by the K-Ar dating technique, range from 1.9 ka to 24.8 Ma (Germa, 2008; Germa et al., 2011a; Germa et al., 2010; Germa et al., 2011b). Four out of the 28 samples (06MT23, 06MT32, 06MT34 and 06MT73) are lavas that erupted below sea level. In addition, most lavas in the St. Anne series erupted below sea level, but it is unclear whether this holds for the St. Anne samples in our suite (e.g., 06MT53, 06MT54 and 06MT68). The chemical and radiogenic isotopic compositions of all of the lavas studied here were reported in Labanieh et al. (2010, 2012). The lavas have SiO₂ contents between 47.3 and 67.4%, are subalkaline, with Na₂O + K₂O ranging from 2.3 to 5.7%, and show large ion lithophile element enrichment, Nb and Ta depletion, and low Ce/Pb ratios, features typical of arc magmas.

7.3. Analytical techniques

Lithium isotopic compositions and concentrations of the samples were analyzed at the Geochemistry Laboratory of the University of Maryland, College Park. Samples were dissolved in screw-top Teflon beakers with a combination of HF-HNO₃-HCl. To achieve complete digestion, some samples were dissolved in HF-HNO₃-HClO₄. Lithium was purified on a cation exchange resin (Bio-Rad AG50w-X12, 200–400 mesh) first in an HCl medium, followed by an HCl-ethanol medium. Before instrumental analysis, sample solutions were diluted to ~50 ppb Li in 2% HNO₃. Lithium isotopes and concentrations were determined on

a Nu Plasma MC-ICP-MS using the standard-sample-bracketing method. Four rock reference materials (BHVO-1, AGV-1, AGV-2 and G-2) were analyzed as accuracy benchmarks. The measured $\delta^7\text{Li}$ are listed in Table 4.3, together with the previously published Li concentrations. The precision of Li isotopic analyses was determined from our long-term analyses of two reference solutions UMD-1 (~50 ppb) and IRMM-16 (~50 ppb), which gave mean $\delta^7\text{Li}$ values of 55.2 ± 0.97 (2σ , $n = 34$) and 0.22 ± 0.67 (2σ , $n = 36$), respectively (see plots in on-line supplement). We adopt $\pm 1\%$ as our 2 sigma analytical uncertainty in this work. The total analytical blank for Li is 1.2 ng, which is insignificant for all of the samples analyzed here. A more detailed description of sample dissolution, column separation and instrumental analysis is available in Qiu et al. (2009) and Teng et al. (2006).

The measured $\delta^7\text{Li}$ for the four rock standards agree with reported values within uncertainty (Table 4.3), and the measured $\delta^7\text{Li}$ values for samples with replicated column chemistry or dissolution are reproducible within error (Tables 4.1 and 4.2).

7.4. Results

7.4.1. Martinique lavas

Lithium isotopic composition and [Li] are given in Table 7.2. The $\delta^7\text{Li}$ values of most Martinique lavas are lower than those of average MORB ($\delta^7\text{Li} = 3.7 \pm 1$, 1σ , Tomascak et al., 2008) (Fig. 7.2a). In addition, the Li isotopes of Martinique lavas are generally lighter than those of other arc lavas, which mostly fall within the MORB range (Fig. 7.2b).

Three lavas have higher $\delta^7\text{Li}$ than MORB (Fig. 7.2, in red). These three samples have the following similarities: (1) they have low $(\text{La}/\text{Sm})_N$ (Fig. 7.3), (2) they are depleted in alkali metals (Fig. 7.4); (3) they have depleted mantle-like radiogenic isotopes (Fig. 7.5), and, most importantly, (4) two of the three are lavas that erupted below sea level (e.g., 06MT73, 06MT34), while the origin of the third lava (06MT073) is less clear but it may have also

erupted as a sub-marine lava. These features distinguish them from the rest of the lavas and they are shown as red symbols in all plots.

Table 7.2. Li isotope compositions of the Martinique lavas.

Sample ID	Location	Age, ka	LOI, wt. %	SiO ₂ wt. %	δ ⁷ Li	[Li], ppm	Y/Li
<i>Recent Arc</i>							
06MT50	14.811	2	0.2	62.0	+1.1	24.7	0.80
06MT50 redissolution ^a	-61.167				+0.3		
06MT51	14.812	2	0	62.7	+1.1	25.8	0.77
06MT51 replicate ^b	-61.165				+2.4		
06MT40	14.849 -61.198	189	0.8	60.0	+0.8	15.7	1.48
06MT37	14.675 -61.085	322	1.1	55.9	+2.1	20.2	0.92
04MT07	14.725	341	0.46	58.8	+0.6	29.1	1.48
04MT07 redissolution	-61.115				+1.5		
06MT18	14.837 -61.218	346	1.0	58.4	+2.8	8.6	2.22
06MT28	14.872	543	1.2	58.5	+1.0	13.5	1.38
06MT28 replicate	-61.182				+2.2		
IAR	14.533	640	0.0	47.7	+4.3	4.9	4.10
IAR replicate	-61.067				+3.1		
06MT21	14.747	893	0.9	63.5	-1	37	0.45
06MT21 redissolution	-61.124				+0.1		
06MT36	14.668	998	1.6	63.0	-0.6	38.9	0.43
06MT36 replicate	-61.083				-0.7		
06MT61	14.507 -61.062	1,175	0.1	54.4	+1.2	7.0	3.27
06MT55	14.47 -61.055	1,332	1.2	59.9	+1.3	10.5	2.94
06MT14	14.769 -61.086	1,530	1.0	58.5	+2.7	30.2	0.63
06MT19	14.720	1750	1.4	57.8	+1.6	24.6	1.07
06MT19 redissolution	-61.161				+2.5		
06MT04	14.626 -61.102	1,870	1.3	60.0	+4.1	28.7	0.85
06MT10	14.736 -61.059	2,111	1.9	59.8	+3.6	26.4	0.96

06MT13	14.728 -61.079	2,550	1.2	58.8	+1.0	20.2	1.13
06MT34*	14.806 -61.007	4,100	0.6	53.8	+7.1	4.9	6.31
06MT23*	14.799 -61.050	4,863	1.2	53.9	+1.4	8.9	2.70
06MT32*	14.835	5,130	0.7	50.7	+1.0	6.21	4.77
06MT32 redissolution	-61.063				+2.0		
06MT32 replicate					+1.0		
<i>Intermediate Arc</i>							
06MT72	14.539 -61.022	7,100	3.8	67.4	+1.9	53.1	0.34
06MT60	14.501	8,760	1.3	60.6	+4.9	26.1	1.04
06MT60 redissolution	-61.017				+4.3		
06MT71	14.546 -60.832	10,300	0.9	49.3	+0.9	17	2.83
06MT69	14.557	10,640	2.0	47.3	+0.7	18.5	2.25
06MT69 redissolution	-60.885				+1.1		
06MT73*	14.596	16,120	2.9	66.5	+13.9	5.1	8.82
06MT73 replicate	-60.898				+14.6		
<i>Old arc</i>							
06MT54**	14.739 -60.91	20,800	1.2	53.3	+3.5	10.5	2.47
06MT53**	14.757 -60.901	23,400	1.4	58.5	+16.3	6.4	4.07
06MT68**	14.452	24,800	1.5	49.1	+1.9	5.5	2.51
06MT68 replicate 1	-60.856				+1.7		
06MT68 replicate 2					+2.9		

Notes:

Major and trace element data are from Labanieh et al. (2012);

*Erupted below seawater;

**These samples, from the St. Anne's suite, may or may not have erupted below seawater;

^aRedissolution means independent sample dissolution and column chemistry;

^bReplicate means independent column chemistry.

Table 7.3. Measured $\delta^7\text{Li}$ and [Li] in rock standards compared with reported values.

Rock standards	This work	Literature
	$\delta^7\text{Li}$	$\delta^7\text{Li}$
BHVO-1		
Dissolution 1	+4.2	+4.0 ~ +6.1
Dissolution 2	+4.5	
Dissolution 3	+4.3	
Dissolution 4	+4.9	
Dissolution 5	+4.4	
Mean	+4.5 ± 0.6	
AGV-1		
Dissolution 1	+5.1	+4.6 ~ +6.7
AGV-2		
Dissolution 1	+6.2	+5.7 ~ +8.1
Dissolution 2	+5.2	
Dissolution 3	+5.3	
Mean	+5.6 ± 1.2	
G-2		
Dissolution 1	-0.6	-1.2 ~ +0.3
Dissolution 2	-0.3	
Dissolution 3	+0.1	
Dissolution 4	-1.3	
Mean	-0.5 ± 1.2	

Notes: \pm values are two sigma of the mean. BHVO-1 literature data are from James and Palmer (2000), Pistiner and Henderson (2003), Chan and Frey (2003), Bryant et al. (2004), Rudnick et al. (2004), Bouman et al. (2004), Magna et al. (2004), Rosner et al. (2007), Aulbach et al. (2008), Halama et al. (2008), Maloney et al. (2008), Halama et al. (2009), Schuessler et al. (2009), Liu et al. (2010, 2013 and 2014), Penniston-Dorland et al. (2010), Halama et al. (2011), Penniston-Dorland et al. (2012). AGV-1 literature data are from Magna et al. (2004), Liu et al. (2010, 2013 and 2014); AGV-2 literature data are from Magna (2004 and 2006) and Tian et al. (2012); G-2 literature data are from James and Palmer (2000), Pistiner and Henderson (2003), Liu et al. (2010) and Barnes et al. (2012).

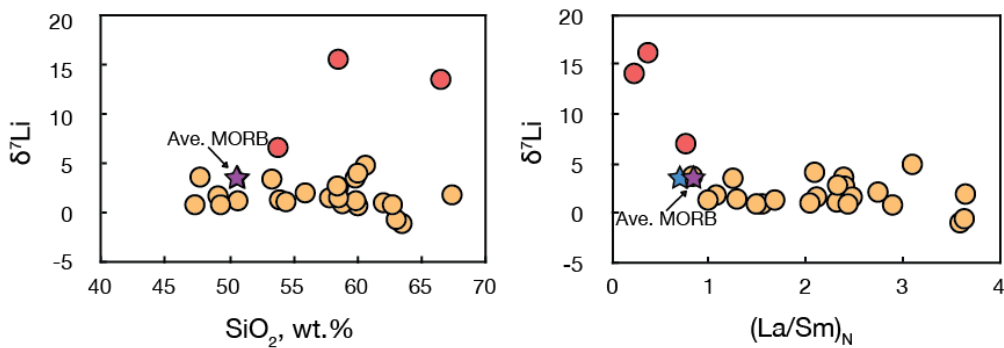


Fig.

7.3. $\delta^7\text{Li}$ vs. SiO_2 and $(\text{La}/\text{Sm})_N$ for Martinique lavas. The red symbols denote the lavas with Li isotopes heavier than MORB. Notice that the three isotopically heavy samples have

relatively high SiO_2 content but low $(\text{La}/\text{Sm})_N$ values. The gray band, shows the $\delta^7\text{Li}$ spread in MORB. A MORB field could not be plotted due to lack of published major and trace element data for many of the samples for which $\delta^7\text{Li}$ has been determined, but for reference $(\text{La}/\text{Sm})_N$ of average global MORB from Arevalo and McDonough (2010) is 0.73 (marked by blue star), average N-MORB is 0.61, while Gale et al. (2013) have average $(\text{La}/\text{Sm})_N$ of MORB = 0.86 (purple star).

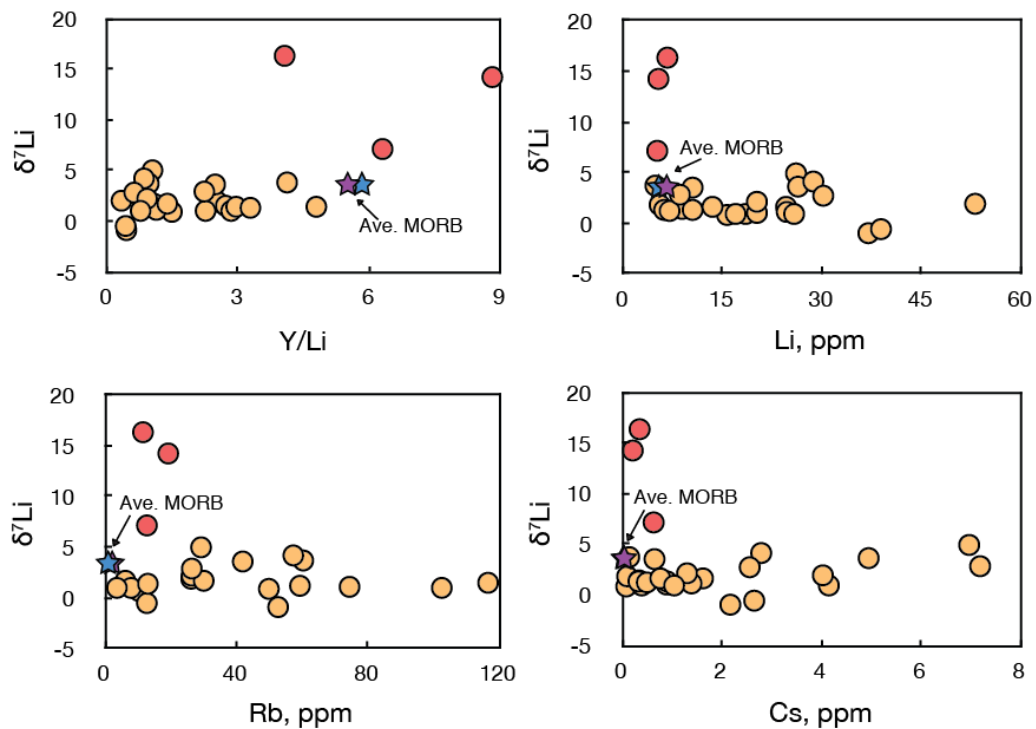


Fig. 7.4. $\delta^7\text{Li}$ vs. Y/Li, [Li], [Rb] and [Cs] for Martinique lavas. Note that the three lavas with heavy Li isotopes all have low alkali metal concentrations, even when SiO_2 is as high as 66.5%. Global MORB values for abscissae shown by stars (values from Arevalo and

McDonough, 2010, blue star, Gale et al., 2013, purple star).

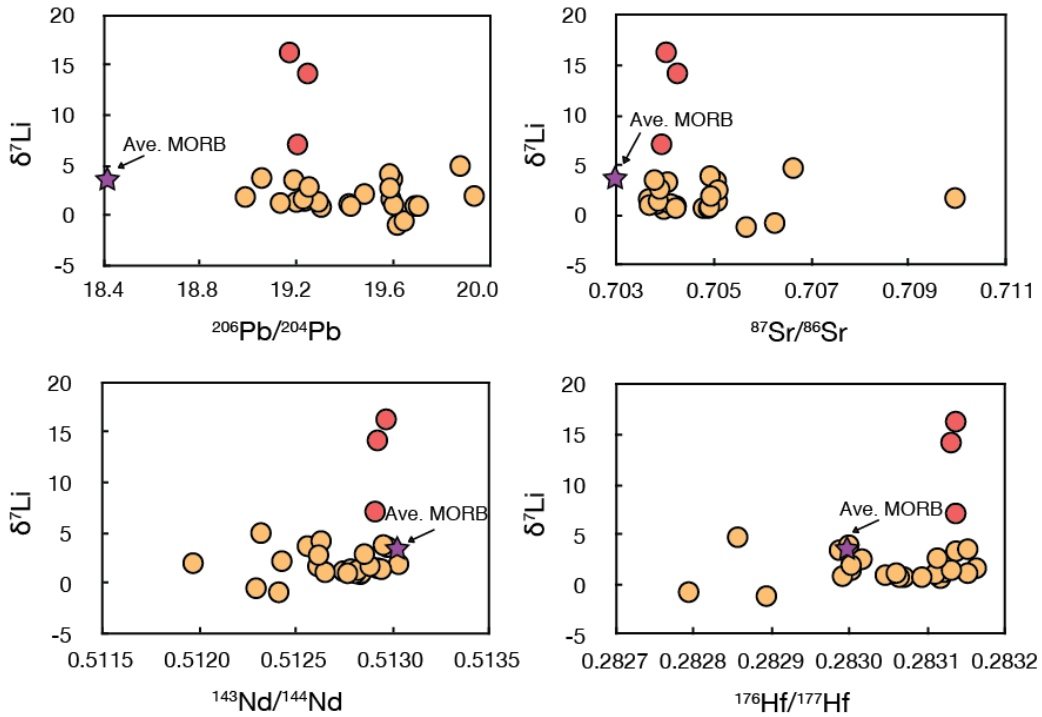


Fig. 7.5. $\delta^7\text{Li}$ vs. Sr-Nd-Pb-Hf isotopes for Martinique lavas. The three high $\delta^7\text{Li}$ samples are characterized by depleted mantle-like radiogenic isotopic compositions. Global MORB values for abscissae shown by purple star (Gale et al., 2013).

4.4.2. Sediments from DSDP Sites 543 and 144

Despite the differences in lithology and chemical composition, the sediments recovered from Sites 543 (mean $\delta^7\text{Li} = -0.8 \pm 1.5$, 1σ) and 144 (mean $\delta^7\text{Li} = -1.3 \pm 2.9$, 1σ) are indistinguishable from each other in terms of their Li isotopes, and both sections are significantly isotopically lighter than MORB. Bouman et al. (2004) previously analyzed four samples from Site 543 that included radiolarian pelagic clay, Mn stained radiolarian clay, zeolitic pelagic clay and calcareous ferruginous claystone. These samples have $\delta^7\text{Li}$ ranging from -0.8 to +1.1, with a mean $\delta^7\text{Li}$ of $+0.4 \pm 0.9$ (1σ), falling within the spread of our data.

The $\delta^7\text{Li}$ values of Site 144 sediments are slightly more variable, consistent with the greater variation in lithology and radiogenic isotopic compositions.

7.5. Discussion

7.5.1. Low $\delta^7\text{Li}$ subducting sediments

The sediments (i.e., those below the décollement) sampled at Sites 543 and 144 have the lightest average Li isotopes among global subducting sediments (Fig. 7.6). Even carbonate-rich sediments from Site 144 have light Li (Table 7.1), reflecting the clay component, which dominates the Li mass balance, as clays have [Li] up to two orders of magnitude higher than carbonates (e.g., Marriott et al., 2004; Teng et al., 2004). The low $\delta^7\text{Li}$ values obtained for the Site 543 samples are similar to those seen in sediments from above the décollement at Site 543 (Bouman et al., 2004). The low $\delta^7\text{Li}$ values of sediments from both drillcores likely reflect the dominance of terrigenous materials from the South America continent (White et al., 1985), which derive, in part, from the highly weathered Guayana Shield (Huh et al., 2001, Carpentier et al. 2013). Previous studies have demonstrated a correlation between $\delta^7\text{Li}$ and weathering intensity recorded in terrigenous sedimentary rocks, with shales derived from more highly weathered provenances, as measured by chemical index of alteration (CIA) values (Nesbitt and Young, 1982), having lower $\delta^7\text{Li}$ and higher [Li] (Qiu et al., 2009). A similar relationship is seen in subducting sediments, of which the Lesser Antilles sediments form an end member (Fig. 7.7).

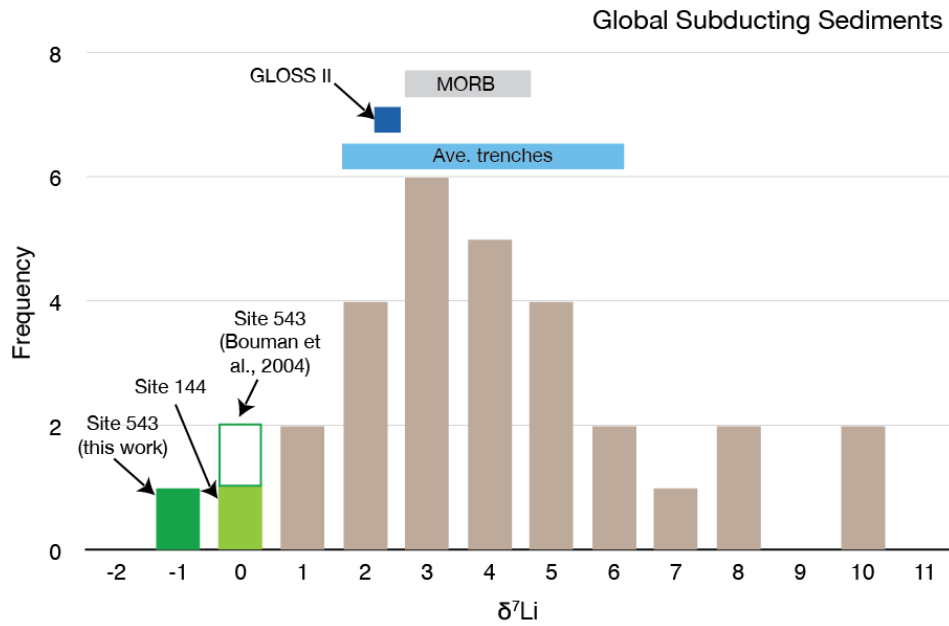


Fig. 7.6. Distribution of average $\delta^7\text{Li}$ in subducting sediments from global trenches. Lithium isotopes of subducting sediments from different trenches (lithology weighted averages of 26 trenches, shown in light brown) are from Plank (2014) and this study (Sites 543 and 144). Carbonate-rich samples were excluded from the average for Site 144 (see text for explanation). Also shown is $\delta^7\text{Li}$ for GLOSS II (Plank, 2014) and the average and standard deviation for the data from the individual trenches (“Ave. trenches”). Readers are referred to Plank (2014) for details of the 26 trenches.

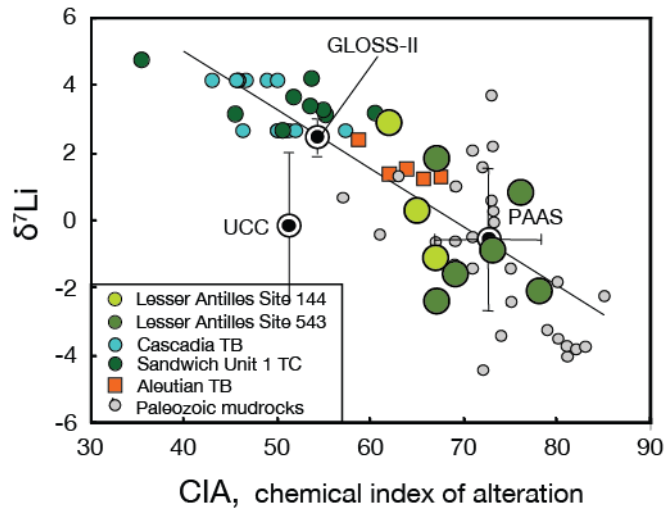


Fig. 7.7. $\delta^7\text{Li}$ vs. CIA for subducting sediments from Lesser Antilles (larger symbols) and other arcs after Plank (2014). We excluded the data from Bouman et al. (2004) that appeared on Plank's original figure for Lesser Antilles, as there is no major element data for these samples. The four high-CaO samples from Site 144 (Table 7.1) are not shown as their CIA values cannot be calculated accurately.

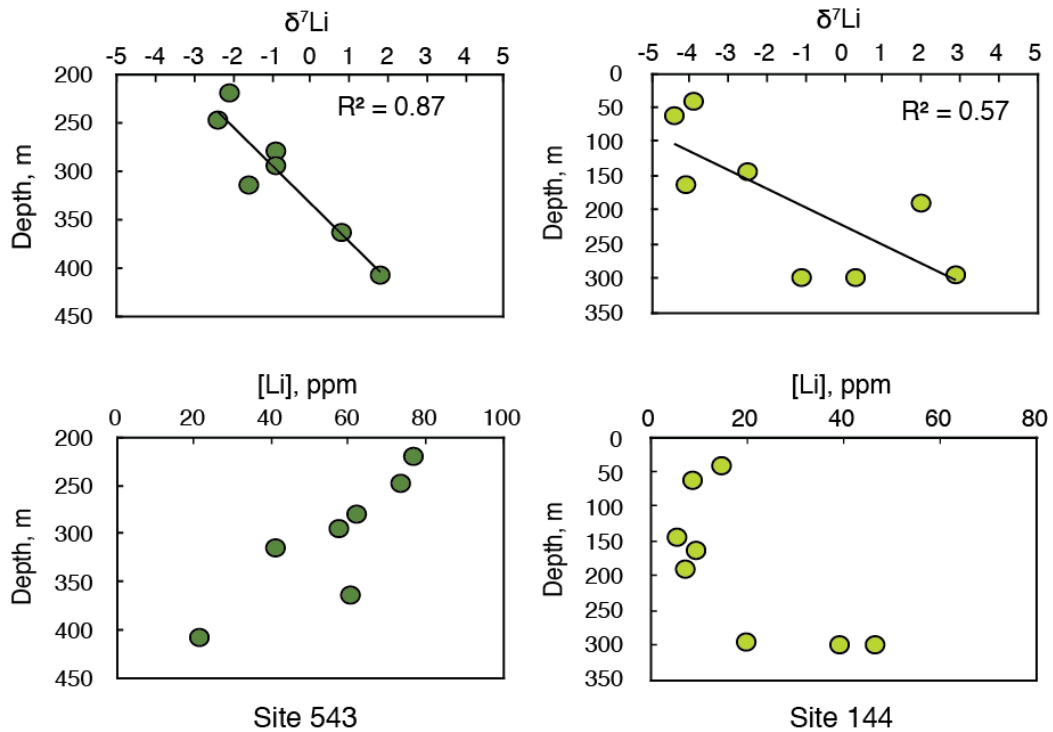


Fig. 7.8. $\delta^7\text{Li}$ and $[\text{Li}]$ as a function of depth for the sediments from DSDP Sites 543 and 144. Note the general positive correlation between $\delta^7\text{Li}$ and depth while the relationship between $[\text{Li}]$ and depth is less clear, in part due to carbonate enrichment in the upper section of Site 144.

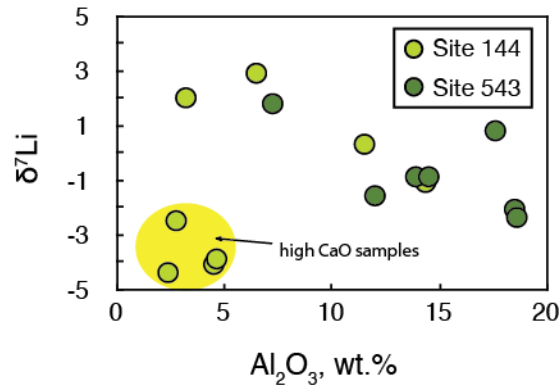


Fig. 7.9. $\delta^7\text{Li}$ negatively correlates with Al_2O_3 contents in the subducting sediments if the four high CaO samples are excluded. This may reflect a lithological control on the Li isotopic compositions in the subducting sediments at DSDP Sites 543 and 144.

At both Sites 543 and 144, $\delta^7\text{Li}$ in the sedimentary pile increases with depth (Fig. 7.8). Similar trends have been observed in sediments from the Tonga and Central America Trenches (Chan et al., 2006) where $[\text{Li}]$ decreases with depth, and $\delta^7\text{Li}$ increases up to +12 at the base of the sedimentary sections. While Chan et al. (2006) suggested that these trends might be controlled by lithology and hydrothermal activity, lithology cannot be the sole control for our data, as lithology in the Site 543 sediments is largely invariable with depth (Table 7.1). At Site 543, $[\text{Li}]$ also decreases with depth but at Site 144, the $[\text{Li}]$ –depth relationship is variable – it first decreases and then markedly increases with depth (Fig. 7.8). Understanding the cause of the depth-dependent changes in $\delta^7\text{Li}$ in these sediments is beyond the scope of this paper, but we provide two suggestions here: (1) the increasing $\delta^7\text{Li}$ and decreasing $[\text{Li}]$ with depth may reflect increasing leaching and sediment-pore water exchange

with depth. Pore waters typically have higher $\delta^7\text{Li}$ than sediments (+7.5 to +45.7, Scholz et al., 2010), and their compositions also tend to change systematically with depth, reflecting Li release during diagenesis as well as uptake of Li during authigenesis (Scholz et al., 2010); (2) If we exclude the four samples significantly diluted by carbonates ($\text{CaO} > 30$ wt. %), $\delta^7\text{Li}$ shows a rough, negative correlation with Al_2O_3 (Fig. 7.9), which may indicate temporal variation in the composition of the sediments, hence provenance, because clay-rich components tend to have high Al_2O_3 contents and low $\delta^7\text{Li}$, as described above. These two explanations are not mutually exclusive and future studies of marine sedimentary $\delta^7\text{Li}$ with depth should help to elucidate which of the two processes is most important or if other processes are at work that we have not recognized.

Though variable, $\delta^7\text{Li}$ values of these sediments show no correlation with other geochemical characteristics such as Li- or LREE-enrichment (Fig. 7.10), and very poor correlations with radiogenic isotopes, particularly Nd and Pb (Fig. 7.11), which have been used to trace sedimentary components in subduction zone magmas. Because Nd and Pb are far more concentrated in the sediments than in the mantle relative to Li, their isotopic compositions in the arc lavas are more sensitive to sedimentary input (either in the mantle source or during shallow assimilation). Collectively, the lack of, or poor correlations between Li isotopes and other geochemical tracers in the sediments may also explain the decoupling between Li isotopes and other geochemical tracers seen in the Martinique lavas, if the variable $\delta^7\text{Li}$ reflects a sedimentary component incorporated into the magma (see supplementary file for Monte Carlo simulation of sediment mixing to a depleted mantle source).

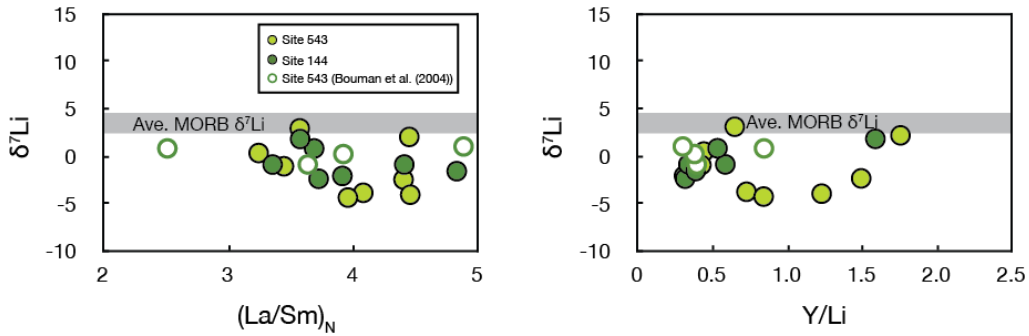


Fig. 7.10. $\delta^7\text{Li}$ vs. $(\text{La}/\text{Sm})_N$ and Y/Li for the subducting sediments from DSDP Sites 543 and 144. Site 543 sediments are all pelagic clays, whereas the lithology of Site 144 sediments is more highly variable, yet the $\delta^7\text{Li}$ of the two sites are indistinguishable. Trace element data are from Carpentier et al. (2009). For comparison, we also plot the data from Bouman et al. (2004), though because the latter sediments lie above the décollement, they will not be subducted into the source region of the arc lavas. Global MORB has $(\text{La}/\text{Sm})_N$ below 1 and Y/Li between 5 and 6 (Arevalo and McDonough, 2010; Gale et al., 2013).

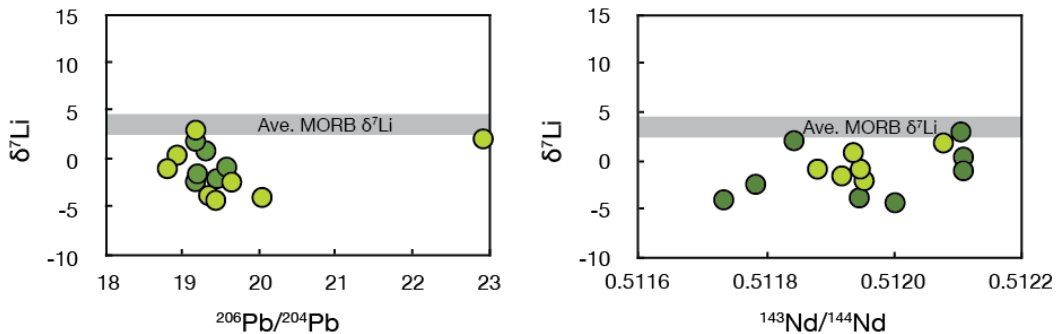


Fig. 7.11. $\delta^7\text{Li}$ vs. Pb and Nd isotopes for the subducting sediments from Sites 543 and 144. Li isotopes show only poor correlations with radiogenic isotopes in these sediments. Radiogenic isotope data are from Carpentier et al. (2008). Global MORB from Gale et al. (2013).

7.5.2. High $\delta^7\text{Li}$ lavas

The three samples with heavy Li isotopes are distinguished from other samples by depletion in alkali metals, low $(\text{La}/\text{Sm})_N$, depleted mantle-like radiogenic isotopes, and, most importantly, their submarine eruption. Labanieh et al. (2012) found that submarine lavas are generally marked by negative [Li] anomalies, while subaerial lavas have positive Li anomalies. These observations suggest that the three samples likely interacted with seawater ($\delta^7\text{Li} \sim +31$), which may have produced their abnormally high $\delta^7\text{Li}$. The depletion in alkali metals, including Li, indicates that these elements might have been leached from the lavas during the interaction with seawater, making them more susceptible to change, while the isotopically heavy compositions suggests some amount of uptake of seawater Li. No matter what process is responsible for producing these high $\delta^7\text{Li}$ values, it seems that they are not primary features of the lavas, and therefore these three samples will not be considered further.

7.5.3. Low $\delta^7\text{Li}$ components in Martinique lavas

The $\delta^7\text{Li}$ values of the remaining lavas show no clear relationship with age (Fig. 7.12a). Furthermore, the samples with the lowest LOI ($\sim 0\%$) are also isotopically light (Fig. 7.12b), suggesting that the low $\delta^7\text{Li}$ values in Martinique lavas are unlikely to be a result of alteration or chemical weathering. The lack of correlation between $\delta^7\text{Li}$ and SiO_2 and $(\text{La}/\text{Sm})_N$ (Fig. 7.13) indicates that the Li isotopic compositions of the lavas are insensitive to magmatic differentiation and the amount of assimilated crustal materials. The $\delta^7\text{Li}$ values also show no real correlation with radiogenic isotopes (Fig. 7.5), and even the least differentiated sample ($\text{SiO}_2 = 47.3\%$) has a $\delta^7\text{Li}$ significantly lower than that of MORB. Collectively, $\delta^7\text{Li}$ does not correlate with either composition or age of the lavas.

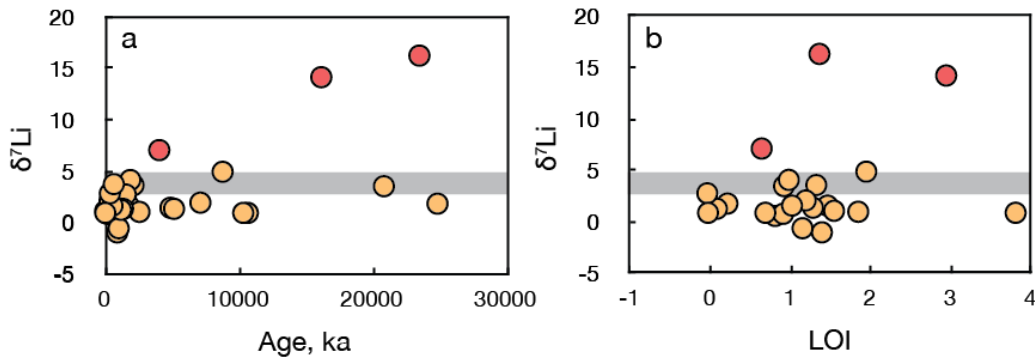


Fig. 7.12. Plots of $\delta^7\text{Li}$ vs. age (a) and LOI (b) for Martinique lavas. The red symbols denote the samples with Li isotopes heavier than MORB.

The Martinique lavas have $\delta^7\text{Li}$ values that overlap with, but are mostly lower than those of MORB (Fig. 7.2), suggesting incorporation of low $\delta^7\text{Li}$ components in their source region and/or assimilation of such components during differentiation within the crust. Light Li isotopes were also observed in olivine-hosted melt inclusions from St. Vincent Island (Bouvier et al., 2008), which also belongs to the Lesser Antilles arc. According to Bouvier et al. (2008), the low $\delta^7\text{Li}$ (down to -10) in the melt inclusions, although seemingly not preserved in bulk lava records, may reflect initial melt heterogeneities and kinetic fractionation in the source region. An alternative explanation is that they reflect diffusive addition of Li into the inclusion from the mineral (e.g., Richter et al., 2014).

Four components may have contributed to the source of arc magmas: depleted mantle, slab fluids, melts derived from fresh/altered oceanic crust (AOC) and melts from marine sediments. As depleted mantle will have the $\delta^7\text{Li}$ of MORB, it cannot be responsible for the low $\delta^7\text{Li}$ we observe. We therefore consider each of the remaining components, in turn.

Slab fluids are expected to be isotopically heavy, as ^7Li is preferentially partitioned into hydrous fluids (Caciagli et al., 2011; Chan et al., 2002b; Marschall et al., 2007; Moriguti and Nakamura, 1998; Tomascak et al., 2000; Wunder et al., 2006; Zack et al., 2003). High Li, low salinity fluids from forearc seamounts that are interpreted to derive from the slab have high

$\delta^7\text{Li}$ ($\sim+20$), supporting this hypothesis (Chan and Kastner, 2000; Benton et al., 2004). Moreover, Ba is a fluid-mobile element that is often used as a tracer of slab fluids (e.g., Labanieh et al., 2008). The Ba/Th of the seven basaltic samples ($\text{SiO}_2 < 55\%$) vary from 51 to 188 with an average value of 112, which is within the 2 sigma range of global MORB ($\sim 80 \pm 52$, 2σ , Arevalo and McDonough, 2010). Therefore, slab fluids are unlikely to account for the isotopically light Li in the Martinique lavas.

Altered oceanic crust has variable Li isotopic composition depending on the temperature of alteration. Low-temperature seafloor weathering of the basaltic crust produces high $\delta^7\text{Li}$ due to uptake of heavy seawater Li into clays (Chan et al., 1992; 2002a), while hydrothermal alteration generates low $\delta^7\text{Li}$ as a result of preferential leaching of ^7Li (e.g., Chan et al., 2002). Metamorphic dehydration of the altered crust may lower $\delta^7\text{Li}$ (Halama et al., 2011; Marschall et al., 2007; Zack et al., 2003), but the extremely low $\delta^7\text{Li}$ observed in some eclogites (down to -21) likely results from kinetic isotopic fractionation during retrograde metamorphism (Marschall et al., 2007). Using the experimentally determined isotopic fractionation factors of Wunder et al. (2006), Marschall et al. (2007) calculated that $\delta^7\text{Li}$ could be lowered by only $\leq 3\%$ during metamorphism of basaltic oceanic crust. These modeling results are supported by later observations on metapelites, which show negligible isotopic fractionation associated with metamorphic dehydration during sub-greenschist to granulite facies metamorphism, even in the presence of significant Li loss (Qiu et al., 2009, 2011a and 2011b; Teng et al., 2007). Thus, any contribution to arc magmas from the altered oceanic crust would come from melts, which should have the same isotopic composition as their source, given that the amount of isotopic fractionation at magmatic temperatures is negligible (Tomascak et al., 1999). However, there is no evidence for melts of the basaltic slab contributing to the source of Martinique lavas. First, the chemical and physical conditions of the slab below Martinique Island ($\sim 780^\circ\text{C}$ and 4.5 GPa, Syracuse and Abers, 2006; Syracuse et al., 2010) do not meet those required for basaltic slab melting (Schmidt and

Poli, 2014). Secondly, the Martinique lavas have uniformly low Sr (28/29 samples < 400 ppm) and Sr/Y ratio (3.5 to 24.7; mean = 11.3), which is inconsistent with addition of slab melts having Sr concentrations > 400 ppm and Sr/Y > 20 (Castillo, 2006; Defant and Drummond, 1990).

Introduction of subducting sediments, or melts therefrom, to the mantle source of the Martinique lavas may produce their low $\delta^7\text{Li}$. As noted earlier, the sediments subducting beneath the Lesser Antilles are end members in having the lowest $\delta^7\text{Li}$ amongst global subducting sediments (Table 7.1, Fig. 7.6). Carpentier et al. (2008; 2009) and Labanieh et al. (2010; 2012) showed that addition of Site 144 sediments to the mantle wedge reproduces the mixing trends seen in plots of radiogenic isotopes in the Martinique lavas. Furthermore, earlier studies have shown that Li may or may not be removed during prograde metamorphism of pelitic rocks, but Li isotopes are unaffected by either metamorphism or partial melting. For example, Penniston-Dorland et al. (2012) suggested that deeply subducted metasedimentary rocks may largely retain their Li inventory to depths of at least 40 km. Bebout et al. (2007) studied ultra high-pressure metasedimentary rocks from the Western Alps and inferred Li retention in such rocks to depths of > 90 km. By contrast, significant Li depletion is seen in amphibolite to granulite-facies rocks in both contact metamorphic aureoles (Teng et al., 2007) and metapelitic residues in the Ivrea Zone, Italy (Qiu et al., 2011b), though this apparently did not change their $\delta^7\text{Li}$. Alternatively, some have suggested that sediments are physically mixed into the mantle wedge of arcs via the rise of buoyant diapirs (Hacker et al., 2011; Behn et al., 2011). Either process (melting or solid diapirs) is capable of introducing isotopically light Li to the source region of arc basalts.

Our Li data cannot rule out the possibility that crustal contamination influenced the composition of the Martinique lavas since the Li isotopic composition of the arc crust beneath Martinique is yet to be constrained. However, crustal contamination, if present, is unlikely to

be the major cause of low $\delta^7\text{Li}$ for two reasons. First, $\delta^7\text{Li}$ shows no correlation with SiO_2 , and is as low as +0.9 even in the most primitive basalt ($\text{SiO}_2 = 47.3\%$). Second, if the low $\delta^7\text{Li}$ was acquired during magma ascent, 10-20% (by mass) sediment assimilation would be required, assuming the assimilated arc crust has the same [Li] and Li isotopic composition as the bulk Site 543 and Site 144 sediments. This is due to the fact that the basaltic magma has much higher [Li] than peridotite in the mantle wedge, and its isotopic composition is therefore less sensitive to sediment addition. The questions then arise (1) whether the thermal budget of the magma allows for such a large extent of sediment assimilation in the crust; (2) whether these magmas would remain basaltic in their compositions after such extent of assimilation, assuming an assimilation/crystallization ratio of 0.25 (Smith et al., 1996). Labanieh et al. (2010) calculated AFC trends but were unable to reproduce the Sr-O isotope data.

7.5.4. Sediment mixed into the source

In order to determine the amount of sediment that was added to the mantle source of the lavas, we must first constrain the composition of the source. While $\delta^7\text{Li}$ in the lavas should reflect that of the source, the same is not true for [Li]. In order to characterize the Li content of the source, we normalize to another element that has a similar partition coefficient: Y. We use the Y/Li ratio, so that mixing will be linear in a plot of Y/Li vs. $\delta^7\text{Li}$.

Lithium and Y have nearly identical solid/melt bulk distribution coefficients in basaltic systems (Ryan and Langmuir, 1987), and their ratio, Y/Li, has frequently been used to infer source composition (e.g., Chan et al., 2002b; Moriguti and Nakamura, 1998; Plank, 2014; Tomascak et al., 2002). Here, we use basaltic samples ($\text{SiO}_2 < 55\%$) in our mixing model, since Y/Li decreases with differentiation, in order to estimate sedimentary input to the mantle source.

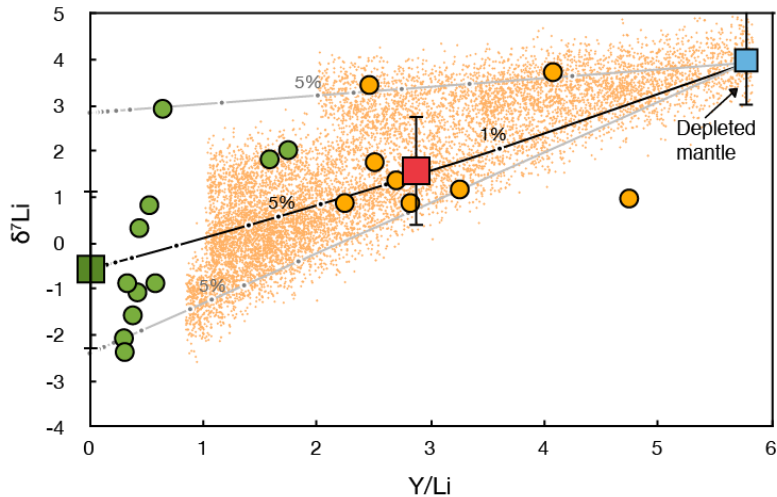


Fig. 7.13. A two-component mixing model between depleted mantle and sediments from Sites 543 and 144 (green dots). The large green square represents the average composition of the sediments (excluding the carbonate-rich sediments from Site 144, which are unlikely to subduct beneath the arc), whereas the large red square represents the average composition of the basalts. Error bars represent 1 sigma standard deviation. The light Li isotopes in the basaltic Martinique lavas (orange dots) can be formed by less than 5% addition of Site 543 and Site 144 sediments to a mantle source (gray mixing lines).

Fig. 7.13 shows two-component mixing between depleted mantle ($[Li] = 0.7$ ppm, $[Y] = 4.07$ ppm (Salters and Stracke, 2004), $\delta^7Li = +4$), and the subducting sediments from Site 543 and Site 144. We estimated the average composition of the subducted sediment by using Site 543 samples that are located only below the décollement (i.e., all of the Site 543 sediments analyzed here, but not the Boumann et al. sediments which are above the décollement) and for Site 144, only the low carbonate sediments, assuming that the sediments deposited closer to the trench, below the carbonate compensation depth, will have much lower carbonate concentrations. We first calculated the concentration weighted mean δ^7Li for Site 144 and Site 543, respectively. Then we used the two concentration weighted mean δ^7Li and the bulk $[Li]$ and $[Y]$ values for the two sites recommended by Carpentier et al. (2009), and calculated

concentration weighted mean $\delta^7\text{Li}$ for the bulk subducting sediments. This yields a bulk $\delta^7\text{Li} = -0.5$, and a mean $[\text{Li}] = 49.1$ ppm, mean $[\text{Y}] = 24.2$ ppm. The average Li isotopic composition and Y/Li ratio represented by the eight basaltic samples from Martinique Island (concentration weighted mean $\delta^7\text{Li} = +1.6$, mean $\text{Y/Li} = 2.9$) require a bulk sedimentary contribution of $\sim 2\%$ by mass to the source. All basaltic samples can be reproduced by less than 5% sediment addition. If the sediment component was added as a partial melt, instead of bulk mixing, then the sediment proportion is even less. However, this calculation assumes no Li loss during sediment dehydration and no contribution from isotopically heavy components such as slab fluids, which may result in an underestimate of the sedimentary input. These two factors tend to cancel each other out with regard to their effects on the calculated sediment proportion. Our estimate of sedimentary input to the mantle source based on Li isotopes agrees well with that determined from the radiogenic isotopic constraints (0.1-5%, Labanieh et al., 2010).

7.5.5. Implications for Li in arc systems

Martinique is currently the only example observed, to date, where intraoceanic arc lavas have low average $\delta^7\text{Li}$ relative to MORB. The Li isotopic compositions of most other arcs generally overlap the MORB range (e.g., Chan et al., 2002; Moriguti et al., 2004; Tomascak et al., 2002, Fig. 7.2). The lack of a clear slab signal in the $\delta^7\text{Li}$ of arc lavas has led to broad discussion on Li recycling and Li isotopic fractionation in arc systems (e.g., Tomascak et al., 2002; Plank, 2014), as well as investigation of Li isotopic compositions of slab components (e.g., Chan et al., 1992, 2002a, 2006; Chan and Kastner, 2000; Benton et al., 2004; Zack et al., 2003; Marschall et al., 2007; Penniston-Dorland et al., 2011; Halama et al., 2011).

Earlier investigations of Li in arc lavas and subarc mantle peridotites explained the similarity in $\delta^7\text{Li}$ between arcs and MORB as being due to chromatographic exchange between slab Li and mantle wedge peridotite (Halama et al., 2009; Tomascak et al., 2002).

Recent experimental data on fluid partitioning suggests that Li carried in slab fluids would indeed not make it through the mantle wedge if the fluids move via porous flow (Caciagli et al., 2011). However, these scenarios fail to explain why arc lavas are generally enriched in Li (low Y/Li) relative to MORB (Plank, 2014). An alternative possibility is that Li from the slab is not isotopically distinct from MORB in most arcs (Halama et al., 2009).

Due to the large quantities of highly weathered terrigenous materials delivered to the sea floor by the Orinoco River, Site 543 and Site 144 sediments have the lightest Li isotopes (concentration weighted mean $\delta^7\text{Li} = -0.5 \pm 1.8$, 1σ) among global trench sediments (Figs. 7.6 and 7.7). Plank (2014) reports a new global subducting sediment estimate (GLOSS-II) with a $\delta^7\text{Li}$ of $+2.4 \pm 0.2$ (the uncertainty represents the maximum difference in the global weighted mean for 90 out of 100 trials). However, using standard error for what is clearly a heterogeneous population is not well justified. Instead, to approximate global subducting sediment we adopt the mean value for 28 sedimentary columns from 26 trenches reported by Plank (2014): 3.9 ± 2.3 (1σ), which is indistinguishable from the average MORB with $\delta^7\text{Li}$ of $+3.7 \pm 1$ (Tomascak et al., 2008). Therefore, the Li isotopes in subducting sediments from other trenches that may be the source of the Li enrichment in arc lavas (Plank, 2014), may not generate measurable or systematic isotopic shifts in the $\delta^7\text{Li}$ of the lavas, thus explaining why arc lavas, in general, do not have $\delta^7\text{Li}$ that is distinct from MORB. As a counter example to the Martinique lavas, arc lavas from Nicaragua are isotopically heavier than MORB, possibly due to the incorporation of high $\delta^7\text{Li}$ sediments in the source region (Chan et al., 2002b; Plank, 2014). The slab Li signatures observed in Lesser Antilles and Nicaragua lavas support the view that the slab derived Li may survive mantle chromatographic processes and reappear in arc lavas.

7.6. Conclusions

1. Lithium isotopes in Martinique lavas are significantly lighter, on average, than those in MORB and other arc lavas. $\delta^7\text{Li}$ in the lavas is independent of SiO_2 , $(\text{La}/\text{Sm})_{\text{N}}$, Y/Li , and radiogenic isotopes, and thus does not appear to be influenced by crustal contamination or igneous differentiation.
2. Subducting sediments to the northeast (Site 543) and southeast (Site 144) of Martinique Island have the lightest Li isotopes (mean $\delta^7\text{Li} = -1.0$) observed for global subducting sediments. The Li isotopic variation is also decoupled from other geochemical indices in these sediments.
3. A $\delta^7\text{Li} - \text{Y}/\text{Li}$ two end-member mixing model indicates that the average Li isotopic composition in the Martinique lavas can be reproduced by ~2% sedimentary input to the mantle source.
4. Slab Li derived from subducted sediments may explain the Li enrichment seen in arc lavas, as suggested by Plank (2014); the MORB-like $\delta^7\text{Li}$ in many arcs may simply reflect the isotopic compositions of the sediments being subducted. Our work demonstrates that if isotopically distinct sediments are subducted, the signature reappears in the arc lavas.

References

- Arevalo, R., McDonough, W.F., 2010. Chemical variations and regional diversity observed in MORB. *Chemical Geology* 271, 70-85.
- Barnes, E.M., Weis, D., Groat, L.A., 2012. Significant Li isotope fractionation in geochemically evolved rare element-bearing pegmatites from the Little Nahanni Pegmatite Group, NWT, Canada. *Lithos* 132–133, 21-36.

- Bebout, G.E., 2014. Chemical and Isotopic Cycling in Subduction Zones, in: The Crust (Rudnick, R.L., Ed.)_Vol. 4 Treatise on Geochemistry (Second Edition)(Holland, H.D., Turekian, K.K., Eds.), Elsevier, Oxford, pp. 703-747.
- Behn, M.D., Kelemen, P.B., Hirth, G., Hacker, B.R., Massonne, H.-J., 2011. Diapirs as the source of the sediment signature in arc lavas. *Nature Geosci* 4, 641-646.
- Benton, L.D., Ryan, J.G., Savov, I.P., 2004. Lithium abundance and isotope systematics of forearc serpentinites, Conical Seamount, Mariana forearc: Insights into the mechanics of slab-mantle exchange during subduction. *Geochemistry, Geophysics, Geosystems* 5, Q08J12.
- Bezard, R., J. P. Davidson, S. Turner, C. G. Macpherson, J. M. Lindsay, and A. J. Boyce (2014), Assimilation of sediments embedded in the oceanic arc crust: myth or reality?, *Earth Planet. Sci. Lett.*, 395(0), 51-60.
- Biju-Duval, B., Le Quellec, P., Mascle, A., Renard, V., Valery, P., 1982. Multibeam bathymetric survey and high resolution seismic investigations on the Barbados ridge complex (eastern Caribbean): A key to the knowledge and interpretation of an accretionary wedge. *Tectonophysics* 86, 275-304.
- Bouman, C., Elliott, T., Vroon, P.Z., 2004. Lithium inputs to subduction zones. *Chemical Geology* 212, 59-79.
- Bouvier, A.-S., Métrich, N., Deloule, E., 2008. Slab-Derived Fluids in the Magma Sources of St. Vincent (Lesser Antilles Arc): Volatile and Light Element Imprints. *Journal of Petrology* 49, 1427-1448.
- Bryant, C.J., Chappell, B.W., Bennett, V.C., McCulloch, M.T., 2004. Lithium isotopic compositions of the New England Batholith: correlations with inferred source rock compositions. *Earth and Environmental Science Transactions of the Royal Society of Edinburgh* 95, 199-214.

- Caciagli, N., Brenan, J.M., McDonough, W.F., Phinney, D., 2011. Mineral–fluid partitioning of lithium and implications for slab–mantle interaction. *Chemical Geology* 280, 384-398.
- Carpentier, M., Chauvel, C., Mattielli, N., 2008. Pb–Nd isotopic constraints on sedimentary input into the Lesser Antilles arc system. *Earth and Planetary Science Letters* 272, 199-211.
- Carpentier, M., Chauvel, C., Maury, R.C., Mattielli, N., 2009. The “zircon effect” as recorded by the chemical and Hf isotopic compositions of Lesser Antilles forearc sediments. *Earth and Planetary Science Letters* 287, 86-99.
- Carpentier, M., Weis, D., Chauvel, C., 2013. Large U loss during weathering of upper continental crust: The sedimentary record. *Chemical Geology*, 340(0): 91-104.
- Castillo, P.R., 2006. An overview of adakite petrogenesis. *Chinese Science Bulletin* 51, 257-268.
- Chan, L.-H., Alt, J.C., Teagle, D.A., 2002a. Lithium and lithium isotope profiles through the upper oceanic crust: a study of seawater–basalt exchange at ODP Sites 504B and 896A. *Earth and Planetary Science Letters* 201, 187-201.
- Chan, L.H., Edmond, J.M., Thompson, G., Gillis, K., 1992. Lithium isotopic composition of submarine basalts: implications for the lithium cycle in the oceans. *Earth and Planetary Science Letters* 108, 151-160.
- Chan, L.-H., Frey, F.A., 2003. Lithium isotope geochemistry of the Hawaiian plume: Results from the Hawaii Scientific Drilling Project and Koolau Volcano. *Geochemistry, Geophysics, Geosystems* 4, 8707.
- Chan, L.-H., Kastner, M., 2000. Lithium isotopic compositions of pore fluids and sediments in the Costa Rica subduction zone: implications for fluid processes and sediment contribution to the arc volcanoes. *Earth and Planetary Science Letters* 183, 275-290.
- Chan, L.-H., Leeman, W.P., Plank, T., 2006. Lithium isotopic composition of marine sediments. *Geochemistry, Geophysics, Geosystems* 7, Q06005.

- Chan, L.H., Leeman, W.P., You, C.F., 2002b. Lithium isotopic composition of Central American volcanic arc lavas: implications for modification of subarc mantle by slab-derived fluids: correction. *Chemical Geology* 182, 293-300.
- Coulon, C., Dupuy, C., Dostal, J., Escalant, M., 1991. Spatial and temporal evolution of the volcanism of Martinique (Lesser Antilles); petrogenetic implications. *Bulletin de la Société Géologique de France* 162, 1037-1047.
- Davidson, J.P., 1983. Lesser Antilles isotopic evidence of the role of subducted sediment in island arc magma genesis. *Nature* 306, 253-256.
- Davidson, J.P., 1985. Mechanisms of contamination in Lesser Antilles island arc magmas from radiogenic and oxygen isotope relationships. *Earth and Planetary Science Letters* 72, 163-174.
- Davidson, J.P., 1986. Isotopic and trace element constraints on the petrogenesis of subduction-related lavas from Martinique, Lesser Antilles. *Journal of Geophysical Research: Solid Earth* 91, 5943-5962.
- Davidson, J.P., 1987. Crustal contamination versus subduction zone enrichment: Examples from the Lesser Antilles and implications for mantle source compositions of island arc volcanic rocks. *Geochimica et Cosmochimica Acta* 51, 2185-2198.
- Davidson, J.P., Harmon, R.S., 1989. Oxygen isotope constraints on the petrogenesis of volcanic arc magmas from Martinique, Lesser Antilles. *Earth and Planetary Science Letters* 95, 255-270.
- Defant, M.J., Drummond, M.S., 1990. Derivation of some modern arc magmas by melting of young subducted lithosphere. *Nature* 347, 662-665.
- Flesch, G.D., Anderson Jr, A.R., Svec, H.J., 1973. A secondary isotopic standard for $^6\text{Li}/^7\text{Li}$ determinations. *International Journal of Mass Spectrometry and Ion Physics* 12, 265-272.
- Gale, A., Dalton, C.A., Langmuir, C.H., Su, Y., Schilling, J.-G., 2013. The mean composition of ocean ridge basalts. *Geochemistry, Geophysics, Geosystems* 14, 489-518.

- Germa, A., 2008. Evolution volcano-tectonique de l'île de la Martinique (arc insulaire des Petites Antilles): nouvelles contraintes géochronologiques et géomorphologiques. Université Paris Sud-Paris XI.
- Germa, A., Quidelleur, X., Labanieh, S., Chauvel, C., Lahitte, P., 2011a. The volcanic evolution of Martinique Island: Insights from K–Ar dating into the Lesser Antilles arc migration since the Oligocene. *Journal of Volcanology and Geothermal Research* 208, 122-135.
- Germa, A., Quidelleur, X., Labanieh, S., Lahitte, P., Chauvel, C., 2010. The eruptive history of Morne Jacob volcano (Martinique Island, French West Indies): Geochronology, geomorphology and geochemistry of the earliest volcanism in the recent Lesser Antilles arc. *Journal of Volcanology and Geothermal Research* 198, 297-310.
- Germa, A., Quidelleur, X., Lahitte, P., Labanieh, S., Chauvel, C., 2011b. The K–Ar Cassinot–Gillot technique applied to western Martinique lavas: A record of Lesser Antilles arc activity from 2Ma to Mount Pelée volcanism. *Quaternary Geochronology* 6, 341-355.
- Hacker, B.R., Kelemen, P.B., Behn, M.D., 2011. Differentiation of the continental crust by relamination. *Earth and Planetary Science Letters* 307, 501-516.
- Halama, R., John, T., Herms, P., Hauff, F., Schenk, V., 2011. A stable (Li, O) and radiogenic (Sr, Nd) isotope perspective on metasomatic processes in a subducting slab. *Chemical Geology* 281, 151-166.
- Halama, R., McDonough, W.F., Rudnick, R.L., Bell, K., 2008. Tracking the lithium isotopic evolution of the mantle using carbonatites. *Earth and Planetary Science Letters* 265, 726-742.
- Halama, R., Savov, I., Rudnick, R., McDonough, W., 2009. Insights into Li and Li isotope cycling and sub-arc metasomatism from veined mantle xenoliths, Kamchatka. *Contrib Mineral Petrol* 158, 197-222.

- Huh, Y., Chan, L.-H., Edmond, J.M., 2001. Lithium isotopes as a probe of weathering processes: Orinoco River. *Earth and Planetary Science Letters* 194, 189-199.
- Huh, Y., Chan, L.-H., Zhang, L., Edmond, J.M., 1998. Lithium and its isotopes in major world rivers: implications for weathering and the oceanic budget. *Geochimica et Cosmochimica Acta* 62, 2039-2051.
- James, R.H., Palmer, M.R., 2000. The lithium isotope composition of international rock standards. *Chemical Geology* 166, 319-326.
- Jordan, T.H., 1975. The present - day motions of the Caribbean plate. *Journal of Geophysical Research* 80, 4433-4439.
- Kısakürek, B., James, R.H., Harris, N.B., 2005. Li and $\delta^7\text{Li}$ in Himalayan rivers: Proxies for silicate weathering? *Earth and Planetary Science Letters* 237, 387-401.
- Kısakürek, B., Widdowson, M., James, R.H., 2004. Behaviour of Li isotopes during continental weathering: the Bidar laterite profile, India. *Chemical Geology* 212, 27-44.
- Labanieh, S., Chauvel, C., Germa, A., Quidelleur, X., 2012. Martinique: a Clear Case for Sediment Melting and Slab Dehydration as a Function of Distance to the Trench. *Journal of Petrology* 53, 2441-2464.
- Labanieh, S., Chauvel, C., Germa, A., Quidelleur, X., Lewin, E., 2010. Isotopic hyperbolas constrain sources and processes under the Lesser Antilles arc. *Earth and Planetary Science Letters* 298, 35-46.
- Liu X.-M., Wanner, C., Rudnick R.L., and McDonough W.F. (2014) Processes controlling $\delta^7\text{Li}$ in rivers illuminated by study of streams and ground waters draining basalts. (in revision, *Earth and Planetary Science Letters*)
- Liu, X.-M., Rudnick, R.L., Hier-Majumder, S., Sirbescu, M.-L.C., 2010. Processes controlling lithium isotopic distribution in contact aureoles: A case study of the Florence County pegmatites, Wisconsin. *Geochemistry, Geophysics, Geosystems* 11, Q08014.

- Liu, X.-M., Rudnick, R.L., McDonough, W.F., Cummings, M.L., 2013. Influence of chemical weathering on the composition of the continental crust: Insights from Li and Nd isotopes in bauxite profiles developed on Columbia River Basalts. *Geochimica et Cosmochimica Acta* 115, 73-91.
- Magna, T., Wiechert, U., Grove, T.L., Halliday, A.N., 2006. Lithium isotope fractionation in the southern Cascadia subduction zone. *Earth and Planetary Science Letters* 250, 428-443.
- Magna, T., Wiechert, U.H., Halliday, A.N., 2004. Low-blank isotope ratio measurement of small samples of lithium using multiple-collector ICPMS. *International Journal of Mass Spectrometry* 239, 67-76.
- Maloney, J.S., Nabelek, P.I., Sirbescu, M.-L.C., Halama, R., 2008. Lithium and its isotopes in tourmaline as indicators of the crystallization process in the San Diego County pegmatites, California, USA. *European Journal of Mineralogy* 20, 905-916.
- Marriott, C.S., Henderson, G.M., Crompton, R., Staubwasser, M., Shaw, S., 2004. Effect of mineralogy, salinity, and temperature on Li/Ca and Li isotope composition of calcium carbonate. *Chemical Geology* 212, 5-15.
- Marschall, H.R., Pogge von Strandmann, P.A.E., Seitz, H.-M., Elliott, T., Niu, Y., 2007. The lithium isotopic composition of orogenic eclogites and deep subducted slabs. *Earth and Planetary Science Letters* 262, 563-580.
- Millot, R., Guerrot, C., Vigier, N., 2004. Accurate and High-Precision Measurement of Lithium Isotopes in Two Reference Materials by MC-ICP-MS. *Geostandards and Geoanalytical Research* 28, 153-159.
- Minster, J.B., Jordan, T.H., 1978. Present - day plate motions. *Journal of Geophysical Research: Solid Earth* (1978-2012) 83, 5331-5354.

- Moore, J.C., Biju-Duval, B., Bergen, J.A., Blackington, G., Claypool, G.E., Cowan, D.S., Duennebier, F., Guerra, R.T., Hemleben, C.H., Hussong, D., 1982. Offscraping and underthrusting of sediment at the deformation front of the Barbados Ridge: Deep Sea Drilling Project Leg 78A. *Geological Society of America Bulletin* 93, 1065-1077.
- Moriguti, T., Nakamura, E., 1998. Across-arc variation of Li isotopes in lavas and implications for crust/mantle recycling at subduction zones. *Earth and Planetary Science Letters* 163, 167-174.
- Moriguti, T., Shibata, T., Nakamura, E., 2004. Lithium, boron and lead isotope and trace element systematics of Quaternary basaltic volcanic rocks in northeastern Japan: mineralogical controls on slab-derived fluid composition. *Chemical Geology* 212, 81-100.
- Nesbitt, H.W., Young, G.M., 1982. Early Proterozoic climates and plate motions inferred from major element chemistry of lutites. *Nature* 299, 715-717.
- Penniston-Dorland, S.C., Bebout, G.E., Pogge von Strandmann, P.A., Elliott, T., Sorensen, S.S., 2012. Lithium and its isotopes as tracers of subduction zone fluids and metasomatic processes: Evidence from the Catalina Schist, California, USA. *Geochimica et Cosmochimica Acta* 77, 530-545.
- Penniston-Dorland, S.C., Sorensen, S.S., Ash, R.D., Khadke, S.V., 2010. Lithium isotopes as a tracer of fluids in a subduction zone mélange: Franciscan Complex, CA. *Earth and Planetary Science Letters* 292, 181-190.
- Pistiner, J.S., Henderson, G.M., 2003. Lithium-isotope fractionation during continental weathering processes. *Earth and Planetary Science Letters* 214, 327-339.
- Plank, T., 2014. The Chemical Composition of Subducting Sediments, in: The Crust (Rudnick, R.L., Ed.)_Vol. 4 Treatise on Geochemistry (Second Edition)(Holland, H.D., Turekian, K.K., Eds.). Elsevier, Oxford, Elsevier, Oxford, pp. 607-629.

- Pogge von Strandmann, P.A., Burton, K.W., James, R.H., van Calsteren, P., Gislason, S.R., Mokadem, F., 2006. Riverine behaviour of uranium and lithium isotopes in an actively glaciated basaltic terrain. *Earth and Planetary Science Letters* 251, 134-147.
- Pogge von Strandmann, P.A.E., Elliott, T., Marschall, H.R., Coath, C., Lai, Y.-J., Jeffcoate, A.B., Ionov, D.A., 2011. Variations of Li and Mg isotope ratios in bulk chondrites and mantle xenoliths. *Geochimica et Cosmochimica Acta* 75, 5247-5268.
- Qiu, L., Rudnick, R.L., Ague, J.J., McDonough, W.F., 2011a. A lithium isotopic study of sub-greenschist to greenschist facies metamorphism in an accretionary prism, New Zealand. *Earth and Planetary Science Letters* 301, 213-221.
- Qiu, L., Rudnick, R.L., McDonough, W.F., Bea, F., 2011b. The behavior of lithium in amphibolite- to granulite-facies rocks of the Ivrea–Verbano Zone, NW Italy. *Chemical Geology* 289, 76-85.
- Qiu, L., Rudnick, R.L., McDonough, W.F., Merriman, R.J., 2009. Li and $\delta^7\text{Li}$ in mudrocks from the British Caledonides: Metamorphism and source influences. *Geochimica et Cosmochimica Acta* 73, 7325-7340.
- Richter, F., Watson, B., Chaussidon, M., Mendybaev, R., Ruscitto, D., 2014. Lithium isotope fractionation by diffusion in minerals. Part 1: Pyroxenes. *Geochimica et Cosmochimica Acta* 126, 352-370.
- Rosner, M., Ball, L., Peucker-Ehrenbrink, B., Blusztajn, J., Bach, W., Erzinger, J., 2007. A Simplified, Accurate and Fast Method for Lithium Isotope Analysis of Rocks and Fluids, and $\delta^7\text{Li}$ Values of Seawater and Rock Reference Materials. *Geostandards and Geoanalytical Research* 31, 77-88.
- Rudnick, R.L., Tomascak, P.B., Njo, H.B., Gardner, L.R., 2004. Extreme lithium isotopic fractionation during continental weathering revealed in saprolites from South Carolina. *Chemical Geology* 212, 45-57.

- Ryan, J.G., Chauvel, C., 2014. The Subduction-Zone Filter and the Impact of Recycled Materials on the Evolution of the Mantle, in: (Carlson, R.W., Ed.) *The Mantle*, Vol. 3 Treatise on Geochemistry (Second Edition)(Holland, H.D., Turekian, K.K., Eds.), Elsevier, Oxford, pp. 479-508.
- Ryan, J.G., Langmuir, C.H., 1987. The systematics of lithium abundances in young volcanic rocks. *Geochimica et Cosmochimica Acta* 51, 1727-1741.
- Salters, V.J., Stracke, A., 2004. Composition of the depleted mantle. *Geochemistry, Geophysics, Geosystems* 5.
- Schmidt, M.W., Poli, S., 2014. Devolatilization During Subduction, in: The Crust (Rudnick, R.L., Ed.)_Vol. 4 Treatise on Geochemistry (Second Edition)(Holland, H.D., Turekian, K.K., Eds.), Elsevier, Oxford, pp. 669-701.
- Scholz, F., Hensen, C., De Lange, G.J., Haeckel, M., Liebetrau, V., Meixner, A., Reitz, A., Romer, R.L., 2010. Lithium isotope geochemistry of marine pore waters—insights from cold seep fluids. *Geochimica et Cosmochimica Acta* 74, 3459-3475.
- Schuessler, J.A., Schoenberg, R., Sigmarsson, O., 2009. Iron and lithium isotope systematics of the Hekla volcano, Iceland — Evidence for Fe isotope fractionation during magma differentiation. *Chemical Geology* 258, 78-91.
- Seitz, H.-M., Brey, G.P., Lahaye, Y., Durali, S., Weyer, S., 2004. Lithium isotopic signatures of peridotite xenoliths and isotopic fractionation at high temperature between olivine and pyroxenes. *Chemical Geology* 212, 163-177.
- Smith, T.E., Thirlwall, M.F., Macpherson, C., 1996. Trace Element and Isotope Geochemistry of the Volcanic Rocks of Bequia, Grenadine Islands, Lesser Antilles Arc: a Study of Subduction Enrichment and Intra-crustal Contamination. *Journal of Petrology* 37, 117-143.
- Syracuse, E.M., Abers, G.A., 2006. Global compilation of variations in slab depth beneath arc volcanoes and implications. *Geochemistry, Geophysics, Geosystems* 7, Q05017.

- Syracuse, E.M., van Keken, P.E., Abers, G.A., 2010. The global range of subduction zone thermal models. *Physics of the Earth and Planetary Interiors* 183, 73-90.
- Teng, F.-Z., McDonough, W.F., Rudnick, R.L., Dalpé, C., Tomascak, P.B., Chappell, B.W., Gao, S., 2004. Lithium isotopic composition and concentration of the upper continental crust. *Geochimica et Cosmochimica Acta* 68, 4167-4178.
- Teng, F.-Z., McDonough, W.F., Rudnick, R.L., Walker, R.J., 2006. Diffusion-driven extreme lithium isotopic fractionation in country rocks of the Tin Mountain pegmatite. *Earth and Planetary Science Letters* 243, 701-710.
- Teng, F.-Z., McDonough, W.F., Rudnick, R.L., Wing, B.A., 2007. Limited lithium isotopic fractionation during progressive metamorphic dehydration in metapelites: a case study from the Onawa contact aureole, Maine. *Chemical geology* 239, 1-12.
- Teng, F.-Z., Rudnick, R.L., McDonough, W.F., Gao, S., Tomascak, P.B., Liu, Y., 2008. Lithium isotopic composition and concentration of the deep continental crust. *Chemical Geology* 255, 47-59.
- Teng, F.-Z., Rudnick, R.L., McDonough, W.F., Wu, F.-Y., 2009. Lithium isotopic systematics of A-type granites and their mafic enclaves: Further constraints on the Li isotopic composition of the continental crust. *Chemical Geology* 262, 370-379.
- Thirlwall, M., Smith, T., Graham, A., Theodorou, N., Hollings, P., Davidson, J., Arculus, R., 1994. High field strength element anomalies in arc lavas: source or process? *Journal of Petrology* 35, 819-838.
- Thirlwall, M.F., Graham, A.M., 1984. Evolution of high-Ca, high-Sr C-series basalts from Grenada, Lesser Antilles: the effects of intra-crustal contamination. *Journal of the Geological Society* 141, 427-445.
- Thirlwall, M.F., Graham, A.M., Arculus, R.J., Harmon, R.S., Macpherson, C.G., 1996. Resolution of the effects of crustal assimilation, sediment subduction, and fluid transport

- in island arc magmas: Pb-Sr-Nd-O isotope geochemistry of Grenada, Lesser Antilles. *Geochimica et Cosmochimica Acta* 60, 4785-4810.
- Tian, S., Hou, Z., Su, A., Hou, K., Hu, W., Li, Z., Zhao, Y., Gao, Y., Li, Y., Yang, D., Yang, Z., 2012. Separation and Precise Measurement of Lithium Isotopes in Three Reference Materials Using Multi Collector-Inductively Coupled Plasma Mass Spectrometry. *Acta Geologica Sinica - English Edition* 86, 1297-1305.
- Tomascak, P.B., Langmuir, C.H., le Roux, P.J., Shirey, S.B., 2008. Lithium isotopes in global mid-ocean ridge basalts. *Geochimica et Cosmochimica Acta* 72, 1626-1637.
- Tomascak, P.B., Ryan, J.G., Defant, M.J., 2000. Lithium isotope evidence for light element decoupling in the Panama subarc mantle. *Geology* 28, 507-510.
- Tomascak, P.B., Tera, F., Helz, R.T., Walker, R.J., 1999. The absence of lithium isotope fractionation during basalt differentiation: new measurements by multicollector sector ICP-MS. *Geochimica et Cosmochimica Acta* 63, 907-910.
- Tomascak, P.B., Widom, E., Benton, L.D., Goldstein, S.L., Ryan, J.G., 2002. The control of lithium budgets in island arcs. *Earth and Planetary Science Letters* 196, 227-238.
- Van Soest, M.C., Hilton, D.R., Macpherson, C.G., Matthey, D.P., 2002. Resolving sediment subduction and crustal contamination in the Lesser Antilles Island Arc: a combined He-O-Sr isotope approach. *Journal of Petrology* 43, 143-170.
- Westbrook, G., Smith, M., 1983. Long décollements and mud volcanoes: Evidence from the Barbados Ridge Complex for the role of high pore-fluid pressure in the development of an accretionary complex. *Geology* 11, 279-283.
- Westbrook, G., Smith, M., Peacock, J., Poulter, M., 1982. Extensive underthrusting of undeformed sediment beneath the accretionary complex of the Lesser Antilles subduction zone.
- Westercamp, D., Andreieff, P., Bouysse, P., Cottez, S., Battistini, R., 1989. Martinique. Carte géologique a 1, 000.

- White, W.M., Dupré, B., 1986. Sediment subduction and magma genesis in the Lesser Antilles: isotopic and trace element constraints. *Journal of Geophysical Research* 91, 5927-5941.
- White, W.M., Dupré, B., Vidal, P., 1985. Isotope and trace element geochemistry of sediments from the Barbados Ridge-Demerara Plain region, Atlantic Ocean. *Geochimica et Cosmochimica Acta* 49, 1875-1886.
- Wimpenny, J., Gíslason, S.R., James, R.H., Gannoun, A., Pogge Von Strandmann, P.A.E., Burton, K.W., 2010. The behaviour of Li and Mg isotopes during primary phase dissolution and secondary mineral formation in basalt. *Geochimica et Cosmochimica Acta* 74, 5259-5279.
- Wunder, B., Meixner, A., Romer, R.L., Heinrich, W., 2006. Temperature-dependent isotopic fractionation of lithium between clinopyroxene and high-pressure hydrous fluids. *Contrib Mineral Petrol* 151, 112-120.
- Zack, T., Tomascak, P.B., Rudnick, R.L., Dalpé, C., McDonough, W.F., 2003. Extremely light Li in orogenic eclogites: The role of isotope fractionation during dehydration in subducted oceanic crust. *Earth and Planetary Science Letters* 208, 279-290.

Appendix

1. Analytical method for Li isotopic measurement

Lithium isotopic measurements were conducted at the Geochemistry Laboratory of the University of Maryland, College Park. The sample powders were dissolved in a ~3:1 mixture of concentrated HF-HNO₃ in Savillex screw-top beakers overnight on a hot plate at T~120°C, followed by replenishment of the dried residua with concentrated HNO₃ overnight and dried again, the picked up in concentrated HCl till solutions were clear. Then the solutions were dried down and re-dissolved in 4 M HCl, and ultrasonic-bathed before column chemistry.

One mL 4 M HCl aliquot was loaded on the first column. Lithium was eluted through three sets of columns, each containing 1 mL cation-exchange resin (BioRad AG50W- \times 8) following the first three column procedures described by Moriguti and Nakamura (1998). For the first column, Li was eluted with 9 mL 2.5 M HCl; for the second column, Li was eluted with 30 mL 0.15 M HCl and for the third column, Li was eluted with 16 mL 30% ethanol 0.5 M HCl mixture. Column # 3 was repeated once to achieve better Li-Na separation.

Lithium isotopes were analyzed using a Multi-Collector-Inductively Coupled Plasma-Mass Spectrometer (MC-ICP-MS) from the Nu-Plasma. Purified Li solutions (\sim 50 ppb Li in 2% HNO₃ solutions) were introduced into the Ar plasma using an auto-sampler (ASX-100 Cetac Technologies) through a desolvating nebulizer (Aridus Cetac Technologies) fitted with a PFA spray chamber and micro-nebulizer (Elemental Scientific Inc.). The solution uptake rate is 50 μ L/min. Prior to Li isotopic measurements, the Na/Li voltage ratio of each solution was evaluated semi-quantitatively with the mass spectrometer. Solutions with a Na/Li voltage ratio > 5 were reprocessed through column chemistry. The two Li isotopes, ^7Li and ^6Li , were measured simultaneously in two opposing Faraday cups (H6 and L5). Each unknown analysis was bracketed before and after by measurement of the L-SVEC standard (Flesch et al., 1973) having similar Li concentration (within \pm 50%). Two other Li standards, Li-UMD-1 (a purified Li solution from Alfa Aesar) and IRMM-016 (Qi et al., 1997), were routinely analyzed during the course of each analytical session. We typically measured a $^7\text{Li}^+$ beam voltage of 1-2 volts (10^{11} ohm resistor). The procedural blank is \sim 10 mV on mass 7. Our in-run precision on 7/6 ratio measurements is $< \pm 0.2\%$ for two blocks of 20 ratios each. The external precision, based on 2σ of repeat runs of pure Li standard solutions, is better than $\pm 1.0\%$.

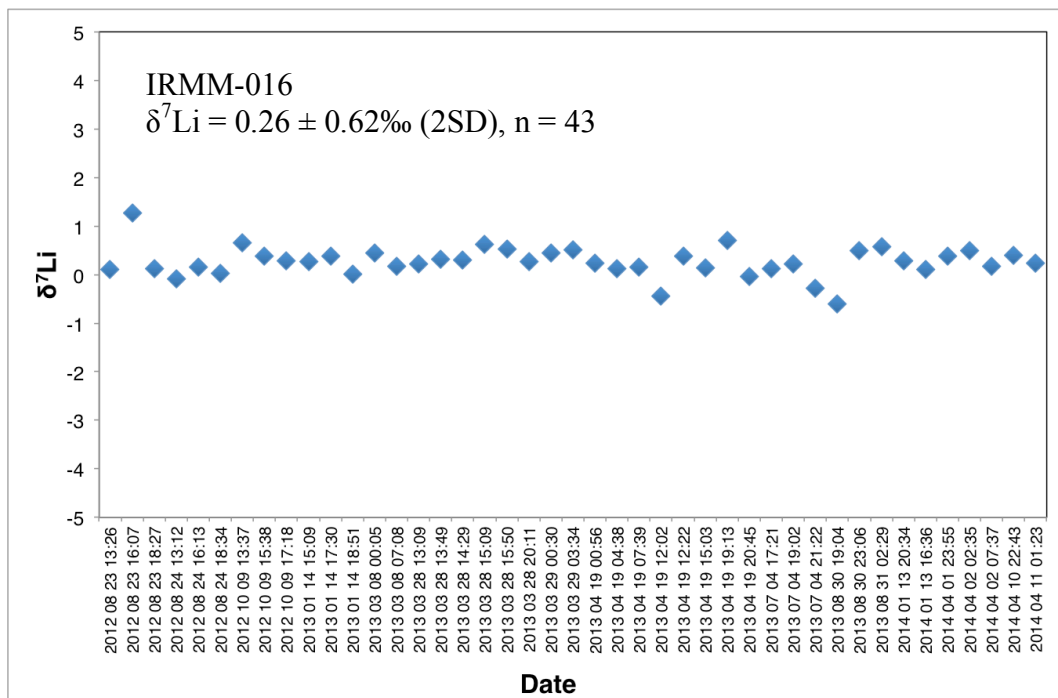
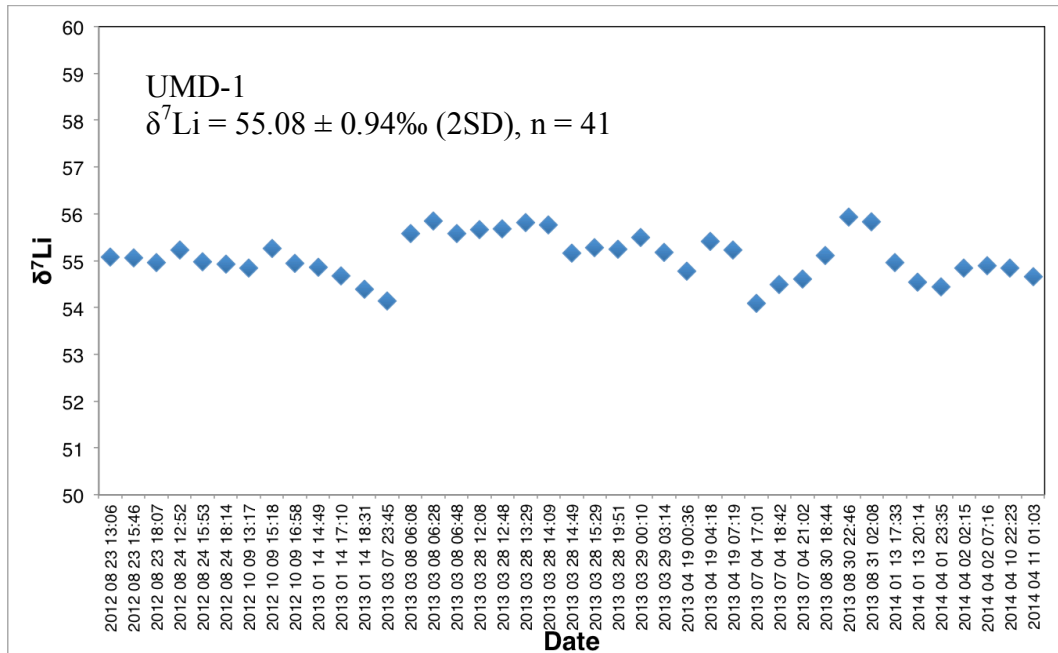


Fig. A7.1. Long-term analyses of Li reference materials UMD-1 and IRMM-016.

2. The lack of correlation between $\delta^7\text{Li}$ and Y/Li and other geochemical indices in the lavas

Although sediments tend to homogenized during subduction, some variability might survive the subduction filter for a number of reasons: (1) all lithologies should not melt or dehydrate in the same way and some might be involved more than others in the source; (2) in Carpentier et al. (2008), they showed clearly that the subducted black shales could be involved in proportions higher than they exist in the average sediment pile (see their figure 6).

In our case, Li and Y behave very differently and are mobilized and transported via different agents. Yttrium is also significantly retained by garnet in the source. It is difficult to constrain the timescale and spatial scale of homogenization of these two elements in the source. Decoupling between other fluid mobile and immobile element pairs, such as Sr and Th, is commonly seen in arc lavas. For these reasons, we are convinced that variability in Li/Y and Li isotopes could occur within an island arc system, at least at local scales.

Given the large variation in Y/Li and $\delta^7\text{Li}$, and the lack of relationship between them in the subducting sediments, mixing between depleted mantle materials and these sediments may not produce lavas with convincing Y/Li- $\delta^7\text{Li}$ correlation, if these sediments are not well homogenized, or Y and Li are decoupled, in the source region. We simulated a random mixing scenario in the source region using the Monte Carlo scheme with 100,000 reiterations. Here we assumed 0-5% sedimentary input. Yttrium contribution from sedimentary components was set to be zero as Y is largely retained by garnet in the slab. Lithium isotopic compositions of the sediments were taken from the sediment dataset in this work. The uncertainty in Li isotopic compositions of all components is +/- 1 permil. For this reason, the correlations between Li isotopes and other geochemical indices, such as radiogenic isotopes, are generally poor.

References

- Carpentier, M., Chauvel, C., Mattielli, N., 2008. Pb–Nd isotopic constraints on sedimentary input into the Lesser Antilles arc system. *Earth and Planetary Science Letters* 272, 199-211.
- Flesch, G.D., Anderson Jr, A.R., Svec, H.J., 1973. A secondary isotopic standard for $^6\text{Li}/^7\text{Li}$ determinations. *International Journal of Mass Spectrometry and Ion Physics* 12, 265-272.
- Moriguti, T., Nakamura, E., 1998. Across-arc variation of Li isotopes in lavas and implications for crust/mantle recycling at subduction zones. *Earth and Planetary Science Letters* 163, 167-174.
- Qi, H.P., Taylor, P.D.P., Berglund, M., De Bièvre, P., 1997. Calibrated measurements of the isotopic composition and atomic weight of the natural Li isotopic reference material IRMM-016. *International Journal of Mass Spectrometry and Ion Processes* 171, 263-268.

Chapter 8. Mechanism of Li diffusion in zircon

[1]. Ming Tang designed the study and carried the analyses assisted by Yulia Goreva and Maitrayee Bose. Dustin Trail supervised the experimental work. Roberta Rudnick and William McDonough contributed to the development of this project, provided funding, and supervised the entire study.

Abstract

Li isotopes in zircon can potentially be used to infer magmatic sources and/or as a speedometer for magmatic and metamorphic processes. Use of $\delta^7\text{Li}$ in zircon is, however, impeded by uncertainty regarding the degree to which Li diffuses in zircon. I studied natural and synthetic zircons to identify the mechanism(s) of Li diffusion in zircon and the possible role of charge coupling between Li and REE+Y.

High spatial resolution ToF SIMS imaging identified sharp Li concentration gradients and NanoSIMS Li isotope profiled along these gradients in natural zircons show that $\delta^7\text{Li}$ variations ($\geq 20\text{‰}$) are prevalent in natural zircons. The range of $\delta^7\text{Li}$ measured within each zircon grain is significantly greater than that observed in all igneous and sedimentary rocks.

I modeled Li in a TTG zircon (C88_29_7_6) that shows a simple Li concentration gradient coupled with a core-rim texture, ideal for studying the Li diffusion mechanism(s). This zircon was previously characterized for its Li isotopic and trace element compositions using conventional SIMS. Within the rim of this zircon, the Li isotope profile correlates with Li/Y ratio and anti-correlates with Li concentration, suggesting an important role for Y (and REE, given their liked behavior due to size and valence) in controlling Li activity and, hence, diffusion. This feature, together with the continuous Li diffusion profiles (dipping $\delta^7\text{Li}$) across the sharp Li concentration boundary, is consistent with the presence of both slow diffusing Li (charge coupled with REE+Y) and fast diffusing Li (charge coupled with other

chemical species) in zircon. During Li diffusion, charge coupling between Li and REE+Y takes place as a substitution reaction, in which Li ions substitute for other chemical species that couple with REE and Y in the zircon lattice. We argue that the ratio of slow/fast-diffusing Li is determined by the numbers of REE+Y coupling sites vs. other charge coupling sites for Li and a substitution coefficient.

8.1. Introduction: Li in zircon as a tracer of magmatic sources or a geospeedometer?

Lithium and its isotopes (^6Li and ^7Li) have seen a wide range of applications in geoscience in the past two decades, including fluid-rock interaction (Liu et al., 2010; Marks et al., 2007; Penniston-Dorland et al., 2010; Teng et al., 2006), geospeedometry in high temperature systems (Gallagher and Elliott, 2009; Gao et al., 2011; Jeffcoate et al., 2007; John et al., 2012; Lai et al., 2015; Parkinson et al., 2007; Teng et al., 2006), crustal recycling into the mantle (Agostini et al., 2008; Elliott et al., 2004; Halama et al., 2008; Halama et al., 2009; Tang et al., 2014; Tomascak et al., 2002; Zack et al., 2003) and chemical weathering of the continental crust (Huh et al., 2001; Kısakürek et al., 2004; Liu et al., 2015; Rudnick et al., 2004; Ryu et al., 2014; Vigier et al., 2008; von Strandmann et al., 2012).

Measurement of Li isotopes in zircon has been suggested to track chemical weathering during the earliest Earth history (Ushikubo et al., 2008). Ushikubo et al. (2008) and Bouvier et al. (2012) argued that Li atoms are charge coupled with slow-diffusing REE and Y atoms in the zircon lattice so that zircon is a “closed box” for Li and can preserve the initial magmatic Li isotopic signatures. This assumption was later challenged by experimental studies (Cherniak and Watson, 2010), which showed that Li can diffuse rapidly in zircon under crustal P-T conditions. Rather than using zircon Li to track magmatic sources, the work by Cherniak and Watson (2010) suggested the possibility of using Li in zircon as a magmatic

and metamorphic speedometer, with the first attempt seen in Trail et al. (2016). However, the experimental studies by Cherniak and Watson (2010) failed to clarify the effect of REE,Y-Li charge coupling on Li diffusion in zircon because the in-diffusion Li flux overwhelmed the REE and Y in the zircon they studied. Therefore, it is still unclear whether these experimentally determined Li diffusivity apply to natural zircons.

8.1.1. Mechanisms of Li isotopic fractionation

Lithium isotopes are readily fractionated by equilibrium fractionation at the Earth's surface because of the relatively large mass difference between ${}^6\text{Li}$ and ${}^7\text{Li}$ (17%). They can also be fractionated at high temperatures due to Li diffusion. Li isotopic compositions are typically reported in delta notation ($\delta^7\text{Li} = (({}^7\text{Li}/{}^6\text{Li})_{\text{sample}} / ({}^7\text{Li}/{}^6\text{Li})_{\text{L-SVEC}}) * 1000$).

Significant Li isotopic fractionation is generated during both subaqueous and subaerial weathering of silicate rocks (Bouman et al., 2004; Chan et al., 1992; Huh et al., 1998; Kısakürek et al., 2005; Kısakürek et al., 2004; Liu et al., 2013; Pistiner and Henderson, 2003; Pogge von Strandmann et al., 2006; Rudnick et al., 2004; Wimpenny et al., 2010). The net effect is that the aqueous phase becomes enriched in ${}^7\text{Li}$ relative to the rock or sediment that has been weathered. Therefore, the Li isotopic compositions of rivers ($\delta^7\text{Li} = +6$ to $+32$, (Huh et al., 1998)) and seawater ($\delta^7\text{Li} = +31$, Millot et al. (2004)) are significantly heavier than those of the continental crust ($\delta^7\text{Li} \sim +1$, Teng et al. (2008)) and mantle ($\delta^7\text{Li} \sim +4$, Seitz et al. (2004)). Moreover, the upper continental crust ($\delta^7\text{Li} = 0 \pm 2$ (1σ), Teng et al. (2004)) is lighter than the upper mantle, the latter of which is inferred to have the same composition as fresh MORB ($+3.7 \pm 1.0$ (1σ), Tomascak et al. (2008)). The isotopically lighter upper crust has been attributed to reflect a chemical weathering signature. $\delta^7\text{Li}$ in seawater, as recorded in planktonic foraminifera, has been used to trace continental weathering through the Cenozoic

(Misra and Froelich, 2010). However, this record only covers the latest ~70 Ma due to diagenetic overprinting of foraminifera.

At magmatic temperatures, Li isotopes can fractionate because ^6Li diffuses faster than ^7Li , and such an effect can be preserved if cooling is rapid enough. Richter et al. (2003) first documented diffusion-induced Li isotopic fractionation in an experimental laboratory study with a Li isotopic profile across the interface of two compositionally distinct end-member lithologies, basalt and rhyolite. Later, Lundstrom et al. (2005) reported diffusive fractionation of Li isotopes in the Trinity Ophiolite. Teng et al. (2006) and Liu et al. (2010) studied the country rocks intruded by pegmatites, and found large Li isotopic variation over tens of meters and extremely low $\delta^7\text{Li}$ (down to -20‰) values, which they interpreted as a result of diffusion-driven fractionation of Li isotopes. Jeffcoate et al. (2007) and Parkinson et al. (2007) observed diffusive fractionation of Li isotopes on a grain scale. These studies demonstrated that Li isotopes could be fractionated over tens of permil by diffusion.

8.1.2. Li isotopes in zircons

Zircon, known for its refractory nature, is the oldest known terrestrial material accessible on Earth. If zircon faithfully records magmatic Li isotopic signatures, it may extend the Li isotope probe of weathering intensity to the Hadean, a time from which time other crustal materials are absent. Ushikubo et al. (2008) reported large $\delta^7\text{Li}$ variations (> 30 , Fig. 8.1) in the Hadean Jack Hills zircons. Some of the zircons analyzed showed extremely low $\delta^7\text{Li}$ (down to -20). These authors interpreted this signature to reflect incorporation of an intensively weathered component into the source region of the granite that crystallized the zircons. Large zircon $\delta^7\text{Li}$ variation was also observed by Bouvier et al. (2012), and they also considered it to reflect the signatures of the magma source materials.

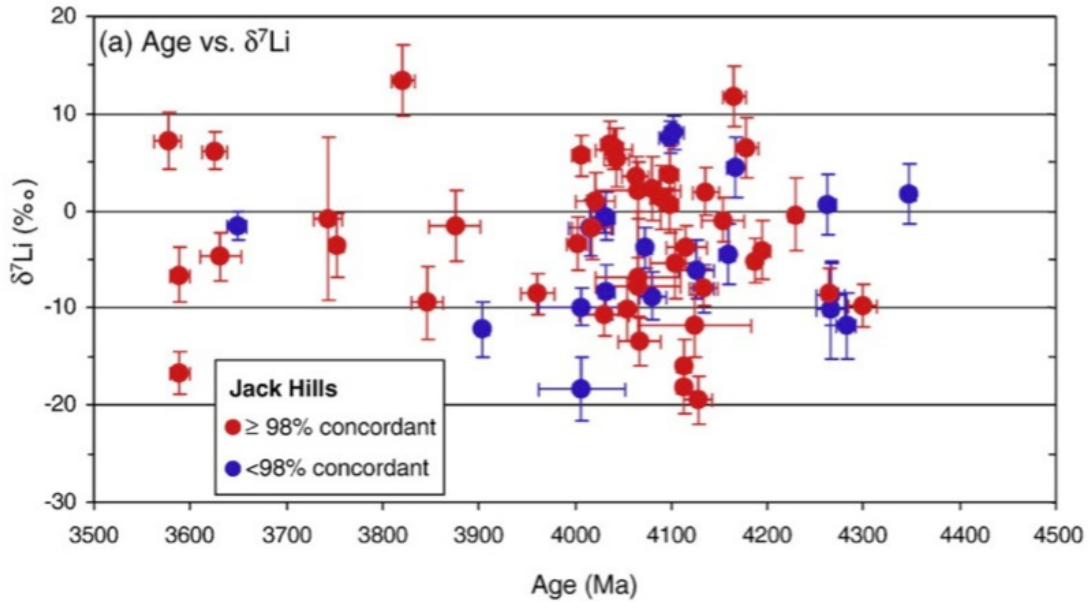


Fig. 8.1. Li isotopic compositions of Jack Hills zircons. Figure from Ushikubo et al. (2008).

One of the assumptions underlying Ushikubo et al. and Bouvier et al.'s interpretations is that Li isotopes do not fractionate during crystallization of zircon from magma and following zircon crystallization. A number of studies have revealed that equilibrium Li isotopic fractionation is limited during metamorphic dehydration, partial melting and fractional crystallization (Marschall et al., 2007; Qiu et al., 2011a; Qiu et al., 2011b; Qiu et al., 2009; Teng et al., 2007; Teng et al., 2009; Tomascak et al., 1999). However, it remains unclear whether or not the Li isotopes in zircon can be fractionated during zircon growth or metamorphic events. If the assumptions of Ushikubo et al. and Bouvier et al. were valid, one would expect to see a similar spread in Li isotopic compositions between igneous zircons and igneous rocks, as is the case with O isotopes (Fig. 8.2). However, the range of $\delta^7\text{Li}$ measured in zircons largely exceeds that of igneous rocks (Fig. 8.2). Moreover, the discrepancy between rocks and minerals mainly results from the extremely negative $\delta^7\text{Li}$ values in the Jack Hills zircons. Such low $\delta^7\text{Li}$ has only been observed in highly weathered regoliths

(Rudnick et al., 2004) and in rocks and minerals that experienced kinetic fractionation associated with Li diffusion (e.g., Jeffcoate et al., 2007; Teng et al., 2006).

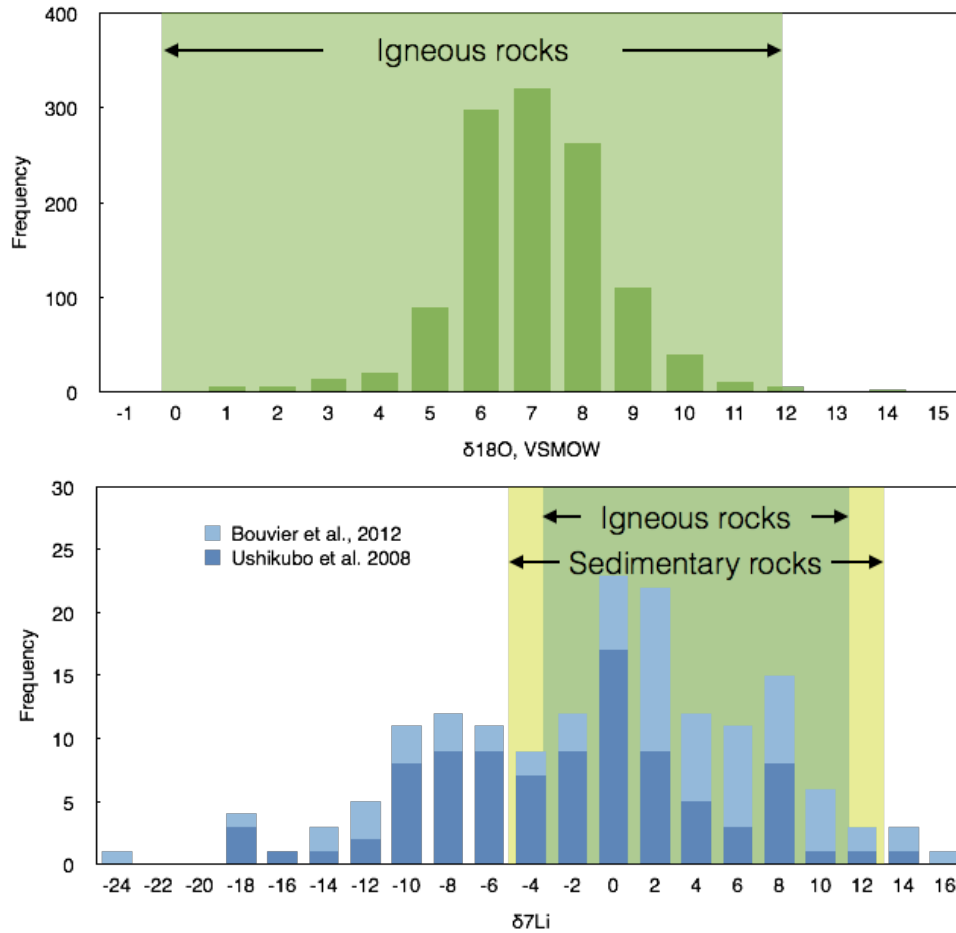


Fig. 8.2. Oxygen and Li isotopic compositions in zircons. Zircon O isotope data from Valley et al. (2005); Zircon Li isotope data from Ushikubo et al. (2008) and Bouvier et al. (2012).

Another interesting observation is that Li isotopes are highly heterogeneous in reference zircons. $\delta^7\text{Li}$ values vary over 7 ‰ in zircon 91500, Plešovice, TEMORA 2 and BR266 (Li et al., 2011). These variations are significant given that the claimed 2σ analytical uncertainty is better than 2 ‰ (obtained on zircon M257 with 0.86 ± 0.22 ppm Li, Li et al. (2011). Li et al. (2011) also noticed that these reference zircons also have heterogeneous Li concentrations [Li] (Table 8.1). On the other hand, the Hf and O isotopes have been demonstrated to be homogeneous within these reference zircons. These phenomena seem to be counterintuitive

in that, if Li isotopes diffuse considerably faster than O and Hf, they should be readily homogenized during melting and/or magma mixing processes.

Table 8.1. Li isotope and concentration data for reference zircons (data from Li et al., 2011).

Zircon	$\delta^7\text{Li}$ (‰)	[Li], ppm
BR266	-1.0 ~ 6.4	0.35 ~ 1.1
Plešovice	-7.7 ~ 2.8	0.52 ~ 8.0
91500	-1.9 ~ 5.3	0.40 ~ 2.3
TEMORA 2	-12.1 ~ 2.8	0.03 ~ 0.50

Recently, Cherniak and Watson (2010) measured the Li diffusion coefficient in a natural zircon (a reference zircon from the Mud Tank carbonatite). They placed a Li source in contact with a slice of zircon for some amount of time at various temperatures to allow Li to diffuse from the source to the zircon. They found that, although Li diffuses significantly slower in zircon than in other minerals, it is among the fastest diffusing elements in zircon. Their experiments also indicated that Li diffusivity in zircon has little anisotropy, and is not affected by the presence of fluid. In order to test whether REEs inhibit the diffusion of Li through coupled substitution (give the coupled substitution equation here), they added Dy to their Li source in one of the experiments and observed no difference in the measured Li diffusion coefficient. However, as these authors noted, Dy did not diffuse into the zircon, so their Dy-bearing source experiment did not evaluate the effect of REE + Y on Li diffusion in zircon. Nevertheless, their experiments indicate that Li may diffuse rapidly in zircon when there is insufficient REE + Y to couple with Li.

My work investigates the REE+Y-Li coupling effect on Li diffusion in zircon. My combined studies of natural and synthetic zircons, with an emphasis on high-resolution Li isotope profile measurements, elucidates whether and how Li diffuses in zircon under crustal conditions.

8.2. Samples

The zircons studied here include two zircons from a Tanzania lower crustal granulite xenolith (SMZ_04 and LB04_19_02), three zircons from Archean Tonalite-Trondhjemite-Granodiorite (TTGs) (DD81_32_6_8, C88_29_7_6 and DD86_25a_3_6), two zircons from a sanukitoid (DD96_10_4_8 and DD96_4_5_11) and one synthetic zircon (ZLi_19_1). The two zircons from the granulite xenolith have very low Li contents (<0.2 ppm) and were only used to develop the ToF SIMS (Time of Flight Secondary Ion Mass Spectrometer) imaging technique. All natural zircons were imaged by ToF SIMS for multi-element distributions including those of Li and Y. The NanoSIMS Li isotope profiling was conducted on all three TTG zircons, one sanukitoid zircon (DD96_4_5_11) and the synthetic zircon. The TTG and sanukitoid zircons were previously characterized by CL (cathodoluminescence) imaging and SIMS spot analyses for their Li isotope and trace element compositions (Bouvier et al., 2012; Ushikubo et al., 2008).

8.3. Methods

8.3.1. ToF SIMS imaging

Ion imaging was performed using the ION TOF GmbH IV TOF-SIMS instrument at the Smithsonian Institution. Surface pre-sputtering was done using a 30 nA Ar target current in a 500 $\mu\text{m} \times 500 \mu\text{m}$ square area. An electron gun was used for charge compensation at the sputtering site. During analyses, a 25KeV Bi⁺ source was used as the primary beam in two different modes:

(1). For whole grain imaging, I used the “High Current Bunched” mode with high mass/low spatial resolution. The pulsed target current was 0.3 pA and mass resolution

($M/\Delta M$) was ~ 8000 at 30 amu. The spot size was $\sim 2 \mu\text{m}$. The image raster size varied with the imaged grain size with an image resolution of 256×256 pixels;

(2). For local (core-rim boundary) imaging, I used the “Burst Alignment” mode with high spatial/low mass resolution to obtain a lateral resolution of 200–400 nm and mass resolution of 1 amu. The pulsed target current was 0.05 pA. Extra long 200 ns pulses were used to enhance the Li signal. Image raster size was $100 \times 100 \mu\text{m}$ with an image resolution of 512×512 pixels.

8.3.2. NanoSIMS isotope profiling

The Cameca NanoSIMS 50L at Arizona State University Chemistry and Biochemistry SIMS lab was used to measure the Li isotope profiles across the core-rim boundaries, and over oscillatory and sector zones in zircons where Li gradients had been documented by ToF SIMS imaging. Each line profile is composed of 20–40 spot analyses. For each spot analysis, a ~ 200 pA primary O^- beam was used to pre-sputter the measurement site, and then a ~ 80 pA primary O^- beam of $\sim 1 \mu\text{m}$ diameter was used for acquisition. The total acquisition sputtering time for each spot analysis varied from 1,200 to 3,000 s, depending on the counts of Li isotopes. ^6Li , ^7Li , ^{30}Si and ^{89}Y were collected by four detectors simultaneously during each analysis.

8.4. Results

8.4.1. ToF SIMS imaging

The two zircons from the Tanzania lower crust xenoliths feature core-rim structures visible in CL (Fig. 8.3) that correspond to the chemical gradients revealed by ToF SIMS imaging (Fig. 8.4). Zircon SMZ_04 shows significantly higher Li concentration in the core

than in the rim but much less differences in Y concentrations across the core-rim boundary (Fig. 8.4). Zircon LB04_19_02 shows a similar phenomenon, with the core enriched in Li (Fig. 8.4) but no difference in Y concentration between the core and rim. These two zircon grains show no correlation between the concentrations of Li and other elements, especially REEs (assumed to follow Y). The high spatial resolution mapping reveals that [Li] zoning is sharp across the core-rim boundary in zircon LB04_19_02 and is inconsistent with common diffusion patterns, which tend to show concentration gradients. LA-ICPMS analyses (UMD) showed that Li concentration in the core of LB04_19_02 grain is on the order of 0.1 ppm, while the rim contains on the order of 0.06 ppm, which is at the detection limit for our ICP-MS. The ion images demonstrated the capability of ToF SIMS in mapping trace Li in zircon with high spatial resolution.

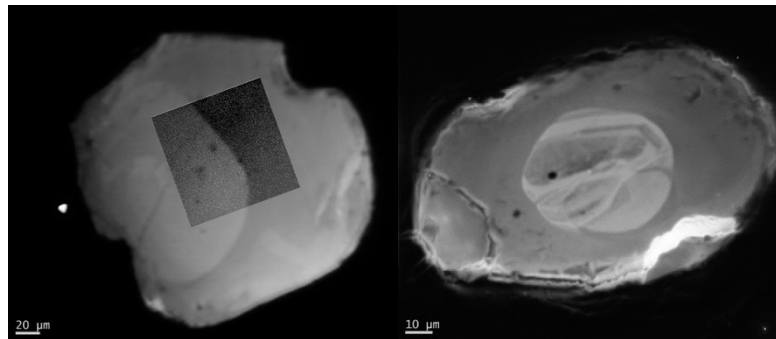


Fig. 8.3. CL images of granulite zircons LB04_19_02 (left) and SMZ_04 (right). The dark square in zircon LB04_19_02 denotes a zoom-in high resolution [Li] mapping area across the boundary (see Fig. 8.5).

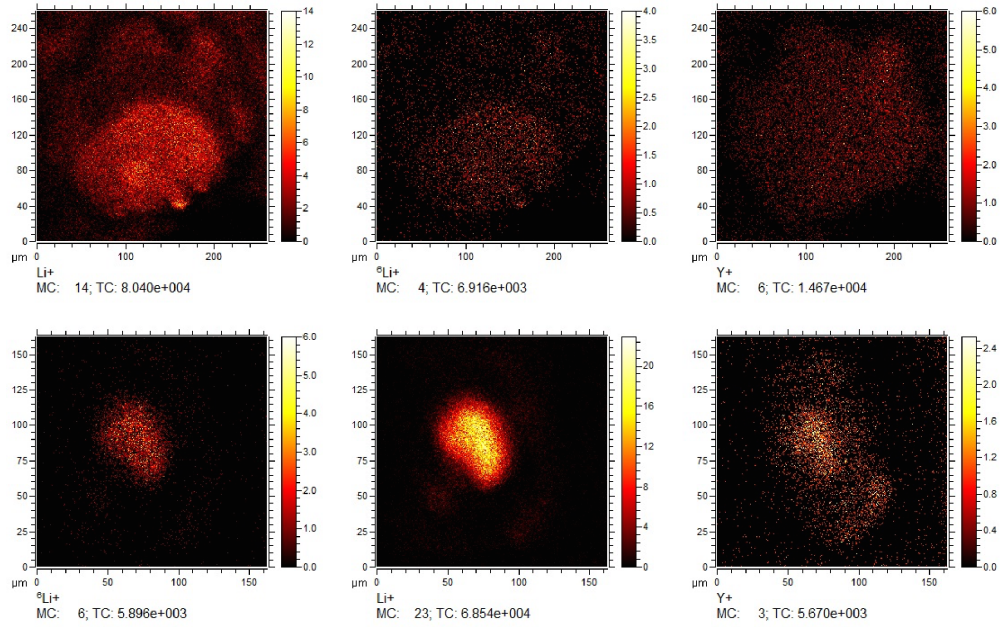


Fig. 8.4. ToF-SIMS positive ion imaging of zircons LB04_19_02 (top) and SMZ_04 (bottom). Relative intensity scale is from low (dark) to high (bright) yield for each of the ionic species. Ion beam size is $\sim 2\mu\text{m}$.

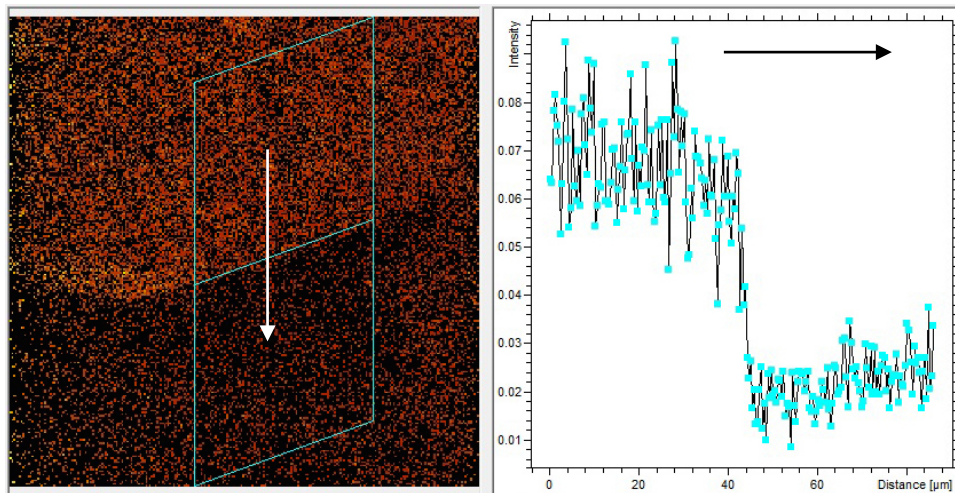


Fig. 8.5. High-resolution (ion beam $\sim 300\text{ nm}$) $[\text{Li}]$ imaging across the core-rim boundary of zircon LB04_19_02. Note: the image is rotated 90° CW with respect to Fig. 8.3. The plot on the right shows the integrated ^7Li and ^6Li intensity profile across the area indicated in the left panel.

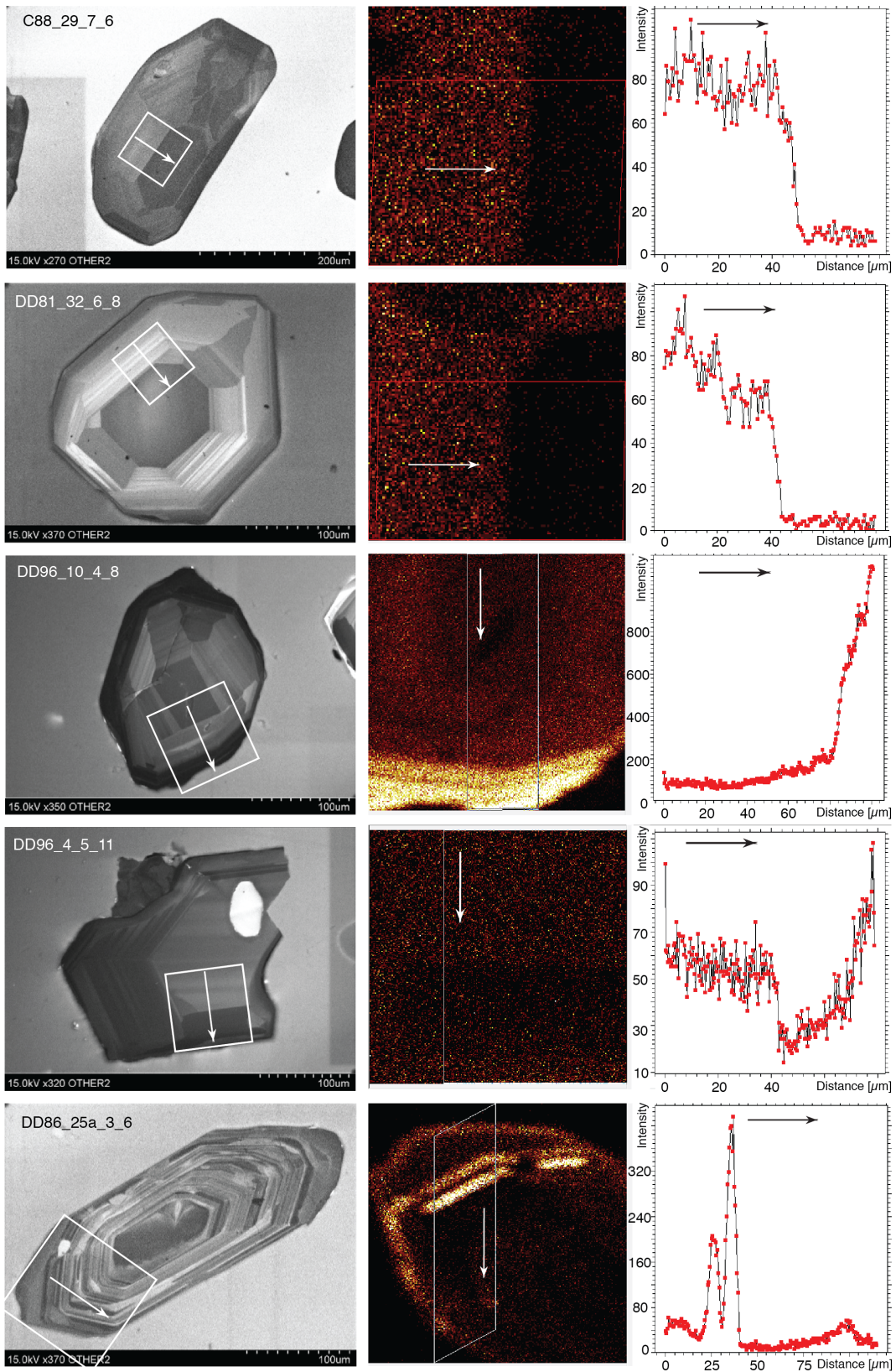


Fig. 8.6. left column: CL images of five natural zircon grains (from Bouvier *et al.*, 2012).

White box represents area imaged using ToF SIMS, arrow indicates direction of profiles. Middle column: High-resolution (ion beam ~ 300 nm) [Li] images of the areas denoted in the left column. White arrow shows the direction of the area-integrated ^7Li intensity profiles shown in the right columns. Li concentrations in these zircons varies from 1 to 14 ppm.

ToF SIMS imaging of the three TTG zircons and two sanukitoid zircons (Fig. 8.6) shows significant Li gradients across core-rim boundaries (C88_29_7_6, DD81_32_6_8 and DD96_10_4_8) and oscillatory zonings (DD86_25a_3_6). Abrupt changes in Li concentrations are seen in all five zircons.

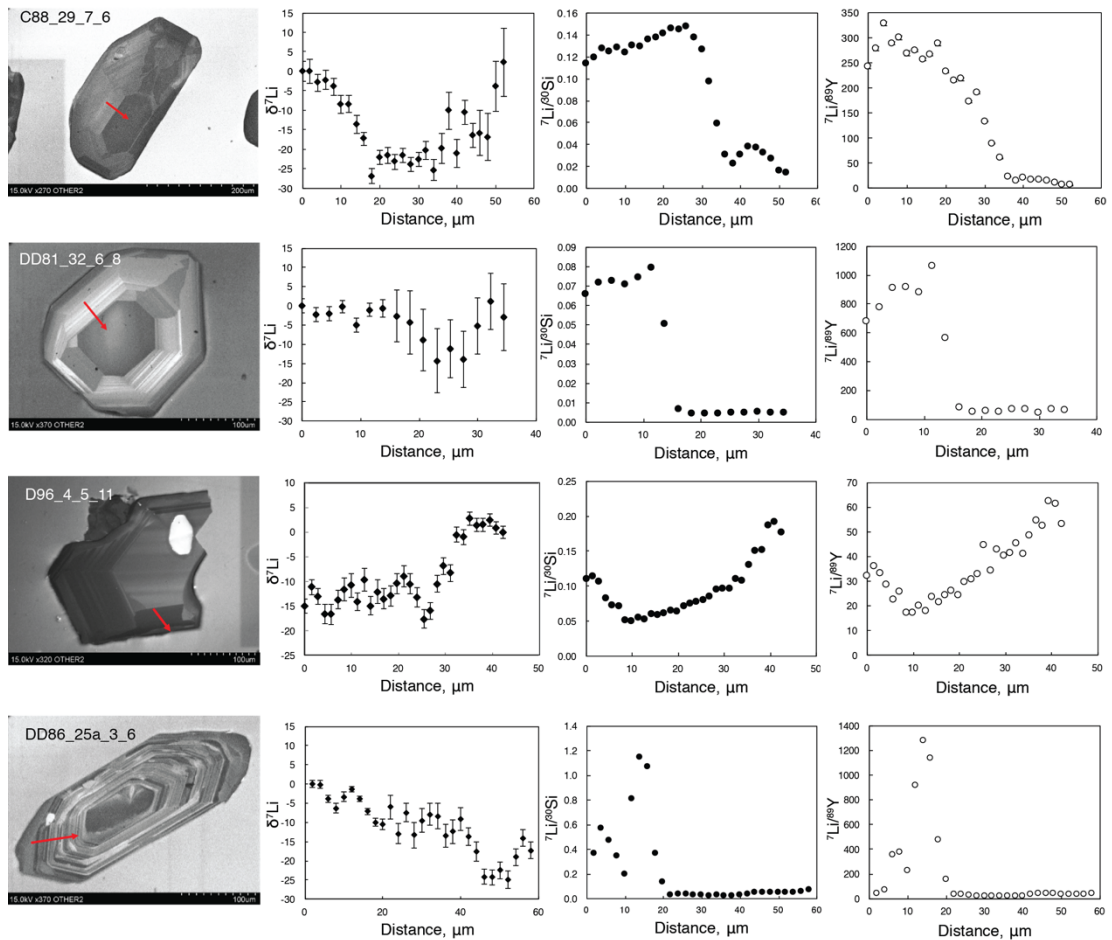


Fig. 8.7. Column 1: CL images of four zircon grains profiled by NanoSIMS. Red arrows indicate the directions of line profiles in columns 2-4. Column 2: Li isotope profiles. Column 3: $^7\text{Li}/^{30}\text{Si}$ profiles. Column 4: $^7\text{Li}/^{89}\text{Y}$ profiles. The $\delta^7\text{Li}$ values were calculated relative to the

first spot analysis of each profile. All $\delta^7\text{Li}$ values were calculated against the first analysis.

Error bars are 1σ .

8.4.2. NanoSIMS

The four zircon grains measured by NanoSIMS display [Li] gradients consistent with ToF SIMS observations (Fig. 8.6). In particular, all of the measured zircons show 20–30 permil Li isotopic variation within 50 μm (Fig. 8.7). These single crystal $\delta^7\text{Li}$ ranges well exceed the entire $\delta^7\text{Li}$ range of igneous and sedimentary rocks that are not affected by diffusion processes (< 15 permil). Zircon C88_29_7_6 and D81_32_6_8 display “dips” in $\delta^7\text{Li}$ profiles and sharp [Li] gradients across the core-rim boundary, characteristics commonly seen in diffusion profiles. Zircon D96_4_5_11 shows generally increasing $\delta^7\text{Li}$ with increasing $^7\text{Li}/^{30}\text{Si}$ and $^7\text{Li}/^{89}\text{Y}$ ratios along the measured profile. Zircon DD86_25a_3_6 has a complicated $\delta^7\text{Li}$ pattern across the oscillatory zonings.

A counterintuitive observation here is that the $\delta^7\text{Li}$ profile in the rim of zircon C88_29_7_6 indicates inward Li diffusion from the low [Li] outer part of the rim to the high [Li] inner part of the rim. This suggests that multiple factors control Li activity in zircon. The fact that the Li/Y ratio decreases from the outer rim to the inner rim implies that charge coupling between Li and REEs+Y may exert influence on Li activity in zircon.

8.5. Modeling and discussion

Here I model Li diffusion during the growth of zircon C88_29_7_6, whose elemental concentration and isotopic patterns represent the least complicated yet typical zircon profiles observed in this study. There are three first-order features in the $\delta^7\text{Li}$ and [Li] profiles in zircon C88_29_7_6 that my modeling work aims to reproduce:

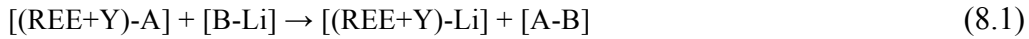
- (1) A sharp gradient in [Li];
- (2) Li diffusion from a low concentration outer rim to a high concentration inner rim;
- (3) A continuous Li isotopic diffusion profile (low $\delta^7\text{Li}$) across the sharp [Li] boundary even though the atomic ratio of $(\text{REE}+\text{Y})/(\text{Li}+\text{P}) > 1$ in the core area (Bouvier et al., 2012).

8.5.1. Assumptions

- (1) Spherical zircon grows from 1 μm to 60 μm in radius at a constant growth rate;
- (2) Temperature linearly decreases from 850 $^{\circ}\text{C}$ to 650 $^{\circ}\text{C}$ during zircon growth;
- (3) Li that is charge-coupled with REE has a diffusivity of zero, and Li that is charge-coupled with other chemical species has a bulk diffusivity equal to that determined by Cherniak and Watson (2010);
- (4) No isotopic fractionation exists between Li charge-coupled with various chemical species;
- (5) [Li] in the zircon rim changes as a function of time, such that the calculated post-diffusion [Li] profile best fits the measured [Li] profile;
- (6) ^6Li diffuses 3% faster than ^7Li . This corresponds to a β value of 0.19, which is a typical β value for Li diffusion in silicate minerals and melts (Parkinson et al., 2007; Richter et al., 2014; Richter et al., 2003).

I consider three scenarios. First, Li does not couple with REEs and Y in zircon and the distribution of REEs+Y in zircon has no influence on Li diffusion in zircon (Cherniak and Watson, 2010). Second, Li strongly couples with REEs and Y in zircon (Ushikubo et al., 2008; Bouvier et al., 2012). In this case, Li does not diffuse until Li atoms occupy all REEs+Y coupling sites. A similar scenario of Li diffusion in pyroxene was modeled by Richter et al. (2014). Third, Li partially couples with REEs and Y in zircon. In this case, Li diffusion in zircon is retarded by REEs+Y, but there are always some Li atoms charge-

coupled with other chemical species in the lattice. The proportion of Li charge-coupled with REE+Y vs. Li charge-coupled with other chemical species is determined by the number of Li atoms, REE+Y and non-REE+Y charge coupling sites and the substitution coefficient k , a new parameter that I introduce to quantify the tendency of Li atoms to enter REE+Y charge coupling sites. This substitution coefficient can be experimentally constrained, and, like all thermodynamic parameters, its value is likely a function of temperature, pressure and matrix composition. In zircon, the 3+ cations REE and Y can be charge coupled with many species including H, P, Mg, Fe, Al, Ca, Li, etc. (see Bouvier et al., 2012 for references). During diffusion, charge coupling between Li and REE+Y takes place as a substitution reaction:



where A is a chemical species that is coupled with REE+Y before Li fills in, and B is a non-REE+Y chemical species that couples with Li. The minus signs “-” in equations (1) and (2) denote charge coupling bonds. Given k 's definition:

$$k = \frac{[(\text{REE}+\text{Y})-\text{Li}]}{[\text{B}-\text{Li}]} = K * \frac{[(\text{REE}+\text{Y})-\text{A}]}{[\text{A}-\text{B}]} \quad (8.2)$$

Where K is the reaction constant. The first and second scenarios essentially represent the two extremes of the third scenario with $k = 0$ for the first scenario and $k = \infty$ for the second.

Table 8.2. Notation used in modelling

Variable	Description	Unit
----------	-------------	------

C_j	total concentration of Li isotope(s) j	mole
C_j^f	concentration of Li isotope j uncoupled to REE+Y	mole
C_{REE+Y}	concentration of REE+Y	mole
D_j	diffusion coefficient of Li isotope j	m ² /s
k	substitution coefficient	n.a.
K	equilibrium constant of the substitution reaction	n.a.
n_{Li}^{REE}	number of REE+Y coupled Li ions	mole
n_{Li}	number of non-REE+Y charge coupled Li ions	mole
n_{REE+Y}	number of REE+Y charge coupling sites	mole
$n_{int.}$	number of non-REE+Y charge coupling interstitial sites	mole
R_i	initial zircon radius	μm
R_f	final zircon radius	μm
r	distance to the zircon crystal center	μm
T	temperature	K
t	time	s
τ	timescale of cooling/crystallization	s

8.5.2. Governing equations

According to assumption (1):

$$\frac{dT}{dt} = \frac{T_f - T_i}{\tau} \quad (8.3)$$

where T_i and T_f are the initial (850 °C) and final temperatures (650 °C) of zircon crystallization, respectively; τ is the timescale of cooling.

Zircon radius increases at a constant rate:

$$\frac{dR}{dt} = \frac{R_f - R_i}{\tau} \quad (8.4)$$

where R_i and R_f are the initial and final zircon radius, respectively.

Redistribution of Li isotopes coupled to non-REE+Y chemical species (indicated by the subscript f in the equation below) is described by Fick's 2nd law:

$$\frac{\partial C_j^f}{\partial t} = D_j \left(\frac{\partial^2 C_j^f}{\partial r^2} + \frac{2}{r} \frac{\partial C_j^f}{\partial r} \right), j = {}^6\text{Li}, {}^7\text{Li}, \quad 0 \leq r \leq R|_t \quad (8.5)$$

with four boundary conditions:

$$\frac{\partial C_j}{\partial r} \Big|_{r=0} = 0, \quad 0 \leq r \leq R|_{t=0} \quad (8.6)$$

$$\frac{\partial C_j}{\partial r} \Big|_{r=R} = 0 \quad (8.7)$$

$$\frac{C_7}{C_6} \Big|_{t=0} = \frac{C_7}{C_6} \Big|_{r=R} = \text{Const} \quad (8.8)$$

where the subscripts 6 and 7 denote the isotopes ${}^6\text{Li}$ and ${}^7\text{Li}$, respectively.

The dimensionless pre-diffusion concentration profiles of Li and REE+Y are described as:

$$C_{7+6} \Big|_{r=R} = 50, \quad \text{when } t < 0.2\tau; \quad (8.9a)$$

$$C_{7+6} \Big|_{r=R} = 5 - 20 \left(\frac{t}{\tau} - 0.2 \right), \quad \text{when } 0.2\tau < t < 0.4\tau; \quad (8.9b)$$

$$C_{7+6} \Big|_{r=R} = 10, \quad \text{when } 0.4\tau < t < 0.5\tau; \quad (8.9c)$$

$$C_{7+6} \Big|_{r=R} = 1, \quad \text{when } 0.5\tau < t < 0.6\tau; \quad (8.9d)$$

$$C_{7+6} \Big|_{r=R} = 50 - 6 \left(\frac{t}{\tau} - 0.6 \right), \quad \text{when } 0.6\tau < t < \tau; \quad (8.9e)$$

$$C_{\text{REE+Y}} \Big|_{r=R} = 31, \quad \text{when } t < 0.2\tau; \quad (8.10a)$$

$$C_{REE+Y}|_{r=R} = 31 - 120\left(\frac{t}{\tau} - 0.2\right), \text{ when } 0.2\tau < t < 0.4\tau; \quad (8.10b)$$

$$C_{REE+Y}|_{r=R} = 7.2 - 6\left(\frac{t}{\tau} - 0.4\right), \text{ when } 0.4\tau < t < \tau; \quad (8.10c)$$

where τ is zircon growth timescale. Equations with only numbers indicate constant [Li] or [REE+Y] during that time interval while equations with the t/τ term describe changing [Li] or [REE+Y] as zircon grows.

Eq. (8.4) states a constant radial growth rate. This translates into a progressively faster dV/dt . The growth rate of zircon as a function of time is poorly constrained. A linear radial growth rate model, like the one use here, requires less computation cost. Eq. (8.6) states that the initial zircon nucleus is homogeneous in [Li]; Eq. (8.7) states that there is zero [Li] gradient in the center of the crystal at all times; Eq. (8.8) states the 7/6 ratio in the initial zircon nucleus and the rim during growth is in equilibrium with the melt i.e., identical.

The pre-diffusion [Li] profile, quantified as $C_{7+\delta}|_{r=R}(t)$ functions during zircon growth in equation (8.9), is a parameter that cannot be directly constrained. This parameter was tuned to best fit the observed post-diffusion ${}^7\text{Li}/{}^{30}\text{Si}$ profile. Because REE and Y are assumed not to diffuse, the [REE+Y] profile, quantified as $C_{REE+Y}|_{r=R}(t)$ function (Equation 8.10) during zircon growth, was modeled according to the measured ${}^{89}\text{Y}/{}^{30}\text{Si}$ profile.

The proportion of REE+Y-charge coupled Li ions at a distance of r to the crystal center is given by:

$$\frac{n_{Li}^{REE}}{n_{Li}}|_r = k \frac{n_{REE+Y}}{n_{int.}}|_r \quad (8.11a)$$

when $n_{Li}^{REE}|_r \leq n_{REE+Y}|_r$,

$$\frac{n_{Li}^{REE}}{n_{Li}}|_r = \frac{n_{REE+Y}}{n_{Li}}|_r \quad (8.11b)$$

where k is the Li substitution coefficient. Li favors the charge coupling sites of REE+Y when $k > 1$, and favors the charge coupling sites of other chemical species when $k < 1$. $n_{int.}$ is the the

number of non-REE+Y charge coupling sites that Li may occupy in the zircon lattice.

$n_{REE+Y}/n_{int.}$ and n_{REE+Y}/n_{Li} are dimensionless variables, and can be approximated by REE+Y concentration (assuming the number of non-REE+Y charge coupling sites is constant) and C_{REE+Y}/C_{Li} divided by their atomic mass ratio, respectively.

$$D_7 = 7.17 \times 10^{-7} \times e^{-2.75 \times \frac{10^5}{8.314T}} m^2 s^{-1} \quad (8.12a)$$

$$D_6 = D_7 * 1.03 \quad (8.12b)$$

7Li diffusivity in zircon is taken from Cherniak and Watson (2010), and 6Li diffusivity is obtained by assumption (6). Eq. (8.3) to Eq. (8.12) are solved numerically and the results are presented as isotopic profiles (relative to the initial 7/6 ratio), [Li] profiles, REE profiles and Li/REE profiles (Fig. 8.8).

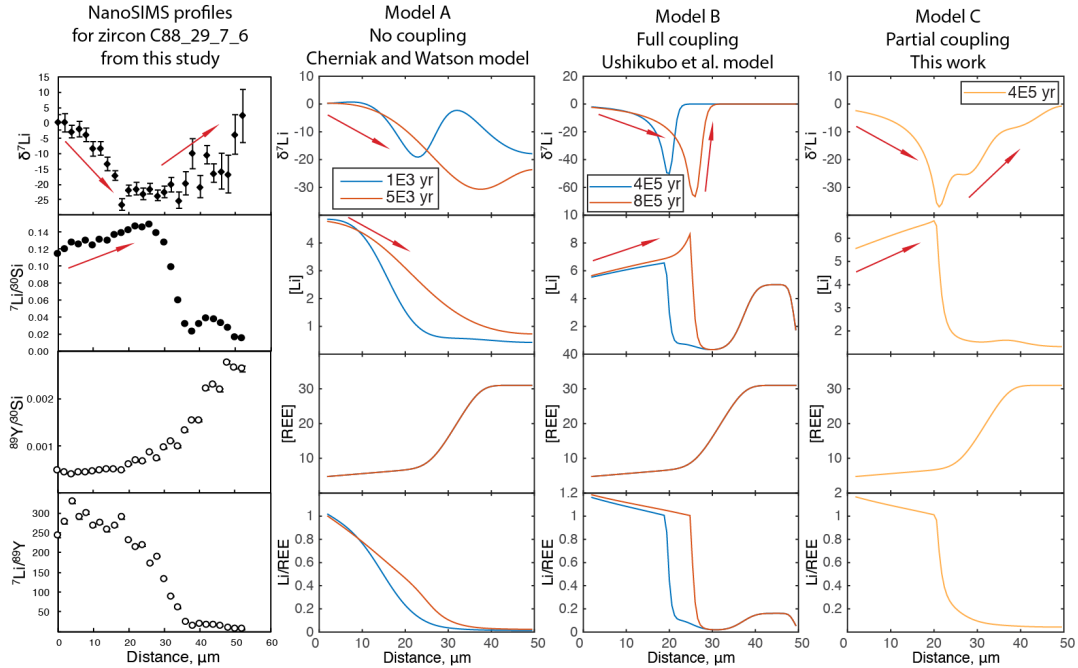


Fig. 8.8. Modeled Li isotopic fractionation during zircon growth assuming no charge coupling ($k = 0$), full charge coupling ($k = 10^8$) and partial charge coupling ($k = 500$).

8.5.3. Implications from modeling

If Li does not couple with REE and Y, then $k = 0$. In this model (Model A in Fig. 8.8), Li gradients are rapidly relaxed (note the timescales used in Model A-C), and Li always diffuses from high to low concentration areas with Li activity only controlled by its concentration. This model produces long Li diffusion profiles but fails to reproduce the anti-correlated $\delta^7\text{Li}$ and [Li] profiles in the rim of zircon C88_29_7_6. On the other extreme, if Li strongly couples with REE and Y (Model B), then $k \gg 1$ ($k = 10^8$ used here). Similar to the Richter et al. (2014) results, this model produces a distinct diffusion front seen in both $\delta^7\text{Li}$ and [Li] profiles, reflected as a sharp $\delta^7\text{Li}$ dip and [Li] discontinuity. Li diffusion instantly stops across the diffusion front. Because the Li activity is controlled by both [Li] and [REE+Y], in this model, Li diffuses from high Li/(REE+Y) to low Li/(REE+Y) areas and may diffuse from a low [Li] area to a high [Li] area. However, this model is inconsistent with the continuous Li diffusion across the sharp [Li] boundary, as indicated by the prolonged low $\delta^7\text{Li}$ profiles. Model C assumes partial coupling between Li and REE+Y, with an assumed $k = 500$ here (Fig. 8.8). This model, to the first order, reproduces the key features in the profiles in zircon C88_29_7_6, including the sharp [Li] gradient, anti-correlated $\delta^7\text{Li}$ and [Li] profiles in the rim, and continuous Li diffusion across the sharp [Li] zoning.

The many assumptions (including zircon growth rate, thermal history, zircon geometry, timescale, etc.) that go into this model demonstrate that it is poorly constrained. The values of many parameters used in this model may not represent a true scenario, and the combination of the parameters used in the model did not explore all of the possible solution space. There could be multiple combinations of these parameters that are able to reproduce the profiles in C88_29_7_6. However, the purpose of the modeling is to test the hypothesis that charge coupling with REE and Y affects Li diffusion in zircon. Models that assume either no charge

coupling or full charge coupling with REE+Y produce profiles with unique features that are inconsistent with the observations from zircon C88_29_7_6.

This substitution reaction proceeds in the direction that lowers the free energy of the system. Like other chemical reactions, the rate at which this substitution happens is controlled by the reaction kinetics. Li diffusion in zircon is thus complicated by the fact that most natural zircons are heterogeneous. The effective Li diffusivity in zircon is sensitive to not only the atomic ratio of Li to REE+Y but also other chemical species that may couple with REE+Y, all of which need to be accounted for in experimental research. In Cherniak and Watson's experiments, charge coupling did not exert an important role during Li diffusion because the Li flux overwhelmed the REE+Y in their zircon samples.

8.6. Conclusions and future work

The diffusion of Li in natural zircons under crustal condition is recognized to be rapid as compared to most other cations, and is controlled by coupled substitution. It is concluded that Li isotopes may be diffusively fractionated during zircon growth.

In zircon Li may charge couple with REE and Y in zircon, but not at the 100% level as Ushikubo et al. (2008) and Bouvier et al. (2012) envisaged. Free interstitial Li can be present even when the atomic ratio of $(\text{REE}+\text{Y})/\text{Li} > 1$ in natural zircons. The proportions of charge coupled Li vs. free interstitial Li can be quantified by a partition coefficient Li between the two types of sites.

My work on Li diffusion in zircon continues. I will further investigate Li diffusion in synthetic zircon under controlled conditions so as to understand the Li-REE+Y charge

coupling effects by experiments. In particular, the partitioning behavior of Li between charge coupling and free interstitial sites can be possibly constrained by experiments.

References

- Agostini, S., Ryan, J.G., Tonarini, S., Innocenti, F., 2008. Drying and dying of a subducted slab: Coupled Li and B isotope variations in Western Anatolia Cenozoic Volcanism. *Earth and Planetary Science Letters* 272, 139-147.
- Bouman, C., Elliott, T., Vroon, P.Z., 2004. Lithium inputs to subduction zones. *Chemical Geology* 212, 59-79.
- Bouvier, A.-S., Ushikubo, T., Kita, N., Cavosie, A., Kozdon, R., Valley, J., 2012. Li isotopes and trace elements as a petrogenetic tracer in zircon: insights from Archean TTGs and sanukitoids. *Contr. Mineral. and Petrol.* 163, 745-768.
- Chan, L.H., Edmond, J.M., Thompson, G., Gillis, K., 1992. Lithium isotopic composition of submarine basalts: implications for the lithium cycle in the oceans. *Earth and Planetary Science Letters* 108, 151-160.
- Cherniak, D.J., Watson, E.B., 2010. Li diffusion in zircon. *Contr. Mineral. and Petrol.* 160, 383-390.
- Elliott, T., Jeffcoate, A., Bouman, C., 2004. The terrestrial Li isotope cycle: light-weight constraints on mantle convection. *Earth and Planetary Science Letters* 220, 231-245.
- Gallagher, K., Elliott, T., 2009. Fractionation of lithium isotopes in magmatic systems as a natural consequence of cooling. *Earth and Planetary Science Letters* 278, 286-296.
- Gao, Y., Snow, J.E., Casey, J.F., Yu, J., 2011. Cooling-induced fractionation of mantle Li isotopes from the ultraslow-spreading Gakkel Ridge. *Earth and Planetary Science Letters* 301, 231-240.

- Halama, R., McDonough, W.F., Rudnick, R.L., Bell, K., 2008. Tracking the lithium isotopic evolution of the mantle using carbonatites. *Earth and Planetary Science Letters* 265, 726-742.
- Halama, R., Savov, I., Rudnick, R., McDonough, W., 2009. Insights into Li and Li isotope cycling and sub-arc metasomatism from veined mantle xenoliths, Kamchatka. *Contr. Mineral. and Petrol.* 158, 197-222.
- Huh, Y., Chan, L.-H., Edmond, J.M., 2001. Lithium isotopes as a probe of weathering processes: Orinoco River. *Earth and Planetary Science Letters* 194, 189-199.
- Huh, Y., Chan, L.-H., Zhang, L., Edmond, J.M., 1998. Lithium and its isotopes in major world rivers: implications for weathering and the oceanic budget. *Geochimica et Cosmochimica Acta* 62, 2039-2051.
- Jeffcoate, A.B., Elliott, T., Kasemann, S.A., Ionov, D., Cooper, K., Brooker, R., 2007. Li isotope fractionation in peridotites and mafic melts. *Geochimica et Cosmochimica Acta* 71, 202-218.
- John, T., Gussone, N., Podladchikov, Y.Y., Bebout, G.E., Dohmen, R., Halama, R., Klemd, R., Magna, T., Seitz, H.-M., 2012. Volcanic arcs fed by rapid pulsed fluid flow through subducting slabs. *Nature Geoscience* 5, 489-492.
- Kısakürek, B., James, R.H., Harris, N.B., 2005. Li and $\delta^{67}\text{Li}$ in Himalayan rivers: Proxies for silicate weathering? *Earth and Planetary Science Letters* 237, 387-401.
- Kısakürek, B., Widdowson, M., James, R.H., 2004. Behaviour of Li isotopes during continental weathering: the Bidar laterite profile, India. *Chemical Geology* 212, 27-44.
- Lai, Y.-J., von Strandmann, P.A.P., Dohmen, R., Takazawa, E., Elliott, T., 2015. The influence of melt infiltration on the Li and Mg isotopic composition of the Horoman Peridotite Massif. *Geochimica et Cosmochimica Acta* 164, 318-332.

- Li, X.-H., Li, Q.-L., Liu, Y., Tang, G.-Q., 2011. Further characterization of M257 zircon standard: A working reference for SIMS analysis of Li isotopes. *Journal of Analytical Atomic Spectrometry* 26, 352-358.
- Liu, X.-M., Rudnick, R.L., Hier-Majumder, S., Sirbescu, M.-L.C., 2010. Processes controlling lithium isotopic distribution in contact aureoles: A case study of the Florence County pegmatites, Wisconsin. *Geochemistry, Geophysics, Geosystems* 11, Q08014.
- Liu, X.-M., Rudnick, R.L., McDonough, W.F., Cummings, M.L., 2013. Influence of chemical weathering on the composition of the continental crust: Insights from Li and Nd isotopes in bauxite profiles developed on Columbia River Basalts. *Geochimica et Cosmochimica Acta* 115, 73-91.
- Liu, X.-M., Wanner, C., Rudnick, R.L., McDonough, W.F., 2015. Processes controlling $\delta^7\text{Li}$ in rivers illuminated by study of streams and groundwaters draining basalts. *Earth and Planetary Science Letters* 409, 212-224.
- Lundstrom, C.C., Chaussidon, M., Hsui, A.T., Kelemen, P., Zimmerman, M., 2005. Observations of Li isotopic variations in the Trinity Ophiolite: Evidence for isotopic fractionation by diffusion during mantle melting. *Geochimica et Cosmochimica Acta* 69, 735-751.
- Marks, M.A.W., Rudnick, R.L., McCammon, C., Vennemann, T., Markl, G., 2007. Arrested kinetic Li isotope fractionation at the margin of the Ilímaussaq complex, South Greenland: Evidence for open-system processes during final cooling of peralkaline igneous rocks. *Chemical Geology* 246, 207-230.
- Marschall, H.R., Pogge von Strandmann, P.A.E., Seitz, H.-M., Elliott, T., Niu, Y., 2007. The lithium isotopic composition of orogenic eclogites and deep subducted slabs. *Earth and Planetary Science Letters* 262, 563-580.

- Millot, R., Guerrot, C., Vigier, N., 2004. Accurate and High-Precision Measurement of Lithium Isotopes in Two Reference Materials by MC-ICP-MS. *Geostandards and Geoanalytical Research* 28, 153-159.
- Parkinson, I.J., Hammond, S.J., James, R.H., Rogers, N.W., 2007. High-temperature lithium isotope fractionation: Insights from lithium isotope diffusion in magmatic systems. *Earth and Planetary Science Letters* 257, 609-621.
- Penniston-Dorland, S.C., Sorensen, S.S., Ash, R.D., Khadke, S.V., 2010. Lithium isotopes as a tracer of fluids in a subduction zone mélange: Franciscan Complex, CA. *Earth and Planetary Science Letters* 292, 181-190.
- Pistiner, J.S., Henderson, G.M., 2003. Lithium-isotope fractionation during continental weathering processes. *Earth and Planetary Science Letters* 214, 327-339.
- Pogge von Strandmann, P.A., Burton, K.W., James, R.H., van Calsteren, P., Gislason, S.R., Mokadem, F., 2006. Riverine behaviour of uranium and lithium isotopes in an actively glaciated basaltic terrain. *Earth and Planetary Science Letters* 251, 134-147.
- Qiu, L., Rudnick, R.L., Ague, J.J., McDonough, W.F., 2011a. A lithium isotopic study of sub-greenschist to greenschist facies metamorphism in an accretionary prism, New Zealand. *Earth and Planetary Science Letters* 301, 213-221.
- Qiu, L., Rudnick, R.L., McDonough, W.F., Bea, F., 2011b. The behavior of lithium in amphibolite- to granulite-facies rocks of the Ivrea–Verbano Zone, NW Italy. *Chemical Geology* 289, 76-85.
- Qiu, L., Rudnick, R.L., McDonough, W.F., Merriman, R.J., 2009. Li and $\delta^7\text{Li}$ in mudrocks from the British Caledonides: Metamorphism and source influences. *Geochimica et Cosmochimica Acta* 73, 7325-7340.
- Richter, F., Watson, B., Chaussidon, M., Mendybaev, R., Ruscitto, D., 2014. Lithium isotope fractionation by diffusion in minerals. Part 1: Pyroxenes. *Geochimica et Cosmochimica Acta* 126, 352-370.

- Richter, F.M., Davis, A.M., DePaolo, D.J., Watson, E.B., 2003. Isotope fractionation by chemical diffusion between molten basalt and rhyolite. *Geochimica et Cosmochimica Acta* 67, 3905-3923.
- Rudnick, R.L., Tomascak, P.B., Njo, H.B., Gardner, L.R., 2004. Extreme lithium isotopic fractionation during continental weathering revealed in saprolites from South Carolina. *Chemical Geology* 212, 45-57.
- Ryu, J.-S., Vigier, N., Lee, S.-W., Lee, K.-S., Chadwick, O.A., 2014. Variation of lithium isotope geochemistry during basalt weathering and secondary mineral transformations in Hawaii. *Geochimica et Cosmochimica Acta* 145, 103-115.
- Seitz, H.-M., Brey, G.P., Lahaye, Y., Durali, S., Weyer, S., 2004. Lithium isotopic signatures of peridotite xenoliths and isotopic fractionation at high temperature between olivine and pyroxenes. *Chemical Geology* 212, 163-177.
- Tang, M., Rudnick, R.L., Chauvel, C., 2014. Sedimentary input to the source of Lesser Antilles lavas: A Li perspective. *Geochimica et Cosmochimica Acta* 144, 43-58.
- Teng, F.-Z., McDonough, W.F., Rudnick, R.L., Walker, R.J., 2006. Diffusion-driven extreme lithium isotopic fractionation in country rocks of the Tin Mountain pegmatite. *Earth and Planetary Science Letters* 243, 701-710.
- Teng, F.-Z., McDonough, W.F., Rudnick, R.L., Wing, B.A., 2007. Limited lithium isotopic fractionation during progressive metamorphic dehydration in metapelites: a case study from the Onawa contact aureole, Maine. *Chemical geology* 239, 1-12.
- Teng, F.-Z., Rudnick, R.L., McDonough, W.F., Gao, S., Tomascak, P.B., Liu, Y., 2008. Lithium isotopic composition and concentration of the deep continental crust. *Chemical Geology* 255, 47-59.
- Teng, F.-Z., Rudnick, R.L., McDonough, W.F., Wu, F.-Y., 2009. Lithium isotopic systematics of A-type granites and their mafic enclaves: Further constraints on the Li isotopic composition of the continental crust. *Chemical Geology* 262, 370-379.

- Teng, F.Z., McDonough, W.F., Rudnick, R.L., Dalpé, C., Tomascak, P.B., Chappell, B.W., Gao, S., 2004. Lithium isotopic composition and concentration of the upper continental crust. *Geochimica et Cosmochimica Acta* 68, 4167-4178.
- Tomascak, P.B., Langmuir, C.H., le Roux, P.J., Shirey, S.B., 2008. Lithium isotopes in global mid-ocean ridge basalts. *Geochimica et Cosmochimica Acta* 72, 1626-1637.
- Tomascak, P.B., Tera, F., Helz, R.T., Walker, R.J., 1999. The absence of lithium isotope fractionation during basalt differentiation: new measurements by multicollector sector ICP-MS. *Geochimica et Cosmochimica Acta* 63, 907-910.
- Tomascak, P.B., Widom, E., Benton, L.D., Goldstein, S.L., Ryan, J.G., 2002. The control of lithium budgets in island arcs. *Earth and Planetary Science Letters* 196, 227-238.
- Trail, D., Cherniak, D.J., Watson, E.B., Harrison, T.M., Weiss, B.P., Szumila, I., 2016. Li zoning in zircon as a potential geospeedometer and peak temperature indicator. *Contrib. Mineral. and Petrol.* 171, 1-15.
- Ushikubo, T., Kita, N.T., Cavosie, A.J., Wilde, S.A., Rudnick, R.L., Valley, J.W., 2008. Lithium in Jack Hills zircons: Evidence for extensive weathering of Earth's earliest crust. *Earth and Planetary Science Letters* 272, 666-676.
- Vigier, N., Decarreau, A., Millot, R., Carignan, J., Petit, S., France-Lanord, C., 2008. Quantifying Li isotope fractionation during smectite formation and implications for the Li cycle. *Geochimica et Cosmochimica Acta* 72, 780-792.
- von Strandmann, P.A.P., Opfergelt, S., Lai, Y.-J., Sigfússon, B., Gíslason, S.R., Burton, K.W., 2012. Lithium, magnesium and silicon isotope behaviour accompanying weathering in a basaltic soil and pore water profile in Iceland. *Earth and Planetary Science Letters* 339, 11-23.
- Wimpenny, J., Gíslason, S.R., James, R.H., Gannoun, A., Pogge Von Strandmann, P.A.E., Burton, K.W., 2010. The behaviour of Li and Mg isotopes during primary phase

dissolution and secondary mineral formation in basalt. *Geochimica et Cosmochimica Acta* 74, 5259-5279.

Zack, T., Tomascak, P.B., Rudnick, R.L., Dalpé, C., McDonough, W.F., 2003. Extremely light Li in orogenic eclogites: The role of isotope fractionation during dehydration in subducted oceanic crust. *Earth and Planetary Science Letters* 208, 279-290.

Chapter 9. Summary and outlook

9.1. Summary

Five years of Ph.D. study has given me the opportunity to examine the geochemistry of crustal formation and evolution from quite a few perspectives. The topics I have investigated have given me an overarching picture of how the silicate Earth works and have highlighted many exciting questions that remain to be explored. Hence, I briefly summarize the main results from the projects that I worked on, and then provide an outlook for on-going and future research.

My Ph.D. training started from the MORB Eu project, which attempts to quantify the Eu anomaly in the MORB source mantle, and test the hypothesis put forward by (Niu and O'Hara, 2009) that the mantle source of MORB hosts the missing Eu from the continental crust. My global survey using high precision measurements of global MORB glasses ($\text{MgO} > 8.5\%$) show no resolvable positive Eu anomaly (mean $\text{Eu}/\text{Eu}^* = 1.025 \pm 0.025$, 2 SE). Combined with quantitative modeling work, I proposed that MORB mantle alone may be insufficient to balance the Eu deficit in the continental crust, and the recycled lower crustal materials, which carry positive Eu anomalies, may have at least partially entered the deep mantle that is sampled by ocean island basalts (OIB). In order to obtain high precision Eu anomaly data in high MgO MORB glasses, I developed a LA-ICP-MS method, which allows me to measure Eu/Eu^* in MORB glasses to a precision of 3% (2 RSD reproducibility). This methodological work serendipitously lead to another study, which came about when making

comparisons between results generated by spot versus line sampling during ablation, and demonstrated that rare earth elements can be fractionated due to the small difference in condensation temperatures and incomplete particle-ion conversion in the ICP. While doing the MORB Eu project, I calculated the Eu deficit in the continental crust based on compiled crustal rock data, which allows me to quantify that the total mass of recycled lower crustal materials through Earth history is $2.9 + 1.1/-0.9$ the mass of modern bulk continental crust.

During my second year, Dr. Rudnick introduced me into the Li isotope world. Then I started my Lesser Antilles Li isotope project. I measured Li isotopes in arc lavas from Martinique and cored sediments offshore of the Lesser Antilles trench. My results show that both Lesser Antilles arc lavas and subducting sediments have distinctively light Li isotopes compared with MORB and OIB. Based on this coupled lava and subducting sediment study, I calculated the sedimentary input to the mantle wedge source to be about 2% by mass. The Lesser Antilles, being the only case where arc lavas show clear crustal Li signatures, thus provides an example of Li recycling in subduction systems. I proposed that recycled crustal Li can reappear in arc lavas, and the fact that most arc lavas have $\delta^7\text{Li}$ similar to MORB suggests that the Li isotopic compositions of subducted sediments in most arcs are similar, on average, to that of the mantle.

My research in kinetic modeling of mantle melting and Li isotopes inspired me to study diffusion-driven Li isotopic fractionation in zircon. This is an ongoing project in collaboration with Yulia Goreva (Smithsonian Institute), Dustin Trail (Univ. Rochester) and Maitrayee Bose (Arizona State Univ.). In this work I am attempting to address the effect of charge coupling between REE+Y and Li on Li diffusion in zircon by analyzing both natural zircons and zircons that were experimentally grown under controlled conditions. I have found that Li activity in zircon is controlled by $\text{Li}/(\text{REE}+\text{Y})$. Li isotopic and concentration profiles

in natural zircons suggest the coexistence of REE+Y coupled Li (low diffusivity) and non-REE+Y coupled Li (high diffusivity).

Studying Li diffusion in zircon provided me with opportunities to operate state-of-art SIMS instruments, including the ToF SIMS at Smithsonian Institute, NanoSIMS and conventional SIMS at ASU. In addition, my collaboration with Yulia Goreva in her Smithsonian ToF SIMS lab allowed me to study further the fractionation mechanism of elements during laser ablation. This second analytical project employed ToF SIMS to image elemental zoning in the laser-induced condensate blanket surrounding the laser ablation site, revealing the plasma condensation controlled elemental fractionation during particle formation around the laser ablation site.

My work on Archean upper crustal evolution utilized Ni/Co and Cr/Zn ratios in terrigenous sedimentary rocks to track the changing MgO content of the upper continental crust. To calculate the MgO content from Ni/Co and Cr/Zn ratios, I conducted Monte Carlo mixing simulation using Archean igneous and metagneous rocks. My results showed a transition from a mafic to a felsic bulk composition of the upper crust from >3.0 to 2.5 Ga, suggesting the onset of global plate tectonics around 3 Ga. I also proposed that the area of the subaerial crust increased five times due to addition of large volumes of granite in the Neoproterozoic.

9.2. Outlook

My Ph.D. work on zircon Li diffusion has raised some interesting questions that can be further investigated. These include determining the compositional dependence of the Li

substitution coefficient between REE+Y and non-REE+Y charge coupling sites (from the Li in zircon study, Chapter 8), and mantle and atmospheric responses to the onset of plate tectonics and crustal evolution in the Archean (from the Archean terrigenous sediment geochemistry project, Chapter 6).

My work on Li diffusion in zircon continues with a focus on experimental studies aimed at gaining a better understanding of the mechanism of Li substitution into zircon and consequences for Li diffusion. My future experimental studies will attempt to constrain (1) diffusive fractionation factor (β) and (2) chemical species that affect charge coupling between Li and REE+Y. To quantify Li diffusive fractionation factor in zircon, I will continue to collaborate with Dr. Trail and perform in-diffusion experiments using Mud Tank zircon following the procedures developed by Cherniak and Watson (2010). Then I will measure the in-diffusion Li isotope profiles either by Cameca 6f SIMS (depth profile) or Cameca NanoSIMS (surface profile) depending on the special resolution requirements. As discussed in Chapter 8, charge coupling between Li and REE+Y during Li diffusion takes place as a substitution reaction, which is affected by other chemical species that charge couple with Li and REE+Y, respectively. Hydrogen is known to charge couple with REE+Y in zircon (De Hoog et al., 2014). If the charge coupling of H-REE+Y has a higher free energy than that of Li-REE+Y, then Li will preferentially charge couple with REE+Y and release H. Compared with many natural zircons, H concentration is extremely low in experimental zircons grown by the flux method. To test the effect of H on Li diffusion, I will grow zircons in a water-saturated medium using the piston cylinder method, and perform in-diffusion experiments using these synthetic H-rich zircons.

Archean upper crust evolution can be further explored in three ways. First, where do the first row transition metals reside in Archean terrigenous sedimentary rocks? These ancient sedimentary rocks typically contain felsic minerals (e.g., detrital quartz and feldspar) and granitic rock fragments, which is inconsistent with their overall high Ni, Co and Cr

concentrations. Dr. Rudnick and I hypothesized that mafic minerals weather congruently and release Ni, Co, Cr and Zn, which are insoluble and are incorporated into clay minerals. This hypothesis can be tested by determining the mineralogical hosts for these elements in Archean shales. Second, can we find geochemical responses in igneous differentiation trends after the onset of plate tectonics? Targets include redox sensitive elemental ratios, granitoid genesis indices, signals of upper crustal recycling in mantle magmas. Third, what are the links between upper crustal evolution and atmospheric evolution? My work suggests that the upper crust attained a felsic bulk composition by the end of Archean, close to the timing of the great oxidation event. Compared with a felsic upper crust, a mafic upper crust has a significantly higher Fe content and generally lower $\text{Fe}^{3+}/\text{Fe}^{2+}$ ratio. In mafic rocks, Fe is largely hosted in olivine and pyroxene, which weather congruently and release Fe. In granitoids, Fe is mostly hosted in biotite and Fe oxides. Biotite alteration produces chlorite, and Fe released by this process is limited. Iron oxides are resistant to weathering. Together, weathering of a mafic upper crust might have provided a significant oxygen sink in addition to seafloor serpentinization (Kasting, 2013) that declined significantly by the end of the Archean. I plan to write a NSF proposal to testify this hypothesis in the near future.

References

- Cherniak, D.J., Watson, E.B., 2010. Li diffusion in zircon. *Contr. Mineral. and Petrol.* 160, 383-390.
- De Hoog, J.C.M., Lissenberg, C.J., Brooker, R.A., Hinton, R., Trail, D., Hellebrand, E., 2014. Hydrogen incorporation and charge balance in natural zircon. *Geochimica et Cosmochimica Acta* 141, 472-486.
- Kasting, J.F., 2013. What caused the rise of atmospheric O₂? *Chemical Geology* 362, 13-25.

Niu, Y., O'Hara, M.J., 2009. MORB mantle hosts the missing Eu (Sr, Nb, Ta and Ti) in the continental crust: New perspectives on crustal growth, crust–mantle differentiation and chemical structure of oceanic upper mantle. *Lithos* 112, 1-17.